University of Alberta

Initial Excited-State Structural Dynamics and Damage Kinetics of Nucleic Acid Derivatives and a Rhodopsin Analogue

by

Swaroop Sasidharanpillai

A thesis submitted to the Faculty of Graduate Studies and Research in partial fulfillment of the requirements for the degree of

Doctor of Philosophy

Department of Chemistry

Fall 2013
Edmonton, Alberta

Dedicated to

My Family

Abstract

Photochemical reactions resulting from the absorption of ultraviolet light are one of the main causes of DNA damage. For any excited-state photochemical reaction, it is the structural changes in the excited state after the absorption of the photon that ultimately decide the photochemical fate of the molecule. In this thesis, I have explored the initial excited-state structural dynamics of nucleic acid derivatives and a rhodopsin analogue to understand the structural distortions upon photon absorption and the correlation between the observed structural dynamics and the known photochemistry.

Resonance Raman spectroscopy was used to probe the initial excited-state structural dynamics of 5,6-dimethyluracil, to understand the effect of mass changes at the C5 and C6 positions, and found that the observed initial excited-state structural dynamics are similar to those of thymine. This study showed that the methyl groups at the C5 and C6 positions are a major factor in determining how the initial excited-state structural dynamics are partitioned between the CH bending and C5=C6 stretching modes, which is directly related to the difference in the photochemistry of uracil and thymine.

The resonance Raman-derived initial excited-state structural changes of homopentamer oligonucleotides lie along similar modes as in the corresponding nucleobases or nucleotides, but with smaller distortions. The smaller excited-state distortions suggest that the initial excited-state structural dynamics are restricted by the polymeric structure. The observed homopentamer homogeneous broadening is consistent with this model.

The sequence dependence of UV-induced miRNA damage was also studied on a

microarray platform. The results suggest that guanine provides a protective effect and sequences with cytosine and uracil are more susceptible to damage, although the errors are large.

The visible resonance Raman spectroscopic studies on a rhodopsin analogue show similar initial molecular distortions along the C=C bond during the isomerization as in rhodopsin. The hydrogen out-of-plane (HOOP) mode is absent in N-alkyalated indanylidene-Pyrroline (NAIP), as expected due to the absence of C-H modes. The computed excited-state trajectories are consistent with the experimentally observed initial distortions along the C=C bond.

Acknowledgements

Apart from the efforts from my side, this thesis would not have been possible without the help, support, encouragement and guidelines of many others. I would like to express by deep sense of gratitude towards my Ph D supervisor, Prof. Glen R. Loppnow for his guidance, supervision, patience and constant motivation. His knowledge and expertise in the field of research has helped me to understand the science better and look at research in different perspective. I thank him for the freedom and choices he gave us in shaping the research and the training in making me a better researcher. Being a great teacher and administrator, discussion with him, both scientific and non-scientific, were fruitful and interesting. His way of preparing ourselves for presentations and talk in group meetings and individual meeting and his critical reviews and suggestions helped us to become better speakers. I am in debt to him, for being a great supervisor and good friend during Ph D career.

I thank Prof. Charles Lucy and Prof. Alexander Brown for being in my supervisory committee and monitoring the progress of my research at different stages of my Ph D career. Their guidance and suggestion helped me use time more efficiently in research. They were always available when I needed some guidance. I also thank, Prof. Wolfgang Jaeger, Juli Gibbs-Davis, Prof. Janice Cooke and Prof. David C. McCamant for serving in candidacy and Ph D defense committees. I am in debt to my colleagues Dr. Amira El Yazbi, Sindhu Nair and Faranak Teimoory, for their help, friendship and understanding. I am also thankful to our former group members Dr. Sulayman Adeyemi Oladepo, Steve Dempster, Christine Pinnock and Zahra Shire.

I gratefully acknowledge the services from Molecular Biology Service Unit (MBSU) especially Dr. Anthony Cornish and Troy Locke, for the help and support with microarray printing and teaching me how to use the microarray scanners and the analysis softwares. I am equally grateful to Dr. Walid El Kayal for the great discussions on microarrays and his help with microarray analysis software and

design.

Helps from people of Analytical and Instrumentation Laboratory, machine shop and glass shop are worth mentioning. The help and support from Wayne Moffat in Analytical and Instrumentation Laboratory need special mention. I am grateful to my friends Dr. Saneej Balakrishnapillai, Dr. Praveen Veluthedathukuzhi and Dr. Archana Kandakkathara for their time and help in formatting the thesis and their support. I am thankful to my all friends and their families in Canada and India for their understanding and moral support.

I am grateful to department of chemistry, FGSR and GSA, university of Alberta for the teaching assistanceship, financial support and travel awards. The help and support from Dr. Norman and Dr. Anna Jordan are gratefully acknowledged.

I would like to express my deep sense of gratitude towards my previous research guides Prof. C. T Aravindakumar, Dr. Indira Priyadharsini and Dr. Beena Singh for their encouragement, support and making be a better researcher.

Last, but not least, I would like to thanks my parents and my family for their encouragement, support and understanding.

Contents

List of Tables

List of Figures

List of Abbreviations

5,6-DMU	5, 6-dimethyluracil
5-MU	5-methyluracil (Thymine)
6-MU	6-methyluracil
A	Absorbance/Adenine
a. u.	Arbitrary units
ADP	Adenosine diphosphate
AMBER	Assisted Model Building with Energy Refinement
AMP	Adenosine monophosphate
ATP	Adenosine triphosphate
BBO	Barium borate
BLA	Bond length alternation
BSA	Bovine serum albumin
C	Cytosine
CASSCF	Complete active space self-consistent field
CCD	Charge coupled device
cDNA	Complementary deoxyribonucleic acid
CPD	Cyclobutyl pyrimidine dimer
Cy5	Cyanine 5
DFT	Density functional theory
DNA	Deoxyribonucleic acid
F	Fluorescence/Fluorophore
FAD	Flavine adenine dinucleotide
FAM	6-carboxyfluorescein
FC	Franck-Condon
FRET	F*ö*rster resonance energy transfer

G	Guanine
HSA	Human Serum Albumin
HOOP	Hydrogen- out-of-plane
HPLC	High performance liquid chromatography
IC	Internal conversion
IR	Infrared
IS	Internal standard
ISC	Intersystem crossing
LBO	Lithium triborate
MB	Molecular beacon
miRNA	micro ribonucleic acid
mRNA	messenger ribonucleic acid
NADP	Nicotinamide adenine dinucleotide phosphate
NAIP	N-alkylated indanylidene-pyrroline
NRS	Normal Raman scattering
P	Phosphorescence
PCR	Polymerase chain reaction
PED	Potential energy distribution
piRNA	Piwi-interacting ribonucleic acid
pri-miRNA	primary micro ribonucleic acid
QM/MM	Quantum mechanics/molecular mechanics
Rh	Rhodopsin
RNA	Ribonucleic acid
ROS	Reactive oxygen species
RREP	Resonance Raman excitation profile
rRNA	Ribosomal ribonucleic acid
RRS	Resonance Raman spectroscopy
S	Singlet state
SA	Self-absorption
SDS	Sodium dodecyl sulphate
SERRS	Surface enhanced resonance Raman spectroscopy
SERS	Surface enhanced Raman spectroscopy

siRNA	Small interfering ribonucleic acid
sr	Steradian
SSC	Saline-sodium citrate
T	Thymine or triplet state
TERS	Tip enhanced Raman spectroscopy
tRNA	Transfer ribonucleic acid
U	Uracil
UV	Ultraviolet
UVC	Ultraviolet C
VR	Vibrational relaxation

List of Symbols

α	Polarizability
α_0	Equilibrium polarizability
α_1	Change in polarizability with vibration
β	Hyperpolarizability
$\beta/\hbar$	Excited-state Slope
Δ	Equilibrium geometry difference between ground and excited state
ϵ	Molar extinction coefficient
ϵ_i	Energy of the initial vibrational state
ϵ_v	Energy of the virtual vibrational state
$(\frac{d\sigma}{d\Omega})$	Differential resonance Raman cross-section
Γ	Homogeneous linewidth
γ	second hyperpolarizability
μ	Dipole moment
ν_{vib}	Frequency of vibration
ν_0	Frequency of incident light
ρ	Depolarization ratio
σ_A	Absolute absorption cross-section
σ_R	Absolute resonance Raman cross-section
θ	inhomogeneous linewidth
Θ	Standard deviation in inhomogeneous linewidth
$\|f>$	final vibrational state
$\|i>$	Initial vibrational state
$\|v>$	virtual vibrational state
$`<E_0>$	Average energy
C	Concentration

d	Raman sample pathlength
E	Electric field or efficiency of the spectrometer
E_0	Zero-zero energy of the electronic transition
E_L	Energy of the incident photon

Chapter 1

Introduction

Light interacts with matter in different ways and changes the properties of both interacting species - the molecules in the substance and the photon with which it is interacting. So, probing the changes in the properties of light after it interacts with the molecule will give us valuable information about the molecular properties of matter. There is a variety of processes that can happen when light interacts with matter. Some of these are absorption, scattering, emission, reflection, refraction, diffraction, dichroism, optical rotation etc. Spectroscopy is the study of the interaction of light with matter. Light, being electromagnetic radiation, has oscillating electric and magnetic fields perpendicular to each other. Molecules can interact with the oscillating electric field and absorb energy from the light.

Nucleic acids can absorb light in the ultraviolet region of the electromagnetic spectrum and get excited electronically. The main chromophores responsible for this absorption are the nucleobases. The excited molecules get rid of the excess energy via different photophysical and photochemical pathways. Photochemical reactions leading to unwanted photoproducts are one of the deactivation pathways, as depicted in Figure 1.1. The formation of these photoproducts changes the structure and biological identity of the nucleic acid, leading to the development of mutations and cancer. So it is important to study the factors determining the extent of photoproduct formation and quantify the amount of DNA damage.

A Jablonski diagram is a simple diagrammatic representation of energy levels of a molecule and the different excited-state processes (Figure 1.1). Most organic molecules have a spin multiplicity of one (singlet state, S) in the electronic ground state (S_0). Once electronically excited, molecules are highly unstable and get rid of the excess energy in different ways. A molecule in the ground state can be

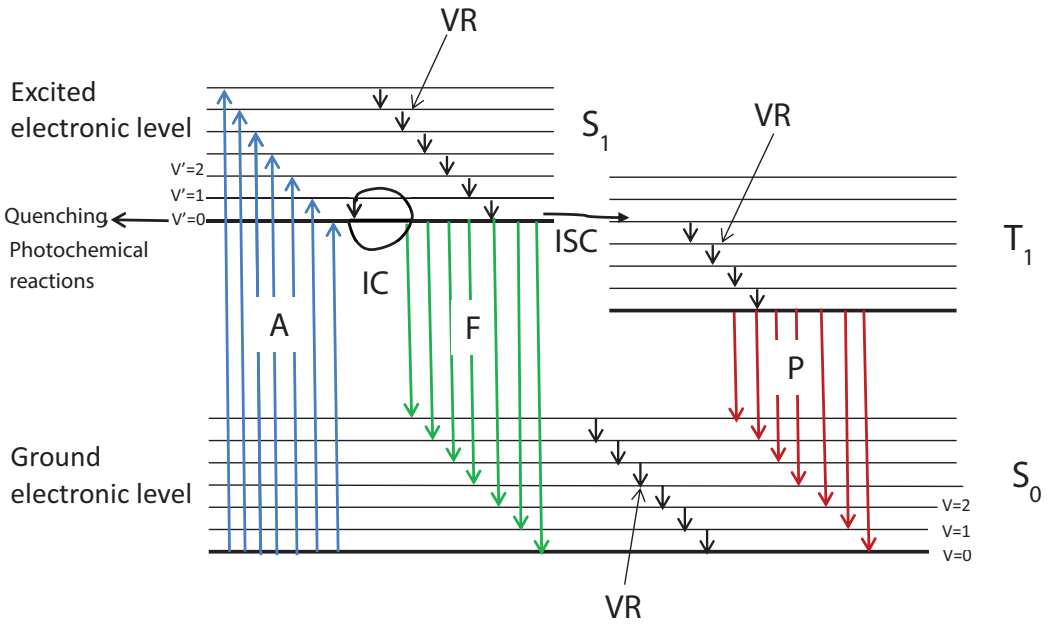

Figure 1.1: Jablonski diagram showing different excited state processes. Molecules in the ground electronic state (S_0) absorbs light (A) and get excited to the next excited electronic level (S_1). From the excited-state molecule relaxes in different ways. Fluorescence (F), intersystem crossing (ISC), internal conversion (IC), vibrational relaxation (VR), excited-state photochemistry and quenching depopulated the S_1 level. T_1 stands for the excited-triplet level and the phosphorescence occurs from that T_1 to S_0 level.

excited to different excited states when the energy of the incident photon matches the energy difference between the ground and excited states. The molecule rapidly decays back to the lower vibrational energy level of the first excited state (S_1) via non-radiative decay called vibrational relaxation (VR) and internal conversion (IC). During vibrational cooling, the excess energy is dissipated as heat. Changes in electronic energy level where the molecule goes from the lowest vibrational level of an electronic state to the highest vibrational level of the next lower electronic level is called internal conversion. The molecule in the lowest vibrational state of the first electronic excited state can undergo radiative decay called fluorescence (F), where the molecule emits excess energy in the form of light and goes back to the ground electronic state. The molecule can change spin multiplicity to the triplet state (T_1) by intersystem crossing (ISC). The molecule may emit energy in the form of light, from the excited triplet state and come back to the ground state, and is called phosphorescence (P). In the excited state, the molecule can undergo excited-state reactions as well, resulting in different types of photoproducts. The excited molecule can interact with a different molecule and undergo electron transfer or non-radiative energy transfer resulting in excited-state deactivation. Fluorescence quenching is a very good example of this type of bimolecular interaction.

Upon electronic excitation, the molecule will undergo nuclear displacement, which is one of the main factors determining the fate of the excited molecule. Thus, one of the factors determining the extent and nature of photoproduct formation is the evolution of the excited-state potential energy surface and the initial excited-state structural changes which happen after the electronic excitation of the molecule. Therefore, an understanding of the initial excited-state structural dynamics is necessary to probe the photochemistry of DNA. In this thesis I have used resonance Raman spectroscopy as a tool to probe the initial excited-state structural dynamics of different oligonucleotides and one of the nucleobase derivatives.

Further, to understand the extent of photoproduct formation in DNA and correlate it with the initial excited-state structural dynamics, we have explored the damaging effect of ultraviolet light on different nucleic acid sequences. I have used fluorescent probe-based detection of DNA damage on custom DNA/RNA microarrays for this purpose.

1.1 Resonance Raman Spectroscopy

1.1.1 Vibrational Spectroscopy

The atoms in a molecule are in constant periodic motion in addition to the translational motions. These periodic motions of the atoms with respect to one another are called molecular vibrations. For a molecule with N number of atoms, there will be 3N-6 normal modes of vibrations if it is a nonlinear molecule and 3N-5 normal modes if it is linear.[1] Infrared (IR) spectroscopy and Raman spectroscopy are two spectroscopic techniques used to measure the vibrational information about the molecule. These two techniques are complementary to each other and can be used to get a full vibrational picture of the molecule.[2] When the frequency of the incident light matches the frequency with which the molecule is vibrating, the light will be absorbed. This absorption will result in a change in the amplitude of that particular vibration. To be IR active, there should be a change in the net dipole moment of the molecule during the vibration. The electrical field of the radiation interacts with the changing dipole moment of the molecule resulting in absorption of light in the infrared frequency. Not all the vibrations in a molecule result in a change in dipole moment and so will be IR inactive. For example, in homonuclear diatomic molecules, symmetric stretching is IR inactive, since there is no change in dipole moment during the vibration.

Chemical bonds are broken and formed during chemical reactions. Each particular kind of bond has a characteristic vibration frequency. Change in the structure of the molecule will change the vibrational intensity as well as the frequency. Corresponding changes in the normal modes of vibrations of the molecule enable us to probe the structure of the molecules and dynamics of the reactions. Time-resolved infrared and Raman spectroscopy are widely used to study reactions and reaction mechanisms of ultra-fast processes.[3,4] IR spectroscopy measures the absolute vibrational energy change whereas Raman spectroscopy probes the shift in energy of the incident photon. Thus, for IR spectroscopy an infrared source is used and in Raman, we can use IR, visible or ultraviolet light sources.

1.1.2 Raman Spectroscopy

When light hits a sample, almost all the scattered photons have the same energy of the incident photon and do not contain any vibrational information about the

interacting molecules. This kind of scattering, where the incident photon and the scattered photon have the same energy is called Rayleigh scattering. The intensity of the Rayleigh scattering depends on the frequency of light used and the size of the particle. But a very small amount of scattered photons will have a change in energy with respect to the incident photon. If the scattered photon has less energy than the incident photon, it is Stokes scattering and if it has a higher energy compared to the incident photon it is called anti-Stokes scattering. This type of inelastic scattering was first observed by Chandrashekhara Venkata Raman and Kariamanickam Srinivasa Krishnan on February 28, 1928 and the phenomenon was named Raman scattering.[5] The theoretical principle associated with this effect was earlier predicted by the French scientist Leon Brillouin in 1922, and by the Austrian scientist Adolf Smekal in 1923.[6]

In Raman scattering, energy can be transferred from the electromagnetic radiation to the molecule. It can excite the molecule to a higher-energy level or de-excite the molecule by taking away the energy from an already excited molecule, as shown in Figure 1.2. The change in energy of the photon corresponds to the change in the energy level within the molecule, and can be electronic, vibrational or rotational. Raman spectroscopy is generally used to get vibrational information about the molecule and used complementarily with infrared spectroscopy to get a full vibrational picture of the molecule. Raman activity arises as a result of change in polarizability along the vibrational coordinate during a particular vibration, whereas a change in dipole moment is necessary for IR activity. Due to symmetry reasons, the modes which are IR-active are Raman inactive and vice versa for a molecule with a center of symmetry. Thus, for a homonuclear diatomic molecule the stretching mode is inactive in the infrared spectrum, but active in Raman spectroscopy.

Raman spectroscopy is a scattering technique in which only a very small fraction of the light is scattered inelastically and hence it is weak. In Raman spectroscopy, the incident light can have any frequency for excitation, since it excites the molecule from the lowest vibrational level of the ground electronic state to a virtual state. Most of the photons will come out without any change in energy, where the molecule returns back to the initial state. But a very small fraction of the incident photons, about 1 in 10 billion, will scatter with a different frequency. The scattered photon can have a frequency less than or greater than the incident photon depending upon the initial vibrational level of the molecule. According to the Maxwell-Boltzmann

distribution, at room temperature, most of the molecules will be in the ground vibrational level and are excited to a higher vibrational level upon irradiation with a photon. So the energy of the scattered photon will be less compared to the incident photon. This kind of scattering where the scattered light has a lower frequency compared to the incident photon is called Stokes scattering.

If the molecule is already in an excited vibrational level, the photon can take up the excess energy and bring it back to a lower vibrational level. In this case the scattered photon will have a higher energy than the incident photon and is called anti-Stokes scattering. The relative intensities of the Stokes and anti-Stokes lines depend upon the initial population of the ground and excited vibrational levels, among other factors. At room temperature (298 K) less than one percent of the molecules are in the vibrationally excited-state for a vibration mode around 1000 cm^{-1} and hence the intensity of anti-Stokes scattering is very weak.

Raman signals are generally weak because only one in ten billion photons scatter inelastically. That was the reason why Raman spectroscopy was not used as a routine spectroscopic tool in early days. Developments in the field of electronics and the invention of lasers led to a rapid advancement in Raman spectroscopy.[7] The availability of different types of high sensitivity detectors like CCDs and powerful monochromatic light sources like lasers helped Raman spectroscopy prevail as a main vibrational spectroscopic tool along with infrared spectroscopy. One advantage of Raman over infrared spectroscopy is the ability to analyze aqueous samples. Since water is a weak Raman scatterer, Raman spectroscopy can be used in biological samples as well as *in vivo* applications. More importantly, water is a strong IR absorber.

Though we can use any wavelength of light for excitation in Raman spectroscopy, a higher frequency of light (shorter wavelength) is often preferred. This is because the intensity of scattered light is proportional to the frequency of incident light to the fourth power. However, if we use visible or ultraviolet light for excitation for a fluorescent molecule, the molecule will absorb the incident light and result in fluorescence from the molecule. Using a longer wavelength of light for excitation can minimize the fluorescence background from the compound which will be in same region as the Stokes scattering. The use of powerful lasers for excitation increases the intensity of the Raman signal, but may also result in the degradation of the sample. So an optimum balance between the choice of excitation wavelength and

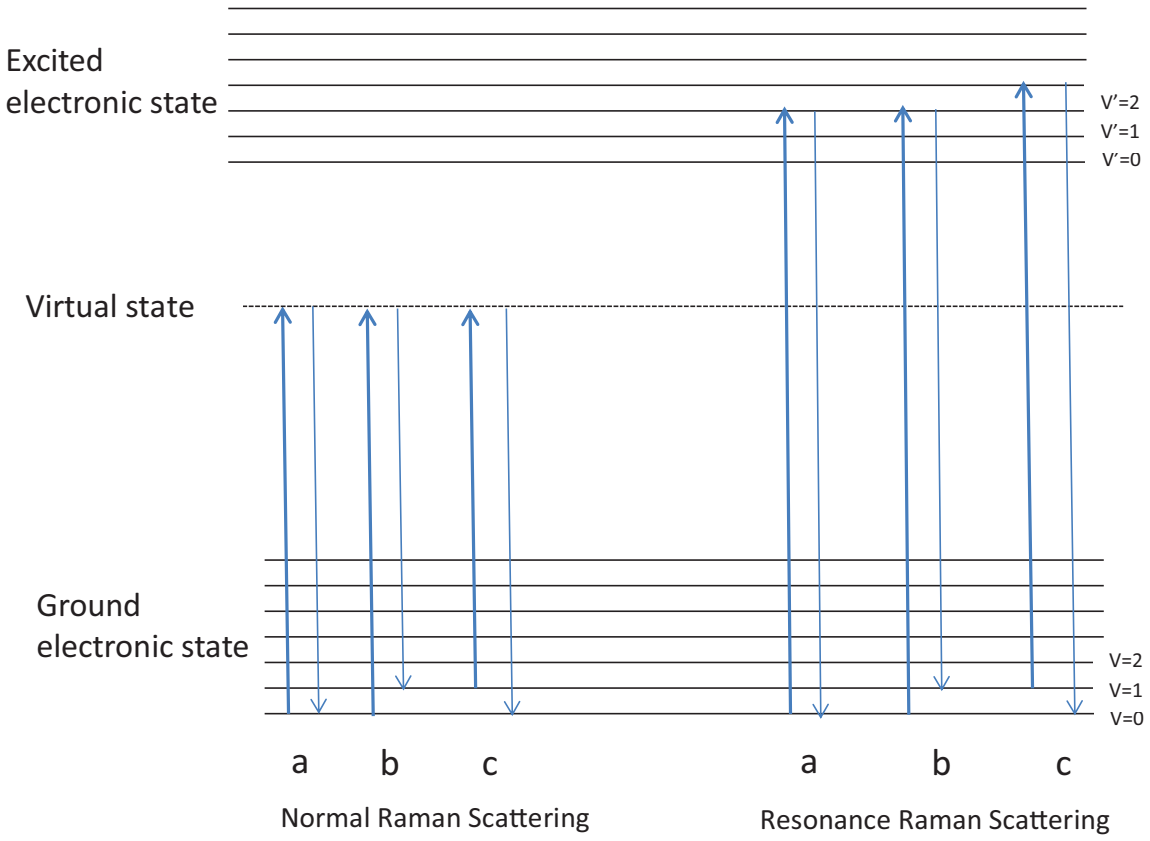

Figure 1.2: Normal Raman and resonance Raman scattering. a) Rayleigh scattering b) Stokes scattering c) Anti-Stokes scattering, v and v' represent the vibrational levels of the ground and excited electronic states, respectively.

laser power is desirable for obtaining good Raman spectra.

1.1.3 Theory of Raman Spectroscopy

When electromagnetic radiation interacts with a molecule, the electrons and the nuclei in the molecule will respond to the electric field of the electromagnetic radiation and start oscillating with the frequency of the incident light, resulting in an induced dipole moment. The induced dipole moment will be proportional to the strength of the applied electric field.

$$\mu_{induced} = \alpha E + \frac{1}{2}\beta E^2 + \frac{1}{6}\gamma E^3..... \tag{1.1}$$

where $\mu_{induced}$ is the induced dipole moment, α is the polarizability, β is the hyperpolarizability, γ is the second hyperpolarizability of the molecule and E is the applied electric field. Polarizability is a measure of the ease with which the electron cloud can be deformed under the influence of an applied electric field, which in turn depends on the molecular structure and nature of the bonds. If the frequency of incident light is ν_0, the electric field strength varies with time (t) according to the following equation.

$$E = E_0\, sin(2\pi\nu_0 t) \tag{1.2}$$

$$\mu_{induced} = \alpha E = \alpha E_0\, sin(2\pi\nu_0 t) \tag{1.3}$$

The oscillating dipole acts as a source of electromagnetic radiation and radiates electromagnetic radiation with the same frequency (ν_0) as that of the incident light. If the molecule undergoes some internal motions like rotation or vibration that change the polarizability of the molecule periodically, that will result in additional frequencies. Then the polarizability will have a static term α_0 and an oscillating term with amplitude α_1. That is,

$$\alpha = \alpha_0 + \alpha_1\, sin(2\pi\nu_{vib} t) \tag{1.4}$$

where α_0 is the equilibrium polarizability and α_1 is the change in polarizability with a particular vibration ν_{vib}. If we assume that the second and third term in Equation 1.1 is negligible, which is generally true in most cases, we have

$$\mu_{induced} = (\alpha_0 + \alpha_1\, sin(2\pi\nu_{vib}t))E_0\, sin(2\pi\nu_0 t) \tag{1.5}$$

$$\mu_{induced} = \alpha_0 E_0\, sin(2\pi\nu_0 t) + \frac{1}{2}\alpha_1 E_0[cos(2\pi(\nu_0 - \nu_{vib})t) - cos(2\pi(\nu_0 + \nu_{vib})t)] \tag{1.6}$$

So classically, the oscillating dipole has frequencies different from the incident frequency, with $\nu_0 - \nu_{vib}$, shorter than the incident frequency and $\nu_0 + \nu_{vib}$ greater than the incident frequency. From the above equation, it should be noted that the Raman shifts observed are independent of the frequency of the incident light. The first term in the equation represents the Rayleigh scattering where there is no change in the frequency of light. The subsequent terms with $cos(2\pi(\nu_0 - \nu_{vib})t)$ and $cos(2\pi(\nu_0 + \nu_{vib})t)$ denote the Stokes and anti-Stokes scattering, respectively.

1.1.4 Resonance Raman Spectroscopy

There are different spectroscopic techniques to enhance the intensity of Raman signals like resonance Raman spectroscopy (RRS), surface-enhanced Raman spectroscopy (SERS)[8], surface-enhanced resonance Raman spectroscopy (SERRS)[9–11], tip-enhanced Raman spectroscopy (TERS)[12] etc. In SERS, the molecule is adsorbed on a rough metal surface. The Raman signal from the adsorbed molecule is significantly enhanced, as much as 10^{10} compared to normal Raman signal intensity.[13] But randomness in the substrate leads to variation in the signal in SERS. In TERS, the substrate is reduced to sharp tip, which can be positioned on sample surface, and thus overcome the substrate randomness in SERS. TERS is generally used as a high-resolution imaging technique. Each of these methods has its own advantages and disadvantages.[14]

When the wavelength of light used for the excitation coincides with the electronic absorption band of the molecule, the Raman signal is highly enhanced and is called resonance enhancement. The schematic representation of resonance Raman scattering is shown in Figure 1.2. If the vibrational motion is coupled to the electronic excitation of the molecule, that mode will be significantly enhanced. Since resonance Raman enhancement is achieved by the electronic excitation of the chromophore, it is possible to selectively enhance a part of the molecule and study a particular chromophore of interest without affecting the other parts of the molecule. Those Raman scattering signals contain information about the rovibronic coupling

dynamics of the excited-state of the chromophore only.[14] Thus, resonance Raman spectroscopy provides a valuable tool to selectively study a part of the molecule or a type of a particular molecule in a mixture if the excitation wavelength is wisely chosen.

1.1.5 Resonance Raman Spectra and Absorption Spectra

The molecule has to be excited with a frequency of light which is close to the electronic absorption frequency of the molecule to see resonance Raman enhancement. If we look at the electronic absorption spectrum of a molecule in the gas phase, we will see a vibrational fine structure in the absence of any other broadening effects. This absorption spectrum is a sum of all individual transitions from the ground vibrational levels of the ground electronic state to different vibrational levels of the excited electronic state. The intensity of each of these transitions depends upon the transition probability and population, which in turn depends on the extent of overlap between the ground-state and excited-state vibrational wave functions (Frank-Condon principle).[15] The vibrational fine structure in the absorption spectrum is lost in solution due to the fact that all these individual vibrational transitions are subjected to different types of broadenings factors like homogeneous and inhomogeneous broadening. So, all vibrational information is lost in the absorption spectrum and a broad featureless band is often observed.[16] If the absorption spectrum is composed of two or more electronic transitions, the resonance Raman enhancement may be different for these two electronic transitions. So a good understanding of the absorption spectrum is essential for the correct interpretation of the resonance Raman spectra.

1.1.6 Initial Excited-State Structural Dynamics

Resonance Raman spectroscopy has been used to study initial excited-state structural dynamics of molecules for over a quarter century now.[17] Because resonance Raman scattering intensity study is a probe of the change in molecular polarizability with molecular vibration in the presence of an oscillating electromagnetic field, it is a measure of dynamic coupling between the electronic and vibrational motion within the molecule. If the excitation wavelength matches the electronic transition of the molecule under investigation, Raman scattering will be dominated by the dynamic coupling of vibrational and electronic levels in the excited state. The in-

tensities of different modes are appreciably enhanced when this resonance condition is achieved.[18] So it is possible to get information about the initial excited-state structural dynamics of the molecule from the resonance Raman intensities within an absorption band of the molecule.

The resonance Raman intensities are converted to resonance Raman cross-sections by comparing the intensities to the Raman intensity of a standard whose cross-section is already known. Resonance Raman cross-sections are a measure of the scattering efficiency of the molecule when it is in resonance with an electronic absorption. Cross-sections are usually measured in area/molecule with units of cm^2/molecule or barn (1 barn= 10^{-24} cm^2/mol). A plot of resonance Raman intensity as a function of excitation wavelength within an absorption band for a particular mode will yield a resonance Raman excitation profile. Relative intensities of resonance Raman excitation profiles are a clear reflection of the relative changes in excited-state structure along those particular vibrational coordinates.

Understanding initial excited-state structural dynamics with the aid of resonance Raman spectroscopy requires accurate normal mode assignments. Raman and IR measurements along with computational methods are being effectively used in determining normal modes.[19,20] Another effective way to assign normal modes is isotopic substitution. On isotopic substitution, the vibrational frequency of the bonds involving the substituted atom will change, without affecting most other modes. So with isotopic substitution of appropriate atoms in the molecule, it is possible to assign vibrational frequencies for unknown modes.

Resonance Raman cross-sections can be calculated quantum mechanically from the sum-over-states expression, which is derived from the dispersion expressions of Kramers and Heisenberg[21] and Dirac[22] using second-order time-dependent perturbation theory

$$\sigma_R = \frac{8\pi^4 M^4 E_S^3 E_L}{9\hbar^4 c^4} \int_0^\infty dE_0 H(E_0) \left| \sum_\nu \frac{< f|v >< v|i >}{\epsilon_v - \epsilon_i + E_0 - E_L - i\Gamma} \right|^2 \qquad (1.7)$$

where σ_R is the resonance Raman cross-section, M is the transition length, $|i>, |v>$ and $|f>$ denote the initial, virtual and final vibrational states respectively, E_L and E_S are the energies of the incident and scattered photons respectively, ϵ_i is the energy of the initial vibrational state and ϵ_v is the energy of the virtual vibrational state. E_0 is the zero-zero energy of the electronic transition (energy difference

between the lowest vibrational level of the ground- and excited-states), Γ denotes the homogeneous linewidth, $H(E_0)$ is the inhomogeneous linewidth function defined by the following equation.

$$H(E_0) = (2\pi\theta)^{-}\frac{1}{2}exp\left\{-(< E_0 > -E_0)^2/2\theta^2\right\} \tag{1.8}$$

θ is the standard deviation in $H(E_0)$ and $< E_0 >$ is the average energy.

For the simplicity of the calculation and for practical use, the time-dependent analog of Equation 1.7 is more appropriate and convenient.

$$\sigma_R = \frac{8\pi e^4 M^4 E_s^3 E_L}{9\hbar^6 c^4}\int_0^\infty dE_0 H(E)_0 \left|\int_0^\infty < f|i(t) > e^{i(E_L+\epsilon_i)t/\hbar}G(t)dt\right|^2 \tag{1.9}$$

where G(t) is the homogeneous linewidth and the propagation of initial vibrational wavefunction on the excited-state potential energy surface is given by $|i(t)>$

$$|i(t) >= e^{-iHt/\hbar}|i > \tag{1.10}$$

The optical absorption cross-section is given by

$$\sigma_A = \frac{4\pi M^2 e^2 E_L}{6\hbar^2 cn}\int_0^\infty dE_0 H(E)_0 \int_{-\infty}^\infty < i|i(t) > exp\left[\frac{i(E_L+\epsilon_i)t}{\hbar}\right]G(t)dt \tag{1.11}$$

$<i|i(t)>$ is the overlap between the initial wave function and the initial ground-state vibrational wave function propagated on the excited-state potential energy surface, and $< f|i(t) >$ is the overlap of the final state vibrational wavefunction with the initial vibrational wavefunction propagated on the excited-state potential energy surface. The overlap between the two wavefunctions depends on the initial force, $\beta/\hbar$, ($\beta/\hbar = \bar{\nu}\Delta$) that the molecule experiences along that particular vibrational co-ordinate in the electronic excited-state. The overlap of $<i|i(t)>$ and $<f|i(t)>$, is dependent on the change in equilibrium geometry between ground and excited state, Δ, which is shown in Figure 1.3. So the resonance Raman cross-section and absorption cross-section are directly related to initial excited-state structural dynamics of the molecule. Thus, it is possible to extract information about the initial excited-state structural dynamics by measuring the resonance Raman cross-section and the absorption cross-section simultaneously. Equation 1.9 and 1.11 are the theoretical relations connecting resonance Raman cross-section and absorption

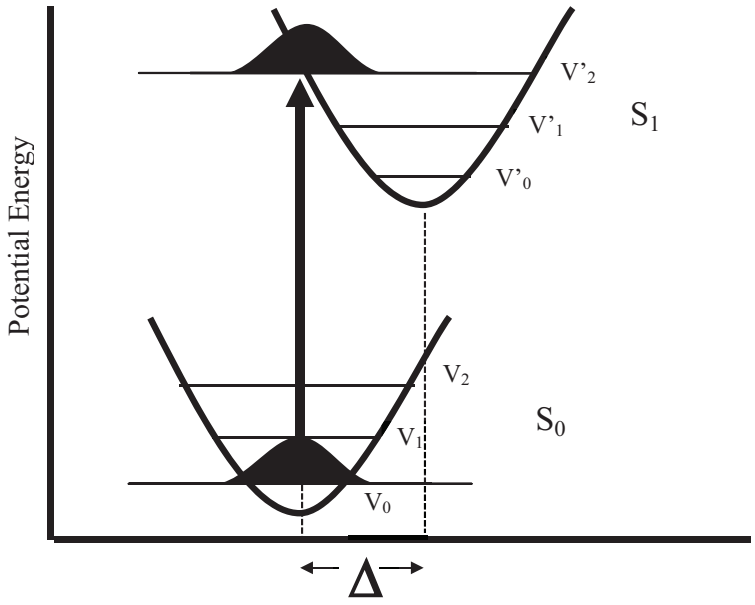

Figure 1.3: Potential energy diagram, showing a change in equilibrium position between the ground and excited-state, denoted by Δ. The vibration levels are denoted by v and v' in the ground and excited electronic states, respectively.

cross-section. It can be easily seen that these two equations depend on similar parameters, but in different ways. It is this commonality between the two equations that enables us to measure the initial excited-state structural dynamics by measuring the absorption spectrum and resonance Raman cross-sections.

Resonance Raman cross-sections are calculated experimentally from resonance Raman intensities using the following equation.

$$\sigma_{Samp} = \sigma_{std} \frac{I_{Samp}[Std] E_{Std} L_{Samp} n_{Samp} (\frac{1+2\rho}{1+\rho})}{I_{Std}[Samp] E_{Samp} L_{Std} n_{Std} (\frac{1+2\rho}{1+\rho})} 10^{dC(\epsilon_{Samp} - \epsilon_{Std})} \tag{1.12}$$

where σ_{Samp} and σ_{std} are absolute resonance Raman cross-sections of the sample and the standard, respectively, I is the resonance Raman intensity, E is the efficiency of the spectrometer, L is the internal field correction which is equal to $[(n^2+3)/3]^4$, n is the refractive index, ρ is the depolarization ratio, d is the pathlength of the Raman sample, C is the concentration of the absorbing species and ϵ is the molar extinction coefficient. As in most cases, if an internal Raman standard is used, then L_{Samp}=L_{Std} and n_{Samp}= n_{Std}. Commonly used internal standards are nitrate, sulphate, cyclohexane, acetonitrile and benzene. The Raman cross-sections of these standards at different resonance Raman excitation wavelengths are known. The differential self-absorption of the Raman signal by the sample is represented by the term, $10^{dC(\epsilon_{Samp} - \epsilon_{Std})}$ where d is the pathlength of the incident laser over which the laser power decreases by half and ϵ is the extinction coefficient at that laser wavelength.

The differential and absolute Raman cross-sections are related by the following equation

$$\sigma_R = \frac{8\pi(1+2\rho)}{3(1+\rho)} \frac{d\sigma_R}{d\Omega} \tag{1.13}$$

where Ω is the solid angle. Combining Equation 1.12 and 1.13 gives the equation of the differential cross-section for samples with internal standard as,

$$\frac{d\sigma_S ample}{d\Omega} = (\frac{d\sigma_{std}}{d\Omega}) \frac{I_{Samp}[Std] E_{Std}}{I_{Std}[Samp] E_{Samp}} 10^{dC(\epsilon_{Samp} - \epsilon_{Std})} \tag{1.14}$$

The resonance Raman intensities of each peaks are calculated from the area under the peak and the self-absorption correction factor is calculated by knowing ϵ_{Samp} and ϵ_{Std} at different absorbing wavelengths. For an internal standard with

a known differential cross-section, the differential cross-section of the sample is calculated by measuring the relative area under the peaks.

1.1.7 Overtone and Combination Bands

Most of the molecular vibrations we see in infrared and Raman spectroscopy arise from the vibrational transition from the ground vibrational level to the first excited vibrational level within the ground electronic level. But the transitions to higher vibrational levels within the ground electronic state are also possible, though they are theoretically forbidden, low intensity bands. Those transitions are called vibrational overtones[23]. The transition from the ground vibrational level to the second vibrational level is called the first overtone $\nu_0 - \nu_2$, and to the third vibrational level is called the second overtone $\nu_0 - \nu_3$, and so on. The frequency of these overtones will be twice and thrice the fundamental frequencies, respectively. In reality, the frequencies will be a little less than the calculated frequencies, due to anharmonicity.

Sometimes there are bands observed at frequencies that correspond to the sum of two fundamental vibrations. For example, it is possible to see bands that correspond to $\nu_1 + \nu_2$ where ν_1 and ν_2 are two fundamental vibrations. Different types of combination between different fundamentals are possible. These kinds of bands resulting from the sum of two different fundamental vibrations are called combination bands.

1.1.8 Applications

Raman spectroscopy has been used along with infrared spectroscopy to gain valuable vibrational information about molecules. Raman spectroscopy is especially useful when dealing with aqueous samples, where water is a weak Raman scatterer.

With the invention of tunable lasers, it is now possible to get almost any desired laser wavelength. This ability allows us to use the capability of resonance Raman spectroscopy to the fullest. Resonance Raman intensities can provide information about the electronic excited states of the molecule where the intensities depend upon the structural dynamics of the molecule along that particular co-ordinate. This makes resonance Raman spectroscopy a powerful tool in understanding the excited-state structural dynamics of molecules. Resonance Raman intensities are proportional to the slope of the excited-state potential energy surface for a given

vibrational co-ordinate. Therefore a higher resonance Raman intensity is observed for modes which lie along the direction of molecular dynamics. This method has been successfully used by different researchers to study the initial excited-state dynamics of a variety of compounds.[24,25,25,26] These kinds of studies have helped in unfolding the relation between excited-state structural dynamics and photochemistry in different systems. Similar resonance Raman spectroscopic techniques have been used in studying inorganic complexes, porphyrins, heme proteins, DNA nucleobases etc.[14]

Resonance Raman spectroscopy has the unique property of selectively enhancing the Raman signals from the molecule in a mixture whose absorption frequency matches the excitation wavelength of the laser. This makes it possible to selectively study a molecule of interest in a mixture by choosing the appropriate excitation wavelength. These kinds of studies are possible in a complex mixture only if the resonance Raman cross-section of the molecule at that excitation wavelength is higher than that of other components present in the mixture. This method has been successfully used in our research group in the past to analyze the active ingredients in sunscreen[27] and to obtain the signal of a DNA damage product, 8-oxodeoxyguanosine, in the presence of other nucleobases.[28]

1.2 Nucleic Acid Properties and Damage

1.2.1 Nucleic Acids

Nucleic acids are biopolymers which serve as the primary storage of genetic information for the propagation of life. There are two kinds of nucleic acids, deoxyribonucleic acid (DNA) and ribonucleic acid (RNA). Nucleic acids are chain polymers of nucleotides. The function and properties of a nucleic acid is determined by the sequence of nucleotides in the chain and the length of the chain. A nucleotide is made of three components: a nucleobase, a sugar and a phosphate group. The pentose sugar in RNA is a ribose sugar and a 2'-deoxyribose sugar (the 2'carbon on the sugar lacks an oxygen atom) in DNA. Nucleobases are heterocyclic, planar purine or pyrimidine derivatives. There are five major nucleobases: adenine (A), cytosine (C), guanine (G), thymine (T) and uracil (U). Adenine and guanine are purines whereas cytosine, thymine and uracil are pyrimidine derivatives. Adenine, guanine, cytosine and thymine are found in DNA and the thymine in DNA is replaced by uracil in

RNA. The nucleobases are linked to the C1 of the pentose sugar through the N9 of purine bases and N1 of pyrimidine bases. The structure of different nucleobases and nucleotides (with different sugars) are given in Figure 1.4.

Although most of the nucleotides in a cell are in DNA or RNA, there are other forms of nucleotides performing functions other than transfer and storage of information. Adenosine triphosphate (ATP), adenosine diphosphate (ADP), adenosine monophosphate (AMP) act as energy transfer devices. Flavin adenine dinucleotide (FAD) is a main constituent of many reduction-oxidation reactions taking place in the cell. Another compound with a similar function is nicotinamide adenine dinucleotide phosphate (NADP).

Nucleotides in nucleic acids are joined together at the 3' and 5' positions of adjacent nucleotides by a phosphate through phosphodiester bonds. The terminal nucleotide whose C3' is free is called the 3' end. The one which has a free C5' is called the 5' end. In 1953, James Watson and Francis Crick proposed the structure of DNA[29]. DNA usually exists as a double helix, with the two strands of DNA held together by hydrogen bonds, where one strand of DNA is running anti-parallel to the other. The hydrogen bonds are formed between the nucleobases on the opposing strands. Thymine forms two hydrogen bonds to adenine and there are three hydrogen bonds between guanine and cytosine, as shown in Figure 1.5. This kind of interaction is called complementary base pairing, and is important in transferring genetic information, replication and other site recognition processes. DNA helices are right handed with the nuclobases inside and the sugar-phosphate backbone outside. There is a major and minor groove in DNA which determines the type of helix. RNAs are usually single stranded and serve as a link between DNA and proteins. There are different kinds of RNAs which have different functions in the cell.

1.2.2 Central Dogma of Biology

The central dogma of molecular biology, describes how the sequential information in DNA is transferred and used in making proteins. The three most important biopolymers, DNA, RNA and protein are involved in this flow of information. The information in DNA is stored in the DNA sequence, which is transcribed to mRNA. The mRNA is then translated to protein.

The sequential information in DNA is preserved by DNA replication, where each

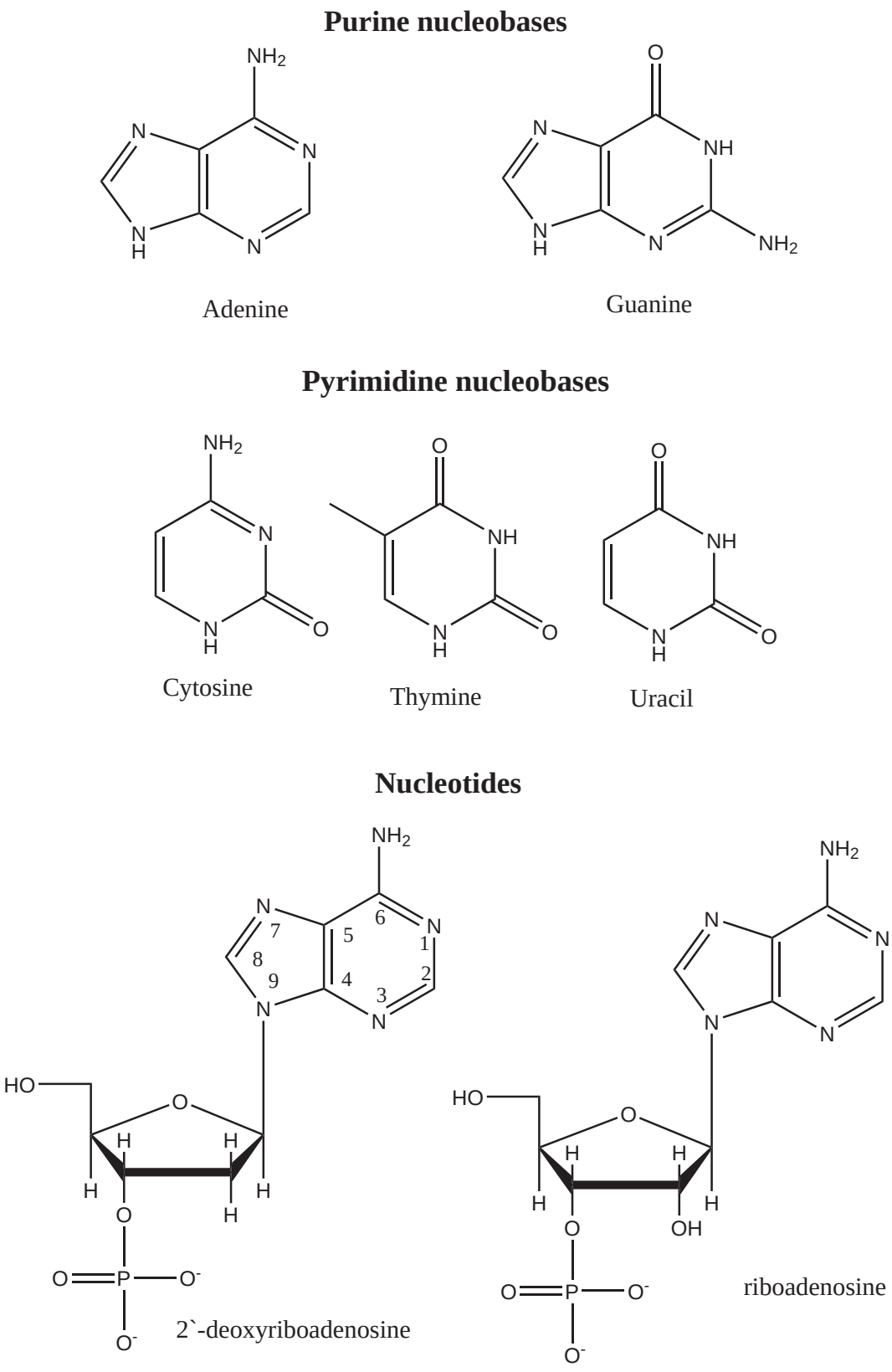

Figure 1.4: Structures of nucleic acid components.

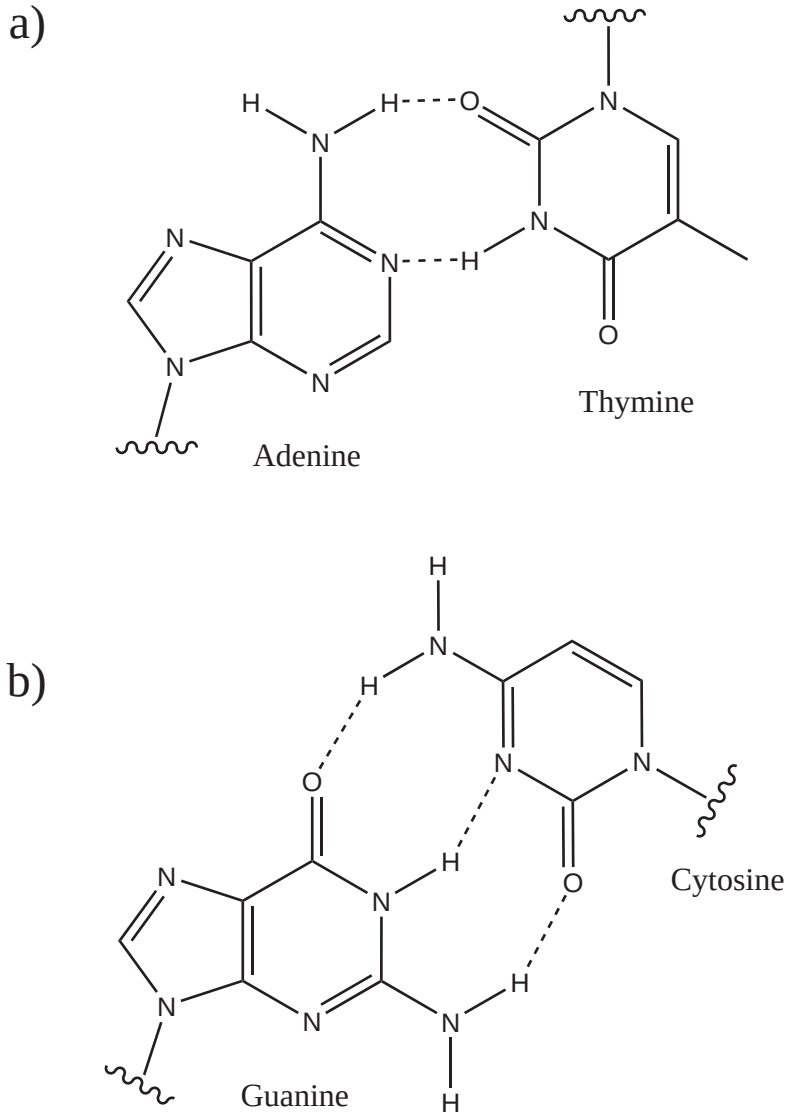

Figure 1.5: Watson-Crick base pairing in DNA. a) Adenine and thymine form two hydrogen bonds and b) guanine and cytosine form three hydrogen bonds.

strand of a double-stranded helical DNA is unwound and each strand is replicated separately. This information is copied on to messenger RNA (mRNA) with the aid of RNA polymerase. Transcription is a well-executed collection of sequential processes. At first, a small portion of the double-stranded DNA is unwound, forming a structure called a transcription bubble. The enzyme helicase moves the transcription bubble across the DNA strand, unwinding the DNA by breaking the hydrogen bonding between the DNA strands. Subsequently, various transcription factors bind to the promoter region of the DNA and facilitate the binding of the RNA polymerase to the DNA strand. RNA polymerase adds the complementary RNA nucleotides to the single stranded DNA in the 3'→5' direction and synthesizing mRNA in 5' →3' direction. The hydrogen bonds formed between the DNA-RNA hybrid break and RNA is released after the chain termination step in the transcription process, in which polyadenylation at the 3' end of RNA occurs.

Translation takes place inside the ribosome. mRNA contains the information for protein synthesis in the form of triplet codons. Each of the triplet codons is specific for an amino acid. The mRNA nucleotide sequence is read by the ribosome subunit and amino acids are added one by one to the C-terminus of the previous amino acid. Transfer RNA (tRNA) transfers specific amino acids to the site of protein synthesis. tRNAs attach to specific amino acid through sites called anticodons. The peptide bond formed between amino acid units elongates the chain and the process of chain termination occurs when it encounters the stop codon.

1.2.3 Different Types of RNA

There are some RNAs which do not code for proteins. Transfer RNA (tRNA) and ribosomal RNA (rRNA), which are involved in the translation process, fall into the non-coding class of RNA. Transfer RNA carries amino acids specified by the triplet codon of mRNA to the site of protein synthesis. Ribosomal RNA is the molecular component of a ribosome. rRNA translates polypeptides by decoding mRNA into amino acids and serves as the site for protein synthesis. There is an entirely different class of RNAs called small RNAs and these are discussed in the following section.

1.2.4 Small RNAs

There are different classes of small RNAs which are believed to be very important in cellular functions. There are three major classes of small RNAs namely microRNA

(miRNA), small interfering RNA (siRNA) and Piwi-interacting RNA (piRNA). This classification is based on the difference in the biogenesis of these small RNAs. The double-stranded small interfering RNAs are processed from long endogenous double-stranded RNA by a Dicer protein, whereas miRNAs are derived from hairpin precursor RNAs, primary miRNA (pri-miRNA). pri-miRNA can be coding or non-coding.[30,31] piRNAs arise from intergenic repetitive elements in the genome called piRNA clusters.[32] But the mechanism and biogenesis of piRNA are still unclear. Since the sequencing of a small RNA for the first time in 1965[33], the number of small RNA classes discovered and identified have been increasing rapidly.

1.2.5 MicroRNAs

miRNAs are 18-24 nucleotide long RNA molecules which take part in gene regulation. Studies have explored the role of miRNAs in animal and plant development.[34–38] The first miRNA was discovered by Ambros, et al. in 1993.[39] It took another 7 years for the second miRNA to be identified.[40] miRNAs regulate the gene expression at different levels of cellular development, both at transcriptional and post transcriptional levels. miRNA cleaves the target mRNA inducing its degradation by imperfect base pairing with the mRNA and suppressing the translation process.[41] Only 2 to 8 bases at the 5' end of the mature miRNA, called the seed sequence, are important in target recognition.[42] There are different computer programs to predict the target mRNA for a specific miRNA.[43,44] All these computational target predicting algorithms use the seed sequence to predict the targets.[43,44] It has been found that each miRNA can regulate about 200 different mRNA targets. Based on that, it is estimated that about 30 percent of total mRNAs in human are controlled by miRNAs.

1.2.6 Electronic Properties of Nucleic Acids

All the photochemical and photophysical properties of nucleic acids arise from both the excited and ground electronic properties of nucleobases. The electronic absorption spectrum of a nucleic acid is characterized by an absorption maximum around 260 nm, which corresponds to the $\pi \rightarrow \pi^*$ transition within the nucleobase. The absorption spectra of individual nucleobases are slightly different from one another, but all have an absorption maximum around 260 nm.[45,46] The absorption spectra of nucleic acids are similar to that of individual nucleobases except that the

absorbance of DNA will be less than the sum of the absorbances of individual bases. This phenomenon is called hypochromism.[47,48] The main reason for the decrease in the absorbance is the base stacking interaction between the bases.

The inherent very low fluorescence quantum yield of nucleobases arises from the very short excited-state lifetimes. That is also the reason for the relatively low quantum yield of photoproducts. The excited-state photophysics and photochemistry of nucleobases and nucleic acid have been studied extensively for the past few decades and the number of reviews about the subject reveal its fast paced advancements and importance.[49–51] The first report of the fluorescent quantum yields of nucleic acid bases at room temperature came from Daniel and Hauswirth in 1971.[52] The reported quantum yields were 2.6×10^{-4}, 3.0×10^{-4}, 0.8×10^{-4}, and 0.5×10^{-4} for adenine, guanine, cytosine, and uracil, respectively. Time-resolved absorption and fluorescence were used to study the excited-state dynamics of the nucleobases. In nucleobases, non-radiative pathways dominate the excited-state deactivation. The $\pi\pi^*$ transition in DNA decays on a femtosecond time scale. Pecourt et al. have measured the lifetimes in DNA nucleosides to be 290, 460, 720 and 540 femtoseconds for adenine, guanine, cytosine and thymine nucleosides, respectively.[53,54] The decay of the S_1 is thought to occur through a conical intersection.[53,54] This photochemical stability of the nucleobases of DNA has helped in the evolution of life on earth. Therefore, it is of great importance to understanding electron transfer processes and energy transfer in DNA. Though nucleotides in the electronic excited-state undergo non-radiative decay on the sub-picosecond timescale, the decay of the electronic excited state in the polymer forms is slower.[49]

To understand the photophysics and photochemistry of DNA and RNA, it is always better to start off with the constituent nucleobases. So the discussion about the excited-state dynamics of nucleobases is essential. Each of the nucleobases has different tautomeric structural forms, and the dynamics may be different for different tautomers. Apart from the allowed $\pi \rightarrow \pi^*$ transition in the UV region, there is an $n \rightarrow \pi^*$ transition resulting from the heteroatom on the nucleobases. But this transitions is highly forbidden in the absence of any strong coupling of the electronic levels.

1.2.7 Vibrational Properties of Nucleic Acid

A full picture of molecular vibration is an essential starting point for any study of the excited-state structural dynamics of nucleobases using resonance Raman spectroscopy. There have been many experimental and computational studies of the vibrational properties of nucleobases and nucleic acid.[19,20,26,55–61] In general, most of the vibrations fall between 300 cm^{-1} and 1700 cm^{-1}. Although the vibrational mode assignment is easy for simple diatomic molecules, it becomes tedious as the molecules become larger. Each vibrational band we see in a Raman spectrum for a polyatomic molecule, is not coming from a single vibration within the molecule. It will be a combination of different internal coordinates in different proportions to arrive at the normal mode of vibration. For example, the 1664 cm^{-1} mode of uracil is assigned to a combination of 71 % C_4-O_{10} stretch, 8 % of C_4-C_5 stretch and 5 % ring deformation.[57] Similarly, the mode at 580 cm^{-1} is combination of 32 % ring deformation 3, 23 % C_2O_8 bending, 18 % C_4O_10, 6 % C_4C_5 stretch and 6 % C_6N_1 stretch. The 789 cm^{-1} mode is composed of 28 % C_4C_5 stretch, 19 percent of N_1C_2 stretch, 13 %ring deformation 1, 10 % N_3C_4 stretch, 7 % ring deformation 3, 6 % C_2N_3 stretch and 6 % C_6N_1 stretch. The most intense mode in uracil at 1235 cm^{-1} is resulting from 33 % C_5-H_{11} bend, 18 % C_6-H_{12} bend, 15 % C_6-N_1 stretch, 10 % N_1-H_7 bend, 7 % N_3-C_4 stretch and 5 % N_1-C_2 stretch and so on. These mode assignments are usually done with the aid of computational calculations.[2,19**?**]

A complete vibrational picture of a polyatomic molecule is only possible by using different vibrational spectroscopic techniques and theoretical calculations.

1.2.8 DNA Photochemistry and UV Damage

The ultraviolet (UV) spectrum is classified into three regions based on the light's physiological effects.[62] The region from 190-290 nm is called ultraviolet C (UVC), region from 290 to 320 is the ultraviolet B (UVB) region, and ultraviolet A (UVA) region of the ultraviolet spectrum is from 320 to 380 nm. UVC radiation is largely absorbed by ozone and oxygen in the stratosphere and does not significantly reach the earth surface. The shortest solar wavelength reaching the earth's surface is 290 nm.[62] The effects of ultraviolet radiation on living things are of particular importance due to two main reasons. Although the amount of ultraviolet rays reaching the earth's surface is small compared to the visible and infrared wavelengths, it is the most energetic radiation reaching the earth's surface under normal conditions.

More importantly, the molecular building units of living system, nucleic acids and proteins, absorb this high energetic radiation and undergo chemical and structural changes.

The harmful effect of ultraviolet radiation has been known for almost a century. Although the bactericidal action of ultraviolet radiation has been known for a long time, there was a tremendous interest in understanding its damaging effect on living systems. Gates found[63] in 1928 that UV light damages biological molecules. The mutagenic actions of ultraviolet light were studied by C. W. Emmons et al.[64] who found that ultraviolet radiation can induce mutations in cultures of dermatophytes and E. Knapp et al.[65] in 1939 quantitatively analyzed the mutation. Ten years later R. L. Sinsheimer et al.[66] initiated studies on the photochemical action of nucleobases and their derivatives. A series of studies on the UV effects on nucleic acid components done towards the end of 1950s helped in understanding the UV-induced changes in nucleic acids.[67–70] It was soon found by Beukers et al. that the irradiation products revert back to thymine when subjected to UV light of the same wavelength.[70] The characterizations of the photoproducts formed were done using molecular weight determination using the Signer isometric method, crystallography, infrared and NMR. All these experiments suggested the formation of a thymine dimer.[71] The first report about thymine dimer formation in living system came in 1962 from the work of Wacker et al.[72]. Most of these earlier studies were done in frozen solutions. The dimer formation was attributed to the thymine concentration and correct orientation of the thymine molecule to undergo the *cis-syn* dimer formation via a $2\pi + 2\pi$ cycloaddition reaction[73] as shown in Figure 1.6. Later, it was found that the photodimer formation is not just limited to thymine. Dimers like C-C, U-U, T-C, T-U were also reported.[74]

Another kind of photoproduct formed during UV irradiation in the presence of water molecules, is the photohydrate. These photoproducts are formed as a result of the addition of water molecule across the pyrimidine C_5=C_6 double bond.[69,75] Another important class of DNA photodamage is the formation of 8-oxo-2'-deoxyguanosine (Figure 1.6). Guanosine, being the nucleobase with the lowest oxidation potential[76], can transfer electrons to a photosensitizer with higher oxidation potential, forming a guanosine cation radical. This cation radical will undergo hydration and subsequent oxidation giving rise to 8-oxo-2'-deoxyguanosine.[77] The extent of all these photoreactions depends on the sequence and environment of the nucleic acid.

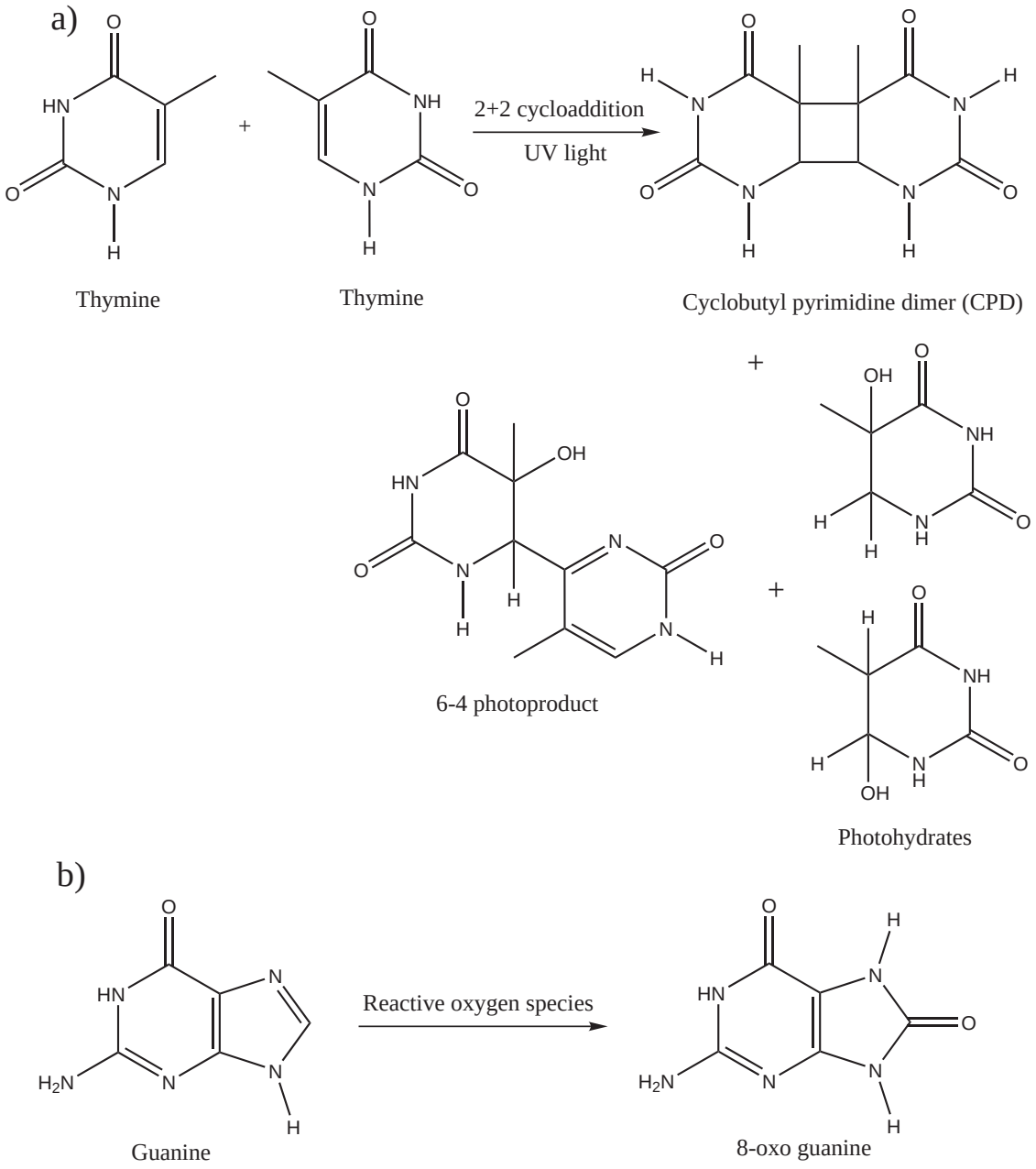

Figure 1.6: DNA photoproduct formation. a) Thymine photoproduct formation in the presence of UV light, b) formation of 8-oxo-guanine in the presence of reactive oxygen species (ROS).

Photoproduct formation is important despite the low photochemical quantum yields. Even small changes in the structure of nucleic acid can have large physiological consequences.[78] Among the different nucleobases, pyrimidine nucleobases are more photolabile than purine nucleobases. Thymine and uracil have the highest photochemical quantum yield, followed by cytosine.[78] Though the photochemical quantum yields are similar for thymine and uracil, the ratio of photoproducts formed are different. In thymine the ratio of cyclobutylpyrimidine dimer to photohydrate is 70:30 and the ratio is reversed in uracil[79]. The only difference between uracil and thymine is the presence of the methyl group at the C5 position in thymine. Our group has successfully used resonance Raman spectroscopy to explore the difference in initial excited-state structural dynamics of thymine and uracil and found that they are different. This difference in initial excited-state dynamics may account for the difference in photoproducts.[56,57] The initial excited-state structural dynamics of thymine lies along the C_5=C_6 bond, which is the most active mode during the dimer formation. In contrast, the most intense mode in uracil is the 1235 cm^{-1} mode, assigned to the C_5-H and C_6-H bending coupled to other bending modes along the ring and the initial excited-state dynamics in uracil occurs along the pyrimidalization of the C_5 and C_6 carbons. So the origin of the difference in the initial excited-state structural dynamics between thymine and uracil is attributed to the greater localization of the vibration in thymine resulting from the presence of methyl group at C_5 position. Loppnow et al. have looked into the reason for this photochemical difference by changing the mass and position of the C-5 substituent.[58,59,61]

Molecules undergo electronic and structural changes in the excited-state following photon absorption. Nucleobases and nucleic acids undergo very fast electronic relaxation from the excited-state and this is one of the reasons for the low photochemical quantum yields of nucleic acids. The electronic changes in nucleic acid and nucleobases excited states have been done using different ultrafast time-resolved techniques and have been reviewed in the past.[49,50]. However, little insight into the photochemical mechanism can be obtained without a structural probe of excited state. Resonance Raman spectroscopy provides the tool for probing the structural dynamics of nucleic acid and its components just after the absorption of a photon and before the electronic relaxation.[24,71] This will tell us about the initial excited-state structural dynamics and provide some insight about the nucleic acid photochemical

mechanism. So studying the initial excited-state structural dynamics will help us to better understand the photochemistry and the factors affecting the excited-state photochemistry.

1.2.9 Fluorescence Spectroscopy

When a molecule absorbs light and gets electronically excited, there are different ways for it to get rid of the excess energy. If the excited-state molecule radiates energy in the form of light and returns to the ground state, it is called fluorescence provided the initial and final state multiplicities are the same. A diagrammatic representation of different excited-state processes is shown in the Jablonski diagram in Figure 1.1. The wavelength of the fluorescent light is higher than the wavelength of the absorbed photon except in the case of resonance fluorescence and multiphoton absorption. The red shift in the wavelength of emitted photon with respect to the absorbed photon is called the Stokes shift.[80] Stokes shift is due to the non-radiative vibrational relaxation from higher vibrational levels to the ground vibrational level of the first excited state. Fluorescence generally occurs from the lowest vibrational level of the first electronic excited state to the different vibrational levels of the ground electronic state. In most cases, fluorescence spectra are mirror images of absorption spectra explained using the Franck-Condon principle.

Fluorescence spectroscopy is used in all disciplines of science, such as chemistry, physics, biology, metrology, medicine etc. The greatest advantage of fluorescence spectroscopy is that it is a zero-background technique. So it is capable of detecting the smallest amount of fluorescence from the sample and even single molecule fluorescence is being used in medicine and molecular biology to track the movement of biomolecules within the cell.[81] Fluorescence labeling of biomolecules like proteins are very common in biology these days.[82] Fluorescence spectroscopy is used to monitor the rate of reaction and quantify the amount of products formed. The capability of microscopy combined with the higher sensitivity of fluorescence spectroscopy has revolutionized the field of molecular imaging and opened up a new area of research called fluorescence imaging.[83] Developing different types of fluorescent molecule for bio-medical applications and changing the color by changing the substituents is another area of research.[84] The ability to tag different molecules with different fluorophores enables the tracking of different molecules and their interactions simultaneously. Förster resonance energy transfer (FRET)[85] and

fluorescence lifetime studies are used in understanding protein interactions. In FRET, it is the change in fluorescence intensity resulting from the energy transfer from the donor to the acceptor molecule that is measured. The extent and efficiency of this energy transfer is dependent on the distance between the donor and acceptor molecules.[86]

1.2.10 Hairpin Probes and Damage Detection

Two strands of DNA and/or RNA form double-stranded structures by hydrogen bonding between complementary bases on opposite strands. If a part of the DNA or RNA is complementary to a different part of the same nucleic acid, it can form a double-stranded region within a single nucleic acid similar to what we see in tRNA structures.

In 1996, Tyagi et al. reported a new set of fluorescent probes called molecular beacons (MBs).[87] Molecular beacons are stem-loop single-stranded nucleic acids, where the loop part is complementary to a target sequence and the ends forming the stem part are complementary to each other. A fluorescent molecule is attached onto one end of the probe and a fluorescent quencher on the other end. The double-stranded stem keeps the fluorescent moiety and the quencher close together, causing fluorescence quenching. When the molecular beacon encounters a perfectly, complementary sequence to the loop, the stem opens up and forms a more stable target-probe hybrid. The formation of the hybrid forces the fluorescent moiety and the quencher far apart, and the probe fluoresces. Bonnet et al. have shown that molecular beacons are thermodynamically more efficient in discriminating mismatches compared to linear unstructured probes.[88]

Due to the high specificity of MBs and hairpin probes, they are widely used in single nucleotide polymorphism studies[89–91]. Since MBs and hairpin probes can differentiate between a perfect complementary sequence and a single base mismatch sequence, these have been used in studying DNA damage as well.[60,92] UV-induced DNA damage affects the structure of the DNA, and thus the stability of the probe-target hybrid. When there is damage, the equilibrium will shift toward the unhybridized form and the fluorescence intensity is expected to decrease. So this decrease in fluorescence intensity will enable us to quantify the amount of DNA damage.

The specificity in base pairing make the oligonucleotide efficient in finding the

perfect match in a large excess of different sequences of nucleotides and this property of molecular recognition by perfect complementarity is being used in molecular biology to study gene expression. In gene expression studies using microarrays, the targets are labeled with a fluorescent molecule and they hybridize to the perfect complementary probe sequence. The intensity of fluorescence from a known probe sequence spot tells us about the amount of complementary target sequence present in the sample. The use of this method in nucleic acid detection requires washing off the unhybridized samples in order to measure the signal for the hybrid. Also this technique demands immobilization of the nucleic acid on to a solid surface. All these limitations make molecular beacon based nucleic acid detection unfit for any real-time monitoring of nucleic acid in solution phase and *in vivo* uses.

1.2.11 DNA/RNA Microarrays

Microarrays are microscopic spots of DNA/RNA or protein spotted on a surface in a periodic pattern. As many sequences of biopolymers can be spotted this method enables the study of a large numbers of sequences simultaneously. Microarrays have been used to study levels of gene expression. Since the introduction of microarrays in 1992 by Fodor[93], advancement in the field of microarray technology has been very rapid and promising[94–97]. In 1995 Schema et al. published the first microarray paper[98] titled "Quantitative monitoring of gene expression patterns with a complementary DNA microarray".

Different techniques are used to fabricate microarray slides. DNA can either be synthesized on the microarray slide itself like Affymetrix slides or DNA-containing solution can be spotted on a microarray slide. Affymetrix slides are fabricated by direct solid-phase DNA synthesis of nucleic acids on the surface of the glass slide with the aid of photolithography[99]. A synthetic linker with a photochemically removable protecting group is attached to the glass surface. Then different areas of the slides are exposed to light to deprotect the linker and facilitate the attachment of building blocks to the linker. Another widely used microarray fabrication technique is the solution phase deposition of nucleic acid onto the modified glass surface. In this method, micro syringes deposit the oligonucleotide solution to the derivatized glass surface via contact or non-contact printing. The oligonucleotide is usually attached to the glass surface through a linker on the 5' or 3' end of the oligonucleotide. The interaction between the chemical linker and the derivatized glass surface facilitate

the attachment of the oligonucleotide to the glass surface. The kind of interaction between the glass surface and the oligonucleotide depends upon the linker and modification on the glass surface. For example, if the glass surface is epoxide coated and the oligonucleotide linker has an amino terminus, it will form a covalent bond at optimum pH.

Microarrays are generally used for studying changes in gene expression[100], comparative genomic hybridization[101] and mutation and single nucleotide polymorphism[102,103]. In gene expression studies, complementary probes to genes of interest are attached to the slide and the complementary DNA (cDNA) corresponding to the RNA from cells in different environment is labeled with the two different fluorophore separately. Then the labeled cDNA is mixed in equal volume and hybridized on the slide under high stringency conditions. The most common type of labeling is fluorescent labeling, where a fluorophore is covalently attached to the probe molecule. Detection of the presence or expression of a certain gene is done by estimating the relative amount of probe-target hybridization from the fluorescence intensity of the target after washing away the unhybridized targets. The intensity of fluorescence from each spot will tell us about the relative levels of expression of genes in each type of cell. Equal fluorescence intensity from both fluorophores from a spot indicates the expression of that particular gene is similar in both the cells. Relative change in the fluorescence intensities of the fluorophores from a spot corresponds to the change in levels of expression of the gene in the respective cells.

1.3 Research outline

Though much research has been done towards understanding DNA damage and the excited-state structural dynamics of nucleobases separately, very little effort has been put in correlating the initial excited-state structural dynamics of DNA and DNA damage. In this thesis, I have tried to understand the differences in nucleobase photochemistry and extended the initial excited-state structural dynamics studies to polymers of nucleotides. In an effort to correlate the observed initial excited-state structural in oligonucleotides to UV damage,I have studied UV RNA damage on microarray platform.

Four different projects are discussed in this thesis. Chapters 2, 3 and 5 make use of resonance Raman spectroscopy as a tool to probe the initial excited-state structural dynamics of different molecules. Initial excited-state structural dynamics

of 5,6-dimethyluracil is studied and discussed in Chapter 2. The results are discussed in an effort to understand the difference in initial excited-state structural dynamics and photochemistry of thymine and uracil. Chapter 3 presents the initial excited-state structural dynamics of homopolymers of nucleotides and are compared to monomers. Resonance Raman spectroscopy can provide insight about structural dynamics of fast reactions and processes like isomerism. Chapter 5 discusses the use of resonance Raman spectroscopy to probe the structural dynamics of N-alkylated indanylidene-pyrroline (NAIP) switch, an analog of the chromophore in visual pigments. UV induced damage of different miRNA sequence and kinetics of the damage are presented in Chapter 4 using a novel RNA microarray. In Chapter 4, I have also discussed the sequence dependence of DNA damage.

References

[1] E. B. Wilson Jr, J. C. Decius, and P. C. Cross. *Molecular Vibrations: The Theory of Infrared and Raman Vibrational Spectra*. Dover Books, 1980.

[2] P. Larkin. *Infrared and Raman Spectroscopy; Principles and Spectral Interpretation*. Elsevier Science, 2011.

[3] J. L. Martin and M. H. Vos. Femtosecond biology. *Ann. Rev. Biophys. Biomol. Struc.*, 21(1):199–222, 1992.

[4] E. T. J. Nibbering, H. Fidder, and E. Pines. Ultrafast chemistry: Using time-resolved vibrational spectroscopy for interrogation of structural dynamics. *Ann. Rev. Phys. Chem.*, 56(1):337–367, 2005.

[5] C. V. Raman and K. S. Krishnan. New type of secondary radiation. *Nature*, 121:501–502, 1928.

[6] A. Smekal. Zur quantentheorie der dispersion. *Naturwissenschaften*, 11:873–875, 1923.

[7] D. L. Gerrard and J. Birnie. Raman spectroscopy. *Anal. Chem.*, 62(12):140R–150R, 1990.

[8] E. C. Le Ru and P. G. Etchegoin. A quick overview of surface-enhanced Raman spectroscopy. In *Principles of Surface-Enhanced Raman Spectroscopy*, chapter 1, pages 1 – 27. Elsevier, Amsterdam, 2009.

[9] A. Sivanesan, G. Kalaivani, A. Fischer, K. Stiba, S. Leimkahler, and I. M. Weidinger. Complementary surface-enhanced resonance Raman spectroscopic biodetection of mixed protein solutions by chitosan- and silica-coated plasmon-tuned silver nanoparticles. *Anal. Chem.*, 84(13):5759–5764, 2012.

[10] M. Kaya and M. Volkan. New approach for the surface enhanced resonance Raman scattering (SERRS) detection of dopamine at picomolar (pM) levels in the presence of ascorbic acid. *Anal. Chem.*, 84(18):7729–7735, 2012.

[11] P. Hildebrandt and M. Stockburger. Surface-enhanced resonance Raman spectroscopy of rhodamine 6G adsorbed on colloidal silver. *J. Phys. Chem.*, 88(24):5935–5944, 1984.

[12] E. Bailo and V. Deckert. Tip-enhanced Raman scattering. *Chem. Soc. Rev.*, 37:921–930, 2008.

[13] E. J. Blackie, E. C. L. Ru, and P. G. Etchegoin. Single-molecule surface-enhanced Raman spectroscopy of nonresonant molecules. *J. Am. Chem. Soc.*, 131(40):14466–14472, 2009.

[14] E. Smith and G. Dent. *Modern Raman Spectroscopy: A Practical Approach.* Wiley, 2005.

[15] J. Franck and E. G. Dymond. Elementary processes of photochemical reactions. *Faraday Trans.*, 21:536–542, 1926.

[16] A. B. Myers. Molecular electronic spectral broadening in liquids and glasses. *Ann. Rev. Phys. Chem.*, 49(1):267–295, 1998.

[17] A. B. Myers and R. A. Mathies. *Biological Applications of Raman Spectroscopy*, volume 2 of *Resonance Raman Spectra of Polyenes and Aromatics*, chapter Resonance Raman intensities: a probe of excited state structure and dynamics, pages 1–58. Wiley, New York, 1987.

[18] B. B. Johnson and W. L. Peticolas. Resonant Raman effect. *Ann. Rev. Phys. Chem.*, 27:465–491, 1976.

[19] M. Shanmugasundaram and M. Puranik. Computational prediction of vibrational spectra of normal and modified DNA nucleobases. *J. Raman Spectrosc.*, 40(12):1726–1748, 2009.

[20] N. Leulliot, M. Ghomi, H. Jobic, O. Bouloussa, V. Baumruk, and C. Coulombeau. Ground state properties of the nucleic acid constituents studied by Density Functional Calculations. 2. Comparison between calculated and experimental vibrational spectra of uridine and cytidine. *J. Phys. Chem. B*, 103(49):10934–10944, 1999.

[21] H. A. Kramers and W. Heisenberg. Uber die streuung von strahlung durch atome. *Zeitschrift fa Physik A Hadrons and Nuclei*, 31:681–708, 1925.

[22] P. A. M. Dirac. The quantum theory of dispersion. *Proc. Roy. Soc. London. Series A*, 114(769):710–728, 1927.

[23] J. L. McHale. *Molecular spectroscopy.* Prentice Hall, 1999.

[24] S. A. Asher. UV resonance Raman studies of molecular structure and dynamics: Applications in physical and biophysical chemistry. *Ann. Rev. Phys. Chem.*, 39(1):537–588, 1988.

[25] C. Liu, R. Du, Y-Y. Zhao, H-G. Wang, and X-M. Zheng. Resonance Raman spectroscopy of the excited state structural dynamics of 6-N,N–dimethyladenine. *Acta Phys. Chim. Sin.*, 27(01):17, 2011.

[26] S. A. Oladepo and G. R. Loppnow. Initial excited-state structural dynamics of 9-methyladenine from UV resonance Raman spectroscopy. *J. Phys. Chem. B*, 115(19):6149–6156, 2011.

[27] S. A. Oladepo and G. R. Loppnow. Ultraviolet resonance Raman spectroscopy as a robust spectroscopic tool for in situ sunscreen analysis. *Anal. Chim. Acta*, 628(1):57 – 66, 2008.

[28] L. M. Kundu and G. R. Loppnow. Direct detection of 8-oxo-deoxyguanosine using UV resonance Raman spectroscopy. *Photochem. Photobiol.*, 83(3):600–602, 2007.

[29] J. D. Watson and F. H. C. Crick. Molecular structure of nucleic acids: A structure for deoxyribose nucleic acid. *Nature*, 171(4356):737–738, 1953.

[30] Y. Lee, M. Kim, J. Han, K-H. Yeom, S. Lee, S. H. Baek, and V. N. Kim. MicroRNA genes are transcribed by RNA polymerase II. *EMBO J.*, 23(20):4051–4060, 2004.

[31] X. Cai, C. H. Hagedorn, and B. R. Cullen. Human microRNAs are processed from capped, polyadenylated transcripts that can also function as mRNAs. *RNA*, 10(12):1957–1966, 2004.

[32] J. Brennecke, A. A. Aravin, A. Stark, M. Dus, M. Kellis, R. Sachidanadam, and G. J. Hannon. Discrete small RNA-generating loci as master regulators of transposon activity in drosophila. *Cell*, 128(6):1089 – 1103, 2007.

[33] R. W. Holley, J. Apgar, G. A. Everett, J. T. Madison, M. Marquisee, S. H. Merrill, J. R. Penswick, and A. Zamir. Structure of a ribonucleic acid. *Science*, 147(3664):1462–1465, 1965.

[34] K. S. Kosik. The neuronal microRNA system. *Nat. Rev. Neurosci.*, 7(12):911–920, 2006.

[35] W. P. Kloosterman and R. H. Plasterk. The diverse functions of microRNAs in animal development and disease. *Dev. Cell.*, 11(4):441–50, 2006.

[36] K. Chen and N. Rajewsky. The evolution of gene regulation by transcription factors and microRNAs. *Nat. Rev. Genet.*, 8(2):93–103, 2007.

[37] M. W. Jones-Rhoades, D. P. Bartel, and B. Bartel. MicroRNAs and their regulatory roles in plants. *Ann. Rev. Plant Biol.*, 57(1):19–53, 2006.

[38] I. Alvarez-Garcia and E. A. Miska. MicroRNA functions in animal development and human disease. *Development*, 132(21):4653–4662, 2005.

[39] R. C. Lee, R. L. Feinbaum, and V. Ambros. The C. elegans heterochronic gene lin-4 encodes small RNAs with antisense complementarity to lin-14. *Cell*, 75(5):843 – 854, 1993.

[40] B. J. Reinhart, F. J. Slack, M. Basson, A. E. Pasquinelli, J. C. Bettinger, A. E. Rougvie, H. R. Horvitz, and G. Ruvkun. The 21-nucleotide let-7 RNA regulates developmental timing in caenorhabditis elegans. *Nature*, 403(6772):901–906, 2000.

[41] R. J. Jackson and N. Standart. How do microRNAs regulate gene expression? *Sci. STKE*, 2007(367):re1, 2007.

[42] D. P. Bartel. MicroRNAs: genomics, biogenesis, mechanism, and function. *Cell*, 116(2):281 – 297, 2004.

[43] B. P. Lewis, I. Shih, M. W. Jones-Rhoades, D. P. Bartel, and C. B. Burge. Prediction of mammalian microRNA targets. *Cell*, 115(7):787–798, 2003.

[44] D. Yue, H Liu, and Y. Huang. Survey of computational algorithms for microRNA target prediction. *Curr. Genomics*, 10(7):478–492, 2009.

[45] D. Voet, W. B. Gratzer, R. A. Cox, and P Doty. Absorption spectra of nucleotides, polynucleotides, and nucleic acids in the far ultraviolet. *Biopolymers*, 1(3):193–208, 1963.

[46] P. R. Callis. Electronic states and luminescence of nucleic acid systems. *Ann. Rev. Phys. Chem.*, 34(1):329–357, 1983.

[47] I. Tinoco. Hypochromism in polynucleotides 1. *J. Am. Chem. Soc.*, 82(18):4785–4790, 1960.

[48] W. Rhodes. Hypochromism and other spectral properties of helical polynucleotides. *J. Am Chem. Soc.*, 83(17):3609–3617, 1961.

[49] C. E. Crespo-Hernandez, B. Cohen, P. M. Hare, and B. Kohler. Ultrafast excited-state dynamics in nucleic acids. *Chem. Rev.*, 104(4):1977–2020, 2004.

[50] C. T. Middleton, K. de La Harpe, C. Su, Y. K. Law, C. E. Crespo-Hernandez, and B. Kohler. DNA excited-state dynamics: From single bases to the double helix. *Ann. Rev. Phys. Chem.*, 60(1):217–239, 2009.

[51] L. Serrano-Andras and M. Merchan. Are the five natural DNA/RNA base monomers a good choice from natural selection?: A photochemical perspective. *J. Photochem. Photobiol. C: Photochem. Rev.*, 10(1):21–32, 2009.

[52] M. Daniel and W. Hauswirth. Fluorescence of the purine and pyrimidine bases of the nucleic acids in neutral aqueous solution at 300 K. *Science*, 171:675–677, 1971.

[53] J-M. L. Pecourt, J. Peon, and B. Kohler. Ultrafast internal conversion of electronically excited RNA and DNA nucleosides in water. *J. Am. Chem. Soc.*, 122(38):9348–9349, 2000.

[54] J-M. L. Pecourt, J. Peon, and B. Kohler. DNA excited-state dynamics: Ultrafast internal conversion and vibrational cooling in a series of nucleosides. *J. Am. Chem. Soc.*, 123(42):10370–10378, 2001.

[55] R. P. Lopes, M. P. M. Marques, R. Valero, J. Tomkinson, and L A. E. B. de Carvalho. Guanine: A combined study using vibrational spectroscopy and theoretical methods. *Spec. Int. J.*, 27:273–292, 2012.

[56] S. Yarasi, P. Brost, and G. R. Loppnow. Initial excited-state structural dynamics of thymine are coincident with the expected photochemical dynamics. *J. Phys. Chem. A*, 111(24):5130–5135, 2007.

[57] S. Yarasi, S. Ng, and G. R. Loppnow. Initial excited-state structural dynamics of uracil from resonance Raman spectroscopy are different from those of thymine (5-methyluracil). *J. Phys. Chem. B*, 113(43):14336–14342, 2009.

[58] B. E. Billinghurst, R. Yeung, and G. R. Loppnow. Excited-state structural dynamics of 5-fluorouracil. *J.Phys. Chem. A*, 110(19):6185–6191, 2006.

[59] S. S. Ng, F. Teimoory, and G. R. Loppnow. Mass-tuned initial excited-state structural dynamics of DNA nucleobases from resonance Raman spectroscopy: 5-deuterouracil. *J. Phys. Chem. Lett.*, 2(18):2362–2365, 2011.

[60] A. F. El-Yazbi, A. Palech, and G. R. Loppnow. Initial excited-state structural dynamics of 2'-deoxyguanosine determined via UV resonance Raman spectroscopy. *J. Phys. Chem. A*, 115(38):10445–10451, 2011.

[61] B. E. Billinghurst, S. A. Oladepo, and G. R. Loppnow. Initial excited-state structural dynamics of thymine derivatives. *J.Phys. Chem. B*, 116(35):10496–10503, 2012.

[62] F .P. Gasparro. *Sunscreen Photobiology: Molecular, Cellular and Physiological Aspects*. Biotechnology Intelligence Unit Series. Springer Verlag, 1997.

[63] F. L. Gates. On nuclear derivatives and the lethal action of ultra-violet light. *Science*, 68(1768):479–480, 1928.

[64] C.W. Emmons and A. Hollander. The action of ultraviolet radiation on dermatophytes II. Mutations induced in cultures of dermatophytes by exposure of spores to monochromatic ultraviolet radiation. *Am. J. Bot.*, 26:467–475, 1939.

[65] E. Reuss, A. Knapp, O. Risse, and H. Schreiber. Quantitative analyse der mutationsauslosenden wirkung monochromatischen UV-lichtes. *Naturwissenschaften*, 27:304–304, 1939.

[66] R. l. Sinsheimer and R Hastings. A reversible photochemical alteration of uracil and uridine. *Science*, 110:525–526, 1949.

[67] A. Rorsch, R. Beukers, J. Ijlstra, and W. Berends. The effect of U.V.-light on some components of the nucleic acids: I. uracil, thymine. *Recueil des Travaux Chimiques des Pays-Bas*, 77(5):423–429, 1958.

[68] R. Beukers, J. Ylstra, and W. Berends. The effect of ultraviolet light on some components of the nucleic acids: II: In rapidly frozen solutions. *Recueil des Travaux Chimiques des Pays-Bas*, 77(8):729–732, 1958.

[69] R. Beukers, J. Ijlstra, and W. Berends. The effect of U.V.-light on some components of the nucleic acids. IV. the influence of oxygen on the extent of the first irreversible reaction, shown by uracil and orotic acid. *Recueil des Travaux Chimiques des Pays-Bas*, 78(11):879–882, 1959.

[70] R. Beukers, J. Ijlstra, and W. Berends. The effect of U.V.-light on some components of the nucleic acids. V. reversibility of the first irreversible reaction under special conditions. *Recueil des Travaux Chimiques des Pays-Bas*, 78(11):883–887, 1959.

[71] C. H. Wei and J. R. Einstein. Characterizations of the monohydrates of the monosodium and dipotassium salts of *cis–syn* thymine photodimer. Crystallographic treatments of mixed crystals containing dimers and monomers resulting from X-ray cleavage of dimers in the solid state. *Acta Cryst. B*, 40(3):271–279, 1984.

[72] A. Wacker, H. Dellweg, and D. Jacherts. Thymin-dimerisierung und uberlebensrate bei bakterien. *J. Molecul. Biol.*, 4(5):410–412, 1962.

[73] S. Y. Wang. Photochemical reactions in frozen solutions. *Nature*, 190(4777):690–694, 1961.

[74] R. B. Setlow and W. L. Carrier. Pyrimidine dimers in ultraviolet-irradiated DNA's. *J. Mol. Biol.*, 17(1):237–254, 1966.

[75] R. Beukers, J. Ijlstra, and W. Berends. The effect of ultraviolet light on some components of the nucleic acids. VI the origin of the U.V. sensitivity of deoxyribonucleic acid. *Recueil des Travaux Chimiques des Pays-Bas*, 79(1):101–104, 1960.

[76] S. Steenken and S. V. Jovanovic. How easily oxidizable is DNA? One-electron reduction potentials of adenosine and guanosine radicals in aqueous solution. *J. Am. Chem. Soc.*, 119(3):617–618, 1997.

[77] H. Kasai, Z. Yamaizumi, M. Berger, and J. Cadet. Photosensitized formation of 7,8-dihydro-8-oxo-2'-deoxyguanosine (8-hydroxy-2'-deoxyguanosine) in DNA by riboflavin: A nonsinglet oxygen-mediated reaction. *J. Am. Chem. Soc.*, 114(24):9692–9694, 1992.

[78] W. M. Horspool and P. S. Song. *Handbook of Organic Photochemistry*. CRC handbook series. Taylor & Francis Group, 1995.

[79] A.G. Griesbeck, M. Oelgemoller, and F. Ghetti. *CRC Handbook of Organic Photochemistry and Photobiology 3E*. Taylor & Francis Group, 2012.

[80] J. R Lakowicz. *Principles of Fluorescence Spectroscopy*. Kluwer Academic / Plenum Publishers, 1999.

[81] C. Joo, H. Balci, Y. Ishitsuka, C. Buranachai, and T. Ha. Advances in single-molecule fluorescence methods for molecular biology. *Ann. Rev. Biochem.*, 77(1):51–76, 2008.

[82] A. Miyawaki, A. Sawano, and T. Kogure. Review: Lighting up cells: labelling proteins with fluorophores. *Nature Cell. Biol.*, 5:S1–S7, 2003.

[83] W. E. Moerner and D. P. Fromm. Methods of single-molecule fluorescence spectroscopy and microscopy. *Rev. Sci. Instrum.*, 74(8):3597–3619, 2003.

[84] T. Suzuki, T. Matsuzaki, H. Hagiwara, T. Aoki, and K. Takata. Recent advances in fluorescent labeling techniques for fluorescence microscopy. *Acta Histochem. Cytochem.*, 40(5):131–137, 2007.

[85] T. Förster. Zwischenmolekulare Energiewanderung und Fluoreszenz. *Ann. Phys.*, 437:55–75, 1948.

[86] J. Michaelis. *Quantitative Distance and Position Measurement using Single-Molecule FRET*, pages 191–214. Wiley-VCH Verlag GmbH & Co. KGaA, 2009.

[87] S. Tyagi and F. R. Kramer. Molecular beacons: Probes that fluoresce upon hybridization. *Nat. Biotech.*, 14(3):303–308, 1996.

[88] G. Bonnet, S. Tyagi, A. Libchaber, and F. R. Kramer. Thermodynamic basis of the enhanced specificity of structured DNA probes. *Proc. Natl. Acad. Sci. USA*, 96(11):6171–6176, 1999.

[89] A. Fiedrich, J. D Hoheisel, N. Marme, and J. P. Knemeyer. DNA-probes for the highly sensitive identification of single nucleotide polymorphism using single-molecule spectroscopy. *FEBS Lett.*, 581(8):1644–1648, 2007.

[90] H. Zhang, M. Wang, Q. Gao, H. Qi, and C. Zhang. Fluorescent detection of single nucleotide polymorphism utilizing a hairpin DNA containing a nucleotide base analog pyrrolo-deoxycytidine as a fluorescent probe. *Talanta*, 84(3):771–776, 2011.

[91] D. Gerion, F. Chen, B. Kannan, A. Fu, W. J. Parak, D. J. Chen, A. Majumdar, and A. P. Alivisatos. Room-temperature single-nucleotide polymorphism and multiallele DNA detection using fluorescent nanocrystals and microarrays. *Anal. Chem.*, 75(18):4766–4772, 2003.

[92] A. F. El-Yazbi and G. R. Loppnow. 2-aminopurine hairpin probes for the detection of ultraviolet-induced DNA damage. *Anal. Chim. Acta*, 726(0):44–49, 2012.

[93] L. F. Rozsnyai, D. R. Benson, S. P. A. Fodor, and P. G. Schultz. Photolithographic immobilization of biopolymers on solid supports. *Angew. Chem. Int. Ed.*, 31(6):759–761, 1992.

[94] P. A. Fodor, R. P. Rava, X. C. Huang, A. C. Pease, C. P. Holmes, and C. L. Adams. Multiplexed biochemical assays with biological chips. *Nature*, 364(6437):555–556, 1993.

[95] A. C. Pease, D. Solas, E. J. Sullivan, M. T. Cronin, C. P. Holmes, and S. P. Fodor. Light-generated oligonucleotide arrays for rapid DNA sequence analysis. *Proc. Natl. Acad. Sci. USA*, 91(11):5022–5026, 1994.

[96] R. B. Stoughton. Applications of DNA microarrays in biology. *Ann. Rev. Biochem.*, 74(1):53–82, 2005.

[97] D. Gresham, M. J. Dunham, and D. Botstein. Comparing whole genomes using DNA microarrays. *Nat. Rev. Genet.*, 9(4):291–302, 2008.

[98] M. Schena, D. Shalon, R. W. Davis, and P. O. Brown. Quantitative monitoring of gene expression patterns with a complementary DNA microarray. *Science*, 270(5235):467–470, 1995.

[99] R. J. Lipshutz, S. P. A. Fodor, T. R. Gingeras, and D. J. Lockhart. High density synthetic oligonucleotide arrays. *Nat. Genet.*, 21:20–24, 1999.

[100] D. Murphy. Gene expression studies using microarrays: Principles, problems, and prospects. *Adv. Physiol. Educ.*, 26(4):256–270, 2002.

[101] A. Theisen. Microarray-based comparative genomic hybridization (aCGH). *Nature Educ.*, 1:1, 2008.

[102] G. L. Palmisano, L. Delfino, M. Fiore, L. Anna, and G. B. Ferrara. Single nucleotide polymorphisms detection based on DNA microarray technology: HLA as a model. *Autoimm. Rev.*, 4(8):510–514, 2005.

[103] C. G. Mullighan. Single nucleotide polymorphism microarray analysis of genetic alterations in cancer. In Lynda J. Campbell, editor, *Cancer Cytogenetics*, volume 730 of *Methods in Molecular Biology*, pages 235–258. Humana Press, 2011.

Chapter 2

Initial Excited-state Structural Dynamics Of 5,6-Dimethyluracil Using Resonance Raman Spectroscopy

2.1 Introduction

The difference in the genetic materials DNA and RNA arises from two factors: the difference in the sugar - in DNA, the pentose sugar is deoxyribose and ribose, in RNA - and the difference in one of the nucleobases. While adenine, guanine and cytosine are found in both DNA and RNA, thymine is only found in DNA and uracil only in RNA. The only difference between thymine and uracil is the presence of a methyl group at the C5 position of thymine instead of the hydrogen in uracil as shown in Figure 2.1. The photochemistry of these two nucleobases is also very different. Thymine forms the cyclobutyl pyrimidine dimer (CPD) as the major photoproduct upon UV irradiation, whereas the photohydrate is the major photoproduct in uracil.[1,2] Only a good understanding of the excited-state structural and electronic dynamics of the nucleobases will help us rationalize the reason for this difference in photochemistry.

Singlet excited states of thymine and uracil decay on the femtosecond timescale.[3] There is an increase in the excited-state lifetime of thymine compared to uracil and that increase has been attributed to C5 pyramidalization.[3] However, the increase in the excited-state lifetime does not explain the difference in photochemistry. A probe of the initial excited-state structural dynamics is essential to understanding the photochemistry of the pyrimidine nucleobases.[4–6] Loppnow et al., have

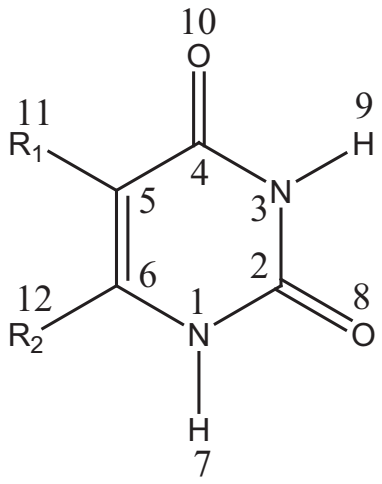

R_1	R_2	Compund
H	H	Uracil (U)
CH_3	H	Thymine (T or 5-MU)
H	CH_3	6-methyluracil (6-MU)
CH_3	CH_3	5,6-dimethyluracil (5,6-DMU)

Figure 2.1: Structure of uracil derivatives.

successfully used resonance Raman spectroscopy to study the initial excited-state structural dynamics of thymine and uracil, and found that they are different.[7,8] Most of the initial excited-state dynamics of uracil is directed along the C5H and C6H bending modes, whereas they are largely oriented along the C5=C6 stretching mode in thymine. Similar studies in other uracil derivatives have also revealed that the excited-state structural dynamics lie along the C5=C6 stretching mode and the C5, C6 pyramidalization modes.[7,8] This difference in structural dynamics between these compounds was attributed to the difference in mass at the C5 position, one of the photochemically active sites in the photochemistry of the molecule. Similarity between the initial excited-state structural dynamics of 5-MU and 5-fluorouracil and the similarity of 5-deuterouracil to both 5-MU and uracil strongly suggested the influence of the mass-effect in initial excited-state structural dynamics of the nucleobases and their derivatives.[9,10] Surprisingly, further studies with methyl substitution at the C6 position of uracil showed that the methyl group at C6 position changes the partitioning of the initial excited-state structural dynamics between the CH bending and stretching modes compared to thymine, though the initial excited-state structural dynamics along the C5=C6 stretching mode is similar in C5 and C6 methyl substituted uracil.[11]

To understand the origin of the difference in photochemistry, I have studied the initial excited-state structural dynamics of 5,6-dimethyluracil (5,6-DMU, Figure 2.1) in this chapter. This uracil derivative has similar masses at the C5 and C6 positions

as in uracil, but C5 and C6 hydrogens are replaced by methyl groups. So the presence of the methyl group at both the C5 and C6 positions will help to differentiate the role of the C5 and C6 position and the mass effect in determining the initial excited-state structural dynamics.[11]

2.2 Experimental

5,6-DMU (2,4-dihydroxy 5,6-dimethylpyrimidine, Sigma-Aldrich, Oakville, ON) and sodium nitrate (99%, EMD Chemicals Inc., Gibbstown, NJ) were used without any further purification. Solutions were prepared by mixing the required amount of 5,6-DMU with sodium nitrate and diluting them with nanopure water from a Barnstead water filtration system (Boston, MA).

The laser excitation wavelengths for the resonance Raman experiments were generated from a picosecond mode-locked, Ti:sapphire laser (Coherent, Santa Clara, CA) pumped by a doubled, continuous-wave, solid-state, diode-pumped Nd:YAG laser (Coherent, Sanata Clara, CA). The Ti:sapphire output was doubled using a lithium triborate (LBO) crystal (Inrad, Northvale, NJ) followed by third harmonic generation using a β-barium borate (BBO) crystal in a harmonic generator (Inrad, Northvale, NJ) to obtain the 250, 257, 266, 275 and 280 nm excitation wavelengths. The third harmonic output powers were typically 5-10 mW depending upon the wavelength. The third harmonic output was spherically focused onto an open stream of flowing solution in a 135° back-scattering geometry. The resonance Raman scattering from the sample was focused into a double-grating spectrometer (Spex Industries, Metuchen, NJ, USA) with water-cooled diode array detector (Princeton Instruments, Trenton, NJ, USA). The spectral linewidths were 5-7 cm^{-1}. Frequencies were calibrated by measuring the Raman scattering of solvents of known frequencies (acetonitrile, cyclohexane, toluene, methanol, ethanol, dimethylsulfoxide and carbon tetrachloride).

The concentration of 5,6-DMU was nominally 5 mM and the sodium nitrate internal standard concentration was 0.3 M. The actual concentration of 5,6-DMU during the experiment was monitored by measuring the absorption spectrum before and after each resonance Raman experiment, using a diode array UV-visible absorption spectrometer (Hewlett-Packard 8452, Sunnyvale, CA). All resonance Raman spectral measurements were done in triplicate. Resonance Raman frequencies for 5,6-DMU reported here are accurate to ± 10 cm^{-1}.

The overtone and combination bands for 5,6-DMU at 257 nm were recorded using a UV Raman microscope (Renishaw, Chicago, IL). Microscope was used due to the large spectral window possible and the ease of calibration. The resonance Raman scattering was obtained by focusing the 257 nm laser wavelength onto a sample solution containing 5 mM 5,6-DMU and 0.3 M sodium nitrate in a 10 ml beaker in the 180° back scattering geometry. The sample stage was constantly moved by using an electronic motor to minimize the photodegradation of the sample. The 1332 cm^{-1} vibration of diamond was used to calibrate the frequencies. Resonance Raman spectra in the overtone region were repeated with three sets of fresh samples. The exact concentrations of the samples were calculated from the absorption spectrum. The absolute resonance Raman cross-sections were calculated from the integrated band intensities using the following equation.

$$(\frac{d\sigma_R}{d\Omega})_{5,6-DMU} = (\frac{d\sigma}{d\Omega})_{IS}\frac{I_{5,6-DMU}}{I_{IS}}\frac{[IS]}{[5,6-DMU]}\frac{L_{IS}}{L_{5,6-DMU}} \times SA \qquad (2.1)$$

In this equation, $d\sigma_R/d\Omega$ is the differential resonance Raman cross-section of the vibrational mode, $I_{5,6-DMU}$ and I_{IS} are the integrated band intensities of the 5,6-DMU and the internal standard modes, respectively, [IS] and [5,6-DMU] are the concentrations of the internal standard and the 5,6-DMU, respectively, $L_{5,6-DMU}$ and L_{IS} are the standard lamp efficiency at the 5,6-DMU and the internal standard vibrational frequencies, respectively, and SA is the differential self-absorption of the resonance Raman scattered light at the 5,6-DMU and internal standard vibrational frequencies. Details of converting the resonance Raman intensities to differential resonance Raman cross-section have been described in Chapter 1. The resonance Raman differential cross-sections for nitrate used for the calculations were 3.68×10^{-11}, 2.43×10^{-11}, 1.53×10^{-11}, 1.02×10^{-11} and 8.37×10^{-12} $Å^2$ $molecule^{-1}sr^{-1}$ at 250, 257, 266, 275 and 280 nm, respectively.

Resonance Raman structural dynamics. The resonance Raman cross-sections as a function of excitation wavelength (excitation profiles) and the absorption spectrum of 5,6-DMU were simulated with a time-dependent formalism as described previously and in chapter 1.[4,5]

$$\sigma_R = \frac{8\pi e^4 M^4 E_s^3 E_L}{9\hbar^6 c^4}\int_0^\infty dE_0 H(E)_0 \left|\int_0^\infty < f|i(t) > exp\left[\frac{i(E_L+\epsilon_i)t}{\hbar}\right] G(t)dt\right|^2 \qquad (2.2)$$

$$\sigma_A = \frac{4\pi M^2 e^2 E_L}{6\hbar^2 cn} \int_0^\infty dE_0 H(E)_0 \int_{-\infty}^{\infty} < i|i(t) > exp\left[\frac{i(E_L + \epsilon_i)t}{\hbar}\right] G(t)dt \quad (2.3)$$

where E_L and E_S are the energies of the incident and scattered photons, respectively, M is the transition length, n is the refractive index, ϵ_i represents the energy of the initial vibrational state, $|i>$ and $|f>$ are the initial and final vibrational wavefunctions in the Raman scattering process, $H(E_0)$ is the normalized inhomogeneous distribution of the zero-zero energies around an average energy, $\overline{E}_0$, $|i(t)>$ is the initial ground-state vibrational wavefunction propagated on the excited-state potential energy surface, and G(t) is the homogeneous linewidth, which represents the dynamics of chromophore-solvent coupling within the high-temperature limit of the Brownian oscillator model. Within the harmonic oscillator approximation, the $< i|i(t) >$ and $< f|i(t) >$ overlaps depend only on the slopes $(\beta/\hbar)$ of the excited-state potential energy surface at the ground-state equilibrium geometry along each normal mode of vibration. The implementation of these equations have been described in detail previously[4–6,12,13] and in Chapter 1. Thus, the resonance Raman intensities reflect the excited-state structural dynamics of the molecule. The simulation of the absorption spectrum and resonance Raman excitation profiles has been performed as follows. For the analysis, the initial guesses for the slopes $(\beta/\hbar)$ along each normal coordinate were estimated from the relative intensities of the resonance Raman vibrations excited at 266 nm, assuming that the intensities were proportional to $(\beta/\hbar)^2$ and setting the slope of the 1665 cm^{-1} mode to 1665 cm^{-1}. The other peaks are scaled relatively to reproduce the experimental absorption spectrum and resonance Raman excitation profile bandwidths. The parameters were then adjusted iteratively to get best agreement between the experimental and simulated absorption spectra and the resonance Raman excitation profiles. The overtones and combination bands were used as additional constraints to optimize the parameters. The mode assignments were done using a density functional theory (DFT) computational calculation at the B3LYP/6-311G(d,p) level of theory with Gaussian09 package and the conversion of internal coordinates from cartesian to symmetry with the GAR2PED package.[14,15]

2.3 Results and Discussion

Figure 2.2 shows the resonance Raman spectra of 5,6-DMU excited at different wavelengths (280, 275, 266, 257 and 250 nm) within the 260 nm absorption band. Peaks are observed at 475, 635, 1135, 1225, 1320, 1410 and 1665 cm^{-1}. The relative intensities of the peaks remain the same at different excitation wavelengths and no change in frequencies for the modes are observed. This observation indicates that the resonance enhancement results from a single electronic transition within the 260 nm absorption band. The two less intense peaks at 475 and 1135 cm^{-1} are not observed at all excitation wavelengths, due to difficulties in differentiating them from the background at some excitation wavelengths.

The resonance Raman spectrum of 5,6-DMU at 257 nm is compared to resonance Raman spectra of other uracil derivatives at the same excitation wavelength in Figure 2.3. The resonance Raman spectra in Figure 2.3 show a gradual change in spectral features on going from uracil to thymine. It can be easily seen that the 5,6-DMU spectrum is a combination of or intermediate between that of 5-methyluracil (thymine) and 6-methyluracil (6-MU). The 5,6-DMU spectrum can be considered as a combination of the thymine and 6-MU spectra, if we allow for the change in frequencies of some of the modes, which probably arises from the difference in masses at the C5 and C6 positions between 5-MU, 6-MU and 5,6-DMU. Even though the spectrum is intermediate between that of thymine and 6-MU, the potential energy distributions (PEDs) for the modes may in fact be very different for 5,6-DMU.

Thymine has five intense bands in the 1000 to 1700 cm^{-1} range and their assignments are given in Table 2.1.[16] The peak at 1175 cm^{-1} is mainly due to the C2N3 stretch[16]. The intense band around 1240 cm^{-1} is attributed to the C5-methyl stretch. The C-H bend of C6 is seen at 1360 cm^{-1}. The 1425 cm^{-1} mode is mainly due to C2N3 stretches. The 1665 cm^{-1} mode in thymine is due to stretches centred at the sp^2 carbons, with approximately a 60% contribution from the C5=C6 stretch and 13% from the C6H12 bend.

The 257 nm excited resonance Raman spectrum of 5,6-DMU has four intense modes. The peaks are observed at 1225, 1320, 1410 and 1665 cm^{-1}. The peaks below 1000 cm^{-1} (475 cm^{-1} and 635 cm^{-1}) are not shown in the spectrum. The presence of the methyl group at the C5 and C6 positions has resulted in some change to the intensities and frequencies of the modes, compared to thymine (5-MU) and

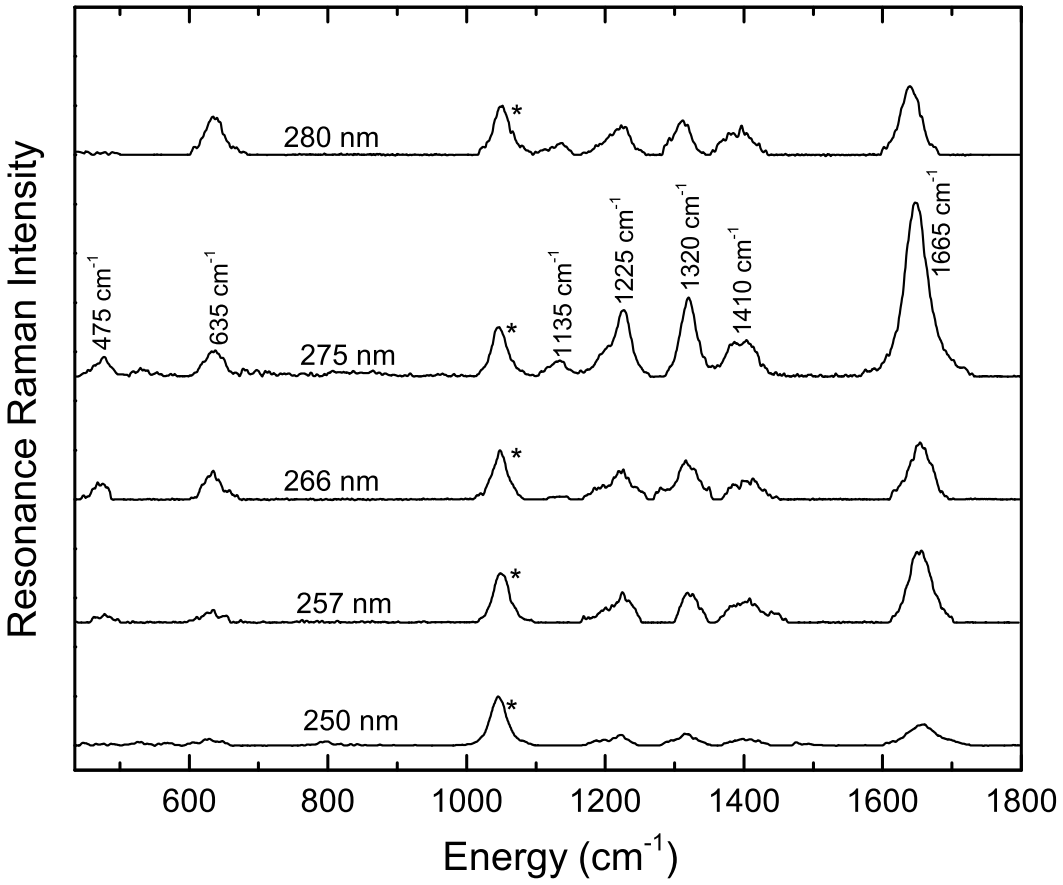

Figure 2.2: Resonance Raman spectra of 5 mM 5,6-DMU excited at different wavelengths within the 260 nm absorption band in the presence of 0.3 M sodium nitrate internal standard. The internal standard peak is denoted by an asterisk (*). All the spectra were normalized with respect to the internal standard peak.

Table 2.1: Harmonic mode parameters for other uracil derivatives

Mode (cm^{-1})	Mode assignments	$\beta/\hbar$ (cm^{-1})
	URACIL (U)[a]	
579	ring def 3 [32], be(C2O8) [-23], be(C4O10) [-18]- ν(C4C5) [-6] + ν(C6N1) [6]	266.3
789	ν(C4C5) [28], ν(N1C2) [19], ring def 1[13], ν(N3C4) [10], ring def 3 [7], ν(C2N3) [6], ν(C6N1) [6]	378.7
1235	be(C5H11) [33], be(C6H12) [18], ν(C6N1) [-15], be(N1H7) [10], ν(N3C4) [7], ν(N1C2) [5]	913.9
1388	ν(C2N3) [18], be(C5H11) [17], ν(N1C2) [15], be(C5H11) [13], be(C6H12) [-12], ν(C5C6) [-8], be(C4O10) [5]	624.6
1623	ν(C5C6) [61], be(C6H12) [-14], ν(C6N1)[-8]	486.9
1664	νC4O10) [71], ν(C4C5) [-8], ring def 2 [5]	998.4
	THYMINE (5-MU)[a]	
567	γ(N1H7) [90], γ(N3H9) [-6]	136.1
641	be(C4O10) [28], be(C2O8) [-27], be(C5C11) [14], ring def 2 [6]	192.3
762	γ(C2O8) [60], ring def 6 [-12], ring def 4 [8], γ(C4O10) [6], γ(N3H9) [-5]	228.6
811	ring def 1 [45], ν(C5H11) [20], ν(N1C2) [-11]	227.1
1173	ν(C2N3) [21], be(C6H12) [20], be(N1H7) [-16], ν(N3C4) [-12], ν(C6N1) [-11]	281.5
1237	ν(C5C11) [29], ν(C6N1) [-21], ring def [-12], ν(N1C2) [-10], ν(C4C5) [-10], ν(C2N3) [8]	544.3
1362	be(C6H12) [42], ν(C5C6) [12], ν(N1C2) [9], ν(C2N3) [-9]	681.0
1423	ν(C2N3) [15], ν(C4C5) [13], CH_3 umb [-11], be(N1H7) [9], ν(N1C2) [-8], be(C4O10) [7], be(C2O8) [7], ring def 2 [-6], be(N3H9) [6]	313.1
1667	ν(C5C6) [61], be(C6H12) [-13], ν(C6N1) [-8], ν(C5H11) [-5]	916.9
	6-METHYLURACIL (6-MU)[a]	
520	ring def 2 [54], ring def 3 [-30]	140.0
550	γ(C6C12) [28], γ(N1H7) [21], γ(C2N3) [11], ring def 6 [10], γ(C4O10) [9], γ (C5H11) [8]	140.0
605	be(C2O8) [35], be(C4O10) [35], be(C6C12) [-14]	160.0
657	γ(C2N3) [75], γ(C6H12) [-8], ring def 4 [-7]	110.0
1235	be(C5H11) [22], γ(C2N3) [17], ν(N3C4) [-17], ν(N1C2) [-9], ν(C4C5) [8]	590.0
1361	be(C5H11) [34], be(N1H7) [-26], ν(C2N3) [-7], ν(N1C2) [6]	180.0
1397	ν(C2N3) [21], ν(N1C2) [-11], be(C2N3) [10], be(C4O10) [-8], ring def 3 [8], ν(C4O10) [-8], ν(C4C5) [-8], ν(C2O8) [6]	410.0
1660	ν(C5C6) [60], ν(C6C12) [-6]	850.0

[a] The frequencies and mode assignments were obtained from references 7, 9 and 8, respectively. [b]Abbreviations: ν – stretching, def - deformation, γ - out-of-plane bending and be - in-plane bending.

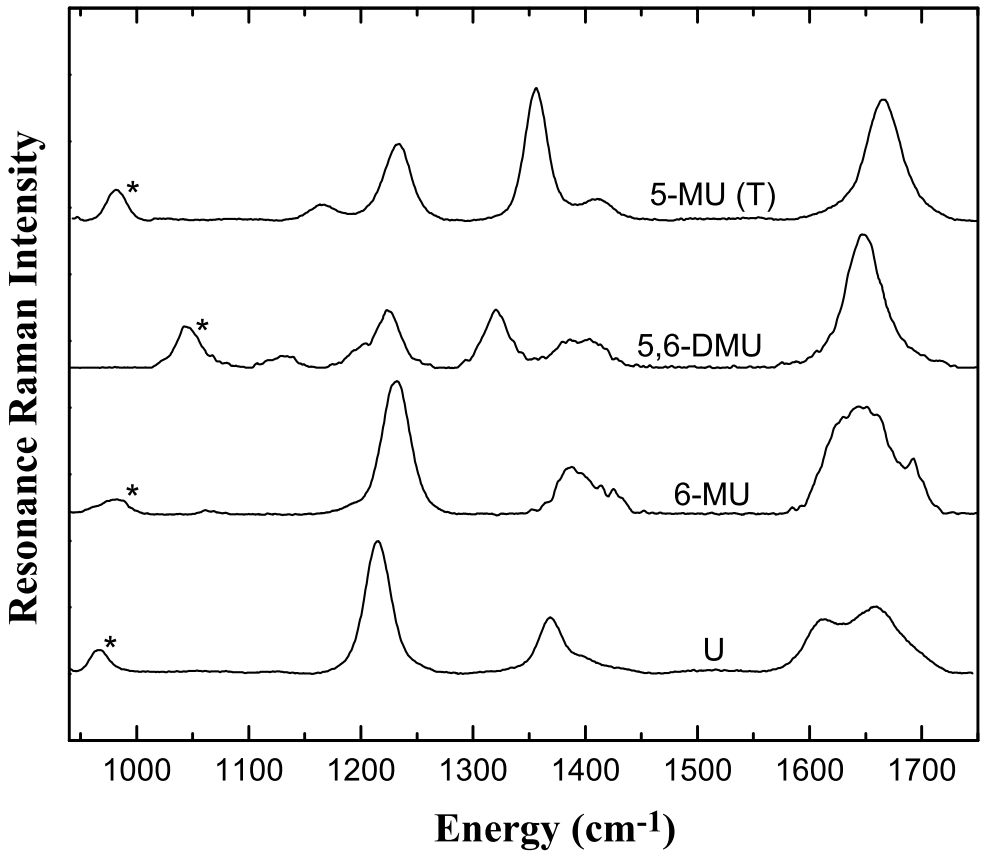

Figure 2.3: Resonance Raman spectra of different uracil derivatives excited at 257 nm. The internal standard peak is denoted by an asterisk (*). For uracil (U), 6-methyluracil (6-MU) and 5-methyluracil (5-MU or T), the internal standard was lithium sulfate and for 5,6-dimethyluracil (5,6-DMU) the internal standard was sodium nitrate. The 5-MU, 6-MU and U spectra were taken from reference 7, 9 and 11 respectively.

6-MU. The peaks at ca. 1225, 1400 and 1660 cm^{-1} are seen in all three methyl derivatives of uracil, though the intensities of the peaks are different and their mode assignments vary. The 5,6-DMU peak at 1225 cm^{-1} has the lowest relative intensity compared to the other two derivatives. The relative intensity of the peak around 1400 cm^{-1} in 5,6-DMU is intermediate between that of 5-MU and 6-MU. The 1320 cm^{-1} band intensity is intermediate in relative intensity to that of the 5-MU and 6-MU derivatives.

The mode assignments of 5,6-DMU are shown in Table 2.2 and are determined by DFT calculations as described in the section 2.2. The 1135 cm^{-1} peak in 5,6-DMU is assigned to the CH_3 deformations. The 1225 cm^{-1} peak has contributions from C5C11 and C6N1 stretches. The band at 1320 cm^{-1} of 5,6-DMU is mainly due to the N1H stretch. CH_3 deformations are the main contributors to the 5,6-DMU peak at 1410 cm^{-1} and the most intense mode at 1665 cm^{-1} is mainly due to the C5=C6 stretch.

In 6-methyluracil, the peak at 1235 cm^{-1} is more intense than that of thymine and has a similar mode assignment, with a change in the potential energy distributions[11]. A complete mode description for different uracil derivatives is given in Table 2.1. The 1360 cm^{-1} band is seen in 6-methyluracil, with similar mode assignments as that of thymine with some additional contribution from the N1H7 stretch[11]. The 1400 cm^{-1} mode also has a mode assignment similar to that of thymine. This mode is more intense in 6-MU than in thymine. The intense mode at 1660 cm^{-1} in 6-MU is mainly due to the C=C stretch, as in all the uracil derivatives. In uracil, the most intense peak was observed at 1235 cm^{-1} which is mainly due to the CH bending mode of the sp^2 hybridized carbon. The C5=C6 stretch is observed at a lower frequency than other uracil derivatives. All these differences between the resonance Raman spectra of different uracil derivatives indicate that there is clear difference in the initial excited-state dynamics induced by the presence of the methyl group. The results from this study and previous studies with uracil derivatives show that the methyl group at the C5 and/or C6 position determines the relative intensities of the 1235 and 1360 cm^{-1} modes.[9–11]

The experimental and simulated absorption spectra of 5,6-dimethyluracil are shown in Figure 2.4. The experimental absorption spectrum and resonance Raman excitation profiles were simulated by adjusting the parameters in Equation 2.2 and 2.3 to get the best agreement between the experimental and simulated spectra.

The deviation between the experimental and the calculated absorption spectra at energies above 38000 cm^{-1} is due to the fact that the higher energy electronic absorptions are not modeled in the simulation. Also the discrepancies below 35000 cm^{-1} may be coming from other possible lower energy transitions in 5,6-DMU, which are also not modeled in the simulation.

The experimental and simulated resonance Raman excitation profiles are shown in Figure 2.5. The simulated resonance Raman excitation profiles reproduce the experimentally measured resonance Raman cross-sections at different wavelengths. The height of the resonance Raman excitation profiles reflect the relative intensities of the peaks in the resonance Raman spectrum in Figure 2.3 and the excited-state slopes ($\beta/\hbar$) along each vibrational mode. The agreement between the experimental and simulated absorption spectrum and resonance Raman excitation profiles indicate that the excited-state parameters obtained from the simulation are accurate. The calculated excited-state slopes, other fitting parameters and the potential energy distributions for different peaks of 5,6-DMU are tabulated in Table 2.2. The most intense modes are assigned to dynamics around the C5 and C6 positions, which are consistent with the expected photochemistry of 5,6-DMU. The C5=C6 lengthening and the change in hybridization of the C5 and C6 carbons are expected in the $^1(\pi\pi^*)$ excited-state and the experimental results are expected for the photochemistry.

The excited-state slopes in Table 2.2 and 2.1 reveal that the initial excited-state dynamics of 5,6-DMU are more similar to thymine than uracil and is a combination of thymine (5-MU) and 6-MU. The assignments of the modes and the observed mode frequencies confirm this observation. The difference in the C5 and C6 substituent compared to thymine and uracil results in a slightly different potential energy distribution pattern in 5,6-DMU. There is only a small difference in the potential energy distribution for the 1225 cm^{-1} mode between all the three uracil derivatives. The 1360 cm^{-1} mode in 5-MU or 6-MU has a large contributions from the C6H and C5H bend respectively. No such mode in 5,6-DMU was observed due to the absence of similar CH bonds. But an additional mode at 1320 cm^{-1}, with a main contribution from the N1H7 bend is observed. The corresponding C5C11 and C6C12 bending modes are shifted to lower frequencies in 5,6-DMU, at 475 and 635 cm^{-1}, respectively. The PED for the 1410 cm^{-1} mode is similar for 5-MU and 6-MU but is very different in 5,6-DMU from the other two uracil derivatives. This indicates

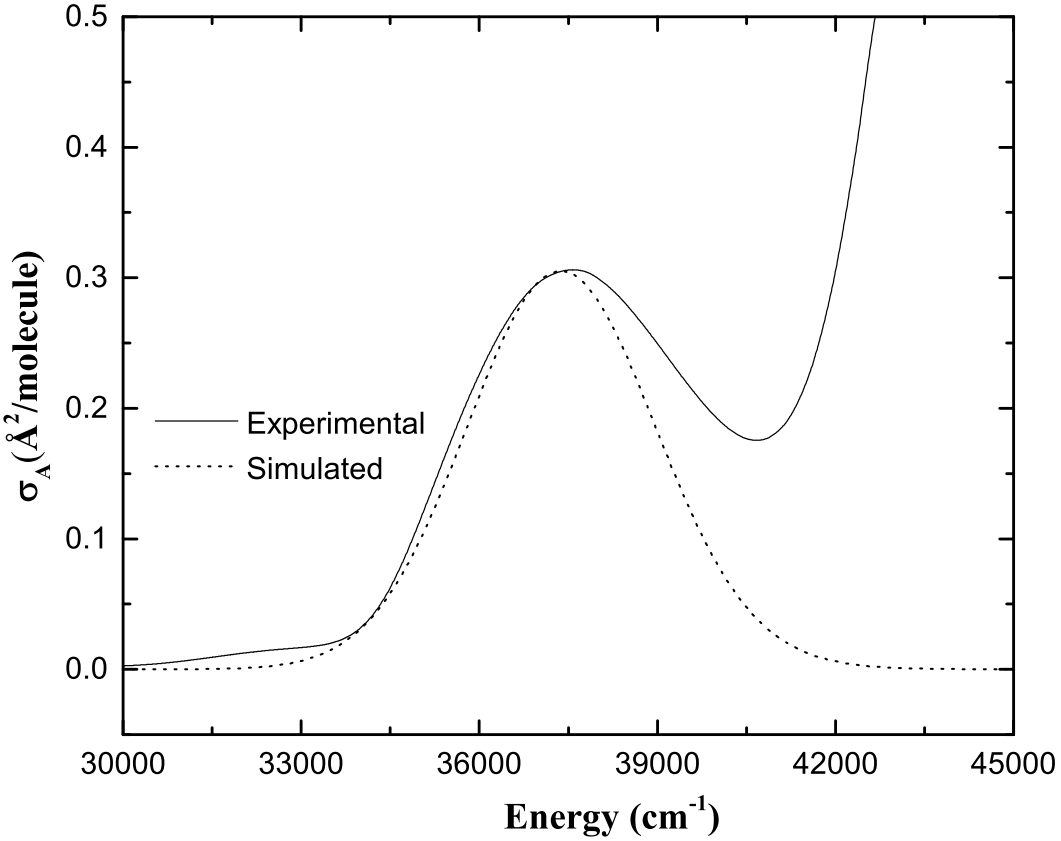

Figure 2.4: Calculated (dashed line) and experimental (solid line) absorption spectrum of 5, 6-DMU. The simulated absorption spectrum was generated using Equation 2.3 and the parameters from Table 2.2. The differences between the experimental and the simulated spectra at higher energies are due to other higher energy transitions which are not modeled in the equation.

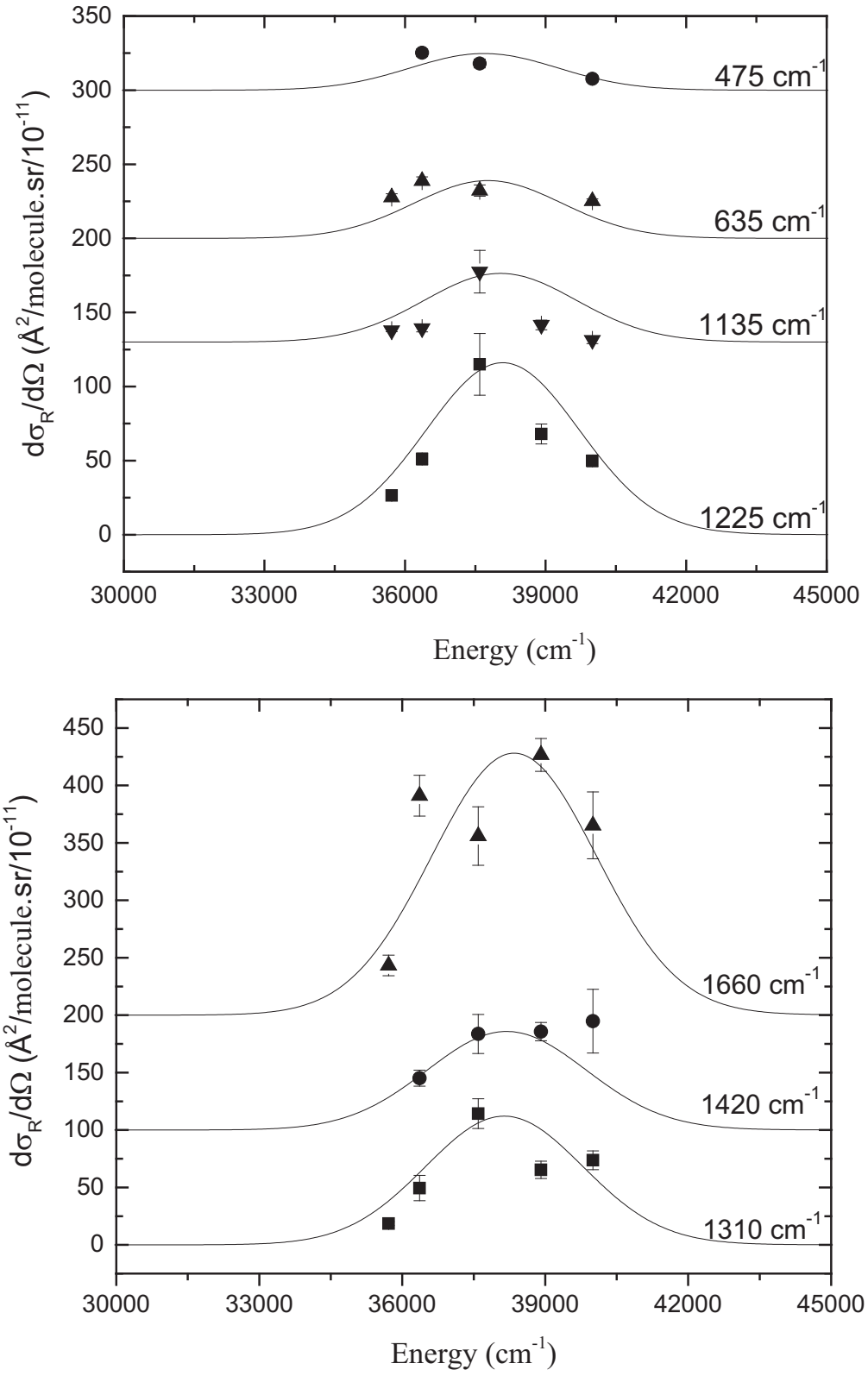

Figure 2.5: Experimental (points) and calculated resonance Raman excitation profiles (solid line) for 5,6-DMU. The excitation profiles were calculated using Equation 2.2 and the parameters in Table 2.2.

Table 2.2: Harmonic mode parameters of 5,6-dimethyluracil

Mode[a] (cm^{-1})	Mode assignment[b]	$\beta/\hbar$ (cm^{-1})
475	Ring def 2 [70], ν(C5C11) [-7], ν(C4N3) [-6]	58
635	be (C4O10) [28], be(C2O8) [-27], -be(C6C12) [14], be)C5C11) [12]	76
1135	CH_{3a} def 4 [22], ν(C6C12) [-17], ν(C4N3) [12], CH_{3a} def 3 [7], ν(C2N3) [-7], be(C5C11) [7]	114
1225	ν(C5C11) [28], ν(C6N1) [-28], Ring def 1 [-9], ν(C5C4) [-9], ν(C2N1) [9]	184
1320	be(N1H7) [18], ν(C2N3) [13], ν(C2N1) [-10], ν(C5C4) [9], be(C5C11) [6], ν(C6N1) [-5], ν(C6C12) [5]	191
1410	CH_{3b} def 1 [57], CH_{3a} def 1 [-17], ν(C6C12) [6]	183
1665	ν(C6C5) [62], ν(C6C12) [-5]	341

[a]Frequencies listed here are experimental frequencies. [b]Abbreviations: ν – stretching, def - deformation, γ - out-of-plane bending and be – in-plane bending. Slope of the excited-state potential energy surface at the Franck–Condon geometry ($\beta/\hbar$) cm^{-1} were obtained by fitting the experimental cross-sections and absorption spectrum with the following parameters in Equation 2.2 and 2.3:temperature, T = 298 K, zero-zero energy, E_0 = 36800 cm^{-1}, Gaussian homogeneous linewidth, Γ_G = 1000 cm^{-1}, inhomogeneous linewidth, θ = 1500 cm^{-1}, transition length, M = 0.675 Å, and Brownian oscillator line shape, $\kappa = \Lambda/D = 0.1$.

that the PED is affected by the presence of the methyl substituents at the C5 and C6 positions. This is expected as the mass at the C5 and C6 positions are changed. A similar change in potential energy distribution were seen in different thymine derivatives where the methyl substitution was at the N1 position.[16]

A quick glance at Table 2.2 will give us an idea about the excited-state slopes for different vibrational modes. Although a mode-to-mode comparison of excited-state slopes is difficult, due to the change in PED and the modes themselves, comparing modes with similar mode description shows that the excited-state slopes are lower for the analogous mode in 5,6-DMU compared to the other uracil derivatives. The presence of the two methyl groups and the higher number of degrees of freedom in 5,6-DMU could explain the observed decrease in excited-state slopes along each mode compared to 5-MU and 6-MU. The presence of the methyl group at both the C5 and C6 positions could constrain the vibration of the C=C bond and the C-C bond between the sp^2 carbon and the methyl carbon, decreasing the excited-state slopes of modes involving these vibrational coordinates. This observed decrease in excited-state slopes may also arise from intramolecular anharmonic coupling of modes and resulting coherence loss in 5,6-DMU.[17]

The relative high intensity for the modes involving the C5 and C6 centres and the calculated excited-state slopes indicate that the initial excited-state structural dynamics of 5,6-DMU are similar to those of 5-MU and 6-MU. These results suggest that the presence of a CH_3 group at an active photochemical center is an important factor in determining the initial excited-state dynamics and not the position of the CH_3 group. Also, it is evident from the excited-state slopes and the mode descriptions that the initial excited-state structural dynamics are oriented along the C5=C6 stretching mode rather than the pyrimidalization modes. But only further photochemistry experiments can provide the relationship between the observed initial excited-state structural dynamics and the photochemistry of the methyl-substituted uracils.

To better constrain the parameters used for the simulation of the absorption spectrum and the resonance Raman excitation profiles, the overtones and combination bands between 1700 cm^{-1} and 3000 cm^{-1} were also measured at 257 nm. The overtones and combination bands above 3000 cm^{-1} were obscured by the broad O-H stretching vibrations of water. The experimental and predicted overtones and combination bands for 5,6-DMU are given in Table 2.3. Most of the calculated

Table 2.3: Experimental and calculated resonance Raman cross-sections for overtone and combination bands of 5, 6-DMU

Mode (cm^{-1})[a]	Mode assignment	$d\sigma_{experimental}/d\Omega$ ($Å^2$/molecule•sr/10^{-11})	$d\sigma_{calculated}/d\Omega$ ($Å^2$/molecule•sr/10^{-11})
2958	1320+1665	4.2 ± 0.8	5.3
2864	1225+1665	4.5 ± 0.9	5.3
2706	1135+1665, 1320+1410	4.1 ± 1.3	4.6
2624	1225+1410, 2 X 1320	2.7 ± 0.8	3.6
2530	1225+1320, 1135+1410	2.4 ± 1.4	3.7
2446	1135+1320, 2 X 1225	2.1 ± 1.0	2.6
2379	1135+1225	1.5 ± .25	1.3
2276	635+1665, 475+1665, 2 X 1135	5.5 ± 1.8	3.6
1953	635+1320, 635+1410	2.5 ± 1.1	1.6
1864	475+1320, 475+1410, 635+1225	2.6 ± 0.6	2.0

[a]Frequencies listed are experimental frequencies. Cross-sections were calculated using Equation 2.1 and the parameters in Table 2.1. Experimental cross-sections were calculated from the resonance Raman spectra of overtone and combination bands of 5,6-DMU at 257 nm.

overtones and combination band intensities are in agreement with the observed intensities within the experimental error. The higher degrees of error in the experimental overtones and combination band cross-sections compared to the fundamental cross-sections are due to both their lower intensity and additional observed imprecision focusing dependent intensities. The agreement between the experimental and calculated cross-sections ensures the accuracy of the parameters used to simulate the absorption and RREPs.

Table 2.4: Comparison of the harmonic parameters for different derivatives of uracil

	5-MU[a]	5,6-DMU	6-MU[b]	U[c]
E_0 energy (cm^{-1})	35650	36800	36700	36500
M (Å)	0.67	0.675	0.72	0.65
Γ_G (cm^{-1})	1700	1000	1470	1450
θ (cm^{-1})	1075	1500	1040	1000

[a,b,c]The parameters for 5-MU, 6-MU and U were obtained from references 7, 9 and 8, respectively. E_0 is the zero-zero energy, M is the transition length, Γ_G is the homogeneous linewidth and θ is the inhomogeneous linewidth.

Table 2.4 compares the electronic and broadening parameters for the different uracil derivatives. The zero-zero energy, transition length and total broadening are similar in all the uracil derivatives, within experimental error except for 5-

MU. This confirms the similarity between the electronic properties of uracil, 5,6-DMU, 5-MU and 6-MU. Inhomogeneous broadening are mainly due to the solvent-solute interaction, which is static within the dephasing timescale[18]. The high inhomogeneous linewidth indicates that there is a broader solvent-induced zero-zero energy in 5,6-DMU compared to other methyluracils. This result is expected as the size of the molecule increases. Homogeneous broadening in the nucleobases is mainly due to solvent-induced dephasing, with a smaller contribution from population decay. The decrease in the homogeneous linewidth in 5,6-DMU compared to 5-MU and 6-MU is a little surprising. This decrease may arise from the steric protecting effect of the methyl group, which may decrease the solvent-solute collisions that lead to dephasing. Further studies on the excited-state life times and its solvent dependence are required to better understand the broadening mechanisms.

2.4 Conclusions

The resonance Raman spectrum of 5,6-DMU is intermediate between that of 5-MU and 6-MU. The presence of the methyl group at both the C5 and C6 positions determines the partition of the initial excited-state structural dynamics between the CH bending and stretching modes. The decrease in the calculated excited-state slopes for the different modes in 5,6-DMU compared to 5-MU and 6-MU can be attributed to the 5,6-DMU geometry constraint imposed by the two methyl groups and the increase in the number of vibrational degrees of freedom. The initial excited-state structural dynamics are oriented along the C5=C6 bond-lengthing coordinate, similar to those of both 5-MU and 6-MU. Also, it is the presence of CH_3 groups, rather than their position at C5 or C6 that appears to determine the initial excited-state structural dynamics. Only further photochemistry experiments with 6-MU and 5,6-DMU to measure the yields of different photoproducts will enable us to establish the relationship between the initial excited-state structural dynamics and the photochemistry.

References

[1] B. P. Ruzsicska and D. G. E. Lemaire. *CRC Handbook of Organic Photochemistry and Photobiology*, chapter DNA Photochemistry, pages 1289–1317. CRC Handbook. CRC Press, 1995.

[2] I. H. Brown, K. B. Freeman, and H. E. Johns. Photochemistry of uridylyl-(3'-5')-uridine. *J. Mol. Biol.*, 15(2):640–662, 1966.

[3] T. Gustavsson, A. Banyasz, E. Lazzarotto, D. Markovitsi, G. Scalmani, M. J. Frisch, V Barone, and R. Improta. Singlet excited-state behavior of uracil and thymine in aqueous solution: A combined experimental and computational study of 11 uracil derivatives. *J. Am. Chem. Soc.*, 128(2):607–619, 2006.

[4] A. B. Myers and R. A. Mathies. *Resonance Raman spectra of polyenes and aromatics*. Wiley, New York, 1987.

[5] A. B. Myers. *Laser techniques in chemistry*. Techniques of chemistry. Wiley, 1995.

[6] A. M. Kelley. Resonance Raman intensity analysis of vibrational and solvent reorganization in photoinduced charge transfer. *J. Phys. Chem. A*, 103(35):6891–6903, 1999.

[7] S. Yarasi, P. Brost, and G. R. Loppnow. Initial excited-state structural dynamics of thymine are coincident with the expected photochemical dynamics. *J. Phys. Chem. A*, 111(24):5130–5135, 2007.

[8] S. Yarasi, S. Ng, and G. R. Loppnow. Initial excited-state structural dynamics of uracil from resonance Raman spectroscopy are different from those of thymine (5-methyluracil). *J. Phys. Chem. B*, 113(43):14336–14342, 2009.

[9] B. E. Billinghurst, R. Yeung, and G. R. Loppnow. Excited-state structural dynamics of 5-fluorouracil. *J. Phys. Chem. A*, 110(19):6185–6191, 2006.

[10] S. S. Ng, F. Teimoory, and G. R. Loppnow. Mass-tuned initial excited-state structural dynamics of DNA nucleobases from UV resonance Raman spectroscopy: 5-deuterouracil. *J. Phys. Chem. Lett.*, 2(18):2362–2365, 2011.

[11] F. Teimoory and G. R. Loppnow. Initial excited-state structural dynamics of 6-methyluracil: the importance of pyramidalization and bond lengthening motions in its photochemistry. submitted to Photochem. Photobiol.

[12] B. Li, A. E. Johnson, S. Mukamel, and A. B. Myers. The Brownian oscillator model for solvation effects in spontaneous light emission and their relationship to electron transfer. *J. Am. Chem. Soc.*, 116(24):11039–11047, 1994.

[13] L. C. T. Shoute and G. R. Loppnow. Excited-state dynamics of alizarin-sensitized TiO_2 nanoparticles from resonance Raman spectroscopy. *J. Chem. Phys.*, 117(2):842–850, 2002.

[14] M. J. Frisch, G. W. Trucks, H. B. Schlegel, G. E. Scuseria, M. A. Robb, J. R. Cheeseman, G. Scalmani, V. Barone, B. Mennucci, G. A. Petersson, H. Nakatsuji, M. Caricato, X. Li, H. P. Hratchian, A. F. Izmaylov, J. Bloino, G. Zheng, J. L. Sonnenberg, M. Hada, M. Ehara, M. Toyota, R. Fukuda, M. Hasegawa, M. Ishida, T. Nakajima, Y. Honda, O. Kitao, H. Nakai, T. Vreven, J. A. Montgomery, Jr., J. E. Peralta, F. Ogliaro, M. Bearpark, J. J. Heyd, E. Brothers, K. N. Kudin, V. N. Staroverov, R. Kobayashi, J. Normand, R. Raghavachari, A. Rendell, J. C. Burant, S. S. Iyengar, J. Tomasi, M. Cossi, N. Rega, J. M. Millam, M. Klene, J. E. Knox, J. B. Cross, V. Bakken, C. Adamo, J. Jaramillo, C. Gomperts, R. E. Stratmann, O. Yazyev, A. J. Austin, R. Cammi, C. Pomelli, J. W. Ochterski, R. L. Martin, K. Morokuma, V. G Zakrzewski, G. A. Voth, P. Salvador, J. J. Dannenberg, S Dapprich, A. D. Daniels, Ö. Farkas, J. B. Foresman, J. V. Ortiz, J. Cioslowski, and D. J Fox. Gaussian 09 Revision A.1, 2009. Gaussian Inc. Wallingford CT.

[15] J. M. L. Martin and C Van Alsenoy. Gar2ped, a program to obtain a potential energy distribution from a Gaussian archive record. University of Antwerp, Belgium, 2007.

[16] B. E. Billinghurst, S. A. Oladepo, and G. R. Loppnow. Initial excited-state structural dynamics of thymine derivatives. *J. Phys. Chem. B*, 116(35):10496–10503, 2012.

[17] M. K. Lawless and R. A. Mathies. Excited-state structure and electronic dephasing time of Nile blue from absolute resonance Raman intensities. *J. Chem. Phys.*, 96(11):8037–8045, 1992.

[18] A. B. Myers. Molecular electronic spectral broadening in liquids and glasses. *Ann. Rev. Phys. Chem.*, 49:267–295, 1998.

Chapter 3

Initial Excited-State Structural Dynamics of DNA Oligonucleotide Homopentamers using Resonance Raman Spectroscopy

3.1 Introduction

As discussed in Chapter 1, it is very well established that the absorption of ultraviolet light by DNA initiates photochemical reactions resulting in DNA damage.[1–6] The main chromophores responsible for UV absorption by DNA are the adenine, guanine, cytosine and thymine nucleobases.[7–9] The evolution of the ground- and excited-state potential energy surfaces of the molecule following absorption of a photon is a significant step in determining the photochemical reaction pathway.[10] Therefore, probing the initial excited-state structural dynamics gives some insight into the photochemical reaction pathways and photoproducts.[10–12]

Much research has been performed examining the excited-state dynamics of nucleobases and their derivatives.[13–25] The structure of the different nucleotides is shown in Figure 3.1. The excited-state lifetimes of different nucleobases have been measured recently with the help of femtosecond transient absorption. Excited-state lifetimes of 290, 460, 720, and 540 fs were found for adenine, guanine, cytosine and thymine nucleosides, respectively.[20,21] These very fast relaxation times result from ultrafast internal conversion.[20,21] However the electronic excited-state lifetime increases as the number of nucleobases increases.[19,22–24,26] Recently, Baribatti and

coworkers have carried out the hopping dynamics calculation on guanine to show photoexcited guanine deactivates by a femtosecond transition through a conical intersection involving the $\pi\pi^*$ excited state and the ground state. The involvement of the $n\pi^*$ state is minimal.[15] Pancur et al., used fluorescence up-conversion spectroscopy to show that the excited states of adenine and its corresponding nucleoside decay rapidly due to strong coupling of the $\pi\pi^*$ and $n\pi^*$ states[16]. Furthermore, the ultrafast non-radiative decay of the $\pi\pi^*$ state of adenine proceeds through a conical intersection between $\pi\pi^*$ and S_0. Gustavsson et al., looked at the singlet excited-state dynamics of the pyrimidine nucleobases and their derivatives in different solvents with femtosecond fluorescence up-conversion spectroscopy.[17,18] The purine nucleobases and their derivatives decay within femtoseconds. The decay was slower in acetonitrile. These studies showed that there is an increase in excited-state lifetime on going from uracil to thymine, which was attributed to the involvement of C5 pyramidalization. Phillips et al., employed femtosecond time-resolved fluorescence and transient absorption spectroscopy to study thymidine and thymine oligonucleotide and found an ultrafast, single base-localized, stepwise mechanism that deactivates the thymine multimer.[25] All these studies examined only the electronic excited-state dynamics not the coincident structural dynamics. It is also important to understand the excited-state structural dynamics, since ultimately it is these structural dynamics that define the excited-state decay mechanism and photochemistry of the molecule.

Resonance Raman spectroscopy can probe the initial excite-state structural dynamics of the molecule when the excitation wavelength of a laser is tuned to the absorption band of the molecule. In resonance Raman spectroscopy, the vibrational modes coupled to the electronic absorption band will be resonantly enhanced and the intensities of these modes are directly proportional to the slope of the excited-state potential energy surface along those vibrational coordinates[27–29]. A higher resonance Raman intensity of a particular mode means a greater molecular structural change along that particular vibrational coordinate in the excited electronic state.

There have been several resonance Raman studies on DNA and DNA components.[30–46] Loppnow and coworkers have successfully used resonance Raman spectroscopy to understand the difference in the photochemistry of different nucleobases and their derivatives.[30–35,42,43] In thymine, the observed resonance Raman inten-

sities suggest that the C5=C6 bond elongation and pyrimidalization of C5 and C6, which are consistent with thymine photochemistry, are the primary structural dynamics.[42] In contrast, the C5H and C6H bending modes are the most intense modes in uracil, where the photohydrate is the major photoproduct.[43] Also, resonance Raman studies were extended to different thymine derivatives which found that the initial excited-state dynamics are similar for thymidine and thymidine monophosphate as for thymine.[42]

The resonance Raman spectra of other nucleobases, nucleosides and nucleotides have also been obtained. The resonance Raman intensities of guanosine nucleotide reflect its photochemically active modes.[42] Puranik et al. have done UV resonance Raman spectroscopy of 8-oxoguanosine, one of the oxidative photoproducts of guanosine and showed that the resonance Raman spectroscopy can be used to identify the site of DNA damage.[45] In addition, 8-oxoguanosine can be used as a site-specific probe for DNA due to its unique spectral features.[45,47] Resonance Raman studies on cytosine suggests that only about one-third of the reorganization energy is along vibrational modes that are photochemically active.[30] All these studies show that there is a pronounced difference in the initial excited-state structural dynamics between nucleobases that are reflected in their photoproducts and photochemical yields. So the initial excited-state structural dynamics play an important role in deciding the photochemistry of the nucleobases.

In this Chapter, we study the excited-state structural dynamics of four DNA homopentamers of adenosine, cytidine, guanosine and thymidine to provide valuable insight into their photochemistry. This work extends the knowledge of nucleobase photophysics and photochemistry to a more relevant DNA-like structure. The results show that the initial excited-state structural dynamics of nucleobases in the pentamers are similar to those of the respective mononucleotides in solution.

3.2 Experimental

Homopentamers of adenosine (5'-dApdApdApdApdAp-3'), cytosine (5'-dCpdCpdCpdCpdCp-3'), guanosine (5'-dGpdGpdGpdGpdGp-3') and thymidine (5'-dTpdTpdTpdTpdTp-3') were from Integrated DNA Technologies Inc. (Coralville, IA) and sodium nitrate (99%) was obtained from EMD Chemicals Inc. (Gibbstown, NJ). Both were used without any further purification. All the samples were diluted to the required concentration using nanopure water from a Barnstead water filtration

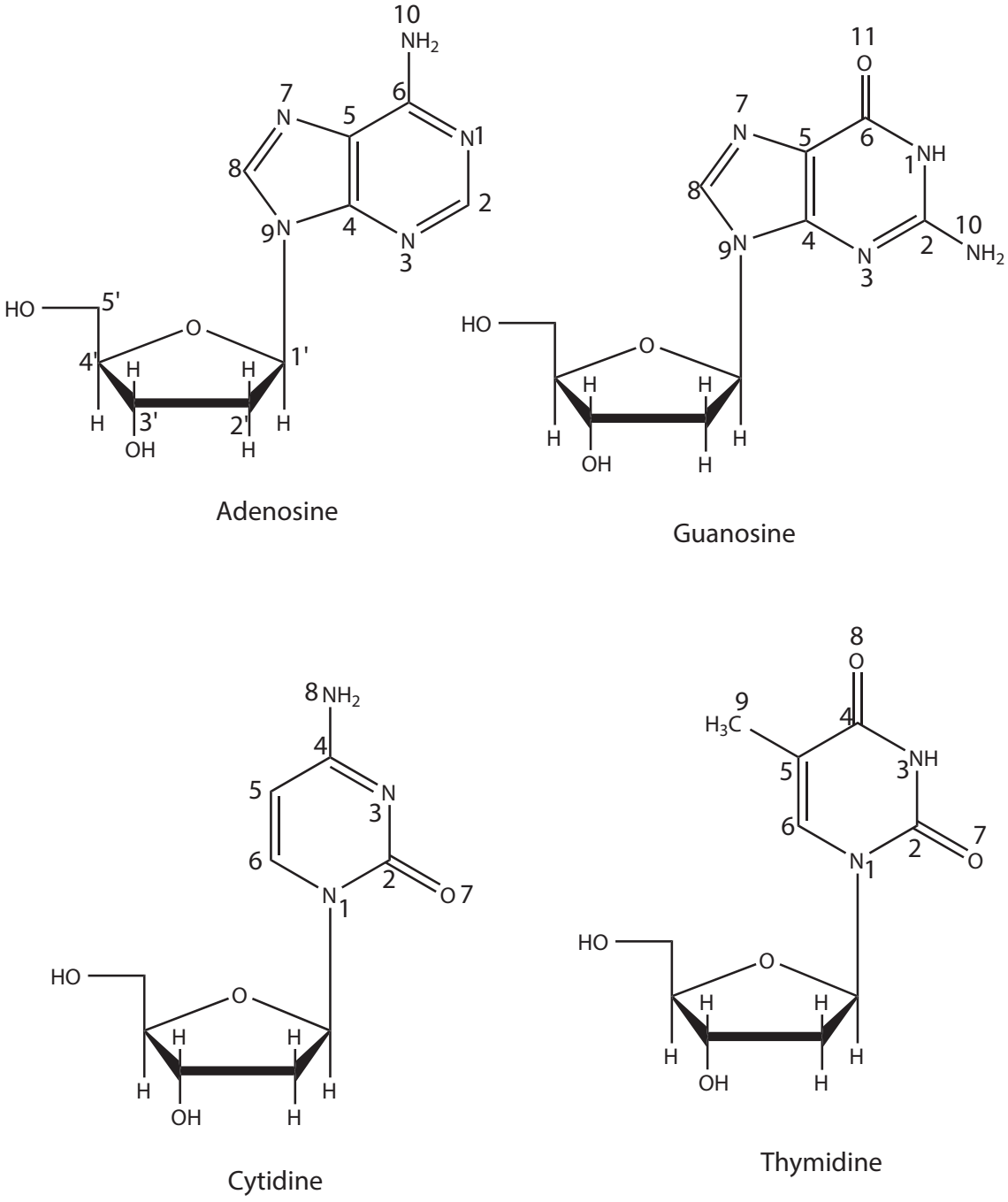

Figure 3.1: Structure of different nucleotides in DNA.

system (Boston, MA).

Resonance Raman excitation laser wavelengths of 250, 257, 266, 275 and 280 nm were obtained from the third harmonic of a tunable picosecond, mode-locked Ti:sapphire laser (Coherent, Santa Clara, CA) which is pumped by a doubled, continuous-wave, solid-state, diode-pumped Nd:YAG laser (Coherent, Santa Clara, CA) as described in Chapter 2. The laser power measured at the sample was 1-6 mW, depending on the wavelength. The third harmonic laser beam was spherically focused on an open stream of flowing sample solution in a 135° backscattering geometry.

Resonance Raman spectra for all excitation wavelengths were obtained using solutions with homopentamer concentrations of 0.2-0.3 mM containing 0.1-0.3 M sodium nitrate as internal standard. Addition of sodium nitrate had no effect on the absorption or resonance Raman spectra of the homopentamers. The exact concentrations of the compounds were calculated from the absorption spectra of the solutions by using a diode array spectrometer (Hewlett-Packard 8452, Sunnyvale, CA). Absorption spectra were measured before and after each resonance Raman experiment to account for any change in concentration due to evaporation and/or sample alteration while acquiring the resonance Raman spectra. All resonance Raman spectral measurements were done in triplicate. Frequency calibration of the resonance Raman spectra were done by measuring the Raman scattering of solvents (acetonitrile, acetic acid, cyclohexane, methanol, DMSO and DMF) for which the frequencies are known. The Resonance Raman frequencies for different homopolymers reported here are accurate to ± 5-10 cm^{-1}. The absolute resonance Raman cross-sections were calculated from the integrated band intensities using the following equation.

$$(\frac{d\sigma_R}{d\Omega})_{Homopent} = (\frac{d\sigma}{d\Omega})_{IS} \frac{I_{Homopent}}{I_{IS}} \frac{[IS]}{[Homopent]} \frac{L_{IS}}{L_{Homopent}} \times SA \qquad (3.1)$$

where $d\sigma_R/d\Omega$ is the differential resonance Raman cross-section of the vibrational mode, $I_{Homopent}$ and I_{IS} are the integrated band intensities of the homopentamer and the internal standard, respectively, [IS] and [Homopent] are the concentrations of the internal standard and the homopentamers, respectively, $L_{Homopoly}$ and L_{IS} refer to the standard lamp efficiency at the homopentamer and the internal standard vibrational frequencies, respectively, and SA is the differential self-absorption of the resonance Raman scattered light at the homopentamer and internal standard

vibrational frequencies. The method used for the conversion of resonance Raman intensities of homopentamers to absolute cross-section and the self-absorption correction has been described previously.[48–50] The nitrate internal standard resonance Raman differential cross-sections were 3.68×10^{-11}, 2.43×10^{-11}, 1.53×10^{-11} and 1.02×10^{-11} Å^2/molecule $\times$ sr at 250, 257, 266 and 275 nm, respectively.

Resonance Raman structural dynamics. The resonance Raman intensities as a function of excitation wavelength (excitation profiles) and the absorption spectra of the homopentamers were simulated with a time-dependent formalism.[27–29]

$$\sigma_R = \frac{8\pi e^4 M^4 E_s^3 E_L}{9\hbar^6 c^4} \int_0^\infty dE_0 H(E)_0 \left| \int_0^\infty < f|i(t) > exp\left[\frac{i(E_L + \epsilon_i)t}{\hbar}\right] G(t)dt \right|^2 \tag{3.2}$$

$$\sigma_A = \frac{4\pi M^2 e^2 E_L}{6\hbar^2 cn} \int_0^\infty dE_0 H(E)_0 \int_{-\infty}^\infty < i|i(t) > exp\left[\frac{i(E_L + \epsilon_i)t}{\hbar}\right] G(t)dt \tag{3.3}$$

where E_L and E_S are the energies of the incident and scattered photons, respectively, M is the transition length, n is the refractive index, ϵ_i represents the energy of the initial vibrational state, $|i>$ and $|f>$ are the initial and final vibrational wavefunctions in the Raman scattering process, respectively, $H(E_0)$ is the normalized inhomogeneous distribution of the zero-zero energies around an average energy $\overline{E}_0$, $|i(t)>$ is the initial ground vibrational wavefunction propagated on the excited-state potential energy surface, and G(t) is the homogeneous linewidth, which represents the dynamics of chromophore-solvent coupling within the high-temperature limit of the Brownian oscillator model. Within the harmonic approximation, the $<i|i(t)>$ and $< f|i(t) >$ overlaps depend only on the slopes $(\beta/\hbar)$ of the excited-state potential energy surface at the ground-state equilibrium geometry along each normal mode of vibration. The implementation of these equations have been described in detail previously[27–29,51,52]. Thus, the resonance Raman intensities reflect the excited-state structural dynamics of the molecule. The simulation of the absorption spectrum and resonance Raman excitation profiles has been performed as previously described[27–35,42,42,43,43,48–50]. For the analysis, the parameters were adjusted so as to get good agreement between the experimental and simulated absorption spectra and the resonance Raman excitation profiles.

3.3 Results

The resonance Raman spectra of the four homopentamers $(dTp)_5$, $(dGp)_5$, $(dCp)_5$ and $(dAp)_5$ are shown in Figure 3.6. $(dTp)_5$ resonance Raman peaks are observed at 1190, 1240, 1380, 1410, 1480 and 1660 cm^{-1}. The spectrum of $(dGp)_5$ shows peaks at 1340, 1410, 1480, 1580 and 1650 cm^{-1} and $(dCp)_5$ has peaks at 780, 1250, 1290, 1360, 1410, 1530 and 1660 cm^{-1}. Seven well defined peaks are observed in $(dAp)_5$ at 730, 1310, 1340, 1410, 1480, 1580 and 1660 cm^{-1}. All the spectra are normalized with respect to the most intense peak in the spectrum. Although other features below 1000 cm^{-1} are observed in the resonance Raman spectra at 266 nm, these were not reproducibly observed at other wavelengths and are not considered further.

The resonance Raman spectrum of $(dTp)_5$ (Figure 3.2) is very similar to the resonance Raman spectra of thymidine and thymidine monophosphate at 266 nm.[42] The full description of individual modes of $(dTp)_5$ is given in Table 3.1. The most intense band is the 1660 cm^{-1} band (C5=C6 stretch) as in all derivatives of thymine.[42] The next intense mode is the 1380 cm^{-1} mode, which is seen at 1376 cm^{-1} in thymidine monophosphate and is assigned to C6-H12 bend. The 1240 cm^{-1} mode is a combination of C5-Me stretch and ring stretch (Table 3.1). The resonance Raman spectra of $(dTp)_5$ at different excitation wavelengths are given in Figure A.1 Appendix A.

The resonance Raman spectrum of $(dGp)_5$ (Figure 3.3) looks similar to that of 2'-deoxyguanosine (2-dG).[35] The different modes of $(dGp)_5$ are assigned by comparing the modes of 2-dG and a full description of individual modes of $(dGp)_5$ is given in Table 3.2. Most of the peaks in 2-dG are observed in $(dGp)_5$ as well. A small peak at 1240 cm^{-1} is seen at three excitation wavelength in $(dGp)_5$, which is absent in 2-dG. The two peaks at 1321 cm^{-1} and 1366 cm^{-1} in 2-dG appear as a single peak around 1340 cm^{-1} in $(dGp)_5$. The most intense band in 2'-deoxyguanosine is at 1490 cm^{-1} and is mainly due to C8H bending, while the two most intense modes in $(dGp)_5$ are 1580 cm^{-1} and the 1340 cm^{-1} mode due to N3-C4 and N7-C8 stretches, respectively. The resonance Raman spectra of $(dGp)_5$ at different excitation wavelengths are given in Figure A.2 in Appendix A.

Comparison of $(dCp)_5$ resonance Raman spectra (Figure 3.4) with that of cytosine (C) reveal the similarity between the monomer and the homopentamer.[30]

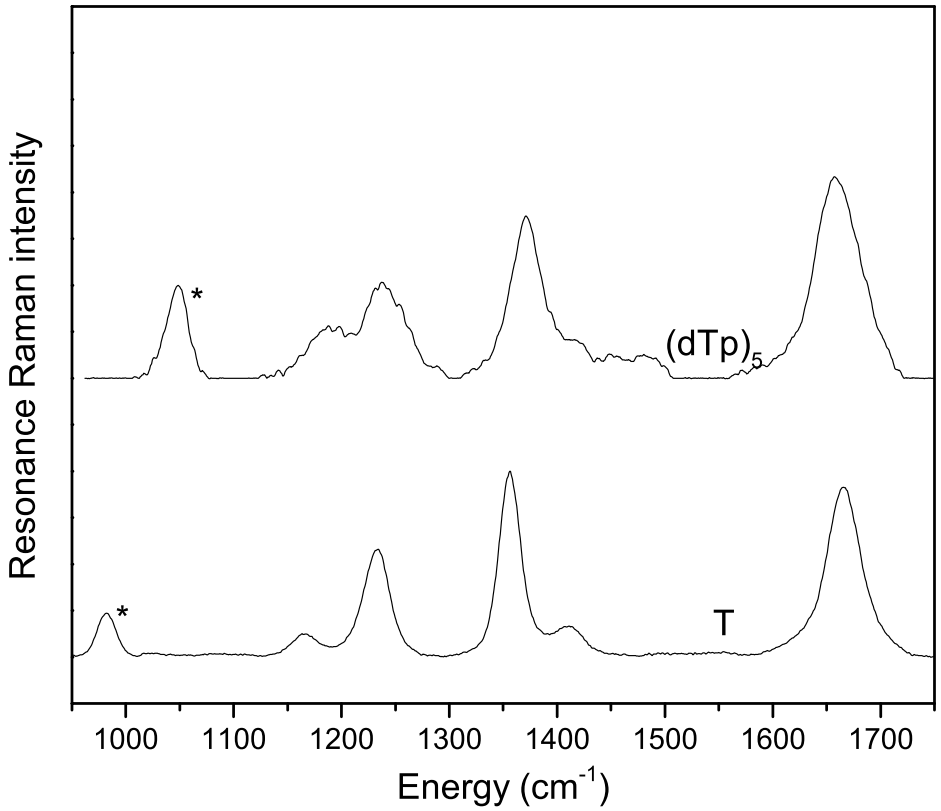

Figure 3.2: Resonance Raman spectra of $(dTp)_5$ (0.3mM) and thymine (T) (3mM) excited at 266 nm. The internal standard (0.1 M sodium nitrate for $(dTp)_5$ and 0.4 M sodium sulfate for Thymine peaks are denoted by an asterisk (*).

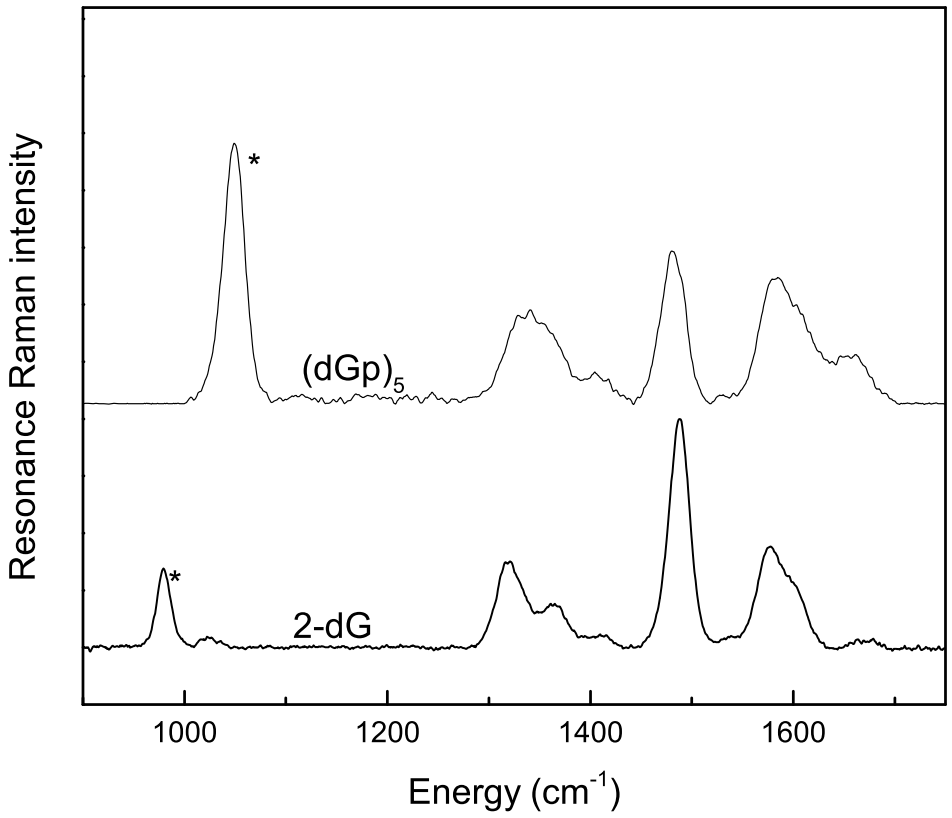

Figure 3.3: Resonance Raman spectra of $(dGp)_5$ (0.3mM) and 2‘-deoxyguanosine (2-dG) (3mM) excited at 257 nm. The internal standard (0.1 M sodium nitrate for $(dGp)_5$ and 0.4 M sodium sulfate for 2‘-deoxyguanosine peaks are denoted by an asterisk (*).

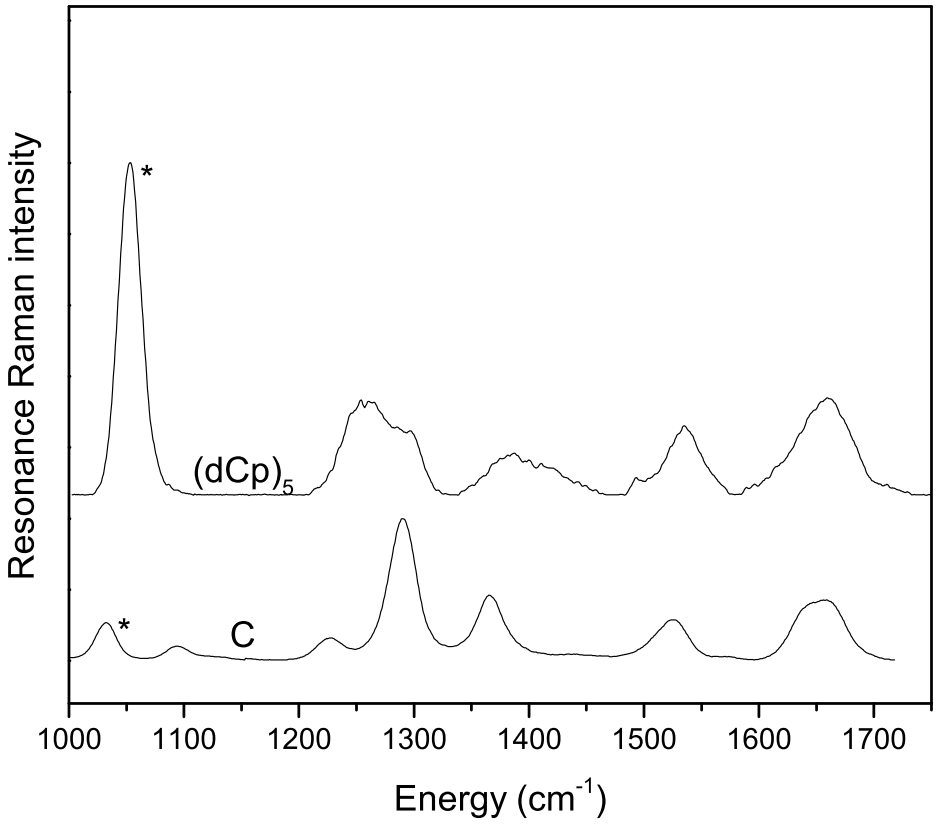

Figure 3.4: Resonance Raman spectra of $(dCp)_5$ (0.3mM) and cytosine (C) (3mM) excited at 266 nm. The internal standard (0.3 M sodium nitrate for $(dCp)_5$ and cytosine peaks are denoted by an asterisk (*).

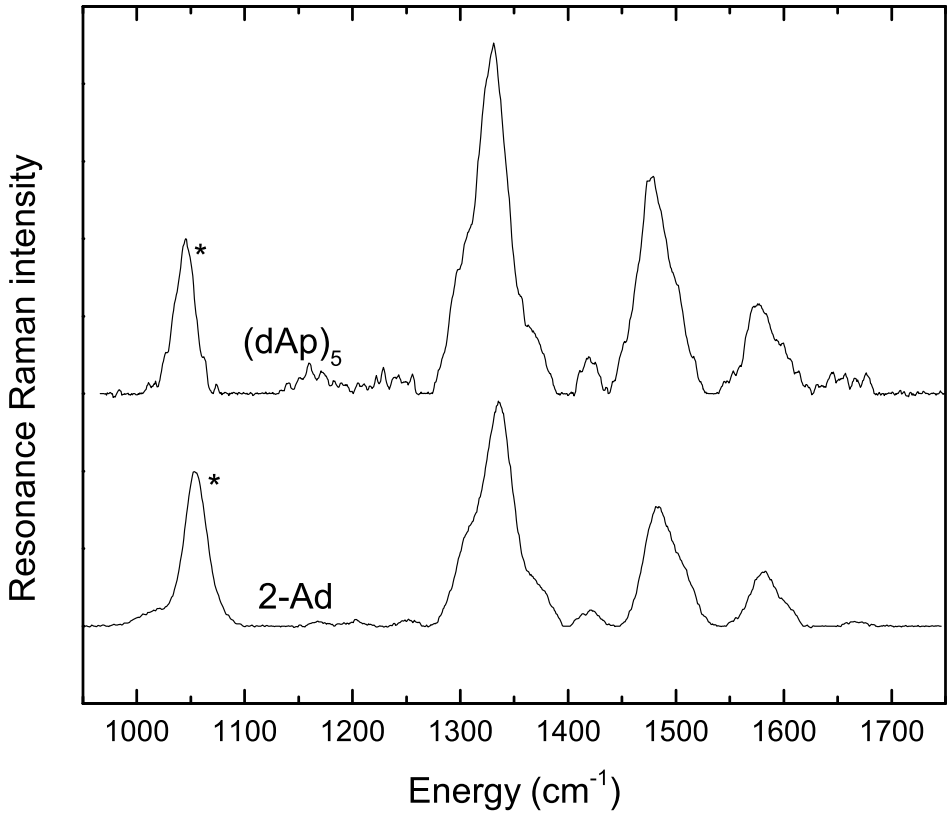

Figure 3.5: Resonance Raman spectra of $(dAp)_5$ (0.3mM) and 2'-deoxyadenosine (2-Ad) (3mM) excited at 266 nm. The internal standard (0.1 M sodium nitrate 0.3 M sodium nitrate for 2-deoxyadenosine peaks are denoted by an asterisk (*).

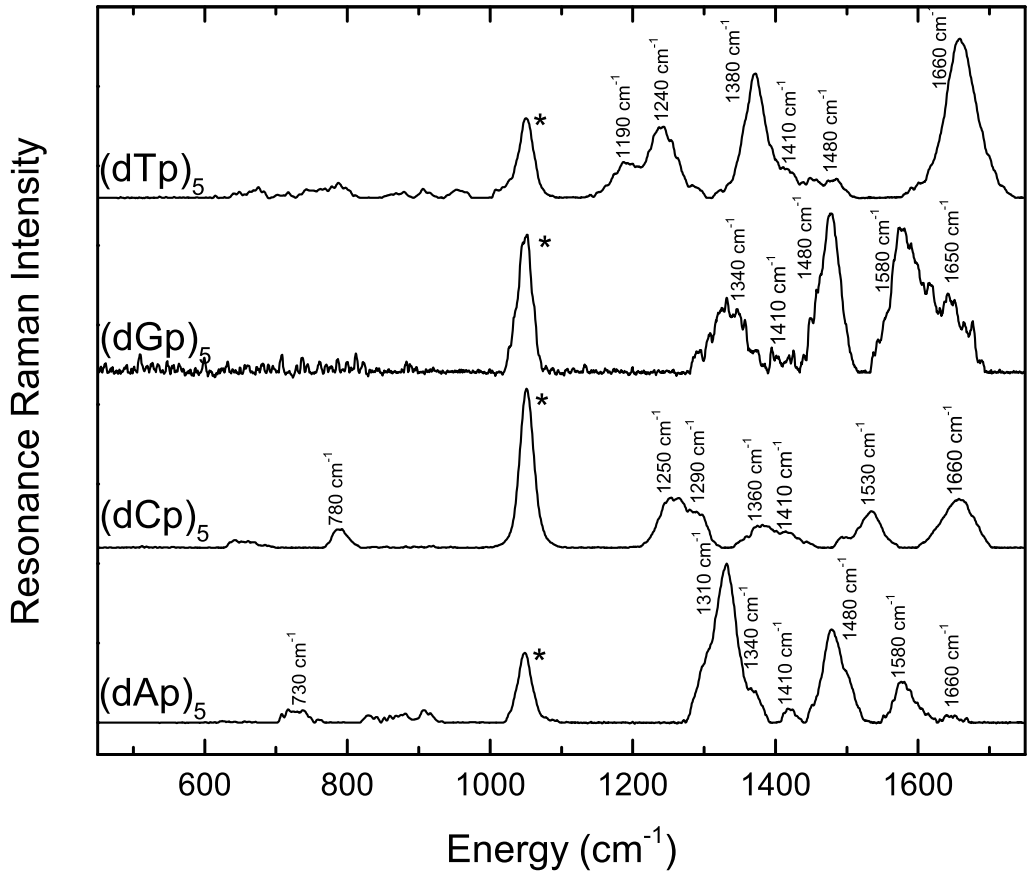

Figure 3.6: Resonance Raman spectra of different homopentamers excited at 266 nm. The internal standard (0.3 M nitrate for $(dCp)_5$ and 0.1 M nitrate for $(dAp)_5$, $(dGp)_5$ and $(dTp)_5$) peaks are denoted by an asterisk (*) in each spectrum. The resonance Raman spectra are normalized with respect to the most intense peak in each spectrum. Spectra have been offset along the y-axis for clarity.

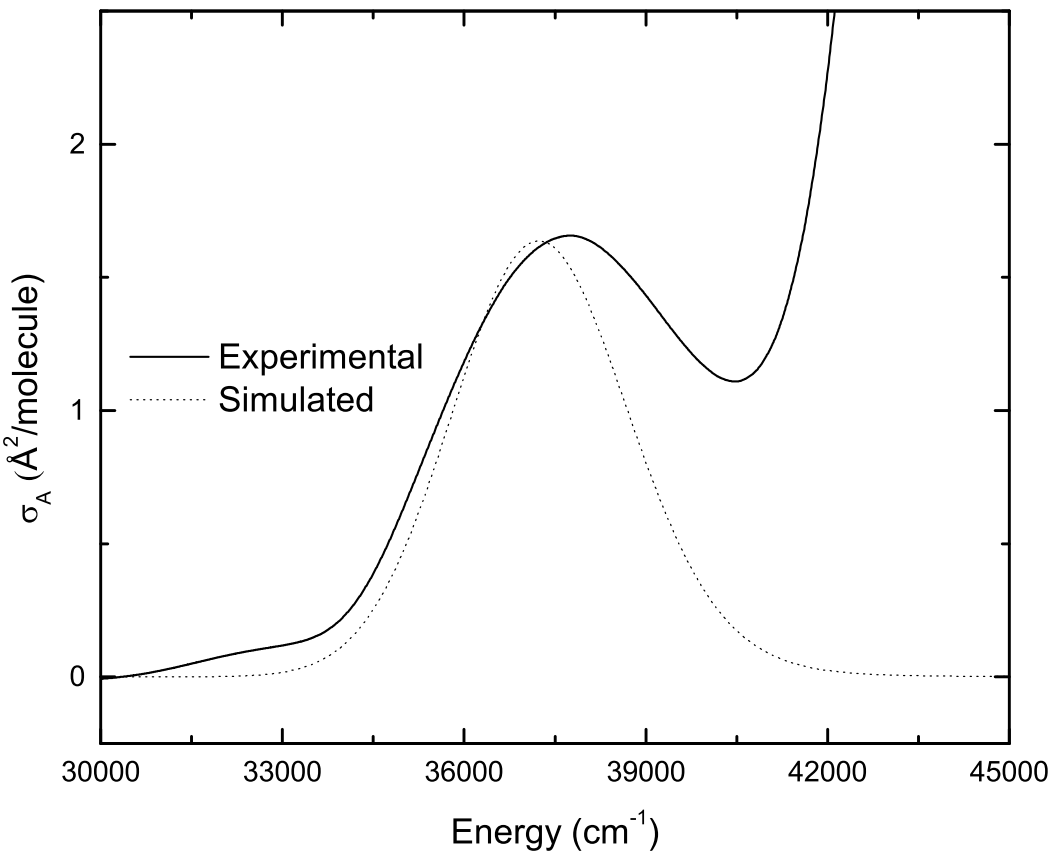

Figure 3.7: Experimental (solid line) and simulated (dotted line) absorption spectra of $(dTp)_5$. The simulated absorption spectrum was generated using Equation 3.3 and the parameters of Table 3.1. The differences between the experimental and simulated spectra at higher energies are other higher energy transitions which are not modeled in the equation.

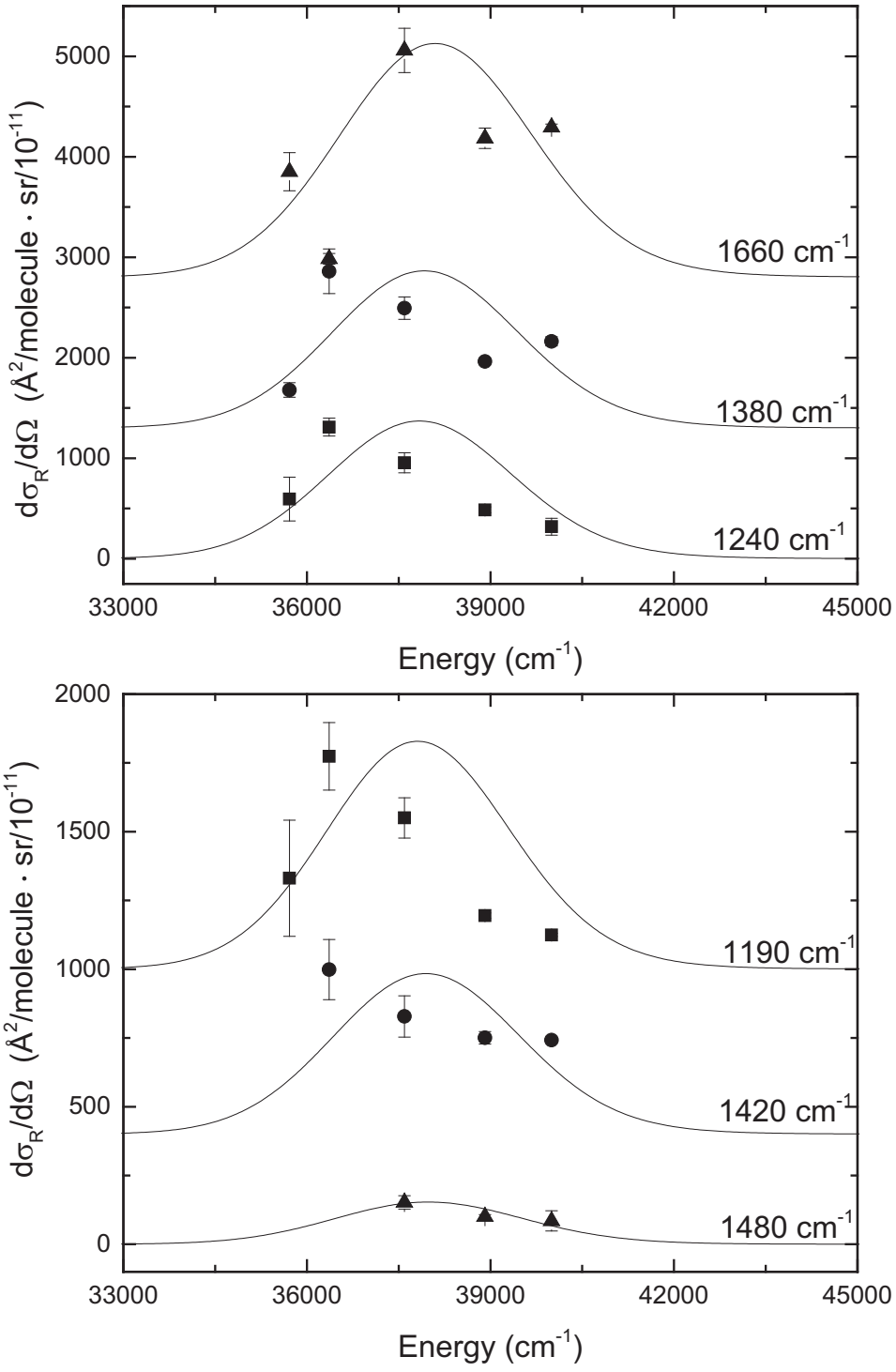

Figure 3.8: Experimental (points) and calculated (solid lines) resonance Raman excitation profile for $(dTp)_5$. The excitation profiles were calculated using Equation 3.2 and the parameters in Table 3.1.

Table 3.1: Harmonic mode parameters for $(dTp)_5$

Mode[a] (cm^{-1})	Mode assignment[b]	$\beta/\hbar$ (cm^{-1})
1190	ν(C2N3) [21], be(C6H12) [20], be(N1H7) [-16], ν(N3C4) [-12], ν(C6N1) [-11]	190.4
1240	ν(C5Me) [29], νC6N1) [-21], ring def 1 [12], ν(N1C2) [10], ν(C4C5) [-10], ν(C2N3) [-8]	248.0
1375	be(C6H) [42], ν(C5C6) [12], ν(N1C2) [9], ν(C2N3) [-9]	275.0
1417	ν(C2N3) [15], ν(C4C5) [13], CH3 umb [11], be(N1H) [9], ν(N1C2) [-8], be(C4O) [7], be(C2O) [7], ring def 2 [-6], be (N3H) [-6]	170.0
1480	ν(C4C5) [24], ν(N1C2) [13]	88.8
1664	ν(C5C6) [61], be(C6H) [13], ν(C6N1) [-8], ν(C5Me)[-5]	366.1

[a]Frequencies listed here are experimental frequencies. [b]Abbreviations: ν - stretching, def - deformation, γ - out-of-plane bending and be - in-plane bending. The slopes of the excited-state potential energy surface at the Franck-Condon geometry ($\beta/\hbar$) in cm^{-1} were obtained by fitting the experimental cross-sections and absorption spectrum with the following parameters in Equation 3.2 and 3.3 :temperature, T = 298 K, zero-zero energy, E_0 = 35700 cm^{-1}, Gaussian homogeneous linewidth, Γ_G = 1800 cm^{-1}, inhomogeneous linewidth, θ = 1150 cm^{-1}, transition length, M = 1.50 Å, and Brownian oscillator line shape, $\kappa = \Lambda/D = 0.1$.

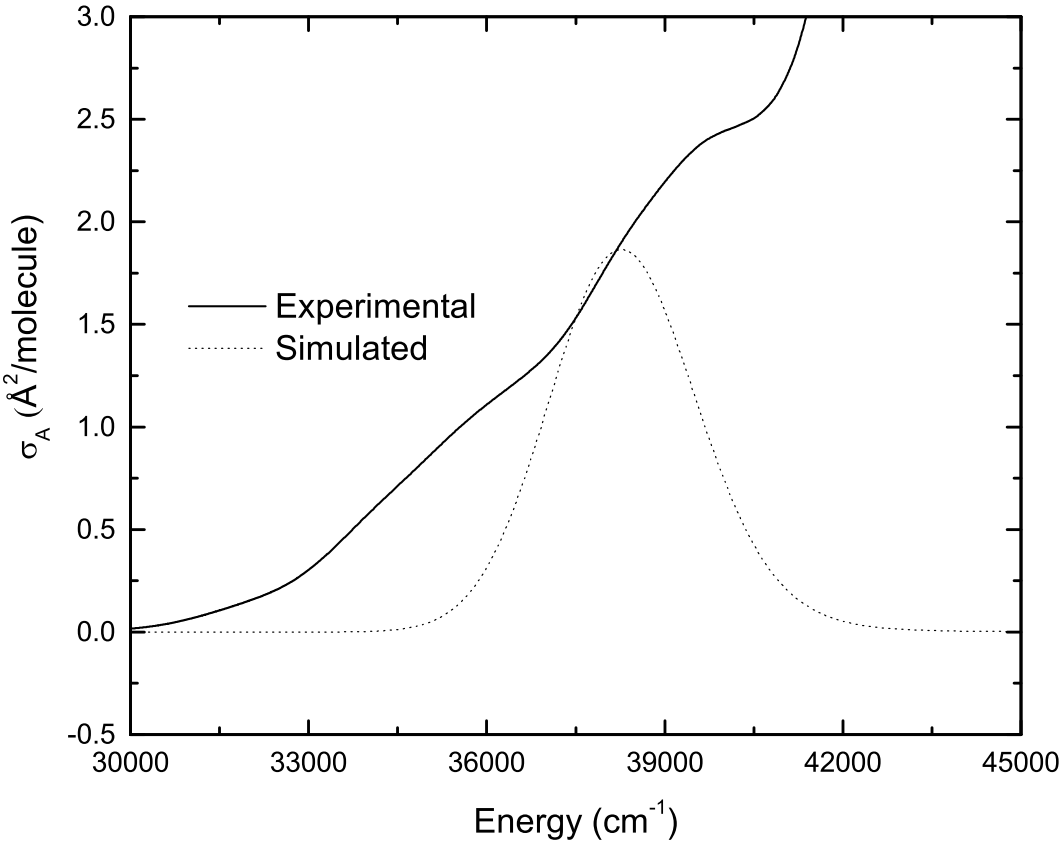

Figure 3.9: Experimental (solid line) and simulated (dotted line) absorption spectra of $(dGp)_5$. The simulated absorption spectrum was generated using Equation 3.3 and the parameters of Table 3.2. The differences between the experimental and the simulated spectra at higher energies are other higher energy transitions which are not modeled in the equation.

Table 3.2: Harmonic mode parameters for $(dGp)_5$

Mode[a] (cm^{-1})	mode assignment[b]	$\beta/\hbar$ (cm^{-1})
1240	ν(N7C8) [+19], be(C8H) [-24]	93.0
1340	ν(N7C8) [-26], ν(N1C6) [-25], ν(N5N7) [+16]	241.2
1410	ν(C4N9) [-33], ν(C5N7) [-24]	126.9
1480	be(C8H) [+40], ν(C8N9) [-32], ν(N7C8) [+21]	207.2
1580	ν(N3C4) [-30], ν(C4C5) [+24], ν(C5N7) [-16]	268.6
1650	ν(C6O) [+48], ν(C5C6) [-21], be(N1H) [-11], ν(C4C5) [+11], ν(N1C6) [-10]	181.5

[a]Frequencies listed here are experimental frequencies. [b]Abbreviations: ν - stretching, def - deformation, γ - out-of-plane bending and be - in-plane bending. The slopes of the excited-state potential energy surface at the Franck-Condon geometry ($\beta/\hbar$) in cm^{-1} were obtained by fitting the experimental cross-sections and absorption spectrum with the following parameters in Equation 3.2 and 3.3 :temperature, T = 298 K, zero-zero energy, E_0 = 36800 cm^{-1}, Gaussian homogeneous linewidth, Γ_G = 1800 cm^{-1}, inhomogeneous linewidth, θ = 900 cm^{-1}, transition length, M = 1.46 Å, and Brownian oscillator line shape, $\kappa = \Lambda/D = 0.1$.

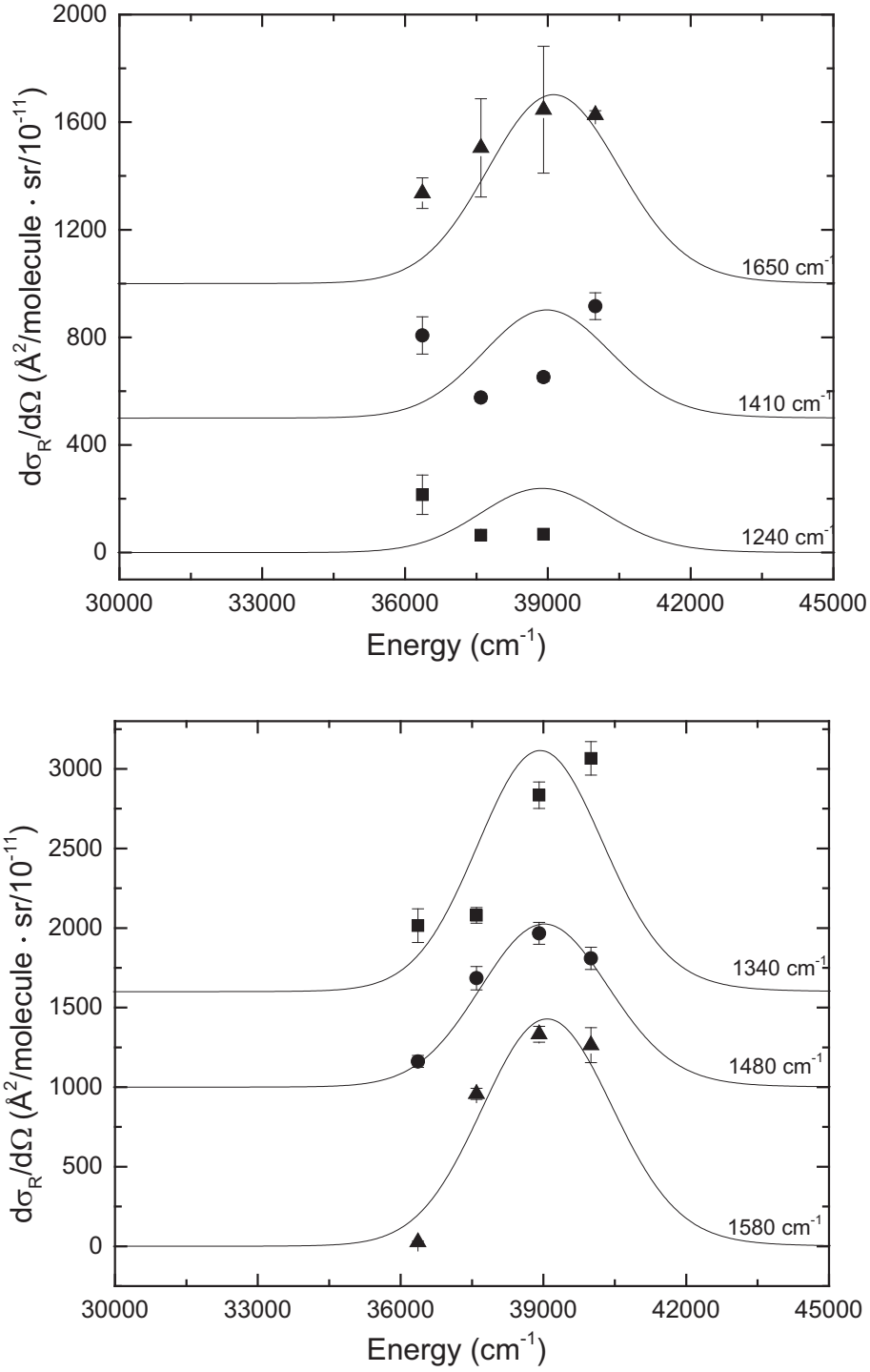

Figure 3.10: Experimental (points) and calculated (solid lines) resonance Raman excitation profile for $(dGp)_5$. The excitation profiles were calculated using Equation 3.2 and the parameters in Table 3.2.

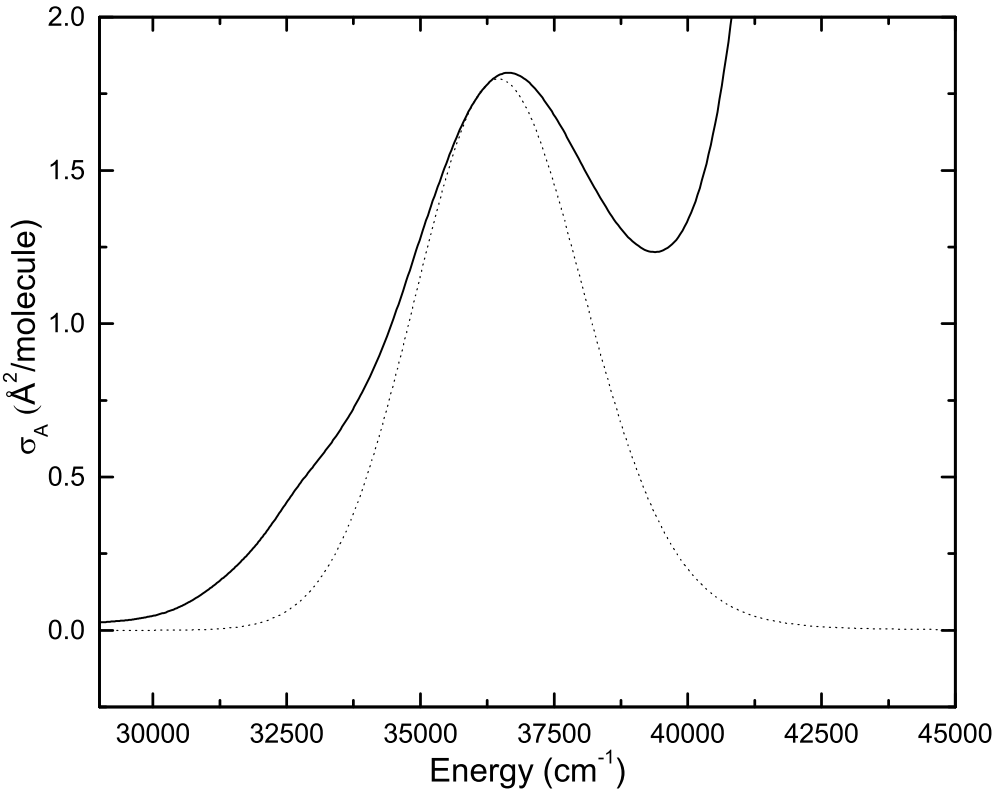

Figure 3.11: Experimental (solid line) and simulated (dotted line) absorption spectra of $(dCp)_5$. The simulated absorption spectrum was generated using Equation 3.3 and the parameters in Table 3.3. The differences between the experimental and the simulated spectra at higher energies are due to other higher energy transitions which are not modeled in the equation.

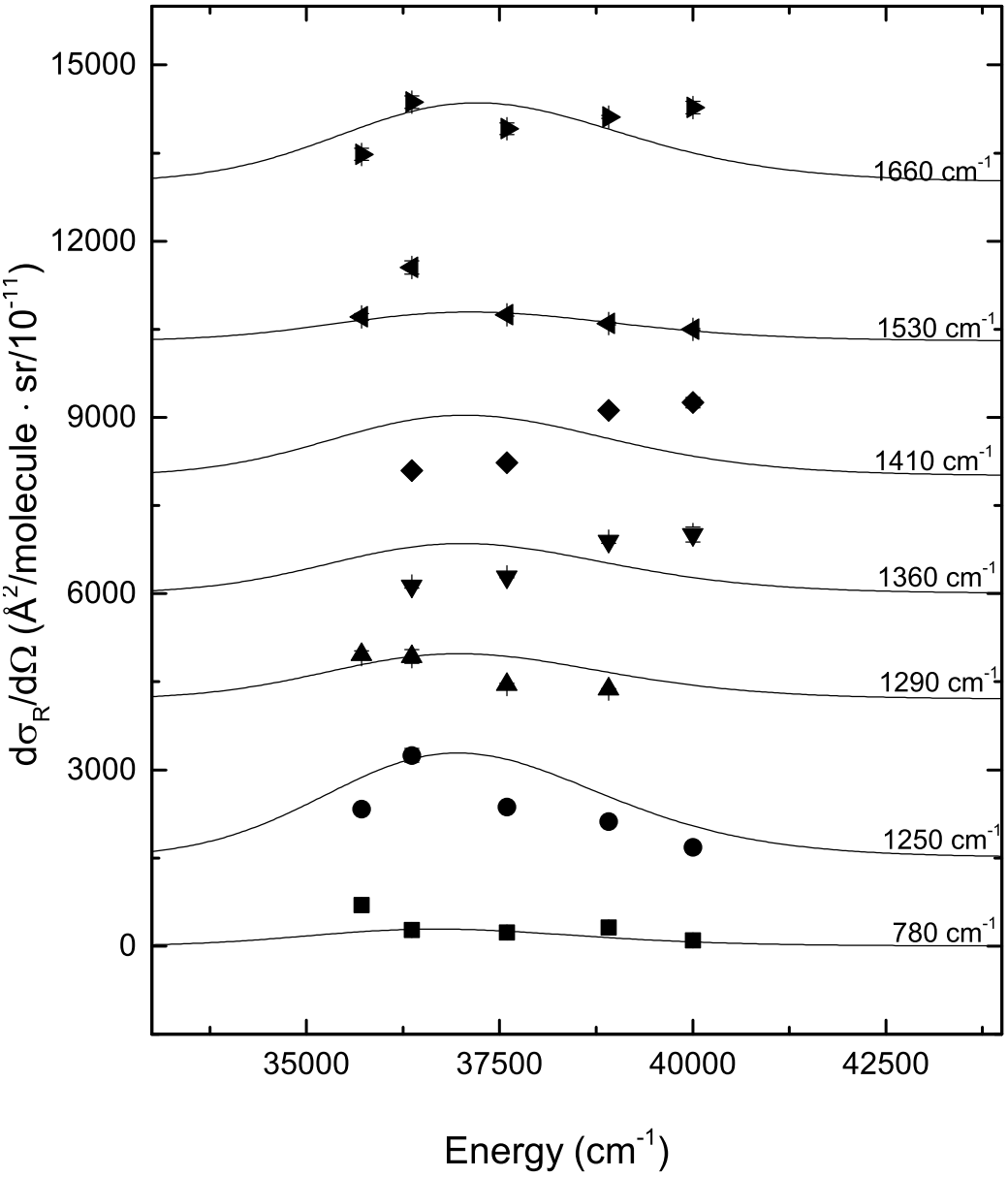

Figure 3.12: Experimental (points) and calculated (solid lines) resonance Raman excitation profile for $(dCp)_5$. The excitation profiles were calculated using Equation 3.2 and the parameters in Table 3.3.

Table 3.3: Harmonic mode parameters for $(dCp)_5$

Mode[a] (cm^{-1})	mode assignment[b]	β/ħ (cm^{-1})
780	def(C2O7) [74], def(C4N8) [8]	117
1250	be(N1C6H) [19], n(N1C6) [18]	300
1290	ν(C2N3) [38], ν(C4N8) [13]	206.4
1360	ν(C4N8) [18], be(C5C6H) [17]	217.6
1410	be(C6N1H1) [30], ν(C6N1) [-19], ν(N3C4) [11]	253.8
1530	ν(C4N8) [17], ν(N3C4) [14]	168.3
1660	ν(C2O7) [76]	298.8

[a]Frequencies listed here are experimental frequencies. [b]Abbreviations: ν - stretching, def - deformation, γ - out-of-plane bending and be -in-plane bending. The slopes of the excited-state potential energy surface at the Franck-Condon geometry (β/ħ) in cm^{-1} were obtained by fitting the experimental cross-sections and absorption spectrum with the following parameters in Equation 3.2 and 3.3: temperature, T = 298 K, zero-zero energy, E_0 = 34400 cm^{-1}, Gaussian homogeneous linewidth, Γ_G = 2100 cm^{-1}, inhomogeneous linewidth, θ = 1200 cm^{-1}, transition length, M = 1.66 Å, and Brownian oscillator line shape, $\kappa = \Lambda/D = 0.1$.

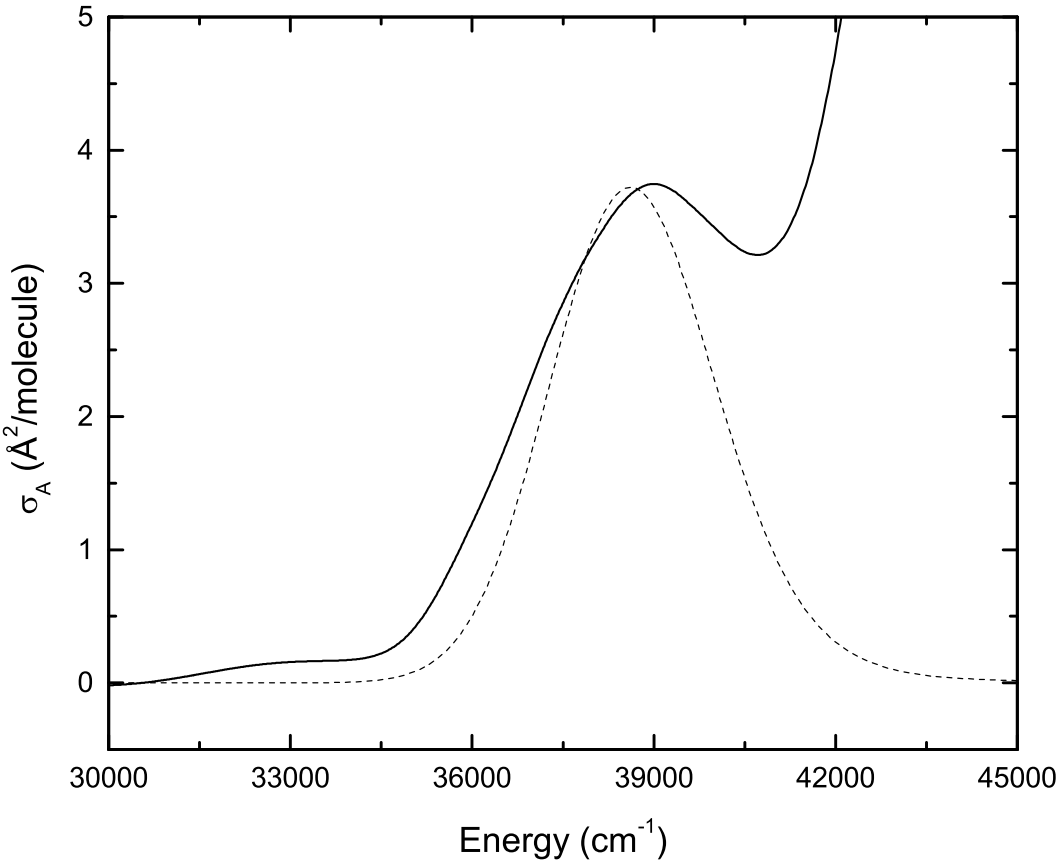

Figure 3.13: Experimental (solid line) and simulated (dotted line) absorption spectra of $(dAp)_5$. The simulated absorption spectrum was generated using Equation 3.3 and the parameters from Table 3.4. The differences between experimental and simulated spectra at higher energies are due to other higher energy transitions which are not modeled in the equation.

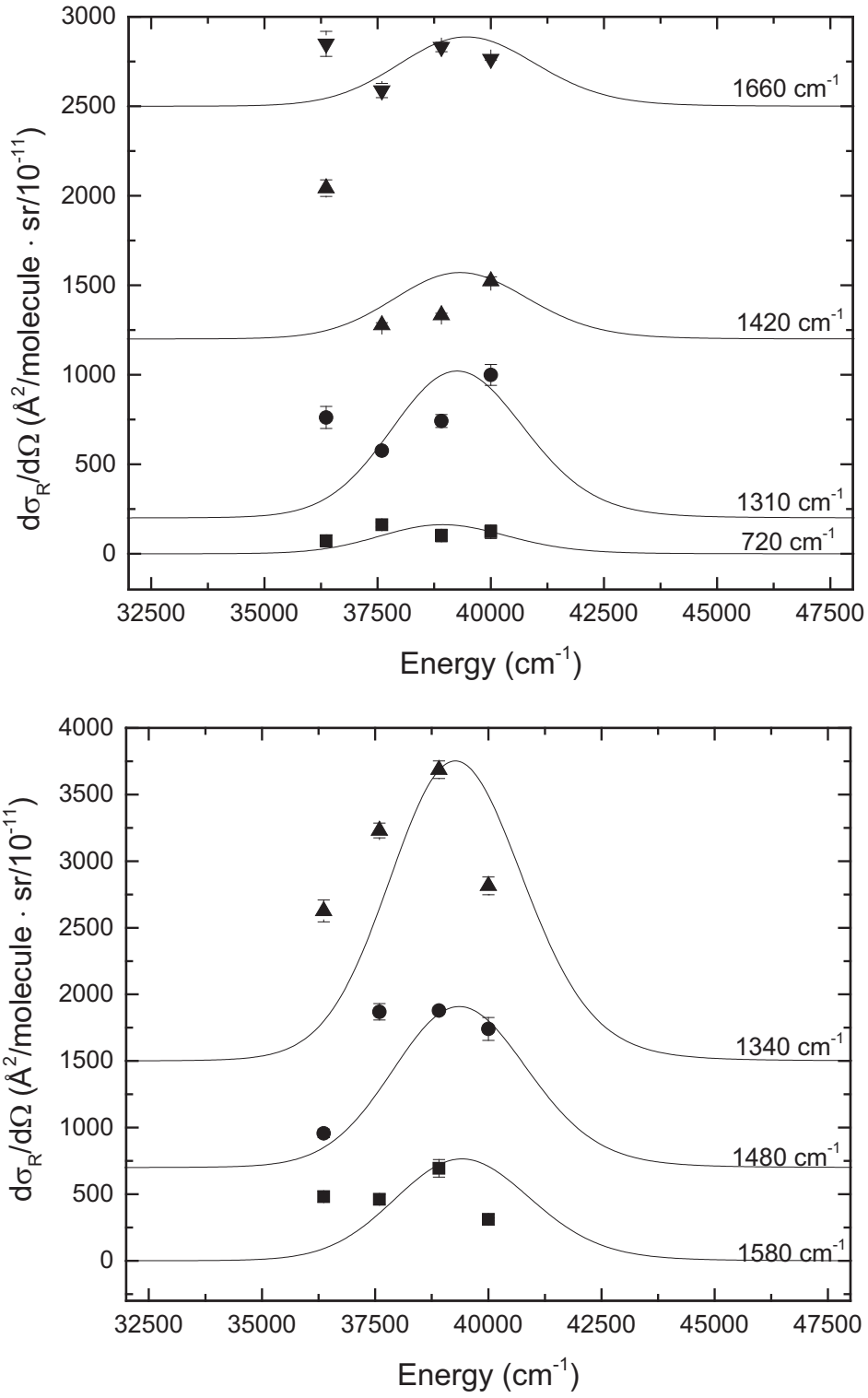

Figure 3.14: Experimental (points) and calculated (solid lines) resonance Raman excitation profile for $(dAp)_5$. The excitation profiles were calculated using Equation 3.2 and the parameters in Table 3.4.

Table 3.4: Harmonic mode parameters for $(dAp)_5$.

Mode[a] (cm^{-1})	mode assignment[b]	β/ħ (cm^{-1})
726	be(N7C8N9) [19], ν(N9C'1) [-14], be(C5N7C8) [12], be(C4N9C8) [11]	50.8
1310	ν(N9C8) [30], ν(N3C2) [14], be(C8H) [14]	124.4
1335	ν(N7C5) [-39], ν(C8N7)[12]	206.9
1410	ν(C4N9) [44], be(C8H)[-15]	84.6
1480	be(C2H) [-29], ν(N9C8) [-19], be(C8H)[15]	155.4
1575	ν(C4C5) [48], ν(C4N3) [-31]	126.0
1660	be(NH_2)[73], ν(C5C6) [15], ν(C6N10) [14]	83.0

[a]Frequencies listed here are experimental frequencies. [b]Abbreviations: ν - stretching, def deformation, γ - out-of-plane bending and be - in-plane bending. The slopes of the excited-state potential energy surface at the Franck-Condon geometry (β/ħ) in cm^{-1} were obtained by fitting the experimental cross-sections and absorption spectrum with the following parameters in Equation 3.2 and 3.3 :temperature, T = 298 K, zero-zero energy, E_0 = 36000 cm^{-1}, Gaussian homogeneous linewidth, Γ_G = 2450 cm^{-1}, inhomogeneous linewidth, θ = 750 cm^{-1}, transition length, M = 2.16 Å, and Brownian oscillator line shape, $\kappa = \Lambda/D = 0.1$.

A complete mode assignment and the corresponding excited-state slope ($\beta/\hbar$) is given in Table 3.3. Most of the intense modes in cytosine are observed in the resonance Raman spectra of $(dCp)_5$ as well. The low frequency, less intense modes at 550 cm^{-1}, 595 cm^{-1}, 950 cm^{-1} and 1115 cm^{-1} in cytosine are not observed in $(dCp)_5$. The 1290 cm^{-1} (C2-N3 stretch) mode is the most intense band in cytosine but the 1250 cm^{-1} (N1C6H12 bend) mode is the most intense one in the homopentamer and the next intense band is the C2=O7 stretch mode at 1660 cm^{-1}. The resonance Raman spectra of $(dCp)_5$ at different excitation wavelengths are given in Figure A.3 in Appendix A.

The resonance Raman spectra of $(dAp)_5$ in Figure 3.5 is similar to the resonance Raman spectra of 2'-deoxyadenosine (Ade).[53] The mode assignment is done by comparing our results with previously reported 2'-deoxyadenosine mode assignments.[44,54] For $(dAp)_5$, the 1660 cm^{-1} mode is assigned to the NH_2 bend, while the 1480 cm^{-1} mode is mainly from the C2H bend. Other observed vibrational modes are at 1410 cm^{-1} (C8-N9 stretch), the most intense mode at 1340 cm^{-1}(N1C2, C5N7 stretches), the 1310 cm^{-1} mode (C8N9 stretches), and the mode at 730 cm^{-1} (imidazole ring deformations). A complete mode assignments and the corresponding excited-state slope ($\beta/\hbar$) is given in Table 3.4. The resonance Raman spectra of $(dAp)_5$ at different excitation wavelengths are given in Figure A.4 in Appendix A.

Figures 3.7, 3.9, 3.11 and 3.13 show the experimental and simulated absorption spectra of $(dTp)_5$, $(dGp)_5$, $(dCp)_5$ and $(dAp)_5$ respectively. Figures 3.8, 3.10, 3.12 and 3.14 show the resonance Raman excitation profiles of $(dTp)_5$, $(dGp)_5$, $(dCp)_5$ and $(dAp)_5$, respectively. All the absorption spectra, except that of $(dGp)_5$, have a well-defined absorption band around 260 nm similar to the respective nucleobases. There is generally good agreement between the experimental and the simulated absorption spectra. The deviation between the experimental and the calculated absorption spectra at higher energies is due to the fact that the higher energy electronic absorptions are not modeled in the simulation. The difference between the experimental and the simulated absorption spectra at lower energies may be due to other lower energy transitions which are also not modeled in the simulation. The difference between the experimental and simulated spectra of $(dGp)_5$ may be due to the presence of impurities. The experimental resonance Raman cross-sections for all the pentamers fit reasonably well with the calculated excitation profiles. The height of each homopentamer excitation profile directly reflects the excited-state geometry

change for that mode, which are given in Table 3.1, 3.2, 3.3 and 3.4.

The resonance Raman spectra of different homopentamers at different excitation wavelengths (Appendix A) are similar to the resonance Raman spectra of the corresponding nucleobases. There are no changes in the frequencies or relative intensities of the peaks observed at different excitation wavelengths (Figures A.1, A.2, A.3 and A.4, Appendix A), indicating that all the resonance Raman spectra are enhanced by a single electronic transition. The relative intensities of the modes in the monomer and the polymer are comparable.

The relative intensities of the modes in the monomer and the polymer are comparable, with the most intense modes in Ade seen in $(dAp)_5$ as well, but some less intense Ade modes are not observed at all in $(dAp)_5$. The resonance Raman excitation profiles for $(dAp)_5$ in Figure 3.12 show a good fit of simulated resonance Raman excitation profiles with the experimental cross-sections. The experimental cross-sections for $(dAp)_5$ at 275 nm are higher than the calculated cross-sections, suggesting another electronic transition resulting in resonance enhancement at lower energy changing the enhancement pattern. The non-zero extinction coefficient at higher wavelength in the absorption spectrum supports this interpretation. The resonance Raman cross-sections and relative slopes (forces) in the excited state are similar in both Ade and $(dAp)_5$.

Figure 3.12 shows the resonance Raman excitation profiles for different modes of $(dCp)_5$ where the simulated excitation profiles fit well with the experimental cross-section for the 1530 cm^{-1}, 1250 cm^{-1} and 780 cm^{-1} modes. The resonance Raman excitation profiles do not exactly fit the distribution of the experimental data points for the other modes, but do account for the heights of the experimental cross-sections. This is a reasonable estimation of the excited-state slopes for different modes, because it is the height of the excitation profiles that determines the excited-state slope, when other parameters are fixed. The 1660 cm^{-1} mode shows a reasonably good fit with the experimental cross-section, except for the 250 nm cross-section. The modes at 1360 cm^{-1} and 1410 cm^{-1} show a different enhancement pattern, suggesting an enhancement from a different electronic transition, and were not considered further. The two modes in cytosine around 1650 cm^{-1} appear as a single mode in the homopentamer. The relative changes in the excited-state geometry along different vibrational coordinate are similar to that of cytosine.

The resonance Raman excitation profiles for different modes of $(dGp)_5$ are shown

in Figure 3.10. There is a reasonably good agreement between the experimental data points and calculated resonance Raman excitation profiles, except for the 1240 and 1410 cm^{-1} modes, where the experimental cross-sections are lower at the 266 and 257 nm excitation wavelengths. This could be due to the relative lower intensity of these two modes and possible errors in processing the spectra.

The resonance Raman excitation profiles for $(dTp)_5$ are shown in Figure 3.8. All modes except for the 1410 cm^{-1} mode show a reasonable agreement between the resonance Raman cross-sections and the simulated resonance Raman excitation profile. The experimental cross-sections for the 1410 cm^{-1} modes are high for the excitation wavelengths, which may be due to the fact that that particular mode is enhanced by a different electronic transition.

Two models were used to fit each homopentamer absorption spectrum and resonance Raman excitation profile. For the first model, parameters similar to that of each monomer were used, with lower excited-state slopes for each mode than the corresponding nucleobases. These lower excited-state slopes were necessary to simulate the absorption and resonance Raman excitation profile with comparable broadening to that of the nucleobases. A comparison of the other fitting parameters for model one used in Equation 3.2 and Equation 3.3 for the hompentamers and the parameters for respective nucleobase/nucleosides are given in Table 3.5. The zero-zero energy ($E_{(0)}$) for the homopentamers are similar to the corresponding monomers, except for $(dCp)_5$ in which it is at lower energy. The trend is seen in the experimental absorption spectrum as well. The transition length (M) increased by a factor of 2-2.5 for all the hompolymers with respect to the monomers. Comparable inhomogeneous and higher homogeneous broadening with respect to the monomers is obtained for all the homopentamers. The calculated excited-state slopes for each homopentamer is lower than the corresponding modes in the monomer. Another interesting outcome of the simulation is that there is not as much difference in the excited-state slopes between different modes in the homopentamer as seen in the monomers.

A second model (see Appendix A), with a higher homogeneous broadening, a lower inhomogeneous broadening and highly red-shifted zero-zero energies with respect to the monomers was used to reproduce the experimental absorption spectra and resonance Raman excitation profiles. This model had higher excited-state slopes than model 1. A homogeneous broadening of 50-80 cm^{-1} and inhomogeneous broad-

ening of 3500 cm^{-1} in model 2 seemed unreasonable compared to the broadening observed in the monomers and this model was not pursued any further.

3.4 Discussion

Initial excited-state structural dynamics. An accurate description of the vibrational modes is a prerequisite for understanding the initial excited-state dynamics of homopentamers using resonance Raman spectroscopy. Unfortunately no vibrational assignments have been done for any of the homopentamers. But the vibrational assignments and resonance Raman studies are reported for the nucleotide monomers.[30,35,42,53] So those reported vibrational frequency assignments are used in further discussion. Though there were studies on the Raman signature of genomic DNA, those studies only show that the intensity and frequencies are sensitive to base sequences, they do not provide any insight into the excited-state structural dynamics.[55]

Thymine photochemistry is well known and the initial excited-state dynamics correlate well with the formation of the cyclobutyl pyrimidine (CPD), 6-4 pyrimidine pyrimidinone photoproduct and the photohydrate with the partitioning of dynamics between the C5=C6 stretch and the C5, C6 pyramidalization coordinates.[33,42] Most of the changes occur around the C5 and C6 atoms, and are reflected in its initial excited-state structural dynamics. The change of C5=C6 in the ground state to C5-C6 in the excited state and the hybridization change from sp^2 to sp^3 are all observed in the most intense resonance Raman modes. The highest excited-state slopes obtained for the 1660 (C5=C6 stretch), 1380 (C6H bend) and 1240 cm^{-1} (C5Me stretch) modes, all lie along the photochemical active mode.

The $(dGp)_5$ homopolymer shows very similar excited-state structural dynamics to that of 2'-deoxyguanosine. Formamidopyrimidine, 8-oxo-dG and oxazolone are the three main UV photoproducts for guanosine.[56] An examination of the photoproducts shows changes around the C8 and N7 atoms in all the guanosine photoproducts. A higher excited-state slope along the 1480 (C8H bend) 1340 (N7C8 stretch) and 1580 cm^{-1} (N3C4 stretch) indicates that the initial excited-state dynamics are oriented along the photochemically active modes and support the formation of oxidative photoproducts in $(dGp)_5$. Guanosine has the lowest oxidation potential among all the nucelobases, and should lose an electron during oxidative damage. The loss of an electron from the HOMO (π antibonding

orbital) will increase the bond order and a corresponding shortening of bonds in the ring structure is expected during charge transfer.[52] It has been found from computational calculations that there is a hybridization change of the exocyclic amino group from partial sp^3 geometry to a planar geometry in guanosine.[57] A shortening of the N1C2, N3C4, C5N7, C6O11, and C8N9 and lengthening of C2N3, C4C5, C5C6, N7C8 are expected in guanosine in the charge transfer state.[35] Similar changes are expected in the homopentamer of guanosine as well. The observed initial excited-state structural dynamics along different modes supports charge transfer oxidation state formation. The resonance Raman spectra and the resonance Raman excitation profiles confirm that the initial excited-state structural dynamics of the $(dGp)_5$ homopentamer lie along the photochemical and oxidative reaction coordinates similar, to 2'-deoxyguanosine.[35]

In cytosine, there are two separate bands at 1630 cm^{-1} and 1650 cm^{-1} that appear as a single mode in $(dCp)_5$ and are expected to have the character of both the 1630 cm^{-1} and 1650 cm^{-1} modes. The 1630 cm^{-1} mode in cytosine was assigned to the stretch along the C5=C6 bond and the 1650 cm^{-1} mode to C2=O7 stretch. The two most intense modes, 1250 cm^{-1} (N1C6H12 bend and N1-C6 stretch) and 1660 cm^{-1} are modes that project on the photochemical reaction coordinate. The 1285 cm^{-1} mode (C2-N3 and C4-N8 stretches) shows the highest excited-state slope in cytosine, but that vibrational mode does not lie along the reaction coordinate. In the homopentamer, the 1250 cm^{-1} mode is of highest intensity and lies along the photochemically active reaction coordinate. The change in relative intensities between the 1250 cm^{-1} peak and 1290 cm^{-1} peaks in the homopentamer with respect to the 1225 cm^{-1} and 1285 cm^{-1} peaks, respectively, in cytosine show a change in the distribution of excited-state slopes between two modes in $(dCp)_5$. This change in potential energy distribution between the monomer and the homopentamer can be attributed to the effect of the N1 mass. A similar trend was seen with N-methylthymine.[42] A higher excited-state slope in the homopentamer compared to cytosine along the 1250 cm^{-1} photochemical active mode suggests that the initial drving force is more oriented along that photochemically active coordinate in the homopentamer. The most common cytosine photoproduct being the photodimer, the initial excited-state structural dynamics of $(dCp)_5$ are in line with the expected photochemistry. The relative intensity change along the 1250 and the 1290 cm^{-1} modes between the monomer and the pentamer may

change the relative distribution of the photochemical quantum yield of the different photoproducts.

Table 3.5: Comparison of different fitting parameters of homopentamer and the corresponding nucleosides or nucleobases.

	$(dAp)_5$	dA[a]	$(dGp)_5$	dG[b]	$(dCp)_5$	C[c]	$(dTp)_5$	T[d]
E_0 energy (cm^{-1})	36000	36200	36800	35750/37600	34400	35900	35700	35650
M (Å)	2.16	0.83	1.46	0.0.56/0.83	1.66	0.61	1.5	0.79
Γ_G (cm^{-1})	2450	1800	1800	1050/1650	2100	185	1800	1150
θ (cm^{-1})	750	800	900	900	1200	1150	1150	1320

[a]The parameters for 2'-deoxyadenosine are taken from reference 52, [b]The parameters for 2'-deoxyguanosine are from reference 25, [c]The parameters for 2'-deoxyadenosine are taken from reference 20 , [d]The parameters for 2'-deoxyadenosine are from reference 42.

The main photoproduct of adenosine is the photodimer formed as a result of the $(2\pi + 2\pi)$ cycloaddition reaction at the N7=C8 of the 5'adenine and the C5=C6 on the 3' adenine. With the known photochemistry of adenine[1] one would expect to see higher excited-state dynamics along the N7=C8 and C5-C6 mode stretching as the hybridization of the atoms changes from sp^2 to sp^3 in the photoproduct and corresponding changes in the bonds associated with N7, C8, C6 and C5 atoms. Also, a change along the C4-C5 bond is expected as the double bond resonates between the C4-C5 and the C5-C6 bonds. The highest intensities are observed along the C5-N7 and N7=C8 stretching modes (1335 cm^{-1}), N9-C8 stretch (1310 cm^{-1} and 1480 cm^{-1}), the C4=C5 stretching and C4-N3 stretching (1575 cm^{-1}) and C5-C6 stretching mode (1660 cm^{-1}). These modes lie along the photochemically active coordinates, and are consistent with the excited-state structural dynamics being coincident with the photochemical reaction coordinate.

All the homopentamers reported here show that the excited-state structural dynamics are similar to their respective nucleotide monomers. However, the excited-state slopes in the pentamers are lower than in the monomers. Though not all vibrations are seen in the resonance Raman spectra, the homopentamers have a large number of vibrational modes compared to the nucleobases. This decrease in excited-state slopes can be attributed to the presence of a large number of low intensity modes that shift the excited-state slopes away from single modes. This is also evident from the large homogeneous broadening compared to the nucelotide monomers.

The smaller excited-state slopes of different modes in the homopentamers compared to larger excited-state slopes in the monomers may result from the constrained geometry change in the homopentamers between the ground and excited electronic states at the Frank-Condon geometry. This geometry constraint may arise from steric hindrance induced by the polymeric structure and the base stacking. These geometry constraints introduce an additional potential energy surface on the modes, with zero slope at the Franck-Condon geometry, reducing the apparent slope of the excited-state potential energy surfaces. Such lower excited-state slopes are consistent with computations.[58] Helix stacking may constrain the change in the excited-state slopes by base interaction and thus the intensity of resonance Raman modes.

A 2 to 2.5 fold increase in the transition length is observed in the homopentamers compared to the monomers. This increase can be attributed to the increase in the extinction coefficient of the homopentamer compared to the nucleotide monomers (Table 3.5. The extinction coefficients of the homopentamers are about 4-6 times higher than that of the corresponding monomers and the 2-2.5 increase in transition length is consistent with that.

Broadening. The total broadening for the homopentamers is higher than the total broadening in the corresponding monomers in the model used to fit the absorption and the resonance Raman excitation profiles (Table 3.5). Both homogeneous and inhomogeneous linewidths contribute to the observed spectral widths. Homogeneous broadening for the nucleic acids and their derivatives are mainly due to solvent-induced dephasing, with population decay playing a much more minor role. The increase in homogeneous linewidths for the different homopentamers compared to the respective monomers is consistent with the increase in size of the molecules, suggesting an increase in the solvent-induced dephasing, which may result from the migration of excitons in the polymeric structure. The presence of more modes with low intensity may give rise to the broadening. With the increase in size on going from the nucleobase to homopentamer, the increase in size will result in better solvent interactions and the solvent induced dephasing. The different types of interaction between the nucleotide units and the solvent may also contribute to the decrease in the excited-state slopes in the homopentamers. The increase in the total broadening also supports this trend. The comparison of initial excited-state structural dynamics of homopentamers and monomers reveals that the photochemi-

cally active modes are similar in homopentamers and the corresponding monomers. Constraints on the possible geometry changes due to the polymeric structure and solvent interaction and base stacking also contribute to the low excited-state slopes observed in homopentamers. This lower-energy multidimensional potential energy surface in the homopentamer compared to the monomers in the initial 10-30 fs after photon absorption can be thus from the presence of dark, non-resonant vibrational modes, geometry constraints and fast molecular dephasing. The increase in size of the molecule will result in an increase in the number of collisions between the molecule and solvent, thus causing an increase in the rate of dephasing, contributing to the greater homogeneous broadening. The higher homogeneous broadening model is in line with the expected trend seen with other systems like thymine where the homogeneous broadening show an increase from thymine to thymidine monophosphate.[42]

Inhomogeneous linewidths arise from a distribution of energies of different solvent interacting structures. The inhomogeneous linewidth for the different homopentamers are similar to that of their respective monomers. This suggests a similar energy distribution for different solvent interacting structures in both the homopentamers and the monomers. This can be interpreted in two ways. A similar number of solvent interacting structures in both polymer and monomer with similar energy distribution, suggesting a similar solvent interaction for both. Or a larger number of solvent interacting structures in homopentamer which are still energetically within the width of the inhomogeneous broadening. Considering the size of the monomers and homopentamer solvent complexes and probable sites for solvent interaction, the number of solvent interacting species is expected to be higher in the polymer. So a very large number of very similar energy solute-solvent complexes are more likely to account for the inhomogeneous linewidth.

3.5 Conclusions

The resonance Raman spectra of the homopentamers of the nucleotides at different excitation wavelengths were obtained. The results presented here clearly demonstrate that the initial excited-state structural dynamics of the homopentamers are similar to that of the respective nucleotides, but with lower excited-state slopes. The increase in the broadening is consistent with the increase in the number of vibrational degrees of freedom and increase in the size of the molecule compared to

corresponding monomers. The calculated 2-2.5-fold increase in the transition length is also consistent with the 4-6 times increase in the extinction coefficient with respect to the monomers. The smaller changes in the excited-state structural dynamics and the narrow distribution of excited-state slopes in each homopentamer compared to the monomer suggests that the potential energy surface is shallower due to increase in the number of degrees of vibration freedom. These findings indicates that the initial excited-state geometry changes are somewhat restricted by the polymeric structure in homopentamers.

References

[1] H. Görner. New trends in photobiology: Photochemistry of DNA and related biomolecules: Quantum yields and consequences of photoionization. *J. Photochem. Photobiol. B*, 26(2):117–139, 1994.

[2] R. P. Sinha and D-P. Hader. UV-induced DNA damage and repair: a review. *Photochem. Photobiol. Sci.*, 1(4):225–236, 2002.

[3] R. B. Setlow and J. K. Setlow. Evidence that ultraviolet-induced thymine dimer in DNA cause biological damage. *Proc. Natl. Acad. Sci. U .S. A.*, 48:1250–1257, 1962.

[4] M. H. Patrick and R. O Rahn. *Photochemistry and photobiology of Nucleic acids: Volume II Biology*, chapter Photochemistry of DNA and polynucleotides:photoproducts, pages 35–95. Academic Press, Newyork, 1976.

[5] J. Jagger. *Photochemistry and photobiology of nucleic acids, Volume II Biology*, chapter Ultraviolet inactivation of biological systems, page 147Ű186. Academic Press, New York, 1976.

[6] J. Cadet, C. Anselmino, T. Douki, and L. Voituriez. Photochemistry of nucleic-acids in cells. *J. Photochem. Photobiol. B*, 15:277–298, 1992.

[7] M. Barbatti, A. J. A. Aquino, and H. Lischka. The UV absorption of nucleobases: Semi-classical ab initio spectra simulations. *Phys. Chem. Chem. Phys.*, 12(19):4959–4967, 2010.

[8] S. Krawczyk and R. Luchowski. Electronic excited states of polynucleotides: A

study by electroabsorption spectroscopy. *J. Phys. Chem. B*, 111(5):1213–1221, 2007.

[9] M. N. Khattak and S. Y. Wang. The photochemical mechanism of pyrimidine cyclobutyl dimerization. *Tetrahedron*, 28(4):945–957, 1972.

[10] A. M. Kelley. Resonance Raman and resonance hyper-raman intensities: Structure and dynamics of molecular excited states in solution. *J. Phys. Chem. A*, 112(47):11975–11991, 2008.

[11] B. B. Johnson and W. L. Peticolas. Resonant Raman effect. *Ann. Rev. Phys. Chem.*, 27:465–491, 1976.

[12] S. A. Asher. UV resonance raman studies of molecular structure and dynamics-Applications in physical and biophysical chemistry. *Ann. Rev. Phys. Chem.*, 39:537–588, 1988.

[13] E. Nir, K. Kleinermanns, L. Grace, and M. S. de Vries. On the photochemistry of purine nucleobases. *J. Phys. Chem. A*, 105(21):5106–5110, 2001.

[14] C. T. Middleton, K. de La Harpe, C. Su, Y. K. Law, C. E. Crespo-Hernandez, and B. Kohler. DNA excited-state dynamics: From single bases to the double helix. *Ann. Rev. Phys. Chem.*, 60(1):217–239, 2009.

[15] M. Barbatti, A. J. A. Aquino, J. J. Szymczak, D. Nachtigallova, P. Hobza, and H. Lischka. Relaxation mechanisms of UV-photoexcited DNA and RNA nucleobases. *Proc. Natl. Acad. Sci. U.S.A.*, 107(50):21453–21458, 2010.

[16] T. Pancur, N. K. Schwalb, F. Renth, and F. Temps. Femtosecond fluorescence up-conversion spectroscopy of adenine and adenosine: experimental evidence for the $\pi\sigma^*$ state? *Chem. Phys.*, 313:199–212, 2005.

[17] T. Gustavsson, A. Banyasz, E. Lazzarotto, D. Markovitsi, G. Scalmani, M. J. Frisch, V. Barone, and R. Improta. Singlet excited-state behavior of uracil and thymine in aqueous solution: A combined experimental and computational study of 11 uracil derivatives. *J. Am. Chem. Soc.*, 128(2):607–619, 2006.

[18] T. Gustavsson, N. Sarkar, E. Lazzarotto, D. Markovitsi, and R. Improta. Singlet excited state dynamics of uracil and thymine derivatives: A femtosecond

fluorescence upconversion study in acetonitrile. *Chem. Phys. Lett.*, 429:551–557, 2006.

[19] W-M. Kwok, C. Ma, and D. L. Phillips. Femtosecond time- and wavelength-resolved fluorescence and absorption spectroscopic study of the excited states of adenosine and an adenine oligomer. *J. Am. Chem. Soc.*, 128(36):11894–11905, 2006.

[20] M. Merchan, R. Gonzalez-Luque, T. Climent, L. Serrano-Andres, E. Rodrguez, M. Reguero, and D. Pelaez. Unified model for the ultrafast decay of pyrimidine nucleobases. *J. Phys. Chem. B*, 110(51):26471–26476, 2006.

[21] P. M. Hare, C. E. Crespo-Hernandez, and B. Kohler. Internal conversion to the electronic ground state occurs via two distinct pathways for pyrimidine bases in aqueous solution. *Proc. Natl. Acad. Sci. U.S.A.*, 104(2):435–440, 2007.

[22] C. E. Crespo-Hernandez and B. Kohler. Influence of secondary structure on electronic energy relaxation in adenine homopolymers. *J. Phys. Chem. B*, 108(30):11182–11188, 2004.

[23] C. E. Crespo-Hernandez, B. Cohen, and B. Kohler. Base stacking controls excited-state dynamics in A-T DNA. *Nature*, 436(7054):1141–1144, 2005.

[24] I. Buchvarov, Q. Wang, M. Raytchev, A. Trifonov, and T. Fiebig. Electronic energy delocalization and dissipation in single- and double-stranded DNA. *Proc. Natl. Acad. Sci. U. S. A.*, 104(12):4794–4797, 2007.

[25] W-M. Kwok, C. Ma, and D. L. Phillips. A doorway state leads to photostability or triplet photodamage in thymine DNA. *J. Am. Chem. Soc.*, 130(15):5131–5139, 2008.

[26] B. Cohen, C.E. Crespo-Hernandez, P.M. Hare, and B. Kohler. Ultrasfast excited-state dynamics in DNA and RNA polymers. In Monique M. Martin and James T. Hynes, editors, *Femtochemistry and Femtobiology*, chapter 90, pages 463 – 470. Elsevier, Amsterdam, 2004.

[27] R. A. Myers, A. B. Mathies. *Resonance Raman spectra of polyenes and aromatics.* Wiley, New York, 1987.

[28] A. B. Myers and T. R. Rizzo. *Laser techniques in chemistry.* Techniques of chemistry. Wiley, 1995.

[29] A. M. Kelley. Resonance Raman intensity analysis of vibrational and solvent reorganization in photoinduced charge transfer. *J. Phys. Chem. A*, 103(35):6891–6903, 1999.

[30] B. E. Billinghurst and G. R. Loppnow. Excited-state structural dynamics of cytosine from resonance Raman spectroscopy. *J. Phys. Chem. A*, 110(7):2353–2359, 2006.

[31] B. E. Billinghurst, R. Yeung, and G. R. Loppnow. Excited-state structural dynamics of 5-fluorouracil. *J. Phys. Chem. A*, 110(19):6185–6191, 2006.

[32] S. Yarasi, B. E. Billinghurst, and G. R. Loppnow. Vibrational properties of thymine, uracil and their isotopomers. *J. Raman Spectrosc.*, 38(9):1117–1126, 2007.

[33] S. Yarasi, P. Brost, and G. R. Loppnow. Initial excited-state structural dynamics of thymine are coincident with the expected photochemical dynamics. *J. Phys. Chem. A*, 111(24):5130–5135, 2007.

[34] S. A. Oladepo and G. R. Loppnow. Initial excited-state structural dynamics of 9-methyladenine from UV resonance Raman spectroscopy. *J. Phys. Chem. B*, 115(19):6149–6156, 2011.

[35] A. F. El-Yazbi, A. Palech, and G. R. Loppnow. Initial excited-state structural dynamics of 2-deoxyguanosine determined via UV resonance Raman spectroscopy. *J. Phys. Chem. A*, 115(38):10445–10451, 2011.

[36] S. P. A. Fodor, R. P. Rava, T. R. Hays, and T. G. Spiro. Ultraviolet resonance Raman spectroscopy of the nucleotides with 266-, 240-, 218-, and 200-nm pulsed laser excitation. *J. Am. Chem. Soc.*, 107(6):1520–1529, 1985.

[37] S. P. A. Fodor and T. G. Spiro. Ultraviolet resonance raman spectroscopy of DNA with 200-266-nm laser excitation. *J. Am. Chem. Soc.*, 108(12):3198–3205, 1986.

[38] J. R. Perno, C. A. Grygon, and T. G. Spiro. Ultraviolet Raman excitation profiles for the nucleotides and for the nucleic acid duplexes poly(rA)-poly-(rU) and poly(dG-dC). *J. Phys. Chem.*, 93(15):5672–5678, 1989.

[39] C. B. Daniel and L. P. Warner. Ultraviolet resonance Raman excitation profiles of pyrimidine nucleotides. *J. Chem. Phys.*, 72(5):3134–3142, 1980.

[40] L. P. Warner and C. B. Dan. Estimation of the distortion of the geometry of nucleic-acid bases in the excited electronic state from the ultraviolet resonance raman intensity of certain normal modes. *Chem. Phys. Lett.*, 63(3):604–608, 1979.

[41] Y. Nishimura, M. Tsuboi, W. L. Kubasek, K. Bajdor, and W. L. Peticolas. Ultraviolet resonance Raman bands of guanosine and adenosine residues useful for the determination of nucleic acid conformation. *J. Raman Spec.*, 18(3):221–227, 1987.

[42] B. E. Billinghurst, S. A. Oladepo, and G. R. Loppnow. Initial excited-state structural dynamics of thymine derivatives. *J. Phys. Chem. B*, 116(35):10496–10503, 2012.

[43] S. Yarasi, S. Ng, and G. R. Loppnow. Initial excited-state structural dynamics of uracil from resonance Raman spectroscopy are different from those of thymine (5-methyluracil). *J. Phys. Chem. B*, 113(43):14336–14342, 2009.

[44] M. Shanmugasundaram and M. Puranik. Computational prediction of vibrational spectra of normal and modified DNA nucleobases. *J. Raman Spec.*, 40(12):1726–1748, 2009.

[45] N. Jayanth, S. Ramachandran, and M. Puranik. Solution structure of the DNA/RNA damage lesion 8-oxoguanosine from ultraviolet resonance Raman spectroscopy. *J. Phys. Chem. A*, 113(8):1459–1471, 2009.

[46] W. L. Kubasek, B. Hudson, and W. L. Peticolas. Ultraviolet resonance Raman excitation profiles of nucleic acid bases with excitation from 200 to 300 nanometers. *Proc. Natl. Acad. Sci. U.S.A.*, 82(8):2369–2373, 1985.

[47] L. M. Kundu and G. R. Loppnow. Direct detection of 8-oxo-deoxyguanosine using UV resonance Raman spectroscopy. *Photochem. Photobiol.*, 83(3):600–602, 2007.

[48] R. Mathies, A. R. Oseroff, and L. Stryer. Rapid-flow resonance Raman spectroscopy of photolabile molecules: Rhodopsin and isorhodopsin. *Proc. Natl. Acad. Sci. U.S.A.*, 73(1):1–5, 1976.

[49] G. R. Loppnow and E. Fraga. Proteins as solvents: The role of amino acid composition in the excited-state charge transfer dynamics of plastocyanins. *J. Am. Chem. Soc.*, 119(5):896–905, 1997.

[50] E. Fraga and G. R. Loppnow. Proteins as solvents: Blue copper proteins as a molecular ruler for solvent effects on resonance Raman intensities. *J.Phys. Chem. B*, 102(39):7659–7665, 1998.

[51] B. Li, A. E. Johnson, S. Mukamel, and A. B. Myers. The brownian oscillator model for solvation effects in spontaneous light emission and their relationship to electron transfer. *J. Am. Chem. Soc.*, 116(24):11039–11047, 1994.

[52] L. C. T. Shoute and G. R. Loppnow. Excited-state dynamics of alizarin-sensitized TiO_2 nanoparticles from resonance raman spectroscopy. *J. Chem. Phys.*, 117(2):842–850, 2002.

[53] A. Friedman, S. Sasidharanpillai, and G. R. Loppnow. Initial excited-state structural dynamics of 2'-deoxyadenosine. manuscript under preparation, 2013.

[54] R. Letellier, M. Ghomi, and E. Taillandier. Normal coordinate analysis of 2-deoxythymidine and 2-deoxyadenosine. *Euro. Biophys. J.*, 14:423–430, 1987.

[55] H. Deng, V. A. Bloomfield, J. M. Benevides, and G. J. Thomas. Dependence of the Raman signature of genomic B-DNA on nucleotide base sequence. *Biopolymers*, 50(6):656–666, 1999.

[56] J. Cadet, T. Delatour, T. Douki, D. Gasparutto, J-P. Pouget, J.-L. Ravanat, and S. Sauvaigo. Hydroxyl radicals and DNA base damage. *Mut. Res.*, 424:9–21, 1999.

[57] P. Cheng, Y. Li, S. Li, M. Zhang, and Z. Zhou. Collision-induced dissociation (cid) of guanine radical cation in the gas phase: An experimental and computational study. *Phys. Chem. Chem. Phys.*, 12(18):4667–4677, 2010.

[58] S. D. Wetmore, R. J. Boyd, and L. A. Eriksson. Radiation products of thymine, 1-methylthymine, and uracil investigated by density functional theory. *J. Phys. Chem. B*, 102(27):5369–5377, 1998.

Chapter 4

UV-Induced miRNA Damage on a Microarray Platform

4.1 Introduction

The genetic materials, deoxyribonucleic acid (DNA) and ribonucleic acid (RNA) are exposed to different exogenous and endogenous factors which adversely affect their structure and function. Ultraviolet (UV) radiation is one of the more important nucleic acid damage agents, forming photoproducts which may cause mutagenesis, carcinogenesis and cell death. The main DNA photoproducts formed on UV exposure are cyclobutyl pyrimidine dimers (CPDs), 6-4 photoproducts and photohydrates.[1]

Many methods such as polymerase chain reaction (PCR) amplification[2,3], capillary gel electrophoresis[4–6], mass spectrometry[7–9], electrochemical methods[10,11], HPLC[10,11], fluorescence spectroscopy[12–16] and absorption spectroscopy[16–19] have been used to identify and quantify DNA damage. Although each of these methods have particular advantages, they can analyze no more than a few samples at a time.

DNA microarrays have been used to study gene expressions and changes in gene expression profiles in different cell states for large numbers of genes simultaneously[20,21]. Initially developed as a method to study differential gene expression from RNA, the fast advancement and refinement in microarray technology has made it a very widely used technique.[22,23] This platform can study a large number of nucleic acid samples simultaneously.[22] Expression of different sets of transcripts from different tissues, different stages of development, different diseases, different genetic background or different experimental conditions can be studied simultaneously.

Microarray technology is being used in almost all fields where analysis of a large

population of nucleic acids or proteins is a necessity. The multiplexing capability of microarrays is being exploited in the pharmaceutical industry to study the effect of drugs, and to identify drug targets and mechanisms.[24] Microarrays are also being used as a diagnostic tool in identifying diseases, and monitoring the progression and response to drugs, especially in cancer treatments.[20,25–27]

Fluorescence-based detection techniques have high sensitivity and are widely used for *in situ* and *in vitro* applications[28,29]. Molecular beacons, first developed by Tyagi et al., are stem-loop oligonucleotide hairpins with a fluorophore on one end and a quencher on the other end[30]. Molecular beacons fluoresce in the presence of a complementary target sequence. Fluorescent hairpin probes are similar to molecular beacons, but have no quencher. Molecular beacons and fluorescent hairpin probes have been successfully used in both solution and microarrays to detect single nucleotide polymorphisms (SNPs).[31–35] The stem-loop structure of molecular beacons and hairpin probes provides a fine balance between the stability of the stem-loop structure and the competing probe-target hybrid to improve the probe specificity, enabling single-base discrimination[36,37]. Molecular beacons have been successfully used in detecting UV-induced photodamage in single-stranded oligonucleotides[38]. So we have tried to combine the multiplexing capability of microarrays and the high sensitivity of the hairpin probes to study UV damage in large numbers of nucleic acids simultaneously.

In this Chapter, I measured the kinetics of UV-induced damage for different sequences of microRNAs (miRNAs) using a microarray platform. MicroRNAs are small, single stranded, 21-24 nucleotide endogenous RNAs that regulate gene expression through sequence-specific translational repression and mRNA degradation.[39] These miRNAs recognize their mRNA targets by sequence complementarity and play an important role in different biological processes, such as development, cell proliferation, differentiation, and apoptosis. Many miRNA genes are found at fragile sites in the genome or in genomic regions that are commonly amplified or deleted in human cancer.[40] Expressions of different miRNAs were found to be deregulated in malignant tumors and tumor cell lines compared to normal tissues. Thus miRNAs are thought to be important in cancer.[41] Since miRNAs play an important role in controlling gene expression, a change in the level of miRNA, or damage to miRNA, may affect the gene expression profile of a cell.[42] Therefore, it is important to study the effect of UV-induced damage on different sequences of miRNAs. We have

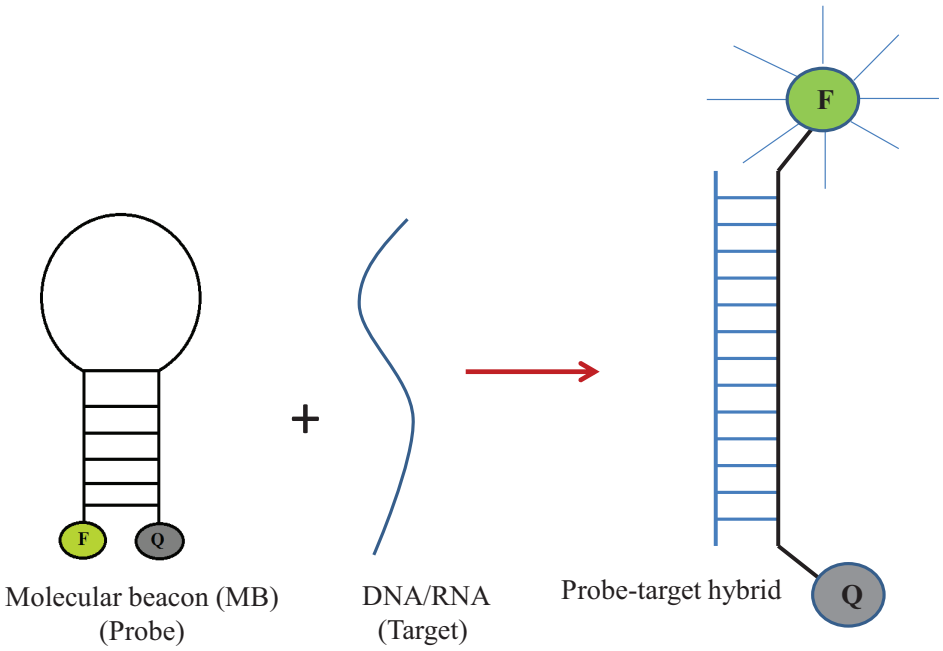

Figure 4.1: Schematic showing molecular beacon based nucleic acid detection where the fluorescent probe (F) and quencher (Q) are forced apart resulting in fluorescence for the probe.

measured here the susceptibility to UV light of different miRNA sequences associated with breast cancer. The main aim of this work is to understand the sequence dependence of DNA/RNA damage kinetics. This work shows that the UV-induced damage kinetics is different for different miRNA sequences.

4.2 Experimental

The miRNAs, hairpin probes and internal standards were synthesized, labeled and purified by Integrated DNA Technologies (IDT) Inc. (Coralville, IA, USA). The miRNAs were purified by IDT using standard desalting and the fluorescently-labeled oligonucleotides (hairpin probes and internal standards) by HPLC. Bovine serum albumin (BSA) and sodium dodecyl sulphate (SDS) were obtained from Sigma-Aldrich Canada Ltd. (Oakville, ON, Canada), sodium citrate and sodium phosphate monobasic monohydrate from Fisher Scientific (Ottawa, ON, Canada), sodium phosphate dibasic heptahydrate from EMD Chemicals Inc. (Gibbstown, NJ, USA), Tris buffer from ICN Biomedicals Inc. (Aurora, OH, USA), and sodium chloride from ACP Chemicals Inc. (Montreal, QC, Canada). Epoxide-coated microarray slides used were obtained from Corning Inc. Life Sciences (Tewksbury, MA, USA). The miRNAs and internal standards were diluted with nanopure water from a Barnstead water filtration system (Boston, MA) and the probes were diluted with Tris buffer (10 mM Tris, 5 mM $MgCl_2$).

Designing target and probe. The miRNA targets and internal standard sequences were modified at the 5' end with a C6-linked amino group. The loop and roughly half of the stem of the hairpin probe was complementary to the target miRNA. The sequences of different miRNA targets and corresponding probes used in this study are given in Tables 4.1 and 4.2, respectively. The hairpin probes were designed in such a way that the melting temperature of the hairpin stem is 5-8° C above the melting temperature of the miRNA-probe hybrid. Either 6-carboxyfluorescein (6-FAM) or cyanine 5 (Cy5) was attached to the 5' end of the hairpin probe. The internal standards used in these experiments were 7-8 nucleotides and the sequences were chosen in such a way that they do not have any thymine or uracil nucleotides.

Sample preparation. Printing solutions containing miRNA targets and internal standard were prepared by mixing the required amounts of 100 μM target stock solutions, 25-50 μM internal standard stock and 450 mM phosphate buffer to

Table 4.1: miRNA sequences used in this work

Sequence no	Name[a]	miRNA sequence[b]
1	*hsa-miR-181b-1*	5'-/5AmMC6/-AAC AUU CAU UGC UGU CGG UGG GU-3'
2	*hsa-miR-100*	5'-/5AmMC6/-AAC CCG UAG AUC CGA ACU UGU G-3'
3	*hsa-miR-29b-2*	5'-/5AmMC6/-UAG CAC CAU UUG AAA UCA GUG UU-3'
4	*hsa-miR-21*	5'-/5AmMC6/-UAG CUU AUC AGA CUG AUG UUG A-3'
5	*hsa-miR-125b-1*	5'-/5AmMC6/- UCC CUG AGA CCC UAA CUU GUG A -3'
6	*hsa-let-7f-1*	5'-/5AmMC6/-UGA GGU AGU AGA UUG UAU AGU U-3'
7	*hsa-let-7a-2*	5'-/5AmMC6/-UGA GGU AGU AGG UUG UAU AGU U-3'
8	*hsa-let-7g*	5'-/5AmMC6/-UGA GGU AGU AGU UUG UAC AGU U-3'
9	*hsa-miR-155*	5'-/5AmMC6/-UUA AUG CUA AUC GUG AUA GGG GU-3'
10	*hsa-miR-145*	5'-/5AmMC6/-GUC CAG UUU UCC CAG GAA UCC CU-3'
11	*hsa-miR-10b*	5'-/5AmMC6/-UAC CCU GUA GAA CCG AAU UUG UG-3'
12	*hsa-miR-17*	5'-/5AmMC6/-CAA AGU GCU UAC AGU GCA GGU AG-3'
13	*hsa-miR-27b*	5'-/5AmMC6/-UUC ACA GUG GCU AAG UUC UGC-3'

[a]Sequence names are taken from the miRNA database- http://www.mirbase.org/, 'hsa' denotes Homo sapiens, 'let' denotes lethal and 'miR' denotes miRNA. [b]All nucleotides listed here are ribonucleotides, '5AmMC6' denotes the heptyl amine linker at the 5' end of the miRNA oligonucleotide.

Table 4.2: DNA probe sequences used in this work

Sequence no.	Probe sequence
1	5'-/ TTG CAC CCA CCG ACA GCA ATG AAT GTT GGG TGC AA /F/-3'
2	5'-/ TTG CAC AAG TTC GGA TCT ACG GGT TTT GTG CAA /F/-3'
3	5'-/ TTG AAC ACT GAT TTC AAA TGG TGC TAG TGT TCA A /F/-3'
4	5'-/ TTG TCA ACA TCA GTC TGA TAA GCT AGT TGA CAA /F/-3'
5	5'-/ TTG CTC ACA AGT TAG GGT CTC AGG GAT TGT GAG CAA /F/-3'
6	5'-/ TTT CAA CTA TAC AAT CTA CTA CCT CAT AGT TGA AA /F/-3'
7	5'-/ TTG CAA CTA TAC AAC CTA CTA CCT CAT AGT TGC AA /F/-3'
8	5'-/ TTG CAA CTG TAC AAA CTA CTA CCT CAA GTT GCA A /F/-3'
9a	5'-/ TTA CAC CCC TAT CAC GAT TAG TAG CAT TAA GGG TGT AA /F/-3'
9b	5'-/ TTG ACC CCT ATC ACG ATT AGC ATT AAG GGT CAA / F/-3'
10	5'-/ TTG AGG GAT TCC TGG GAA AAC TGG ACT CCC TCA A /F/-3'
11	5'-/ TTG CCA CAA ATT CGG TTC TAC AGG GTA GTG GCA A / F/-3'
12	5'-/ TGG CCT ACCTGC ACT GTA AGC ACT TTG TAG GCC A /F/-3'
13	5'-/ TTG GCA GAA CTT AGC CAC TGT GAA CTG CCA A /F/-3'

/F/ refers to the fluorophore (6-FAM or Cy5) FAM stands for carboxyfluorescein and Cy5 denotes cyanine 5. The fluorophore was different for different experiments. The underlined nucleotides at the 3′ and 5’ ends indicate the bases that form the stem of the hairpin probes.

get a final concentration of 50 μM targets in 150 mM phosphate buffer at pH 8.4. The concentrations of internal standard were varied from 1 to 5 μM for different experiments and for different internal standards. The internal standard dyes used were Cy5 and FAM. All the solutions printed on a slide had a constant concentration of internal standard. The probe solutions were prepared by diluting a stock solution of probe (50-100 μM) in Tris buffer (10 mM Tris, 5 mM $MgCl_2$, pH 7.6) to get a final probe concentration of 5-8 μM for each probe. BSA wash solution was prepared by diluting 20×SSC (3 M NaCl, 0.3 M sodium citrate), 10% Sodium dodecyl sulfate (SDS) and bovine serum albumin with nanopure water to get a final concentration of 5×SSC, 0.1% SDS and 0.2% BSA. Wash 1 solution is 0.1×SSC and was prepared by a 200× dilution of 20×SSC. Wash 2 solution is 0.2% SDS and 2×SSC, which is prepared by mixing appropriate volumes of 20×SSC and 10% SDS and diluting with nanopure water. All the solutions were filtered through a 0.22 μm Millipore membrane filter prior to use.

Methods. Solutions were spotted on an epoxide-coated microarray slide using stealth spotting pins (SMP3) from Arrayit Corporation (Sunnyvale, CA, USA) with a GeneMachine Omni Grid 100 arrayer from Genomic Solution (Ann Arbor, MI, USA) housed in the Microarray and Proteomics Facility, University of Alberta. The design of the slides and number of pins were varied for different experiments. The printed solutions were allowed to dry and typical spot diameters were 100-150 micrometers.

The slides were first scanned in the internal standard channel to ensure the quality of the printing. The scanning of the slides was done using either an Arrayworx biochip reader from Applied Precision (Issaquah, WA, USA) or Genepix 4000 B microarray scanner from Molecular Devices (Sunnyvale, CA, USA). For the Cy5 channel the excitation wavelength was 635 nm with 30 nm band pass and the emission was recorded at 685 nm with bandpass filter cut-offs of 655 nm and 695 nm. Similarly, the FAM channel was excited with light of 480 nm with a bandpass of 30 nm and the emission was recorded at 530 nm with a bandpass of 40 nm. Subsequently the slides were treated with preheated BSA wash solution at 42° C for 1 hour to block unreacted sites on the slide and subsequently washed 5 minutes each with three sets of wash 1 solution and nanopure water. The slides were then dried by centrifuging at 1400 rpm for 6-9 minutes and transferred to a Corning slide holder (Corning model 40082), purged with nitrogen and sealed air tight. The slides

were again scanned in the internal standard channel.

The scanned slides were transferred to an altered Corning slide holder where one side of the slide holder was removed to enable slide exposure to light. A sliding metal block was used to control the exposure of the microarray slide to UV light. Different irradiation periods for different subarrays of the microarray were achieved by moving the sliding metal block after each interval. The whole assembly was painted black to minimize reflection and to maximize the opacity of the system. UVC irradiation of the microarray was carried out in a Luzchem EDU/DEV photoreactor (Ottawa, ON, Canada). The microarray irradiations were performed using 4 UVC lamps (8 watts) fitted at the top of the chamber. The chamber was purged with nitrogen during the entire irradiation period. For some of the experiments discussed here, a custom-made, fully automated slide mover was used. This remote slide mover (RSM) exposed different subarrays to different preset periods of time according to programmed instructions. For all experiments, two control slides were used, one slide inside the irradiation chamber fully covered (dark control) and one unirradiated slide in a desiccator (desiccator control).

After irradiation, the slides were hybridized. The probe solution was prepared by mixing equal amounts of each probe and diluting with Tris buffer to the required concentration (5-8 μM). The probe solution was annealed by heating the final solution to 80-85° C and slowly cooling down to room temperature. Each microarray slide was kept inside a Corning 2551 hybridization chamber (Nepean, ON, Canada) and two hybridization methods were used, depending upon the type of cover slip used. In the first method, three aliquots of 30 μL probe solution were pipetted on the microarray at equal distances along the length of the slide and the slide was subsequently covered with a hybrid-slip (Sigma-Aldrich H0784-100EA) put into a hybridization chamber, and incubated at 32° C in the dark for 16 hours. When the Combi-lifter cover slip was used, the cover slip was put on top of the microarray slide first and the 60 μL probe solution was pipetted along the bottom of the coverslip.

The slides were treated with preheated (40-42° C) wash 2 solution after hybridization to remove the cover slip, transferred to a second wash 2 solution for 5 minutes and transferred to a room temperature wash 1 solution for 5 minutes. The process was repeated for 2 more sets of wash 1 solution. The slide was then dried by centrifuging at 1400 rpm for 6-9 minutes, purged with nitrogen and sealed. The washes were either done in Coplin jars filled with wash solutions or in Arrayit

wash stations. The hybridized slides were then scanned in both the internal standard channel and the probe channel. The slides were stored in a slide jacket under nitrogen and covered with aluminum foil thereafter.

Data analysis. The average spot intensity in different channels for each spot at different stages of the experiment was obtained using GenePix Pro 6.1 software. The grid is manually aligned, so that it covers the spots and differentiates the background well. The average fluorescence intensity of each spot was then measured.

Experiments. In experiment 1, only 4 miRNA sequences (*hsa-miR-100, hsa-miR-29b-2, hsa-miR-21* and *hsa-miR-155*) were used. Each miRNA sequence was printed in two rows within a subarray and each row had 20 spots of the same miRNA sequence. So 40 replicates of each miRNA sequence were printed within a subarray. Four subarrays were irradiated for each time period. Therefore, there were 160 total replicates for each miRNA sequence for each irradiation period. The probe fluorophore was FAM and internal standard fluorophore was TYE665. The miRNA internal standard concentration was 50 and 2 μM, respectively. The concentration of each probe was 8 μM.

In experiment 2, eight miRNAs (*hsa-miR-181b-1, hsa-miR-100, hsa-miR-29b-2, hsa-miR-125b-1, hsa-let-7f-1, hsa-let-7a-2, hsa-let-7g* and *hsa-miR-155*) were used. Each subarray had all the miRNA sequences, and each miRNA sequence and its 20 replicates were printed in the same row within a subarray, but the row position of each miRNA was varied for each subarray. Four subarrays were irradiated for each time period. Therefore, there were 80 total replicates of each miRNA subjected to each irradiation time in experiment 2. The probe fluorophore used was FAM and the internal standard fluorophore was Cy5. The irradiation times were 0, 15, 30 and 60 minutes for both experiments 1 and 2. The concentration of the internal standard was increased to 4 μM and the concentration of each miRNAs was 50 μM.

For experiment 3, the probe fluorophore was Cy5 (5 μM of each probe) and the internal standard fluorophore was FAM (0.5 μM). Eight target sequences (*hsa-miR-29b-2, hsa-miR-21, hsa-miR-125b-1, hsa-miR-155, hsa-miR-145, hsa-miR-10b, hsa-miR-17* and *hsa-miR-27b*), some the same as in experiment 2, were used in experiment 3. The slide design was similar to that of experiment 2. Irradiation times were 0, 10, 20 and 30 minutes.

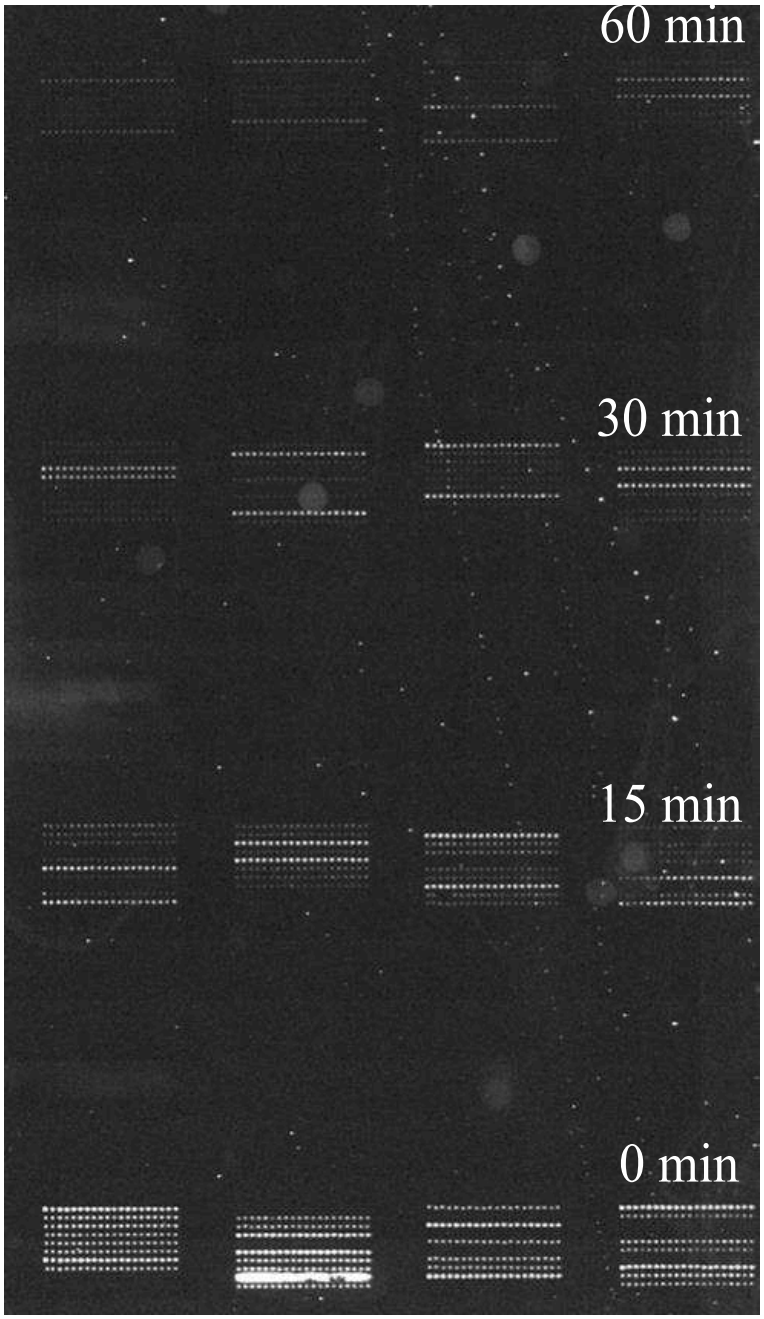

Figure 4.2: 685 nm (probe channel) image of a miRNA microarray slide after irradiation with UVC light and hybridized with the Cy 5 hairpin probes in experiment 1. Irradiation times for each row of subarrays is shown on the slide. Each row in each subarray represents a different miRNA sequence. Each sequence is replicated in 2 rows of 20 spots each within a subarray.

4.3 Results and Discussion

Figure 4.2 shows the image of a miRNA microarray slide scanned in the 685 nm probe channel after UVC irradiation as described in experiment 1. Each subarray contains spots of 4 different miRNA sequences with 40 replicates. Each row within a subarray contains only one miRNA sequence and there are two rows of each miRNA within each subarray. Each rows of the slide contains four subarrays. Thus, there are 160 spots of each miRNA for each irradiation time. The position of each miRNA in each subarray is different. The irradiation time for each row of subarrays is shown on the slide. There is an obvious decrease in the probe fluorescence intensity with increasing irradiation time for different sequences of miRNAs indicating that there is a decrease in binding between miRNA and the fluorescent hairpin probe specific for that miRNA sequence. Equation 4.1 shows the equilibrium between miRNA, the complementary probe and the miRNA-probe hybrid. Upon irradiation with UV light, miRNA undergoes photochemical damage and the equilibrium in the Equation 4.1 shifts towards the left, decreasing the amount of miRNA-probe hybrid, and leading to a decrease in fluorescence.

$$miRNA + probe \rightleftharpoons hybrid \tag{4.1}$$

Figure 4.3 shows the plot of probe fluorescence intensity as a function of irradiation time for miRNAs *hsa miR-29b -2* and *hsa miR-155*. The damage plots for all the sequences are shown in Appendix B. The plot reflects the decrease in fluorescence intensity with irradiation time as seen in the slide image in Figure 4.2. Because the amount of fluorescence is directly proportional to the amount of bound probe, the signal is an indication of the miRNA damage due to the UV irradiation. The decrease in fluorescence intensity is fitted with an exponential decay to obtain the damage constant. It is clear that these two sequences exhibit different damage kinetics. All the miRNA sequences studied here show first-order damage kinetics upon UV irradiation. The error bars represent the standard deviation for each time point based on the replicate measurements. The high values of standard deviations were due to the large differences in the average fluorescence intensities of different spots of the same miRNA sequence at the same irradiation time as shown in Figure 4.2.

We have tried to account for the change in fluorescence intensity arising as a

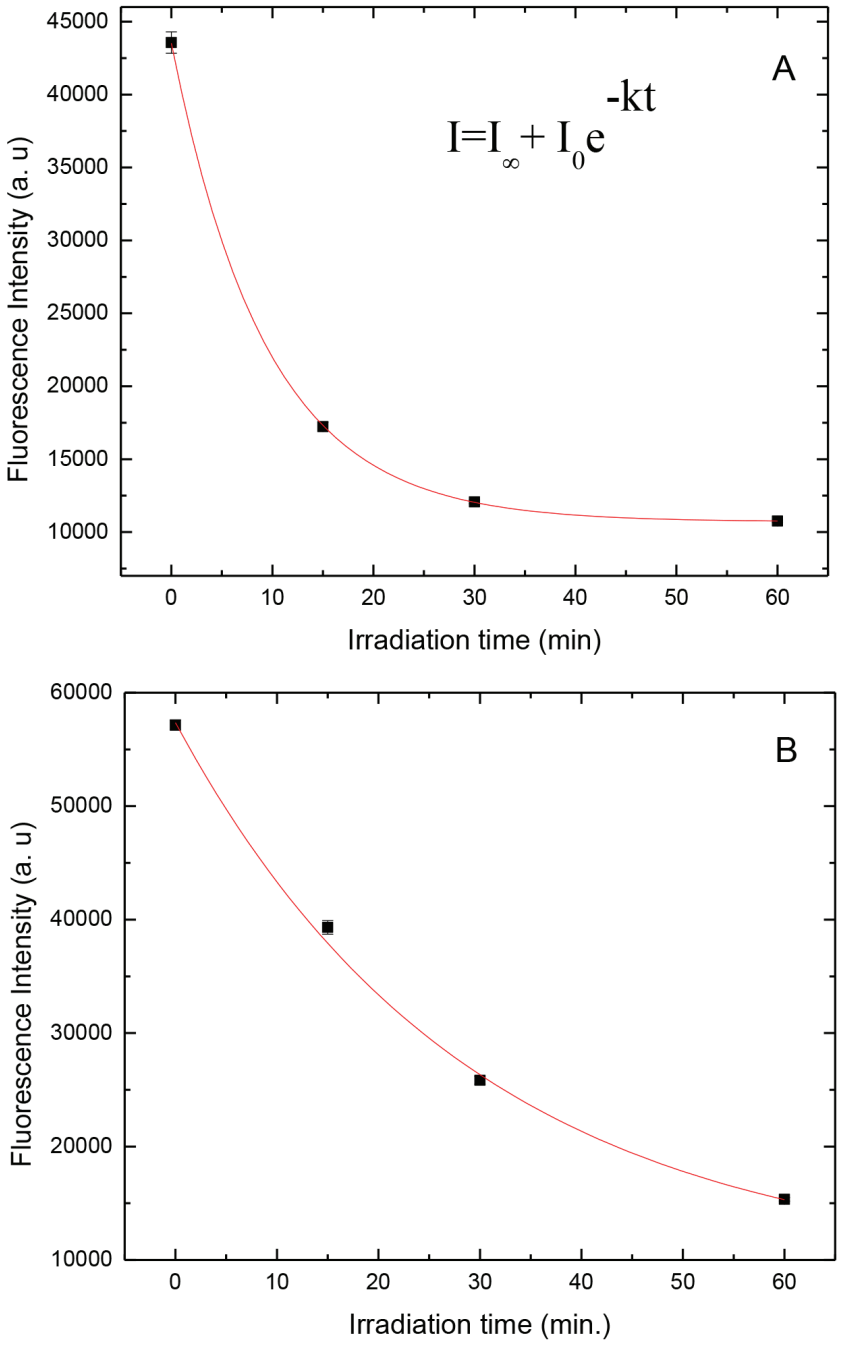

Figure 4.3: Probe fluorescence intensity at 530 nm as a function of UV irradiation time for miRNAs *hsa-miR-29-b-2*(A) and *hsa miR-155*(B). The equation used for fitting the decrease in fluorescence intensity as a function of time is shown in Figure A. I is the fluorescence intensity, I_0 fluorescence intensity at zero time, I_∞ is the fluorescence intensity at infinite time and k is the time constant in min^{-1}.

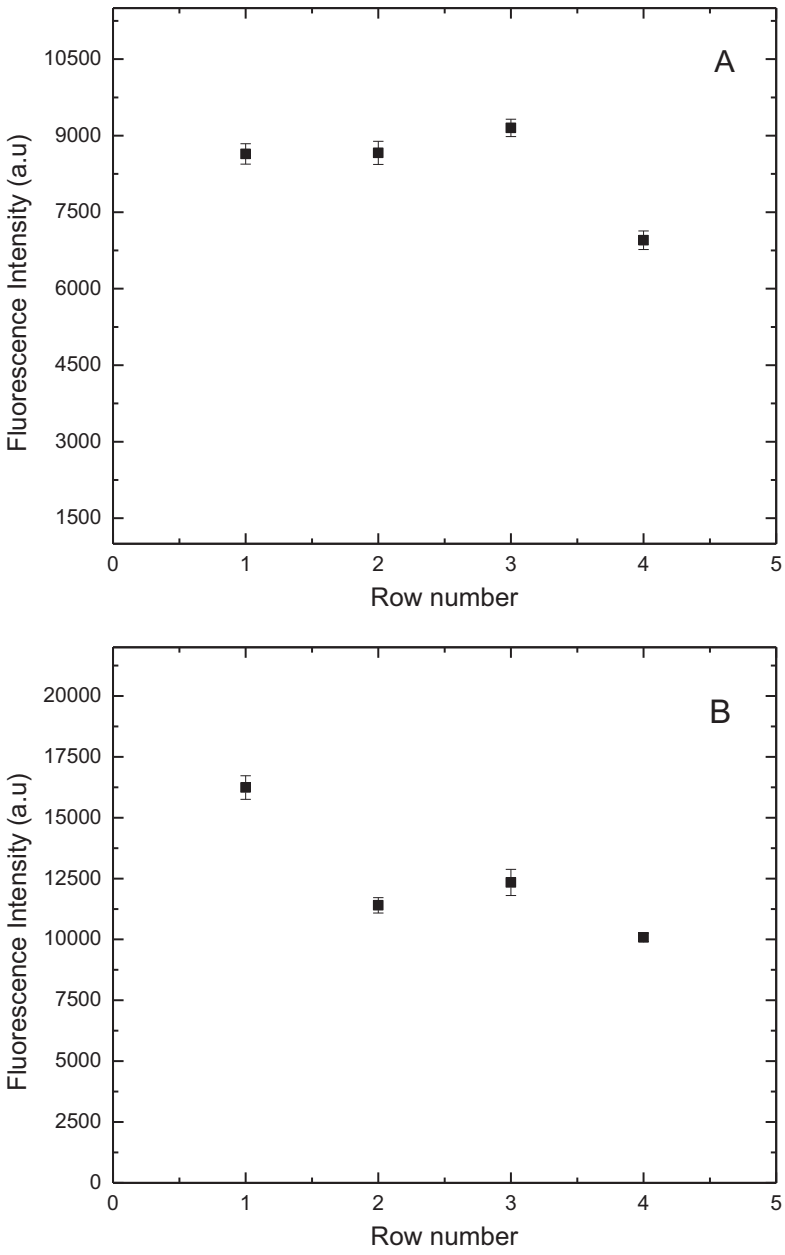

Figure 4.4: Probe fluoroscence intensity as a function of row number for miRNA *hsa-miR-21* (A) and *hsa miR-125b-1* (B) for the control which was inside the irradiation chamber but not exposed to UV light.

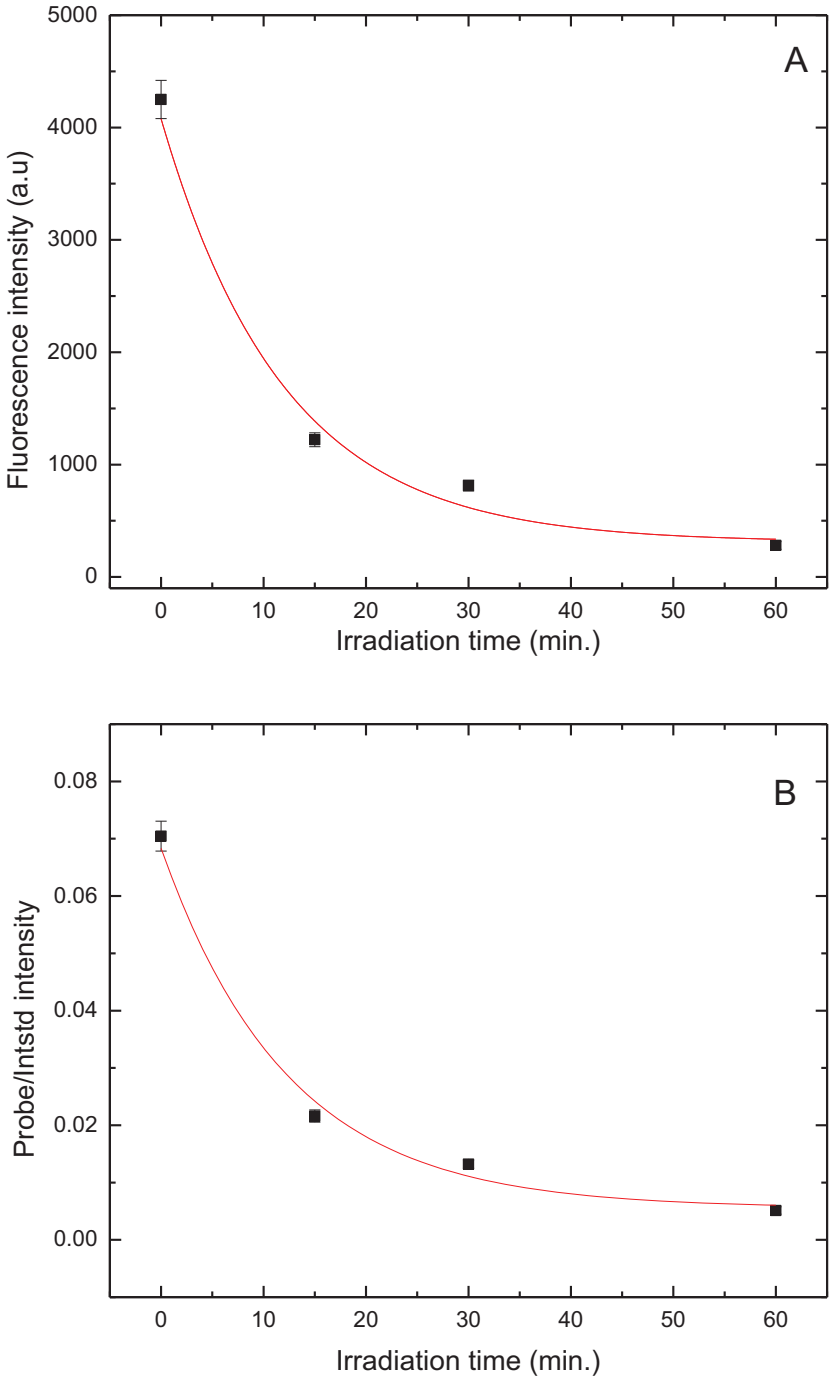

Figure 4.5: Fluorescence intensity of probe (A) and ratio of fluoresence intensities of probe and internal standard (B) as a function of irradation time for experiment 2 for miRNA *hsa-miR-100*.

result of difference in the size of the miRNA spots by dividing the probe fluorescence intensity by the internal standard fluorescence intensity of each spot as a way of reducing the error bars. The plot of the intensity ratio as a function of irradiation time for different miRNA sequences were done and this correction for the difference in spot size did not decrease the fluorescence intensity standard deviation of each time point. Attempts were made to fit the kinetics with a linear fit as well to see the accuracy of the fit. But this did not improve the quality of the fit and it was clear that the kinetics were not linear. Also, it is evident from the control experiments (Figure 4.4) that the fluorescence intensity decrease is mainly due to the UVC exposure of the miRNAs.

Table 4.3 shows the damage constants obtained for different miRNA sequences from different experiments. Table 4.4 compares different factors that may affect the UV damage kinetics. The large standard deviations in the time constants arise from two factors; one is the difference in fluorescence intensity of each spot for a particular time of irradiation and the other is the accuracy of the fit. The large errors in the time constants make the comparison of data and their corresponding interpretation difficult.

Among the four miRNAs studied in experiment 1, the damage constant of *hsa-miR-155* is reproducibly longer compared to other sequences studied. A close examination of the sequences shows that the percentage of pyrimidine is lower while the percentage of guanine is higher in *hsa-miR-155* (Table 4.4) than in the other three sequences. The number of pyrimidine doublets is also less in *hsa-miR-155* compared to the other sequences. Another difference seen in Table 4.4 between *hsa-miR-155* and the other sequences in experiment 1 is the number of guanine doublets; *hsa-miR-155* has three guanine doublets whereas *hsa-miR-100, hsa-miR-29b-2* and *hsa-miR-21* have no guanine doublets. Guanine has been previously shown to have a protective effect [43,44] by acting as a hole sink.

In experiment 2, the kinetics of *hsa-let-7f-1* and *hsa-let-7g* show faster damage compared to other sequences studied. These two miRNAs have very similar sequences as seen in Table 4.1 and similar kinetics are expected. These miRNAs have the largest number of uridines and very low percentages of cytosine (Table 4.4). These two sequences are very similar except for the two nucleobases; the 11^{th} nucleobase from the 5' end is an adenine for *hsa-miR-7f-1* and the 17^{th} nucleobase is a uracil, whereas it is a uracil and a cytosine, respectively, in *hsa-let-7g*. Also, it is

worth mentioning that the miRNA *hsa-let-7a-2* is very similar to miRNAs *hsa-let-7f-1* and *hsa-let-7g*, but appears to exhibit slightly longer damage kinetics, miRNA *hsa-let-7a-2* in the 11^{th} nucleobase, position compared to adenine in *hsa-let-7g*. The 17^{th} nucleobase in all the three sequences are pyrimidines, uracil in sequences *hsa-let-7f-1* and *hsa-let-7a-2*, and cytosine in *hsa-let-7g*. It is reasonable to believe that presence of guanine close to the uracil doublet may have some protecting effect towards UV damage[43,44].

In experiment 3, miRNAs *hsa-miR-29b-2, hsa-miR-125b-1, hsa-miR-155* and *hsa-miR-10b* are more resistant to UV damage, whereas miRNA *hsa-miR-21* is more prone to UVC-induced photodamage. Upon comparing different sequences, there were no striking similarities between the miRNAs less prone to UV damage. In *hsa-miR-21* there were no other nucleobase doublets except for the two uracil doublets. Sequences *hsa-miR-145*, *hsa-miR-17* and *hsa-miR-27b* show different damage constants for the two runs and make it very difficult to do any sequence dependence comparisons.

If we consider miRNAs *hsa-miR-29b-2* and *hsa-miR-155*, which are common in all experiments, the damage kinetics are faster in *hsa-miR-29b-2*, which has three uracil doublets and one cytosine doublet against only one uracil doublet and no cytosine doublet in miRNA *hsa-miR-155*. Sequences *hsa-miR-29b-2* and *hsa-miR-155* have 38% uridine and 19% and 10% cytidine, respectively. Also the number of pyrimidine doublets (UU, CC or UC) are higher in *hsa-miR-29b-2*, with five doublets of pyrimidine in *hsa-miR-29b-2* and only three in *hsa-miR-155*. So it is reasonable to believe that the presence of a higher number of uracil doublet and/or a higher number of pyrimidine doublet will result in faster damage kinetics upon UV irradiation. Again, these preliminary results are consistent with known photochemical quantum yields[1]

Again, if we look at sequences for which at least two sets of data are available for kinetics in Table 4.3, (*miRNAs hsa-miR-100, hsa-miR-29b-2, hsa-miR-21, hsa-miR-125b-1*and *hsa-miR-155*), miRNA *hsa-miR-155* is less prone to damage and miRNA *hsa-miR-21* is more susceptible to UV induced damage compared to other sequences. *hsa-miR-155* has 4 pyrimidine doublets, 3 guanine doublets and 3 UGs, whereas miRNA *hsa-miR-21* has 3 pyrimidine doublets, 4 guanine doublets and 4 UGs. this is again consistent with the higher photochemical quantum yields of pyrimidines and the guanine hole sink model. It is difficult to compare the kinetics of

Table 4.3: Calculated damage constants for different miRNA sequences.

Sequence no.	Name	Exp. 1		Exp. 2		Exp. 3	
		A	B	A	B	A	B
1	*hsa-miR-181b-1*			9.1±0.1	8±2		
2	*hsa-miR-100*	7.5±0.1	8.7±0.4	8±2	14±4		
3	*hsa-miR-29b-2*	9.2±0.1	8.5±0.1	7±3	7.6±0.3	18±1	12±1
4	*hsa-miR-21*	8.0±0.0	7.0±0.9			8.4±0.6	7.7±0.9
5	*hsa-miR-125b-1*			11±4	14±1	15±3	33±11
6	*hsa-let-7f-1*			4±2	7±1		
7	*hsa-let-7a-2*			10±1	10±1		
8	*hsa-let-7g*			5.0±0.2	5.4±0.2		
9	*hsa-miR-155*	33±4	47.4±0.9	12±2	10.5±0.7	43±8	27±17
10	*hsa-miR-145*					11±2	14±2
11	*hsa-miR-10b*					22±13	16.6±0.5
12	*hsa-miR-17*					14±7	20±11
13	*hsa-miR-27b*					26±12	16±5

Time constants and deviations reported here are in minutes^{-1}. 'A' and 'B' represent experimental replicates. Details of experiments 1, 2 and 3 are discussed in the text.

Table 4.4: Amount of nucleobases and nucleobase doublets in different miRNAs.

	Base percentage					Doublets[a]					
Sequence no.	%A	%G	%U	%C	%pyrimidine	A	G	U	C	pyrimidine[b]	UG
hsa-miR-181b-1	*18*	*32*	*36*	*14*	50	1	2	2	0	5	6
hsa-miR-100	*29*	*24*	*24*	*24*	48	2	0	1	3	6	4
hsa-miR-29b-2	*33*	*19*	*38*	*19*	57	2	0	3	1	5	4
hsa-miR-21	*24*	*24*	*38*	*14*	52	0	0	2	0	4	3
hsa-miR-125b-1	*24*	*19*	*29*	*33*	62	1	0	1	4	9	3
hsa-let-7f-1	*29*	*33*	*43*	*0*	43	0	1	2	0	2	5
hsa-let-7a-2	*24*	*38*	*43*	*0*	43	0	2	2	0	2	7
hsa-let-7g	*24*	*33*	*43*	*5*	48	0	1	3	0	3	6
hsa-miR-155	*29*	*33*	*38*	*10*	48	2	3	1	0	3	4
hsa-miR-145	*19*	*19*	*33*	*38*	71	1	1	3	5	12	2
hsa-miR-10b	*29*	*24*	*33*	*24*	57	2	0	2	3	6	4
hsa-miR-17	*33*	*33*	*24*	*19*	43	2	1	1	0	2	3
hsa-miR-27b	*19*	*24*	*33*	*24*	57	1	1	2	0	5	4

[a]Doublets are counted so that a UUU sequence is counted as 2 UU doublets.
[b]Pyrimidine doublets are CC, UU, UC and CU

miRNAs hsa-miR-100, hsa-miR-29b-2, hsa-miR-21, which all show similar kinetics in experiment 1, but different kinetics in experiments 2 and 3 between *hsa-miR-100* and *hsa-miR-29b-2* and *hsa-miR-29b-2* and *hsa-miR-21*, respectively. All these 3 sequences are showing faster damage kinetics than *hsa-miR-155*. The miRNA *hsa-125b-1* also show different kinetics in each experiment and each replicate making any comparison of the kinetics difficult.

There seems to be a variety of factors which are important in determining the stability of the damaged target-probe hybrid and the observed decay constants. These include the amount of uracil doublets, the presence of guanine near the photolabile centers, the position of the damage, etc. Factors such as the number of nucleobase triplets, doublets like UG, CG, AG and the positions of nucleobases were also considered, but no clear correlation between these factors and the observed damage kinetics were seen. All the correlation plots are given in Appendix B. From the correlation plots it can be seen that the damage kinetics become faster as the number of cytosines increases or as the number of guanines decreases in experiment 1. But this trend is not as clear in experiments 2 or 3.

Uracil and cytosine, being the most photochemically active nucleobases are more prone to UV damage[1]. The photohydrate is the major photoproduct, which can be formed from a single uracil or cytosine, the formation of the cyclobutyl dimer is also expected. There is no simple correlation between the number of uracil bases and the observed damage constants. But an increase in the damage kinetics with increase in the number of cytosines is seen, which is supported by the known nucleic acid photochemistry. Surprisingly, an increase in the number of uracils did not show any correlation with the increase in the difference in damage kinetics. This may be due to the fact that the number of uracil is higher than four in all the sequences. Therefore, with a relatively large number of uracils in the sequences, any further addition of uracil nucleobases does not significantly affect the kinetics. Also, there appears to be a decrease in the damage kinetics with an increasing number of guanines. Guanine, has the lowest oxidation potential among the nucleobases and may act as a hole, leading to a decrease in the potential photochemical damage of the sequences containing high numbers of guanines[45]. Looking at the uracil doublets, miRNAs *hsa-miR-100, hsa-miR-125b-1, hsa-miR-155* and *hsa-miR-17* have only one uracil doublet and all these sequences show a longer damage constant. Similarly, sequences *hsa-miR-29b-2, hsa-let-7g* and *hsa-miR-145* have three uracil doublets

and are expected to have faster damage kinetics, which is true except for *hsa miR-29b-2* in experiment 3. But, if we inspect the sequence of different miRNAs studied here, miRNAs *hsa-miR-181b-1, hsa-miR-21, hsa-let-7f-1, hsa-let-7a-2, hsa-let-7g, hsa-miR-155, hsa-miR-17* and *hsa-miR-27b* do not have any cytosine doublets. However, sequences *hsa-let-7f-1* and *hsa-let-7a-2* do not have any cytosine but have 2 uracil doublets, and their damage constants are different. So it is difficult to correlate the presence of uracil doublets/pyrimidine doublets alone to the observed damage kinetics. There are no trends observed with change in the number of each nucleobase as well. For example, miRNA *hsa-let-7a-2* has the highest percent of guanine and no cytosine and the miRNA *hsa-miR-125b-1* has the least amount of guanine (17%) and 33% of cytosine, but they show similar kinetics. Another factor which may be important in the observed kinetics will be the position of the nucleotides. There are three uracils adjacent to each other at the center of the sequence *hsa-miR-29b-2*, which are known to be more prone to damage and the probes may be more sensitive to damage in the centre of the sequence[46]. Other evidence supporting this conclusion can be seen in the damage kinetics for *hsa-miR-145*, which has 4 uracils at the center of the sequence and show relatively faster damage kinetics compared to the other sequences in experiment 3.

4.4 Conclusions

The damage kinetics of different miRNA sequences upon UVC irradiation were studied and compared. The damage constants were correlated to sequence differences. There appears to be an increase in the damage kinetics with the increase in the number of cytosines. The large standard deviation in the damage constant restricts any thorough correlation between the sequence and damage constants. Though factors like amount of uracil doublets, presence of guanine near the photolabile centers, position of the damage and sensitivity of the probe appear to be important in determining the stability of the target to UVC-induced damage, it is not clear how significant is each factor. Further studies are required to investigate the effect of each factor and their contribution to the observed damage kinetics.

References

[1] B. P. Ruzsicska and D. G. E. Lemaire. *CRC Handbook of Organic Photochemistry and Photobiology*, chapter DNA Photochemistry, pages 1289–1317. CRC Handbook. CRC Press, 1995.

[2] J. H. Santos, J. N. Meyer, B. S. Mandavilli, and B. Houten. Quantitative PCR-based measurement of nuclear and mitochondrial DNA damage and repair in mammalian cells. In Daryl S. Henderson, editor, *DNA Repair Protocols*, volume 314 of *Methods in Molecular Biology*, pages 183–199. Humana Press, 2006.

[3] K. A. Grimaldi and J. A. Hartley. PCR-based methods for detecting DNA damage and its repair at the subgene and single nucleotide levels in cells. In *Meth. Mol. Biol.*, volume 90, pages 157–180. 1997.

[4] K. J. Angelis, M. Dusinska, and A. R. Collins. Single cell gel electrophoresis: Detection of DNA damage at different levels of sensitivity. *Electrophoresis*, 20(10):2133–2138, 1999.

[5] R. F. Lee and S. Steinert. Use of the single cell gel electrophoresis/comet assay for detecting DNA damage in aquatic (marine and freshwater) animals. *Mut. Res.*, 544(1):43–64, 2003.

[6] A. L. Kindzelskii and H. R. Petty. Ultrasensitive detection of DNA damage by the combination of the comet and TUNEL assays. In VladimirV. Didenko, editor, *In Situ Detection of DNA Damage*, volume 203 of *Methods in Molecular Biology*, pages 195–201. Humana Press, 2002.

[7] K. Taghizadeh, J. L. McFaline, B. Pang, M. Sullivan, M. Dong, E. Plummer, and P. C. Dedon. Quantification of DNA damage products resulting from deamination, oxidation and reaction with products of lipid peroxidation by liquid chromatography isotope dilution tandem mass spectrometry. *Nat. Protoc.*, 3(8):1287–1298, July 2008.

[8] T. L. Merrigan, C. A. Hunniford, D. J. Timson, M. Catney, and R.W. McCullough. Development of a novel mass spectrometric technique for studying DNA damage. *Biochem. Soc. Trans.*, 37:905–909, 2009.

[9] A. Jenner, T G. England, I. O. Aruoma, and B. Halliwell. Measurement of oxidative DNA damage by gas chromatography-mass spectrometry: Ethanethiol prevents artifactual generation of oxidized DNA bases. *J. Biochem.*, 331:365–369, 1998.

[10] H. Kaur and B. Halliwell. Measurement of oxidized and methylated DNA bases by HPLC with electrochemical detection. *J. Biochem.*, 318:21–23, 1996.

[11] H. J. Helbock, K. B. Beckman, M. K. Shigenaga, P. B. Walter, A. A. Woodall, H. C. Yeo, and B. N. Ames. DNA oxidation matters: The HPLC-electrochemical detection assay of 8-oxo-deoxyguanosine and 8-oxo-guanine. *Proc. Natl. Acad. Sci. USA*, 95(1):288–293, 1998.

[12] R. Jain and M. Sharma. Fluorescence postlabeling assay of DNA damage induced by n-methyl-n-nitrosourea. *Can. Res.*, 53(12):2771–2774, 1993.

[13] Y. Yamazaki, A. Zinchenko, and S. Murata. Assessment of the DNA damage using the fluorescence microscope. *Nucl. Acids Symp. Series*, 53(1):47–48, 2009.

[14] W. Schlörmann and M. Glei. Detection of DNA damage by comet fluorescence in situ hybridization. In Lotte Bjergbak, editor, *DNA Repair Protocols*, volume 920 of *Methods in Molecular Biology*, pages 91–100. Humana Press, 2012.

[15] Z. J. Shire and G. R. Loppnow. Molecular beacon probes for the detection of cisplatin-induced DNA damage. *Anal. Bioanal. Chem.*, 403(1):179–184, 2012.

[16] Z. J. Shire and G. R. Loppnow. Molecular beacon probes of oligonucleotides photodamaged by psoralen. *Photochem. Photobiol.*, 88(3):645–650, 2012.

[17] C. Marzano, D. Fregona, F. Baccichetti, A. Trevisan, L. Giovagnini, and F. Bordin. Cytotoxicity and DNA damage induced by a new platinum(II) complex with pyridine and dithiocarbamate. *Chem. Biol. Int.*, 140(3):215–229, 2002.

[18] A. Besaratinia, J. Yoon, C. Schroeder, S. E. Bradforth, M. Cockburn, and G. P. Pfeifer. Wavelength dependence of ultraviolet radiation-induced DNA damage as determined by laser irradiation suggests that cyclobutane pyrimidine dimers are the principal DNA lesions produced by terrestrial sunlight. *FASEB J.*, 25(9):3079–3091, 2011.

[19] A. F. El-Yazbi and G. R Loppnow. 2-aminopurine hairpin probes for the detection of ultraviolet-induced DNA damage. *Anal. Chim. Acta*, 726(0):44–49, 2012.

[20] P. F. Macgregor and J. A. Squire. Application of microarrays to the analysis of gene expression in cancer. *Clin. Chem.*, 48(8):1170–1177, 2002.

[21] D. J. Duggan, M. Bittner, Y. Chen, P. Meltzer, and J. M. Trent. Expression profiling using cDNA microarrays. *Nat. Genet.*, 21:10–14, 1999.

[22] R. B. Stoughton. Applications of microarrays in biology. *Ann. Rev. Biochem.*, 74(1):53–82, 2005.

[23] J. K. Peeters and P. J. Van der Spek. Growing applications and advancements in microarray technology and analysis tools. *Cell Biochem. Biophys.*, 43:149–166, 2005.

[24] S. Wang and Q. Cheng. Microarray analysis in drug discovery and clinical applications. *Methods Mol. Biol*, 316:49–65, 2005.

[25] S. Mohr, G. D. Leikauf, G. Keith, and B. H. Rihn. Microarrays as cancer keys: An array of possibilities. *J. Clinic. Oncol.*, 20(14):3165–3175, 2002.

[26] L. Hoopes. Genetic diagnosis: DNA microarrays and cancer. *Nature Education*, 1:1, 2008.

[27] R. Kumar, A. Sharma, and R. K. Tiwari. Application of microarray in breast cancer: An overview. *J. Pharm. Bioall. Sci.*, 4(1):21–26, 2012.

[28] Y. Yang and L. Zhao. Sensitive fluorescent sensing for DNA assay. *Trends Anal. Chem.*, 29(9):980–1003, 2010.

[29] B. Wischmann, M. Toft, M. Malten, and K. C. McFarland. Biomass conversion determined via fluorescent cellulose decay assay. In H. J. Gilbert, editor, *Cellulases*, volume 510 of *Methods in Enzymology*, chapter 2, pages 19–36. Academic Press, 2012.

[30] S. Tyagi and F. R. Kramer. Molecular beacons: Probes that fluoresce upon hybridization. *Nature Biotech.*, 14(3):303–308, 1996.

[31] C. G. Mullighan. Single nucleotide polymorphism microarray analysis of genetic alterations in cancer. *Methods Mol. Biol.*, 730:235–58, 2011.

[32] X. Mao, B. D. Young, and Y. J. Lu. The application of single nucleotide polymorphism microarrays in cancer research. *Curr. Gen.*, 8:219–228, 2007.

[33] N. Patil, N. Nouri, L. McAllister, H. Matsukaki, and T. Ryder. *Single-Nucleotide Polymorphism Genotyping Using Microarrays*, pages 2.9.1–2.9.16. Current Protocols in Human Genetics. John Wiley & Sons, Inc., 2001.

[34] D. I. Stimpson, S. M. Knepper, M. Shida, K. Obata, and H. Tajima. Three-dimensional microarray platform applied to single nucleotide polymorphism analysis. *Biotechnol. Bioeng.*, 87(1):99–103, 2004.

[35] N. R. Treff, K. Northrop, L. E. Kasabwala, J. Su, and R. T. Levy, B. Scott Jr. Single nucleotide polymorphism microarray-based concurrent screening of 24-chromosome aneuploidy and unbalanced translocations in preimplantation human embryos. *Fertil. Steril.*, 95(5):1606–1612, 2011.

[36] P. V. Riccelli, F. Merante, K. T. Leung, S. Bortolin, R. L. Zastawny, R. Janeczko, and A. S. Benight. Hybridization of single-stranded DNA targets to immobilized complementary DNA probes: Comparison of hairpin versus linear capture probes. *Nucleic Acids Res.*, 29(4):996–1004, 2001.

[37] A. Tsourkas, M. A. Behlke, S. D. Rose, and G. Bao. Hybridization kinetics and thermodynamics of molecular beacons. *Nucleic Acids Res.*, 31(4):1319–1330, 2003.

[38] S. Yarasi, C. McConachie, and G. R. Loppnow. Molecular beacon probes of photodamage in thymine and uracil oligonucleotides. *Photochem. Photobiol.*, 81(2):467–473, 2005.

[39] R.C. Lee, R. L. Feinbaum, and V. Ambros. The C. elegans heterochronic gene lin-4 encodes small RNAs with antisense complementarity to lin-14. *Cell*, 75(5):843–854, 1993.

[40] G. A. Calin, C. Sevignani, C. D. Dumitru, T. Hyslop, E. Noch, S. Yendamuri, M. Shimizu, S. Rattan, F. Bullrich, M. Negrini, and C. M. Croce. Human

microRNA genes are frequently located at fragile sites and genomic regions involved in cancers. *Proc. Natl. Acad. Sci. U.S.A.*, 101(9):2999–3004, 2004.

[41] S. Sassen, E. A. Miska, and C. Caldas. MicroRNA-implications for cancer. *Virchows Archiv.*, 452:1–10, 2008.

[42] J. Lu and A. G. Clark. Impact of microRNA regulation on variation in human gene expression. *Genome Res.*, 41:3201–3216, 2012.

[43] M. F. Sistare, S. J. Codden, G. Heimlich, and H. H. Thorp. Effects of base stacking on guanine electron transfer: Rate constants for G and GG sequences of oligonucleotides from catalytic electrochemistry. *J. Am. Chem. Soc.*, 122(19):4742–4749, 2000.

[44] J. C. Genereux and J. K. Barton. Mechanisms for DNA charge transport. *Chem. Rev.*, 110(3):1642–1662, 2010.

[45] S. Steenken and S. V. Jovanovic. How easily oxidizable is DNA? One-electron reduction potentials of adenosine and guanosine radicals in aqueous solution. *J. Am. Chem. Soc.*, 119:617–618, 1997.

[46] T. Naiser, J. Kayser, T. Mai, W. Michel, and A. Ott. Position dependent mismatch discrimination on DNA microarrays - Experiments and model. *BMC Bioinformatics*, 509(9):1–12, 2008.

Chapter 5

Initial Excited-State Structural Dynamics of an N-Alkylated Indanylidene-Pyrroline Rhodopsin Analog[1]

5.1 Introduction

The photoisomerization of the retinal chromophore of rhodopsin (Rh)[1] is one of the most efficient (ca. 70% quantum yield) and fastest chemical reactions in Nature.[2–4] Furthermore, it represents a model for light-to-mechanical energy conversion and for assisting the design of molecular devices. Indeed, in recent years Olivucci and coworkers have shown that the N-alkylated indanylidene-pyrroline (NAIP) framework shown in Figure 5.1, provides the basis for the development of a novel class of molecular switches capable to mimic, in solution, different aspects of the Rh photoisomerization dynamics.[5] In particular, and in spite of their reduced but still not negligible ca. 20% quantum yield, NAIP switches undergo a picosecond photoisomerization displaying a ca. 200 fs excited state lifetime and ca. 300 fs product appearance time. Most remarkably, both measurements[6] and simulations[7] support the observation of light-induced 50-100 cm^{-1} vibrational coherent oscillations during few picoseconds after isomerization and matching the 60 cm^{-1} coherent oscillations observed for Rh.[8] This process suggests that in NAIPs, as well as in Rh, light-energy is mainly funnelled into one or few specific vibrational modes that have recently been identified as the twisting of the newly formed double

[1]The computational work mentioned in this study was done by Tadeusz Andruniow (Institute of Physical and Theoretical Chemistry, Wroclaw University of Technology, Poland) and Massimo Olivucci (Bowling Green State University, Bowling Green, USA)

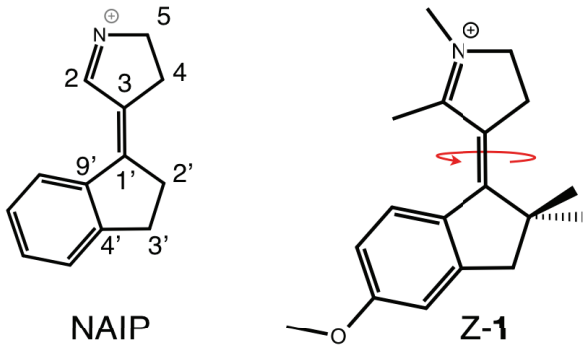

Figure 5.1: Structure of N-alkylated indanylidene-pyrroline (NAIP) and Z-1.

bond.

In order to better comprehend the mechanism of light-to-mechanical energy transduction in NAIPs and provide information useful for the design of NAIP-based molecular devices, we present below a combined experimental and computational investigation focusing on the initial (<70 fs), photoisomerization dynamics of 2-methyl-2'-dimethyl-p-methoxy-4-benzylidene-3,4-dihydro-2H-pyrrolinium (Z-1) chloride in methanol solution. Accordingly, to study the impulsive dynamics driving the system out of the Franck-Condon (FC) region, we record and simulate the Resonance Raman (RR) spectra of Z-1. It is shown that, like in Rh, the initial structural dynamics of the switch involve relaxation along the C=N and C=C double bonds stretches. However, obviously, the intense HOOP motion seen in the RR spectra of Rh is replaced by a relatively weak and slower pyrrolinium deformation making the initial NAIP dynamics dominated by stretchings. This is found to be consistent with the initial dynamics extracted by a classic excited state trajectory where a combined double-bond expansion and single-bond contraction (i.e. bond length alternation, BLA) mode appears to be the only early contribution with later events involving pyrrolinium ring inversion coupled with reactive C=C twisting.

5.2 Experimental and Computational Methods

Materials. Z-1 was synthesized by Olivucci et al. as previously described[9] and used as received. Methanol (Caledon laboratories, Georgetown Hills, ON

Canada) and cyclohexane (Fisher Scientific, Ottawa, ON Canada) solvents used were reagent/spectra grade.

Resonance Raman Spectroscopy. Resonance Raman excitation wavelengths were generated from a picosecond, mode-locked Ti:sapphire laser (Coherent, Santa Clara, CA) pumped by a doubled, continuous wave, solid-state, diode-pumped Nd:YAG laser (Coherent, Santa Clara, CA). The Ti:sapphire output was doubled using an LBO crystal (Inrad, Northvale, NJ) to generate 366, 385, 400 and 412 nm light. The laser powers measured at the sample were 25-50 mW. The laser beam was spherically focussed onto an NMR tube containing the sample solution in a 135° back-scattering geometry. The sample (0.2 M) was dissolved in methanol (69%) and cyclohexane (31%), with the cyclohexane acting as an internal intensity standard. For flowing samples, the NMR tube was replaced with a capillary tube of 2 mm diameter connected to a reservoir and pump. The flow velocity was maintained such that the single-pass photoalteration parameter[10] was <0.1 and the bulk photoalteration parameter was even less. The resulting resonance Raman scattered light was focussed into the first half of a double monochromator (Spex Industries, Metuchen, NJ)fitted with a liquid nitrogen-cooled CCD detector (Princeton Instruments, Trenton, NJ). All spectral measurements were done in triplicate. Absorption spectra were recorded before and after each RR experiment using a diode array spectrometer (model 8452, Hewlett-Packard, Sunnyvale, CA), to measure any evaporation and/or photochemically-induced changes during spectral acquisition. Frequency calibration was done by measuring the Raman scattering of solvents for which the peak positions are known. Frequencies reported here are accurate to ±5-10 cm^{-1}.

Trajectory Computation. The ground state (S_0) equilibrium structure, first excited state (S_1) dynamics and vibrational frequencies of Z-1 in methanol solution are obtained using conventional electrostatic embedding quantum mechanics/molecular mechanics (QM/MM) geometry optimization. As illustrated in Figure 5.2, a guess Z-1 geometry is placed in a solvent box with methanol molecules and one chloride counter-ion, described by the Amber[11,12], force field. The dimension of the box was chosen such that each atom of the switch is at least 10 Å away from the boundary. The Z-1 structure is described at the complete active space self-consistent field method (CASSCF) level which allows to treat spectral and dynamics properties in a balanced way. All conjugated π molecular orbitals

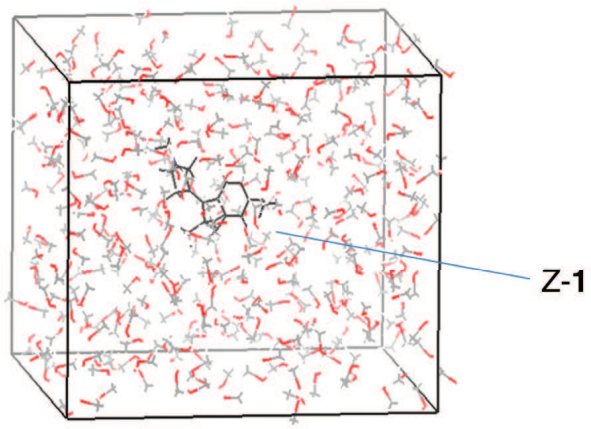

Figure 5.2: Geometry of Z-1 in methanol and one chloride counter ion using quantum mechanics/molecular mechanics (QM/MM) geometry optimization.

are included within the active space of 10 electrons in 10 orbitals, except for the lone pair on the hydroxyl oxygen. During the optimization the first solvation shell (defined by all solvent molecules with at least one atom within 4 Å distance from any atom of the switch) are relaxed by using the micro-iteration method[13]. The CASSCF/AMBER[14] QM/MM calculations were performed using the Molcas 7[15], Gaussian03[16] and Tinker 5 programs[17].

The trajectories are computed using the velocity Verlet algorithm[18] with the forces necessary to propagate the Newton's equations of motion obtained from the QM/MM calculation over successive time steps of 1 fs. In order to ensure that the forces employed in the calculation belong to the correct electronic state we carry out single-point CASPT2 computations on top of the CASSCF/AMBER calculation to improve the electronic energy accuracy and establish the correct state ordering at each time-step (it is currently impractical if not impossible to carry out CASPT2 trajectory computations for a system of the size of Z-1). This protocol is assumed to be adequate if one is interested in the mechanistic aspects of the initial NAIP dynamics. The CASPT2 energies and corresponding wavefunctions reveal that, at the FC geometry, the spectroscopically active state S_1 corresponds to the third, rather than second. Only after 5 fs trajectory propagation S_1 becomes the second CASSCF root. This had already previously found for other NAIP switches[7]. As

a consequence, the energies and gradients of the three lowest CASSCF roots are constantly calculated along the trajectory using state-average CASSCF with equal weights. At FC geometry the trajectories started on the third CASSCF root but after five steps, it continued on the second CASSCF root to follow the potential energy surface of the spectroscopic state.

Resonance Raman Spectra. To simulate RR spectra the FC factors (B_k) were obtained within harmonic approximation assuming identical vibrational frequencies and normal coordinates in the ground and excited electronic states. FC parameters were calculated as described previously[19]. Subsequently, we applied two different formalisms to evaluate relative Raman intensities: 1) Albrecht's sum-over-states formalism[20] and 2) Petrenko and Neese's implementation[21] of Heller's time-dependent theory[22]. The former method was simplified with the typical assumption that the $S_0 \rightarrow S_1$ electronic transition is in resonance with the 0-0 band. In such a case, the intensity of each v_k vibration is proportional to half of the square of the B_k dimensionless parameter[22]. Our realization of this approach is justified by the fact that only fundamentals display significant activity in the calculated spectra and the dependence of the relative RR intensities on the laser frequency is practically negligible.

To improve the agreement between calculated and experimental frequencies, and specifically to accurately reproduce the position of the most intense band located at ca. 1589 cm^{-1}, the calculated vibrational frequencies were scaled by 0.904. The scaling factors may also account for errors due to incomplete treatment of electron correlation and basis set truncation. Please also notice that Dushinsky rotation, frequency change, finite-temperature effects, anharmonicity and nonadiabatic effects were not included into our FC model due to the size of the systems studied. The spectra were obtained as a superposition of Lorentzian curves with a linewidth of 20 cm^{-1} and homogeneous line broadening $\Gamma = 250$ cm^{-1}. Simulated spectra based on Heller's approach were calculated for the 412, 400, 385 and 366 nm experimental laser excitation wavelengths. However, as for the sum-over-states approach, the change of excitation wavelength doesn't significantly change the RR intensity pattern. Thus, we discuss only spectra computed for the 400 nm laser excitation.

Resonance Raman Intensities. The A-term[20] resonance Raman cross-sections of cyclohexane at different excitation wavelengths were calculated for the

802 cm^{-1} ring breathing and CH_2 deformation mode according to Equations 5.1 and 5.2,

$$\sigma_R(\nu_0) = KF_A^2(\nu_0) \tag{5.1}$$

$$F_A^2(\nu_0) = \frac{\nu^2(\nu_0^2 + \nu_e^2)}{(\nu_0^2 - \nu_e^2)^2} \tag{5.2}$$

where K is the coupling strength, ν_0 is the incident laser wavenumber, ν_e is the excited-state wavenumber, and ν=ν_0-802 cm^{-1} is the Raman scattered wavenumber for cyclohexane. For these calculations, we used K=90 x 10^{-21} cm^2 and ν_e = 115,000 cm^{-1} [23] The resonance Raman intensities of the indanylidene pyrroline switch (Z) were converted to absolute cross-sections as described previously[24].

Resonance Raman Structural Dynamics. The resonance Raman intensities as a function of excitation wavelength (excitation profiles) and the absorption spectrum of the Z-1 switch were simulated with a time-dependent formalism[25] and described in Chapter 1 in detail.

The resonance Raman intensities reflect the excited-state structural dynamics of the molecule. The simulation of the absorption spectrum and resonance Raman excitation profiles has been described in Chapter 2. For the analysis presented here, two separate models of the absorption and RR excitation profiles were tested. In one, the parameters were adjusted to get as good as possible agreement between the experimental and simulated absorption spectra. In the second model, the parameters were adjusted to fit the experimental and simulated resonance Raman excitation profiles.

5.3 Results and Discussion

Simulated and experimental resonance Raman Spectra. The Z-1 experimental Resonance Raman spectra as a function of wavelength are shown in Figure 5.3 and the simulated spectra are shown in Figure 5.4. The original sample contained 92% Z isomer and 8% E isomer. To ensure that the RR spectra reflected only the Z isomer contribution, we also measured the spectrum of Z-1 in a single-pass flow configuration with single pass and bulk photoalteration parameters <10%. The identical spectra obtained in the two ways and shown in Figure 5.4 demonstrate that the RR spectra are reflective of only the Z isomer. Although the spectral

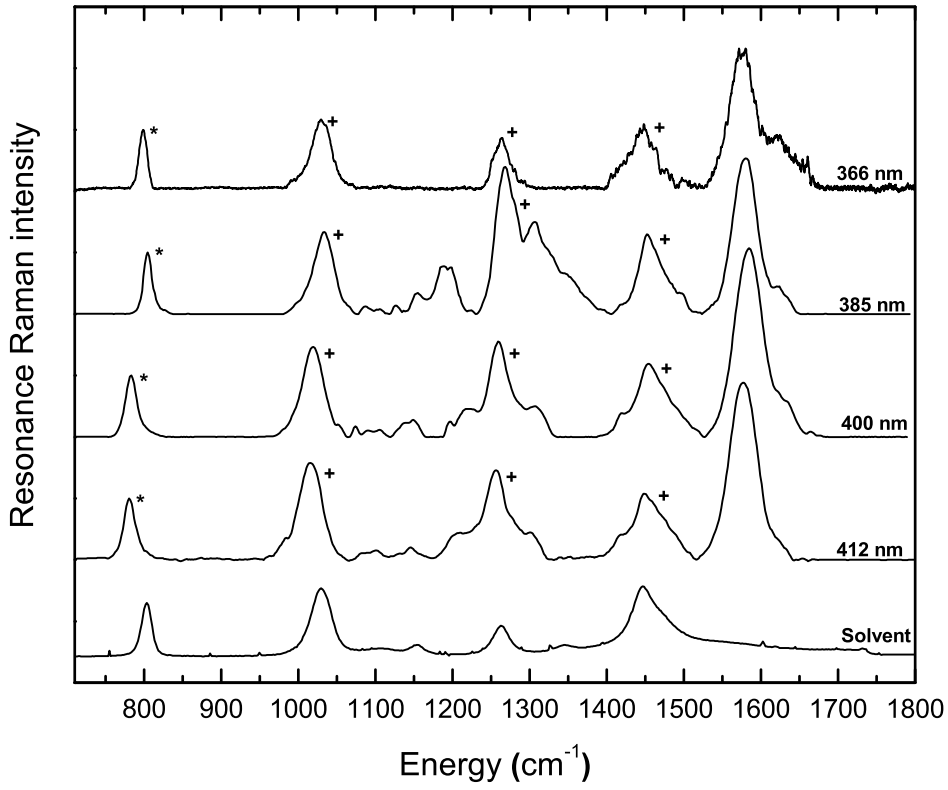

Figure 5.3: Resonance Raman spectra of 0.2 mM Z-1 in methanol/cyclohexane (69:31) excited at different wavelengths within the 385 nm absorption band. Peaks due to the internal standard (2.87 M cyclohexane) are denoted by asterisks (*) and due to methanol are marked with a "+".

quality is fair, several bands due to Z-1 are readily observable, allowing the initial excited-state structural dynamics to be determined. The relative intensities of the vibrational modes in the measured spectra do not change significantly with excitation wavelength, indicating that they are all enhanced by a single electronic transition.

The calculated RR spectra of Z-1 is qualitatively similar to the measured spectrum within the 800-1700 cm^{-1} spectral range. The highest-frequency mode at 1647 cm^{-1} in the experimental spectrum corresponds to the calculated 1653 cm^{-1} peak and can be safely assigned to the C=N stretching mode. While the intensity of this band seems to be somewhat exaggerated by CASSCF, it may well be hidden under the fairly broad band at 1589 cm^{-1} which is the most intense line in the spectrum and mainly involves inter-ring C=C stretching. The weak 1554 and 1499 cm^{-1} modes are superimposed on the left wing of the intense 1589 cm^{-1} band.

The band due to the CH_3 pyrroline deformation vibration, most likely reflecting a ring inversion motion, is of rather modest intensity and is predominantly localized at the 1444 cm^{-1} mode. This mode nicely matches the observed band both in terms of location and intensity. The analysis of the vibrational activity applied to 1300-1400 cm^{-1} region reveals two bands calculated at 1348 cm^{-1} and 1323 cm^{-1} with the latter one being more dominant. Both modes contain large contributions from CH_2 wagging vibrations of the indane and pyrroline rings and C-C stretches. Experimentally only 1308 cm^{-1} mode can be detected. Closer inspection at the calculated intensity pattern supports the experimental findings that the 1323 cm^{-1} peak dominates the 1200-1400 cm^{-1} region.

In the 1200-1300 cm^{-1} region the most intense peak calculated at 1279 cm^{-1} was ascribed to the phenol C-C stretchings and cyclopentane CH_2 twisting. Both 1270 cm^{-1}, and two less intense peaks at 1263 and 1257 cm^{-1} having contributions from cyclopentane twisting coupled with O-CH_3 stretching and a mixture of the pyrroline CH_2 deformations and CH phenol bending, respectively, are hard to detect in the experimental spectrum as they may be hidden under the very intense and broad band at 1260 cm^{-1} ascribed to solvent.

The calculated spectrum at ca. 1200 cm^{-1} reveals two low-intense fundamentals at 1224 and 1193 cm^{-1} that correspond to the vibrational modes involving phenol CH bendings, CH_3 deformations, and indane C-C stretchings. The simulated spectrum closely mirrors the observed band in this spectral region.

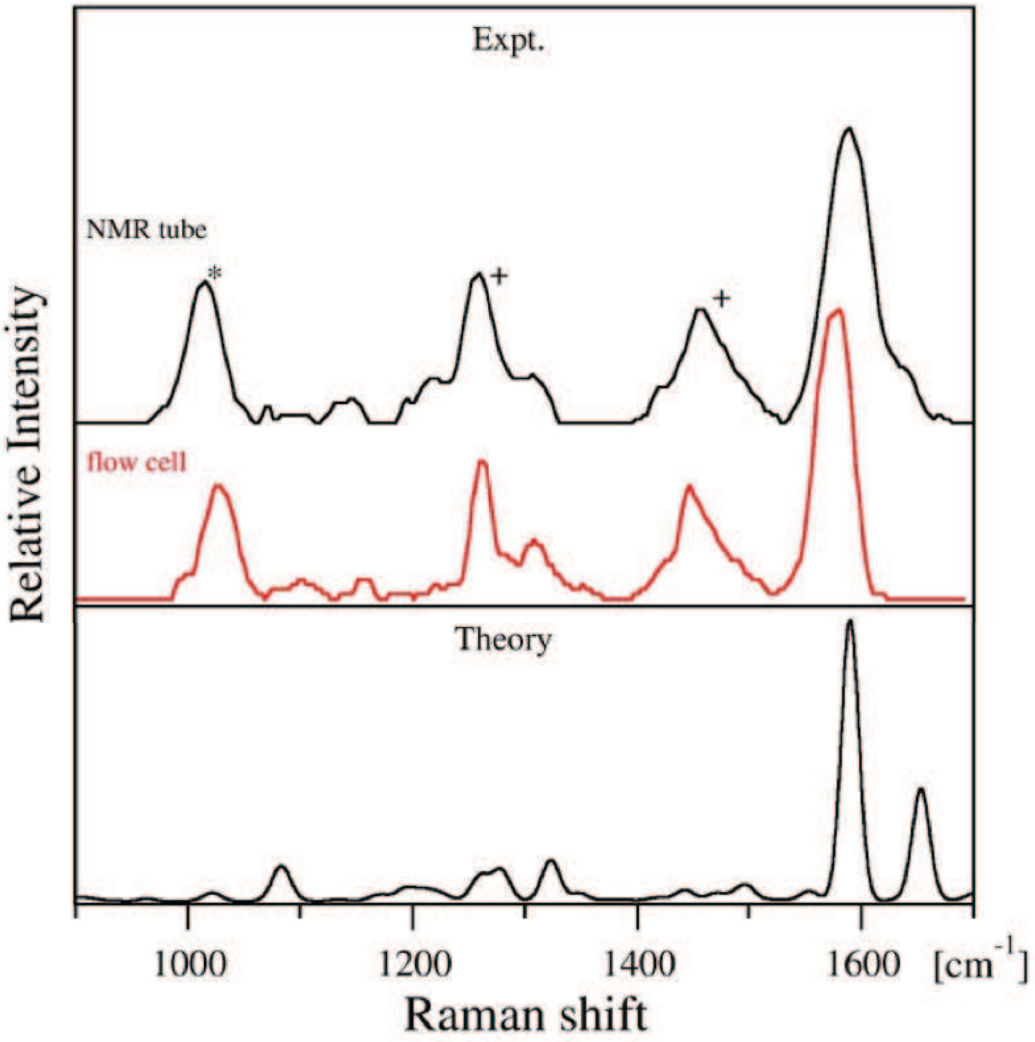

Figure 5.4: Experimental and simulated Resonance Raman spectra of Z-1.

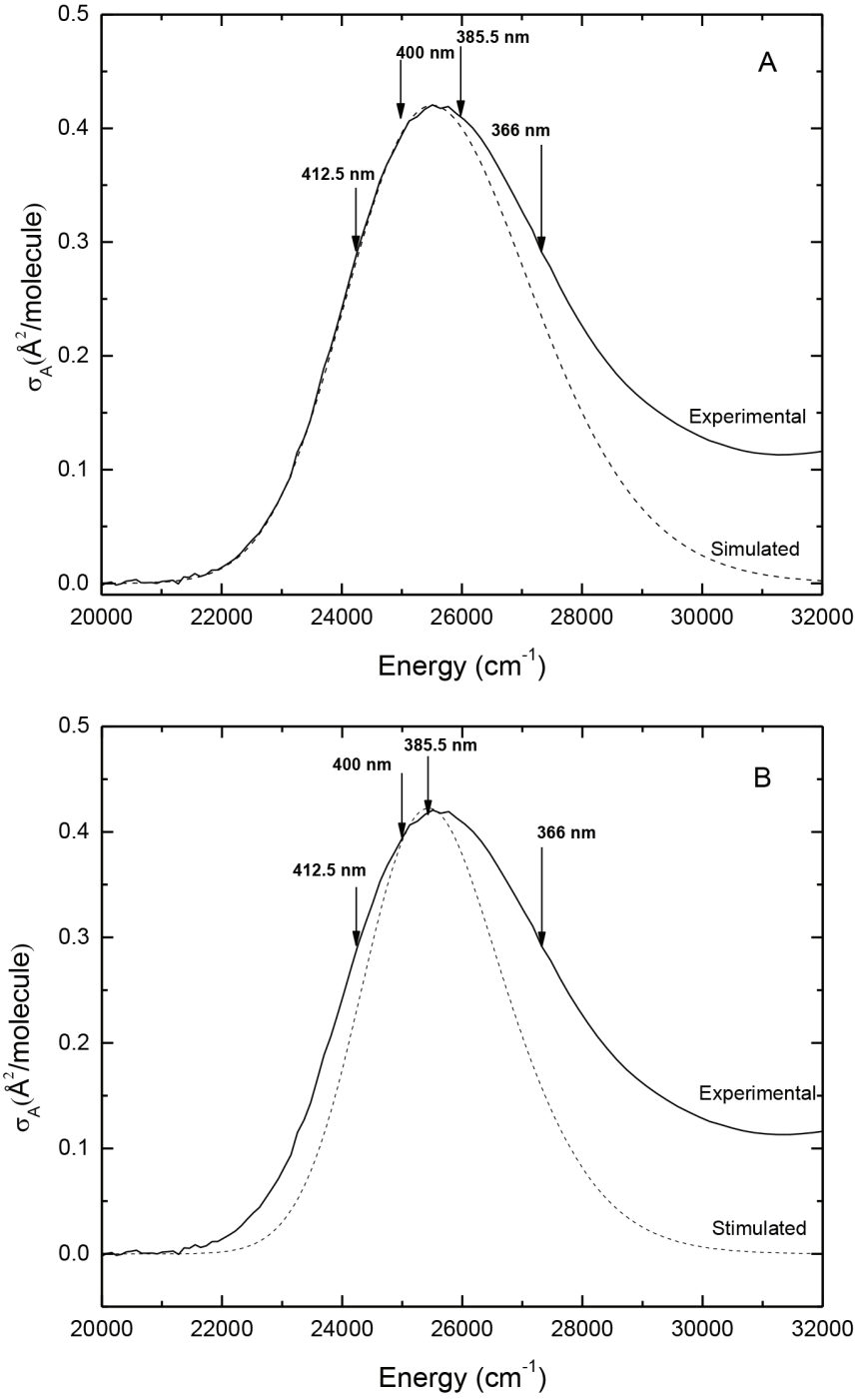

Figure 5.5: Calculated (dashed line) and experimental (solid line) absorption spectrum of Z-1, "A" represents model 1 (optimized for fitting the absorption spectrum) and B represents model 2 (optimized for fitting the resonance Raman excitation profile). The simulated absorption spectrum was generated using Equation 1.9 and the parameters from Table 5.1. The differences between the experimental and the simulated spectra at higher energies are due to other higher energy transitions which are not modeled in the equation.

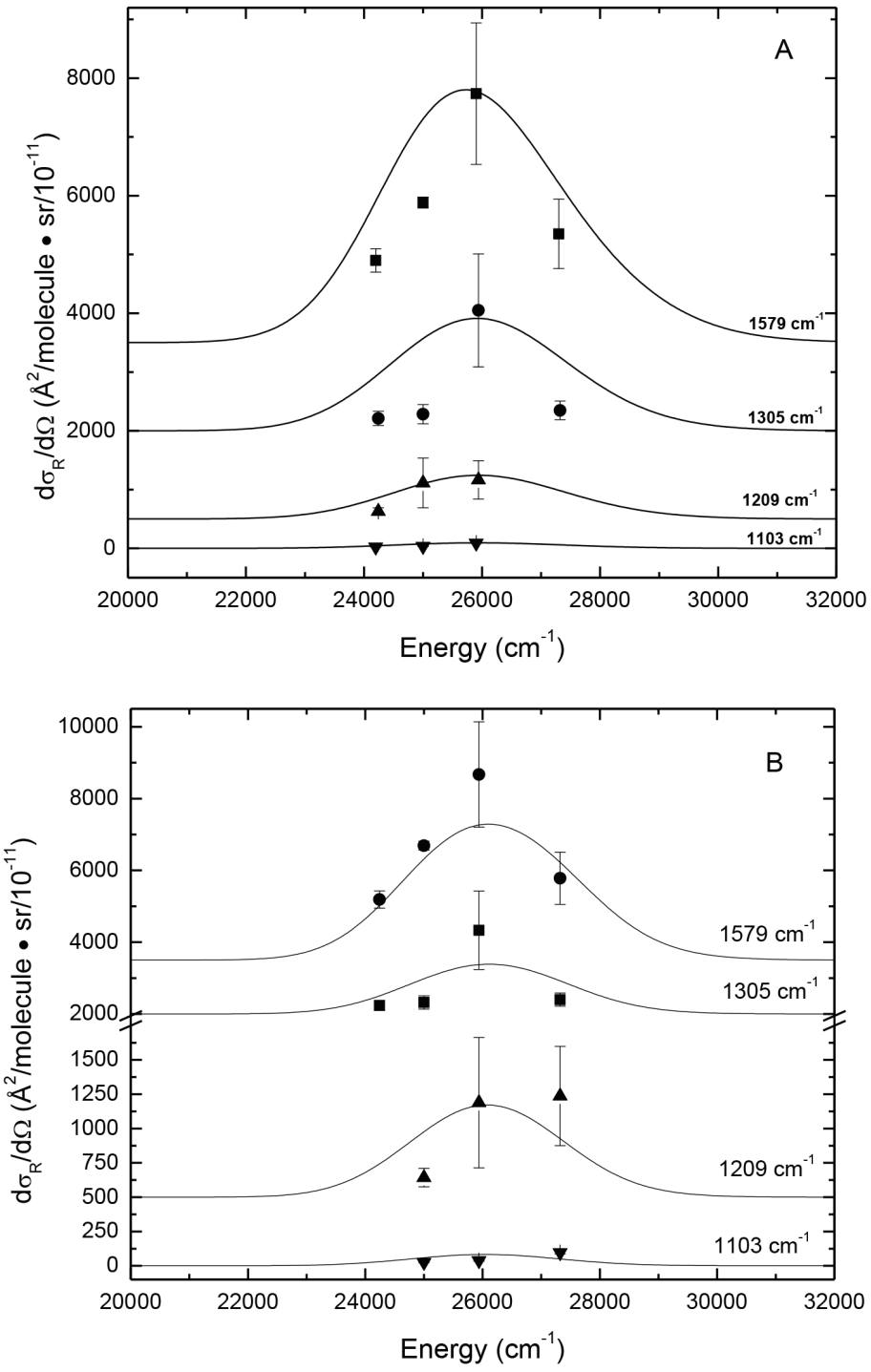

Figure 5.6: Experimental (points) and calculated resonance Raman excitation profiles (solid line) for Z-1. "A" represents model 1 (optimized for fitting the absorption spectrum) and "B" represents model 2 (optimized for fitting the resonance Raman excitation profile) The excitation profiles were calculated using Equation 1.11 and the parameters in Table 5.1.

The 1000-1100 cm^{-1} spectral region is characterized by pyrroline deformations. In the calculated RR spectra three modest bands are observed at 1087, 1081, and 1021 cm^{-1}. They reveal different intensity pattern. The strongest line at 1081 cm^{-1} is attributed to the phenol CH bending vibration, and pyrroline C-C stretching and CH_3 deformation. One of the calculated peaks at ca. 1080 cm^{-1} may correspond to the experimental band at 1074 cm^{-1}, although the experimental band is likely to be obscured by the solvent.

Initial excited state dynamics. The short time evolution of Z-1 along S_1 is shown in Figure 5.7. At the CASSCF level, the trajectory starts on the third root and immediately hops to the second root after 5 steps. As already pointed out above, the inclusion of the dynamic electron correlation at the CASPT2 level reveals that at a more accurate level of theory the excited state evolution occurs exclusively along the second root (S_1). Figure 5.7B shows the energy difference is largest in the first 10-15 fs. The energy is diminished by 40 kcal mol^{-1}. During this initial period there is no significant torsion along the exocyclic double bond C4=C1' and also there is no inversion of the indalydine or the pyrroline rings (see Figure 5.7 C). However, there is a remarkable coincident of the C=N/C=C bond stretching and the C-C bond contraction. Analogous deformations have been identified to be the first reaction coordinate of the 11-cis-retinal photoisomerization in rhodopsin. The largest bond stretching of 0.15 Å is observed for the N=C5 bond and the biggest contraction is 0.13 Å for the neighbor single bond C5-C4 (see Figure 5.7 D). The bond lengths and the energy gap oscillate with a comparable amplitude. After one full oscillation period the torsion around the exocyclic C4=C1' double bond reaches -30°, since this bond effectively become a single bond. In consequence of the increasing distortion the bond continues stretching in contrast to the endocyclic bonds.

The trajectory is inline with the assigned peaks of the RR spectrum (see above). It shows that the initial combination of bond-stretching/-contraction determines the initial geometrical deformation following the vertical excitation and moving the molecule out of the Frank-Condon region. It also shows that a torsional motion is setting in after the exocyclic double bond turns into a single bond. This sequence of geometrical changes is akin to the naturally designed switch 11-cis-retinal in rhodopsin.

Resonance Raman Excitation Profiles. Two models were attempted to

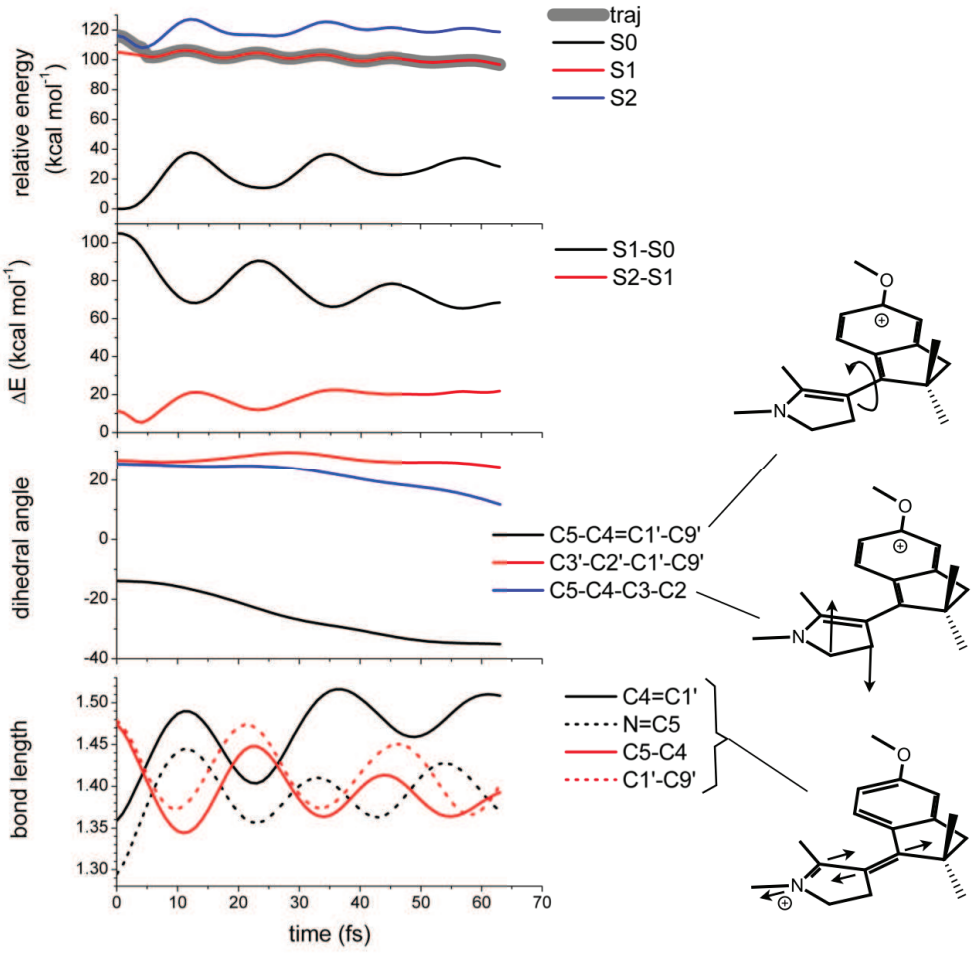

Figure 5.7: Initial excited-state trajectory of Z-1. (A) Energy evolution of the three calculated states S_0, S_1 and S_2. (B) Energy gap between S_0-S_1 and S_1-S_2. Evolution of the dihedral angle. (D) Single and double bond lengths.

Table 5.1: Mode assignments and excited-state slopes of Z-1.

Assignment	Theory	Expt.	β/ħ (cm^{-1})[b]	β/ħ (cm^{-1})[c]
C=N pyr stretch	1653	1647		
C=C inter stretch	1590	1589	1300	1000
C=C phe stretch	1554			
(O)-CH_3 phe def + C=C phe stretch	1499			
(N)-CH_3 pyr def	1444	1423		
CH_2 pent wag + CH_2 pyr wag	1348			
CH_2 pyr wag + C-C pyr stretch	1323	1308	640	440
CH_2 pent twist + C-C phe stretch	1279			
CH_2 pent twist + O-CH_3 stretch	1263	1260*		
CH_2 pyr twist + CH phe bend	1257			
CH_3 pent def + (N)-CH_3 pyr def + CH_2 pent wag + pyr def + C-C pent stretch	1224	1223		
CH phe bend +C-C phe stretch + CH_3 pent def + CH_2 pyr twist + N-(CH_3) pyr def	1193	1195	350	280
C-H phe bend + C-C pyr stretch + CH_3 pyr def	1087		110	90
CH phe bend + phe def + C-C pyr stretch + CH_3 pyr def	1081	1074		
C-N pyr stretch +C-C pyr stretch + C-CH_3 pyr stretch	1021	1016*		

Abbreviations are 'ind' indane ring; 'pyr' pyrroline ring; 'phe' phenol ring; 'pent' cyclopentane ring; 'inter' inter-ring; 'wag' wagging vibration; 'twist' twisting vibration; 'def' deformation; 'bend' bending vibration; and 'stretch' stretching vibration. Experimental frequencies are taken from the resonance Raman spectrum excited at 400 nm taken with sample in NMR tube. Experimental frequencies denoted by asterisks (*) refer to solvent peaks.

[a]This vibrational mode in Z isomer is of negligible intensity.

[b]These excited-state slopes are for model 1. Other fitting parameters are temperature (T) 298 K, Brownian oscillator line shape $\kappa = \Lambda/D = 0.1$, Gaussian homogeneous line width, $\Gamma_G = 250$ cm^{-1}, inhomogeneous line width, $\theta = 1200$ cm^{-1}, zero-zero energy, $E_0 = 24950$ cm^{-1}, and transition length, M = 0.953Å.

[c]These excited-state slopes are for model 2. Other fitting parameters are temperature (T) 298 K, Brownian oscillator line shape $\kappa = \Lambda/D = 0.1$, Gaussian homogeneous line width, $\Gamma_G = 200$ cm^{-1}, inhomogeneous line width, $\theta = 1100$ cm^{-1}, zero-zero energy, $E_0 = 25200$ cm^{-1}, and transition length, M = 0.870Å.

simulate the experimental absorption band and RR excitation profiles, one to best fit the absorption band (model 1) and one to best fit the RR excitation profiles (model 2). The results are shown in Table 5.1 and Figures 5.5 and 5.6.

Figures 5.5A and 5.6A show that model 1 does indeed fit the absorption spectrum better than model 2, particularly on the low energy (red) edge of the absorption

band. However, Figures 5.5B and 5.6B show that model 1 over-estimates the breadth of the experimental RR excitation profiles. Thus, model 2 was chosen as the better model. It is clear from Figure 5.6B, that model 2 does indeed simulate the RR excitation profiles better, yielding more accurate excited-state slopes.

Table 5.1 shows that the vast majority of initial excited-state structural dynamics occurs along the C-N and C-C bond stretching, resembling the inversion of the bond length alternation (BLA) coordinate observed for rhodopsin.[26] Using reorganization energies, $E = (\beta/\hbar)^2/2\omega$), we calculate that the C=C double bond stretch accounts for 75% of the initial excited-state structural dynamics, very similar to that obtained for the 11-cis retinal chromophore in rhodopsin. The displacement Δ, in Å, between the ground and excited-state potential minima along a particular internal coordinate can be found using the following equation.

$$\delta = 5.8065 \sum A_{ij} \overline{\omega}_j{}^{-\frac{1}{2}} \Delta_j \tag{5.3}$$

where A_{ij} is the normal mode coefficients, $\overline{\omega}_j$ is the mode wavenumber and Δ_j is the dimensionless displacement. If we consider only the 1579 cm^{-1} mode as a pure (A_{ij}=100%) C=C inter-ring stretching vibration with an excited-state slope of 1000 cm^{-1} ($\Delta_j = 0.625$), a change in the C=C bond length of 0.09 Å is obtained in the excited-state within the first 100 fs of evolution on the excited-state surface. This value compares favorably to transition-state double bond changes in other barrierless excited-state reactions, such as those of thymine[27,28] and 5-fluorouracil[29].

Broadening. Solvents may contribute significantly to the breadth of the absorption spectrum in the condensed phase through either inhomogeneous or homogeneous mechanisms. These two factors affect the observed absorption spectrum and RR excitation profiles differently. The inhomogeneous line width is due to ensemble "site" effects while the homogeneous line width represents contributions from excited-state population decay and pure dephasing. The relative contributions of these two broadening terms cannot be determined using the absorption spectrum alone as they both broaden the absorption spectrum. However, homogeneous broadening also damps the RR excitation profile. For rhodopsin[22] and Z-1 here, both the inhomogeneous and homogeneous line widths must be relatively large to reproduce the experimental absorption spectrum and RR excitation profiles.

Solvent-induced dephasing normally dominates homogeneous broadening in the condensed phase, although population decay may also contribute. In order to

accurately model the magnitude of the resonance Raman cross-sections for Z-1 and diffusiveness of the absorption spectrum, a Gaussian homogeneous line width of 200 cm^{-1} was required. The excited-state lifetime of rhodopsin has been measured by time-resolved absorption spectroscopy to be on the order of 200 fs[19]. A 200 cm^{-1} Gaussian linewidth yields a 1/e excited state lifetime of 25 fs. This is much shorter than the lifetime of 200 fs observed for rhodopsin[30]. Therefore, the amount of homogeneous broadening due to population decay is relatively small compared to solvent induced dephasing for rhodopsin.

Inhomogeneous broadening arises because there can be a number of different solvation structures in solution leading to a distribution of electronic transition energies. Inhomogeneous broadening is considered static on the time scale of the RR experiment. In order to accurately model the magnitude of the RR cross sections and diffusiveness of the absorption spectrum, a Gaussian inhomogeneous line width of 1100 cm^{-1} was required. This is slightly higher than the 800 cm^{-1} inhomogeneous linewidth needed for rhodopsin[26], indicating that the cyclohexane/methanol solvent for Z-1 is somewhat more polar and interacting than the opsin protein in which the 11-cis retinal chromophore is embedded.

5.4 Conclusions

The absorption and RR spectra and excitation profiles have been measured for Z-1, a conformationally-locked NAIP analogue of the 11-cis retinal chromophore of the dim-light visual pigment Rh. Both NAIPs and Rh have a polyeniminium cation as the chromophoric unit (a protonated and alkylated imine in Rh and NAIPs respectively). It is therefore expected that the nature of the spectroscopic state and initial dynamics will be similar in the two systems. Furthermore, the five member rings in the pyrrolinium and indanylidene units impose torsional constraints on all double-bonds except the exocyclic C=C double bond somehow mimicking the constraints imposed by the protein cavity during the torsional of the Rh chromophore. This is the process that results in the stereoselective isomerization of the central double bond exclusively. However, due to the replacement of the C-H bonds with C-C bonds in vinylic position at the isomerizing C=C bond, an HOOP-like mode is not likely to be observed in the RR spectra, and therefore is not expected to contribute to the early dynamics of the visual pigment is not detected in Z-1.

Above we have shown that the observed and simulated RR spectra and excitation

profiles yield qualitative and quantitative insight into the initial Z-1 excited-state structural dynamics that fully confirm the above expectations. In fact, it is confirmed that the RR activity, and therefore initial excited-state structural dynamics, occurs along the C=N and C=C double bond stretches mainly spanning the pyrrolinium unit and central double of the NAIP framework. These stretchings combine with C-C contraction in a bond length alternation (BLA) mode. We therefore conclude that initial, impulsive dynamics do not correlated with the late twisting (isomerization) motion about the reactive central double bond and, ultimately, it does not correlate with the vibrational coherence observed in the E-1 photoproduct. Such vibrational coherence must therefore reflect exclusively later dynamics imposed by the excited-state minimum path and conical intersection driving the isomerization motion.

The analysis of the computed excited-state trajectory provides information on the sequential activation of different modes during the early, <70 fs, excited-state evolution of Z-1. The above mention BLA stretching mode is activated at time zero. The second mode to activate is the reactive mode corresponding to the central C=C torsional deformation that starts to change 15 fs after photon absorption. Later on, on a 30 fs timescale, the activation of the out-of-plane (ring inversion) deformation of the pyrrolinium ring. In contrast, the heavier and stiffer (due to the presence of the condensed aromatic ring) five membered indanylidene ring remains instead substantially unchanged on the time scale of our simulation.

References

[1] G. Wald. The molecular basis of visual excitation. *Nature*, 219(5156):800–807, 1968.

[2] R. W. Schoenlein, L. A. Peteanu, R. A. Mathies, and C. V. Shank. The first step in vision: Femtosecond isomerization of rhodopsin. *Science*, 254(5030):412–415, 1991.

[3] H. Kandori, Y. Shichida, and T. Yoshizawa. Photoisomerization in rhodopsin. *Biochem.*, 66:1197–209, 2001.

[4] P. Kukura, D. W. McCamant, S. Yoon, D. B. Wandschneider, and R. A.

Mathies. Structural observation of the primary isomerization in vision with femtosecond-stimulated Raman. *Science*, 310(5750):1006–1009, 2005.

[5] A. Sinicropi, E Martin, M. Ryazantsev, J. Helbing, J. Briand, D. Sharma, J. Laonard, S. Haacke, A. Cannizzo, M. Chergui, V. Zanirato, S. Fusi, F. Santoro, R. Basosi, N. Ferra, and M. Olivucci. An artificial molecular switch that mimics the visual pigment and completes its photocycle in picoseconds. *Proc. Natl. Acad. Sci. USA*, 105(46):17642–17647, 2008.

[6] J. Briand, O. Bram, J. Rehault, J. Leonard, A. Cannizzo, M. Chergui, V. Zanirato, M. Olivucci, J. Helbing, and S. Haacke. Coherent ultrafast torsional motion and isomerization of a biomimetic dipolar photoswitch. *Phys. Chem. Chem. Phys.*, 12(13):3178–3187, 2010.

[7] J. Leonard, I. Schapiro, J. Briand, S. Fusi, R. Rossi Paccani, M. Olivucci, and S. Haacke. Mechanistic origin of the vibrational coherence accompanying the photoreaction of biomimetic molecular switches. *Chem. Eur. J*, 18(48):15296–15304, 2012.

[8] Q. Wang, R. W. Schoenlein, L. A. Peteanu, R. A. Mathies, and C. V. Shank. Vibrationally coherent photochemistry in the femtosecond primary event of vision. *Science*, 266(5184):422–424, 1994.

[9] F. Lumento, V. Zanirato, S. Fusi, E. Busi, L. Latterini, F. Elisei, A. Sinicropi, T. Andruniaw, N. Ferra, R. Basosi, and M. Olivucci. Quantum chemical modeling and preparation of a biomimetic photochemical switch. *Ang. Chem. Intl. Edn*, 46(3):414–420, 2007.

[10] R. Mathies, A. R. Oseroff, and L. Stryer. Rapid-flow resonance Raman spectroscopy of photolabile molecules: Rhodopsin and isorhodopsin. *Proc. Natl. Acad. Sci. USA*, 73(1):1–5, 1976.

[11] P. A. Kollman, R. Dixon, W. Cornell, T. Fox, C. Chipot, and A. Pohorille. The development/application of a 'minimalist' organic/biochemical molecular mechanic force field using a combination of ab initio calculations and experimental data. In A. Wilkinson, P. Weiner, and Wilfred F. van Gunsteren, editors, *Computer Simulation of Biomolecular Systems*, volume 3. Elsevier, Amsterdam, The Netherlands, 1997.

[12] D. A. Case, T. E. Cheatham, T. Darden, H. Gohlke, R. Luo, K. M. Merz, A. Onufriev, C. Simmerling, B. Wang, and R. J. Woods. The Amber biomolecular simulation programs. *J. Computl. Chem.*, 26(16):1668–1688, 2005.

[13] F. Melaccio, M. Olivucci, R. Lindh, and N. Ferra. Unique QM/MM potential energy surface exploration using microiterations. *Intl. J. Qtm. Chem.*, 111(13):3339–3346, 2011.

[14] N. Ferre and M. Olivucci. Probing the rhodopsin cavity with reduced retinal models at the CASPT2//CASSCF/AMBER level of theory. *J. Am. Chem. Soc.*, 125:6868–6869, 2003.

[15] F. Aquilante, L. De Vico, N. Ferre, G. Ghigo, P. Malmqvist, P. Neograd y, T. B. Pedersen, M. R. M. Pitonok, B. Roos, L. Serrano-Andras, M. V. V. Urban, and R. Lindh. MOLCAS 7: the next generation. *J. Computl. Chem.*, 31(1):224 – 247, 2010.

[16] M. J. Frisch, G. W. Trucks, H. B. Schlegel, G. E. Scuseria, M. A. Robb, J. R. Cheeseman, J. A. Montgomery, Jr., T. Vreven, K. N. Kudin, J. C. Burant, J. M. Millam, S. S. Iyengar, J. Tomasi, V. Barone, B. Mennucci, M. Cossi, G. Scalmani, N. Rega, G. A. Petersson, H. Nakatsuji, M. Hada, M. Ehara, K. Toyota, R. Fukuda, J. Hasegawa, M. Ishida, T. Nakajima, Y. Honda, O. Kitao, H. Nakai, M. Klene, X. Li, J. E. Knox, H. P. Hratchian, J. B. Cross, V. Bakken, C. Adamo, J. Jaramillo, R. Gomperts, R. E. Stratmann, O. Yazyev, A. J. Austin, R. Cammi, C. Pomelli, J. W. Ochterski, P. Y. Ayala, K. Morokuma, G. A. Voth, P. Salvador, J. J. Dannenberg, V. G. Zakrzewski, S. Dapprich, A. D. Daniels, M. C. Strain, O. Farkas, D. K. Malick, A. D. Rabuck, K. Raghavachari, J. B. Foresman, J. V. Ortiz, Q. Cui, A. G. Baboul, S. Clifford, J. Cioslowski, B. B. Stefanov, G. Liu, A. Liashenko, P. Piskorz, I. Komaromi, R. L. Martin, D. J. Fox, T. Keith, M. A. Al-Laham, C. Y. Peng, A. Nanayakkara, M. Challacombe, P. M. W. Gill, B. Johnson, W. Chen, M. W. Wong, C. Gonzalez, and J. A. Pople. Gaussian 03, Revision C.02. Gaussian, Inc., Wallingford, CT, 2004.

[17] J. W. Ponder and F. M. Richards. An efficient newton-like method for molecular mechanics energy minimization of large molecules. *J. Computl. Chem.*, 8(7):1016–1024, 1987.

[18] W. C. Swope, H. C. Andersen, P. H. Berens, and K. R. Wilson. A computer simulation method for the calculation of equilibrium constants for the formation of physical clusters of molecules: Application to small water clusters. *J. Chem. Phys.*, 76:637–649, 1982.

[19] A. ten Wolde, H. J. C. Jacobs, F. W. Langkilde, K. Bajdor, R. Wilbrandt, F. Negri, F. Zerbetto, and G. Orlandi. Triplet state resonance Raman and absorption spectroscopy of a configurationally locked (Z)-hexatriene: 1,2-divinylcyclopentene. *J. Phys. Chem.*, 98(38):9437–9445, 1994.

[20] C. A. Andreas. On the theory of Raman intensities. *J. Chem. Phys.*, 34(5):1476–1484, 1961.

[21] T Petrenko and F. Neese. Analysis and prediction of absorption band shapes, fluorescence band shapes, resonance Raman intensities, and excitation profiles using the time-dependent theory of electronic spectroscopy. *J. Chem. Phys.*, 127(16):164319,1–15, 2007.

[22] F. Negri and G. Orlandi. Electronic and vibronic spectra of molecular systems: Models and simulations based on quantum chemically computed molecular parameters. In M. Olivucci, editor, *Computational Photochemistry*, volume 16 of *Theoretical and Computational Chemistry*, chapter 4, pages 129–169. Elsevier, 2005.

[23] M. O. Trulson and R. A. Mathies. Raman cross-section measurements in the visible and ultraviolet using an integrating cavity: Application to benzene, cyclohexane, and cacodylate. *J. Chem. Phys.*, 84(4):2068–2074, 1986.

[24] E. Fraga, M. A. Webb, and G. R. Loppnow. Charge-transfer dynamics in plastocyanin, a blue copper protein, from resonance Raman intensities. *J. Phys. Chem.*, 100(8):3278–3287, 1996.

[25] S-Y. Lee and E. J. Heller. Time-dependent theory of Raman scattering. *J. Chem. Phys.*, 71(12):4777–4788, 1979.

[26] G. R. Loppnow and R. A. Mathies. Excited-state structure and isomerization dynamics of the retinal chromophore in rhodopsin from resonance Raman intensities. *Biophys. J.*, 54(1):35–43, 1988.

[27] B. Durbeej and L. A. Eriksson. Reaction mechanism of thymine dimer formation in DNA induced by UV light. *J. Photochem. Photobiol. A*, 152:95–101, 2002.

[28] S. Yarasi, P. Brost, and G. R. Loppnow. Initial excited-state structural dynamics of thymine are coincident with the expected photochemical dynamics. *J. Phys. Chem. A*, 111(24):5130–5135, 2007.

[29] B. E. Billinghurst, R. Yeung, and G. R. Loppnow. Excited-state structural dynamics of 5-fluorouracil. *J. Phys. Chem. A*, 110(19):6185–6191, 2006.

[30] M. Yan, D. Manor, G. Weng, H. Chao, L. Rothberg, T. M. Jedju, R. R. Alfano, and R. H. Callender. Ultrafast spectroscopy of the visual pigment rhodopsin. *Proc. Natl. Acad. Sci. USA*, 88(21):9809–9812, 1991.

Chapter 6

Conclusion and Future Works

6.1 General conclusions

The work presented in this thesis examines the two extreme ends of the photochemical reaction time scale for DNA components. In an effort to understand the very first excited-state process happening after photon absorption in DNA components and their derivatives, we have probed the initial excited-state structural dynamics of nucleic acid components and their derivatives using resonance Raman spectroscopy. To probe the other extreme, the consequences of these photochemical reactions of nucleic acid components are then tested on a microarray platform.

Resonance Raman spectroscopy is a powerful tool in probing the initial excited-state structural dynamics of molecules following photon absorption. Chapters 2 and 3 demonstrate the capability of resonance Raman spectroscopy to study the initial excited-state structural dynamics of DNA components. In Chapter 2, one of the uracil derivatives is studied to understand the effect of methyl substitution at photochemical reaction centre and differentiate the factors causing the difference in photochemistry between thymine and uracil. Different homopolymers of DNA were studied in Chapter 3 and this study shows that the initial excited-state structural dynamics are similar and less in magnitude for the homopolymers compared to nucleobases or nucleosides. The kinetics of UV-induced photochemical damage of oligonucleotides on a microarray platform is studied in Chapter 4. This Chapter also examines the factors responsible for determining the damage kinetics, particularly the sequence dependence on the damage kinetics. Chapter 5 again uses resonance Raman spectroscopy to probe the initial excited-state structural dynamics of a rhodopsin analogue switch to understand the initial forces in the excited state driving the isomerization process.

6.1.1 Chapter 2

The study of initial excited-state structural dynamics of 5,6-dimethyluracil is presented in Chapter 2. This chapter demonstrates the capability of resonance Raman spectroscopy as a tool to study the initial excited-state structural dynamics of molecules. Nucleic acids absorb ultraviolet light at 260 nm and undergo photochemical reactions resulting in unwanted structural changes. The first step in a photochemical reaction is the absorption of the photon by the reacting molecules. The main chromophore responsible for this UV absorption is the nucleobases. Thymine and uracil are two structurally similar nucleobases, though nature has a clear distinction between these two compound and their uses in biology. The photochemistry of these two nucleobases is very different, despite their structural similarity. Resonance Raman spectroscopy was successfully used to study the difference in the initial excited-state structural dynamics. The difference in the observed photochemistry is attributed to the presence of a methyl group at the C5 position of the thymine molecule. Further studies with different substitutions at C5 and C6 elucidate the factors responsible for the difference in the photochemistry. Our results shows that, the mass at the each end of the C5=C6 bond is a significant determinant for the difference in photochemistry. To confirm the effect of mass on C5 and C6, we have studied the initial excited-state structural dynamics of 5,6-dimethyluracil using resonance Raman spectroscopy. This work shows that the resonance Raman spectra of 5,6-dimethyluracil is intermediate between that of thymine (5-methyluracil) and 6-methyluracil. The observed excited state slopes are lower than that of any other uracil derivatives studied.

The initial excited-state structural dynamics are similar to thymine (5-MU) and 6-methyluracil (6-MU) rather than uracil which has equal masses at the C5 and C6 positions in terms of the distribution of excited-state slopes between different photochemically active modes. Comparison between the potential energy distributions for different modes in different uracil derivatives shows that there is a redistribution of the potential energy induced by the substitution at C5 or C6, or both. This study shows that it is the presence of one or more methyl groups, not their position, that determine the initial excited-state dynamics of uracil derivatives. It is evident from this work that the presence of a methyl group at both the C5 and C6 positions also determines the partitioning of the initial excited-state structural

dynamics between the CH bending and the C5=C6 stretching modes. All these results suggest that the influence of the methyl group at the C5 and C6 position of uracil is a key factor in the nature and magnitude of the initial excited-state structural dynamics between different uracil derivatives. This study has helped confirm that the difference in the photochemistry of uracil and thymine is due to the methyl group at C5. We now have a model in which the presence of one or more methyl groups, changes the partitioning of potential energy distribution between different modes, explaining the difference in photochemistry. So the introduction of a methyl group can be effectively used in redefining the initial excited-state structural dynamics or deciding th photochemistry of different molecules.

6.1.2 Chapter 3

Understanding DNA photochemistry is important in determining the molecular mechanism of DNA damage and its consequences. Although the initial excited-state structural dynamics of nucleobases and their derivatives are important in understanding the photochemistry of DNA, extending this understanding to the oligonucleotides will bring us closer to understanding DNA photochemistry. We have performed the first initial excited-state structural dynamics determinations of different homopolymers of DNA nucleotides in Chapter 3.

Resonance Raman spectroscopy was used to probe the initial excited-state dynamics of these homopentamers. The resonance Raman spectra of these homopolymers resemble those of the corresponding nucleobases. The experimental results show that the initial excited-state structural dynamics of homopolymers are similar, but smaller than those of the nucleotides or nucleobases. The decrease in the initial excited-state geometry changes in homopolymers compared to the corresponding nucleobases are attributed to the increase in the size of the molecular systems,the presence large number of low intensity vibrational modes and the geometry change restrictions imposed on the excited-state potential energy surfaces by the additional steric constraints of the polymeric homopolymer. So this chapter opens up a whole new field of molecular systems to be explored in detail, investigating the origin of the differences between the initial excited-state slopes of the nucleobases and the nucleic acids.

Our results show that the initial excited-state slopes are lower, leading to slower excited-state dynamics, consistent with the longer excited-state lifetimes of nucleic

acids compared to the nucleobases[1]. This can give rise to two different situations: the quantum yields of the photoproducts will be smaller due to the lower initial driving force, or the photoproduct quantum yields will be higher due to the increased excited-state lifetime. But which of these will happen, will depend upon the factors affecting the excited-state electronic dynamics like electronic state crossing during the later stage of the reaction. So a better understanding of the effect of each factors on the initial excited-state structural dynamics is also necessary.

6.1.3 Chapter 4

The attempt to understand the relationship between the initial excited-state structural dynamics and the photochemistry in DNA will not be complete until we study the effect of UV light on nucleic acids and quantify the amount of damage. In an attempt to explore the effect of UV light on different sequences of nucleic acids and their damage kinetics simultaneously, we have studied the UV damage of different miRNA sequences on a microarray platform and tried to correlate the damage kinetics to the difference in sequences. Thirteen different sequences of miRNA were studied and the damage kinetics for different miRNA sequences were obtained. Different miRNA sequences had different damage kinetics upon UV irradiation. The kinetics show some correlation with the sequences of different miRNA, but the large experimental error in the time constants do not permit a thorough correlation of the sequences with the damage kinetics. However, a general platform for studying UV-induced nucleic acid is designed and tested with different sequences of miRNA. With further refinements and advancement in the microarrays, this technique can be used to study DNA damage quantitatively in a large number of sequences.

With the current understanding of the role of the miRNAs in controlling the gene expressions, the study of miRNA damage itself is very important. A good understanding of the UV stability of different miRNAs may provide us with an insight about why some miRNAs are down-regulate or up-regulate during cancers and other diseases. Also, for the bigger picture, miRNA damage studies will provide valuable input in understanding, whether the change in miRNA expression is a cause or consequence of cancer.

6.1.4 Chapter 5

In this chapter, the initial excited-state structural dynamics of an N-alkylindanylidene-pyrroline (NAIP) switch is studied with the help of visible resonance Raman spectroscopy. This chapter demonstrate the ability of resonance Raman spectroscopy to probe the initial excited-state structural dynamics of photo-labile compounds and the usefulness of coupling computational calculations with the experimental results. This study shows that the initial excited-state structural dynamics of NAIP lie along the C=C stretch, similar to those in the 11-cis retinal chromophore of rhodopsin. The computed excited-state trajectory show that the bond length alternation (BLA) modes are activated along with the electronic excitation and provide good insight about the sequential activation of different modes during the first 70 fs of the process. The hydrogen-out-of plane (HOOP) mode contribution is not observed in NAIP, because of the replacement of C-H bonds with the C-C bonds. This study has shown how to channel the initial excited-state dynamics towards the desired modes by making necessary structural changes in the molecules. This will have implications in designing molecular switches and other molecular devices.

6.2 Future work

The work presented in this thesis examines the initial excited-state structural dynamics of DNA oligonucleotides and rhodopsin using resonance Raman spectroscopy and uses a microarray platform to understand the kinetics of UV-induced nucleic acid damage and their sequence dependence in multiple sequences of RNA simultaneously. The future work suggested below is based on the conclusions for each chapter and for better overall understanding of the systems studied.

6.2.1 Initial excited-state structural dynamics of 5,6-DMU and photochemistry

The work presented in Chapter 2, along with studies on the initial excited-state structural dynamics of other uracil derivatives, show that the masses at C5 and C6 determine the partitioning between the CH bending and C5=C6 stretching modes. Therefore, it will be interesting to see the initial excited-state structural dynamics of 5, 6-dideuterouracil, which will be an intermediate of uracil and 5,6-DMU in terms of masses at C5 and C6 positions. This study will help us better understand how the position and the mass at C5 and C6 determine the partitioning of initial

excited-state structural dynamics between the CH bending and C5=C6 stretching modes. Also, it is worth examining the effect environment in the initial excited-state structural dynamics and difference harmonic parameters by doing similar studies in different solvents. Comparing the initial excited-state structural dynamics of different thymine and uracil derivatives[2–7] will provide a better insight into the factors affecting the difference in initial excited-state structural dynamics of uracil derivatives and now we can incorporate this knowledge in better designing molecules with desired photochemistry.

Initial excited-state structural dynamics probe the geometry changes happening 10-30 fs after the photon absorption. The work described in Chapter 2 show that the initial excited-state structural dynamics of the 5,6-DMU is more similar to thymine[3]. But how the potential energy surface for different uracil derivatives evolve during the later stage of the photochemical reaction is unknown. So it is important to study the photochemistry of these derivatives and see that they follow the photochemistry expected from initial excited-state structural dynamics studies. These experiments can be done in solution phase as well as in frozen solutions, by irradiating the solution with UV light and analyzing the photoproduct and finding their photochemical quantum yields. This will help us correlate the initial excited-state structural dynamics and the observed photochemistry[8].

On a different note, it will be interesting to see how the potential energy surface changes with time and how the photoproducts are formed following photon absorption. This study requires time-resolved experiments to probe the excited-state electronic dynamics of the molecules[1]. Femtosecond time resolution is necessary, as the observed photochemistry of natural nucleobases happens in that time regime. A particularly insightful experiment would be femtosecond time-resolved resonance Raman spectroscopy[9] of various nucleobases and their derivatives, taking the resonance Raman spectra of the compound at different times after the excitation pulse. The change in spectral features will provide valuable insight into the molecular dynamics. Putting all this together will improve our understanding of the molecular dynamics during photochemical reactions of nucleic acids.

6.2.2 Initial excited-state structural dynamics of oligonucleotides and photochemistry

One of the main challenges in studying the initial excited-state structural dynamics of homopentamers in Chapter 3 was the lack of photochemistry information for homopolymers. So doing the photochemistry and electronic excited-state dynamics of homopolymers are important as suggested in the previous section.

In order to correlate the initial excited-state structural dynamics of DNA and the known DNA photochemistry, it is advisable to do the initial excited-state structural dynamics studies with oligonucleotides with different nucleotides and also double stranded oligonucleotides to see the effect of neighboring bases, hydrogen bonding and base stacking. This will bring us one step closer in connecting the initial excited-state structural dynamics to the consequent DNA photochemistry via the excited-state dynamics in between. This will help us establish the sequence dependence of DNA photochemistry and will provide an idea about the hot spots for DNA damage. The initial excited-state structural dynamics of mixed oligonucleotides will be extremely challenging, due to the fact that all the nucleobases will be resonantly enhanced simultaneously and overlapping peaks in different nucleotides will be difficult to resolve. Base analogues, could be incorporated into the DNA strand to selectively excite specific nucleobases or the nucleobase analogues. In this way we could study the effect of neighboring groups on initial excited-state structural dynamics. Similar approaches can be used in time-resolved experiments as well. Locking the nucleobases at certain orientations in the solid phase and studying the importance of base stacking and its importance in excited-state dynamics is also possible. X-ray diffraction techniques[10,11] can be used to understand the orientation of nucelobases in the solid phase or solution phase[12].

6.2.3 Kinetics of nucleic acid damage

The miRNA kinetics data presented in Chapter 4 have the limitation of large errors, making the interpretation of the observed kinetics and any comparison difficult. So a significant amount of effort should be directed to improve the quality of the data and making it more meaningful. One of the main factors causing the large standard deviation in the fluorescence intensity of different spots of the same miRNA sequence at the same irradiation time is the difference in the amount of solution put onto the slide and the slide chemistry. The use of internal standard to account

for the difference in spots size does not work well, because of possible interaction of the internal standard with the target sequence. So an internal standard that does not interact with the target sequence is required. The use of quantum dots as internal standards in the microarray is an alternative[13–16], though optimizing the concentration and understanding the binding chemistry is another hurdle. Changing the slide chemistry or knowing the number of binding sites on the slides will also improve the understanding of the damage kinetics.

Alternatively, solution phase studies can be done to understand the kinetics of damage. For solution phase studies, molecular beacons, smart probes[17,18] or other alternative probes need to be used. This will be easier for miRNAs as they are single stranded. Fluorescence[19,20] or absorption spectroscopy[21] can be used to probe the kinetics of damage depending upon the choice of probes.

Use of hybridization techniques to study the kinetics of UV-induced damage has different limitations. The stability of the target-probe hybrid may be sensitive to the position of the damage site. Also, different types of damage affect the stability of the target-probe hybrid differently. So a technique that can identify and is equally sensitive to all kind of damages is necessary.

6.2.4 Techniques to detect nucleic acid damage

Another important aspect of nucleic acid damage detection is the sensitivity and selectivity of different probes used for nucleic acid damage detection. All probes are not equally sensitive to different types and positions of damages on nucleic acid. So a universal method of detecting any kind of damage at any position of the nucleic acid sequence is necessary. All types of nucleic acid damages will induce some change in the molecular structure of the nucleic acid and can be detected by different spectroscopic techniques like nuclear magnetic resonance (NMR) or resonance Raman spectroscopy. Resonance Raman spectroscopy has been used to detect 8-oxodeoxyguanosine[22,23] and a similar approach can be used for different types of damages. So, creating a library of vibrational markers for different types of damage by examining all possible damage products of DNA can be used as a benchmark of the qualitative analysis. Most of the damaged products absorb more or less at the same wavelength as the nucleobases and that will be resonantly enhanced. Also, knowing the absorption spectra of the different damaged product will help us selectively enhance the excitation of the damage product if the absorption

spectra is different from that of the DNA and get the resonance Raman spectra for the damaged product. The important challenge in this approach will be the low concentration of the damaged oligonucleotides compared to the undamaged oligonucleotides. We may have to increase the concentration of the damaged oligonucleotides by isolating the damaged oligonucleotides.

Another approach will be to selectively tag the damaged products with different molecular fluorescent probes. Having different tags for different types of damaged nucleotides will help us identifying and quantifying damaged nucleotides[24,25].

References

[1] C. T. Middleton, K. de La Harpe, C. Su, Y. K. Law, C. E. Crespo-Hernandez, and B. Kohler. DNA excited-state dynamics: From single bases to the double helix. *Ann. Rev. Phys. Chem.*, 60(1):217–239, 2009.

[2] B. E. Billinghurst, R. Yeung, and G. R. Loppnow. Excited-state structural dynamics of 5-fluorouracil. *J. Phys. Chem. A*, 110(19):6185–6191, 2006.

[3] S. Yarasi, P. Brost, and G. R. Loppnow. Initial excited-state structural dynamics of thymine are coincident with the expected photochemical dynamics. *J. Phys. Chem. A*, 111(24):5130–5135, 2007.

[4] S Yarasi, B. E. Billinghurst, and G. R. Loppnow. Vibrational properties of thymine, uracil and their isotopomers. *J. Raman Spectrosc.*, 38(9):1117–1126, 2007.

[5] S. Yarasi, S. Ng, and G. R. Loppnow. Initial excited-state structural dynamics of uracil from resonance Raman spectroscopy are different from those of thymine (5-methyluracil). *J. Phys. Chem. B*, 113(43):14336–14342, 2009.

[6] S. S. Ng, F. Teimoory, and G. R. Loppnow. Mass-tuned initial excited-state structural dynamics of DNA nucleobases from UV resonance Raman spectroscopy: 5-deuterouracil. *J. Phys. Chem. Lett.*, 2(18):2362–2365, 2011.

[7] B. E. Billinghurst, S. A. Oladepo, and G. R. Loppnow. Initial excited-state structural dynamics of thymine derivatives. *J. Phys. Chem. B*, 116(35):10496–10503, 2012.

[8] B. P. Ruzsicska and D. G. E. Lemaire. *Organic Photochemistry and Photobiology*. CRC Handbook Series. CRC Press, 1995.

[9] P. Kukura, D. W. McCamant, and R. A. Mathies. Femtosecond stimulated Raman spectroscopy. *Ann. Rev. Phys. Chem.*, 58(1):461–488, 2007.

[10] M. J. Packer and C. A. Hunter. Sequence-dependent DNA structure: The role of the sugar-phosphate backbone. *J. Mol. Biol.*, 280(3):407 – 420, 1998.

[11] M. J. Packer, M. P. Dauncey, and C. A. Hunter. Sequence-dependent DNA structure: tetranucleotide conformational maps. *J. Mol. Biol.*, 295(1):85 – 103, 2000.

[12] X. Zuo, G. Cui, K. M. Merz Jr, L. Zhang, F. D. Lewis, and D. M. Tiede. X-ray diffraction fingerprinting of DNA structure in solution for quantitative evaluation of molecular dynamics simulation. *Proc. Natl. Acad. Sci. U. S. A.*, 103(10):3534–3539, 2006.

[13] G. Karlin-Neumann, M. Sedova, M. Falkowski, Z. Wang, S. Lin, and M. Jain. Application of quantum dots to multicolor microarray experiments. In M. P. Bruchez and C. Z. Hotz, editors, *Quantum Dots*, volume 374 of *Methods in Molecular Biology*, pages 239–251. Humana Press, 2007.

[14] A. Zajac, D. Song, and T. Qian, W. andZhukov. Protein microarrays and quantum dot probes for early cancer detection. *Colloids Sur. B Biointerfaces*, 58(2):309–314, 2007.

[15] X. Sun, B. Liu, and Y. Xu. Dual-emission quantum dots nanocomposites bearing an internal standard and visual detection for Hg^{2+}. *Analyst*, $137(5) : 1125 - -1129, 2012$.

[16] R. Q. Liang, W. Li, Y. Li, C. Tan, J. X. Li, Y. X. Jin, and K. C. Ruan. An oligonucleotide microarray for microRNA expression analysis based on labeling RNA with quantum dot and nanogold probe. *Nucleic Acids Res.*, 33(2):e17, 2005.

[17] S. A. Oladepo and G. R. Loppnow. Self-quenching smart probes as a platform for the detection of sequence-specific UV-induced DNA photodamage. *Anal. Bioanal. Chem.*, 397(7):2949–2957, 2010.

[18] S. G. Nair and G. R. Loppnow. Multiplexed, UVC-induced, sequence-dependent DNA damage detection. *Photochem. Photobiol.*, 89:884–90, 2013.

[19] Z. J. Shire and G. R. Loppnow. Molecular beacon probes of oligonucleotides photodamaged by psoralen. *Photochem. Photobiol.*, 88(3):645–650, 2012.

[20] Z. J. Shire and G. R. Loppnow. Molecular beacon probes for the detection of cisplatin-induced DNA damage. *Anal. Bioanal. Chem.*, 403(1):179–184, 2012.

[21] A. F. El-Yazbi and G. R. Loppnow. 2-aminopurine hairpin probes for the detection of ultraviolet-induced DNA damage. *Anal. Chim. Acta*, 726(0):44 – 49, 2012.

[22] L. M. Kundu and G. R. Loppnow. Direct detection of 8-oxo-deoxyguanosine using UV resonance Raman spectroscopy. *Photochem. Photobiol.*, 83(3):600–602, 2007.

[23] N. Jayanth, S. Ramachandran, and M. Puranik. Solution structure of the DNA damage lesion 8-oxoguanosine from ultraviolet resonance Raman spectroscopy. *J. Phys. Chem. A*, 113(8):1459–1471, 2009.

[24] W Liao, M.A. McNutt, and W. G. Zhu. The comet assay: A sensitive method for detecting DNA damage in individual cells. *Methods*, 48(1):46 – 53, 2009.

[25] E. I. Cortes-Gutierrez, M. I. Davila-Rodraŋguez, J. L. Fernandez, C. Lapez-Fernandez, A. Goselbez, and J. Goselbvez. New application of the comet assay: Chromosome comet assay. *J. Histochem. Cytochem.*, 59(7):655–660, 2011.

Appendix A

Resonance Raman Spectra and Twostate (Model-2) for Homopentamers

The Resonance Raman spectra of different homopentamers at different excitation wavelengths and the alternative model (model 2) used to reproduce the experimental absorption and resonance Raman excitation profile for the homopentamers are given below.

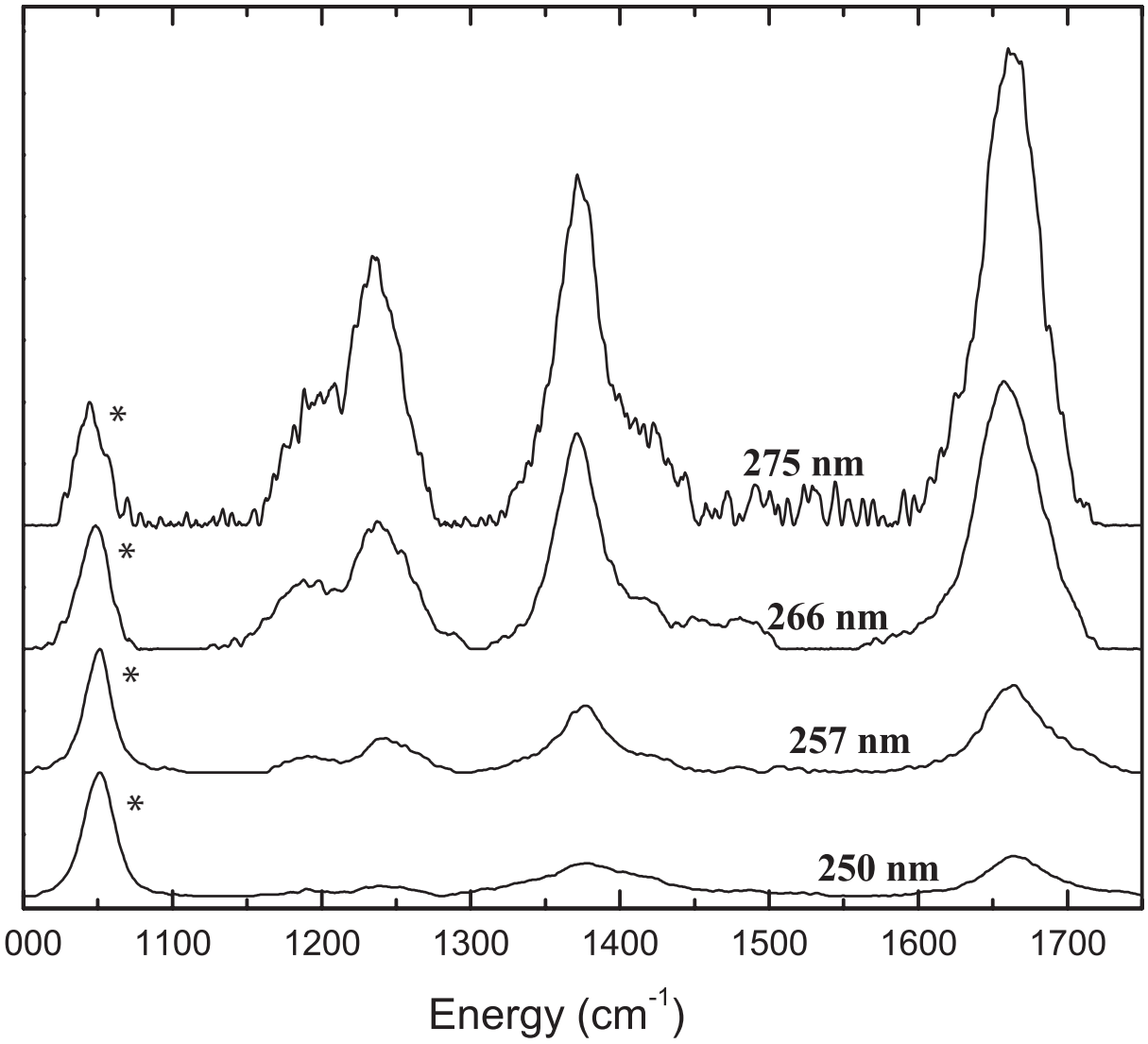

Figure A.1: Resonance Raman spectra of 0.3 mM $(dTp)_5$ excited at different wavelengths. The internal standard peak (0.1M nitrate) is denoted by asterisk (*).

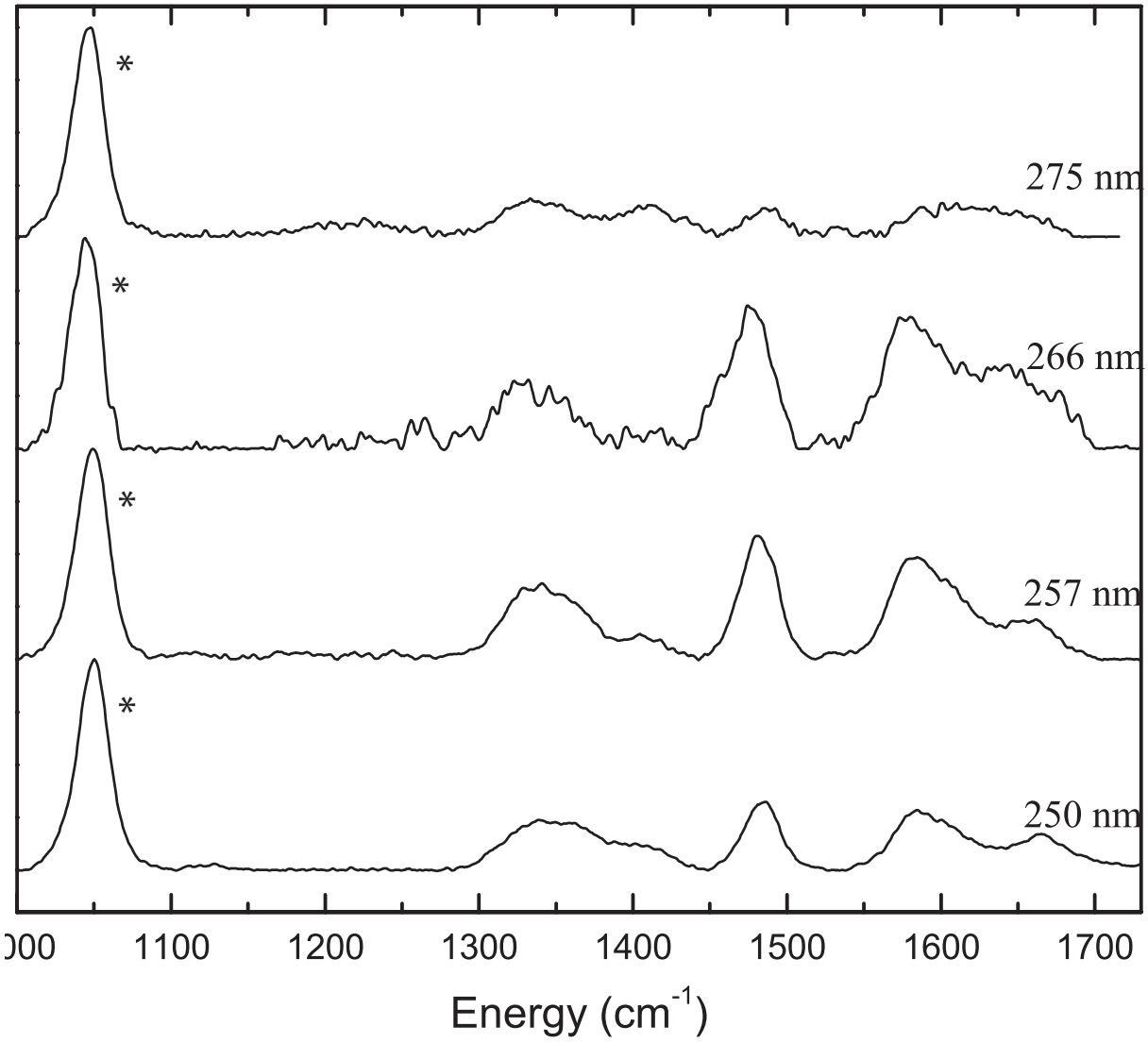

Figure A.2: Resonance Raman spectra of 0.3 mM $(dGp)_5$ excited at different wavelengths. The internal standard peak (0.1M nitrate) is denoted by asterisk (*).

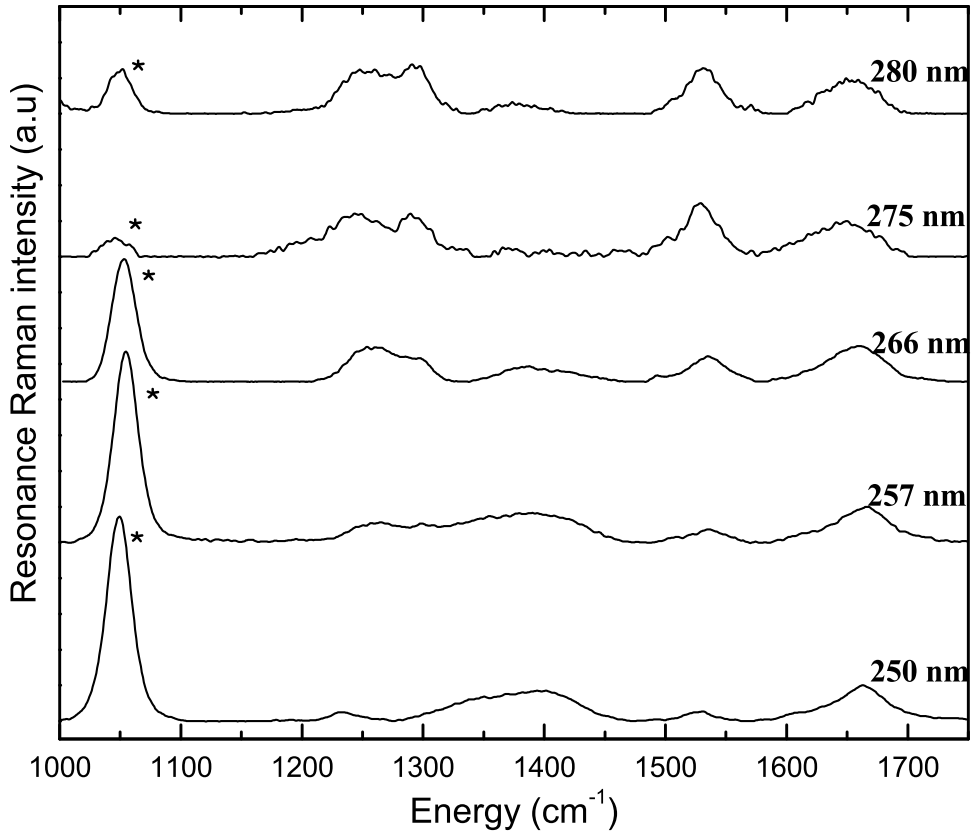

Figure A.3: Resonance Raman spectra of 0.3 mM $(dCp)_5$ excited at different wavelengths. The internal standard peak (0.3M nitrate for 266, 257 and 250 and 0.1 M for 275 and 280 nm) is denoted by asterisk (*).

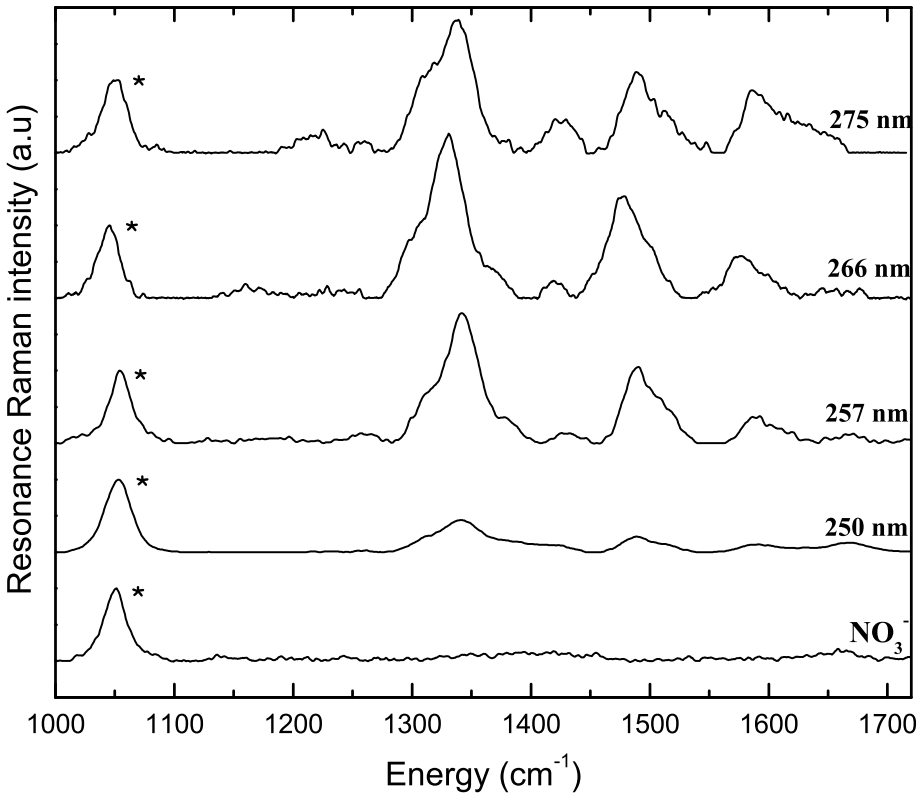

Figure A.4: Resonance Raman spectra of 0.3 mM $(dAp)_5$ excited at different wavelengths. The internal standard peak (0.1M nitrate) is denoted by asterisk (*).

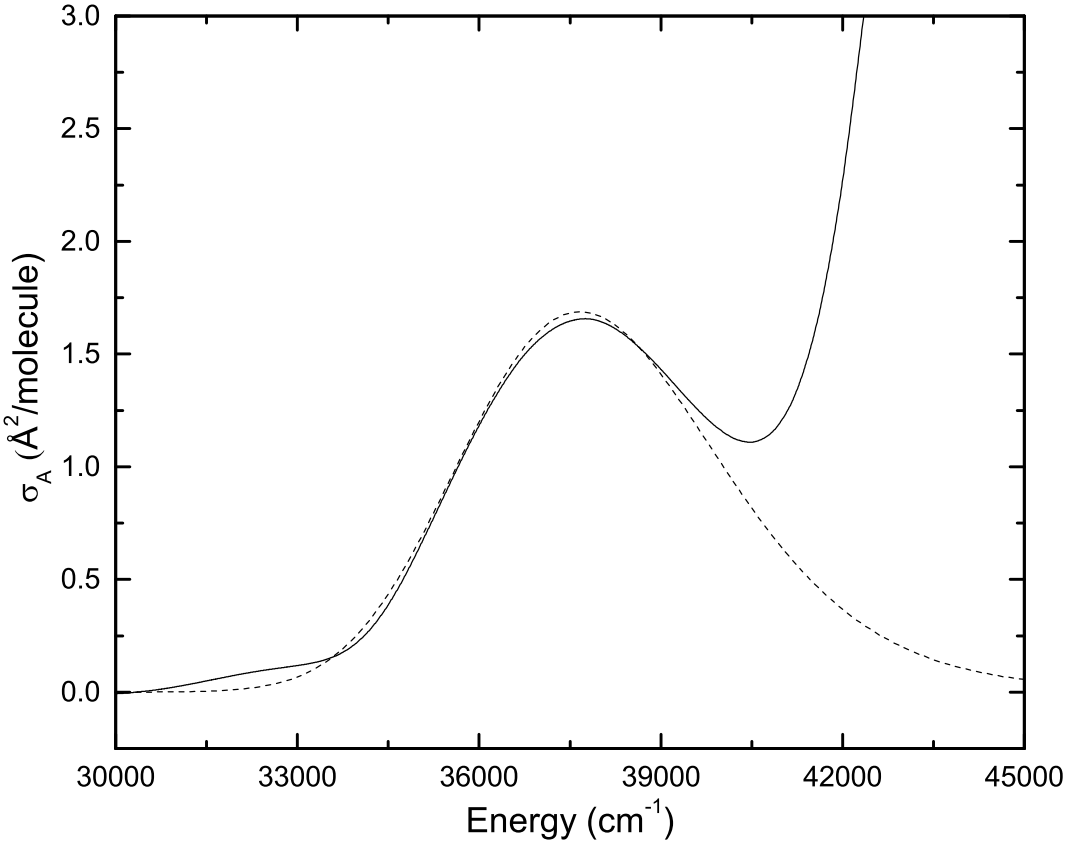

Figure A.5: Experimental (solid line) and simulated (dotted line) absorption spectra of $(dTp)_5$. The simulated absorption spectrum was generated using Equation 3.3 and the parameters of Table A.1. The differences between the experimental and simulated spectra at higher energies are other higher energy transitions which are not modeled in the equation.

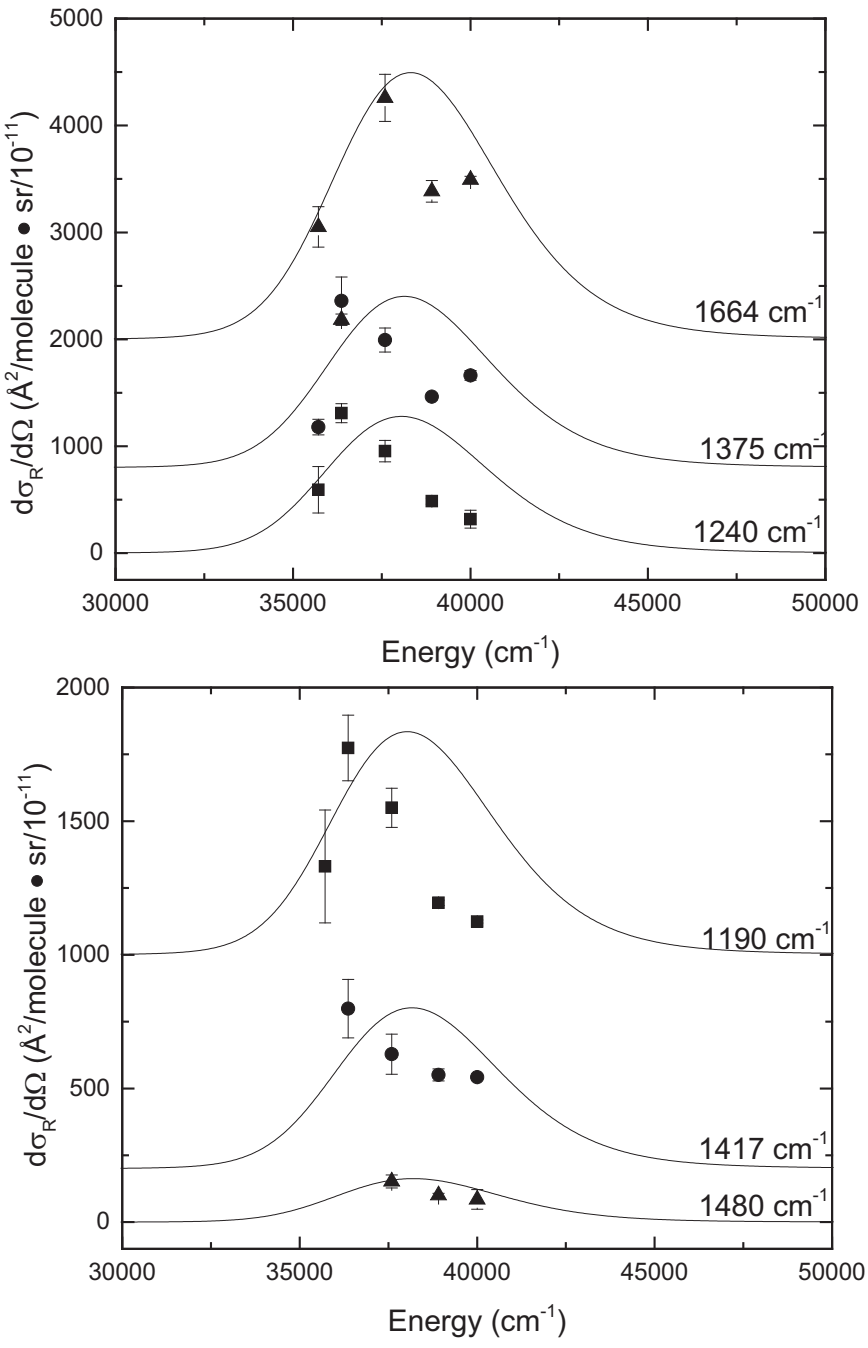

Figure A.6: Experimental (points) and calculated (solid lines) resonance Raman excitation profile for $(dTp)_5$. The excitation profiles were calculated using Equation 3.2 and the parameters in Table A.1.

Table A.1: Harmonic mode parameters for $(dTp)_5$

Mode[a] (cm^{-1})	mode assignment[b]	β/ħ (cm^{-1})
1190	ν(C2N3) [21], be(C6H12) [20], be(N1H7) [-16], ν(N3C4) [-12], ν(C6N1) [-11]	559.3
1240	ν(C5Me) [29], νC6N1) [-21], ring def 1 [12], ν(N1C2) [10], ν(C4C5) [-10], ν(C2N3) [-8]	694.4
1375	be(C6H) [42], ν(C5C6) [12], ν(N1C2) [9], ν(C2N3) [-9]	783.75
1417	ν(C2N3) [15], ν(C4C5) [13], CH3 umb [11], be(N1H) [9], ν(N1C2) [-8], be(C4O) [7], be(C2O) [7], ring def 2 [-6], be (N3H) [-6]	481.78
1480	ν(C4C5) [24], ν(N1C2) [13]	251.6
1664	ν(C5C6) [61], be(C6H) [13], ν(C6N1) [-8], ν(C5Me)[-5]	998.4

[a]Frequencies listed here are experimental frequencies. [b]Abbreviations: ν - stretching, def - deformation, γ - out-of-plane bending and be - in-plane bending. The slopes of the excited-state potential energy surface at the Franck-Condon geometry (β/ħ) in cm^{-1} were obtained by fitting the experimental cross-sections and absorption spectrum with the following parameters in Equation 3.2 and 3.3 :temperature, T = 298 K, zero-zero energy, E_0 = 35700 cm^{-1}, Gaussian homogeneous linewidth, Γ_G = 3700 cm^{-1}, inhomogeneous linewidth, θ = 80 cm^{-1}, transition length, M = 1.83 Å, and Brownian oscillator line shape, $\kappa = \Lambda/D = 0.1$.

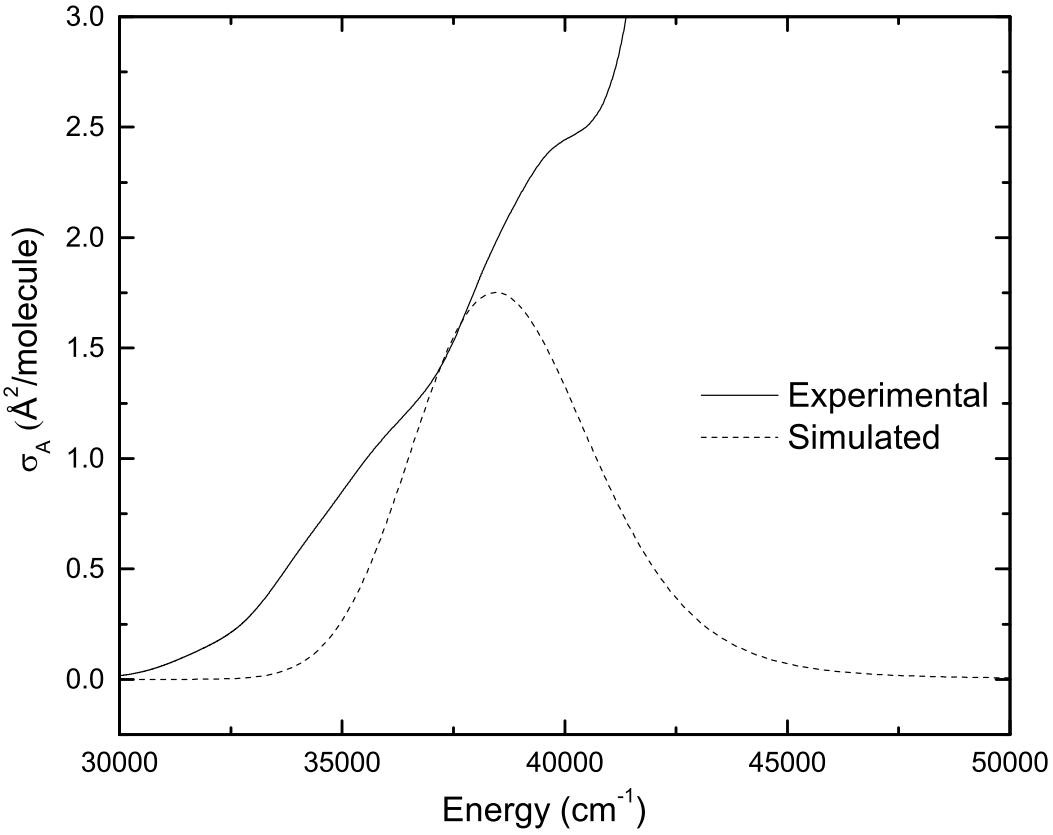

Figure A.7: Experimental (solid line) and simulated (dotted line) absorption spectra of $(dGp)_5$. The simulated absorption spectrum was generated using Equation 3.3 and the parameters of Table A.2. The differences between the experimental and the simulated spectra at higher energies are other higher energy transitions which are not modeled in the equation.

Table A.2: Harmonic mode parameters for $(dGp)_5$

Mode[a] (cm^{-1})	mode assignment[b]	$\beta/\hbar$ (cm^{-1})
1240	ν(N7C8) [+19], be(C8H) [-24]	223.2
1340	ν(N7C8) [-26], ν(N1C6) [-25], ν(N5N7) [+16]	670
1410	ν(C4N9) [-33], ν(C5N7) [-24]	352.5
1480	be(C8H) [+40], ν(C8N9) [-32], ν(N7C8) [+21]	532.8
1580	ν(N3C4) [-30], ν(C4C5) [+24], ν(C5N7) [-16]	632
1650	ν(C6O) [+48], ν(C5C6) [-21], be(N1H) [-11], ν(C4C5) [+11], ν(N1C6) [-10]	445.5

[a]Frequencies listed here are experimental frequencies. [b]Abbreviations: ν - stretching, def - deformation, γ - out-of-plane bending and be - in-plane bending. The slopes of the excited-state potential energy surface at the Franck-Condon geometry ($\beta/\hbar$) in cm^{-1} were obtained by fitting the experimental cross-sections and absorption spectrum with the following parameters in Equation 3.2 and 3.3 :temperature, T = 298 K, zero-zero energy, E_0 = 32200 cm^{-1}, Gaussian homogeneous linewidth, Γ_G = 3700 cm^{-1}, inhomogeneous linewidth, θ = 80 cm^{-1}, transition length, M = 1.8 Å, and Brownian oscillator line shape, $\kappa = \Lambda/D = 0.1$.

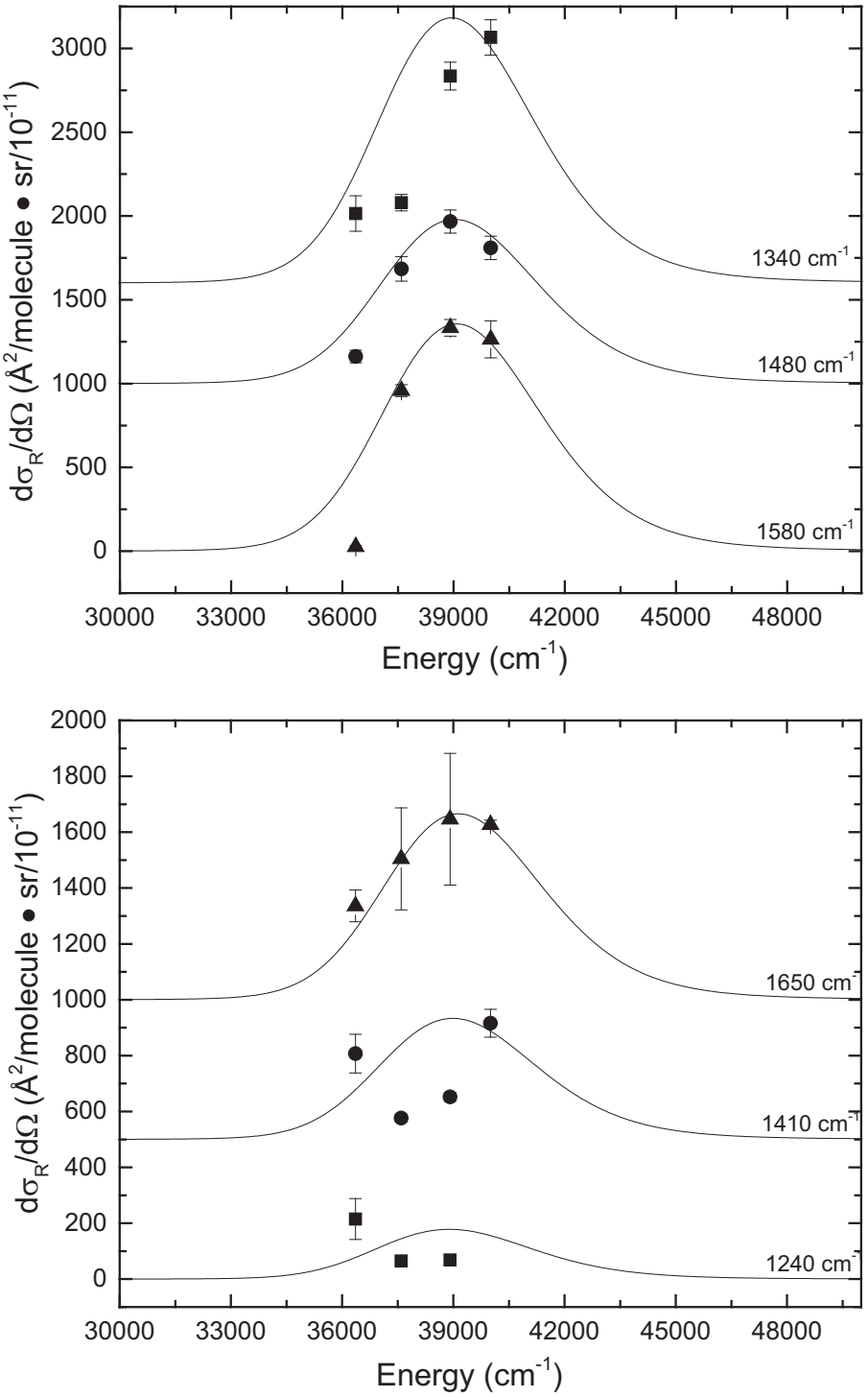

Figure A.8: Experimental (points) and calculated (solid lines) resonance Raman excitation profile for $(dGp)_5$. The excitation profiles were calculated using Equation 3.2 and the parameters in Table A.2.

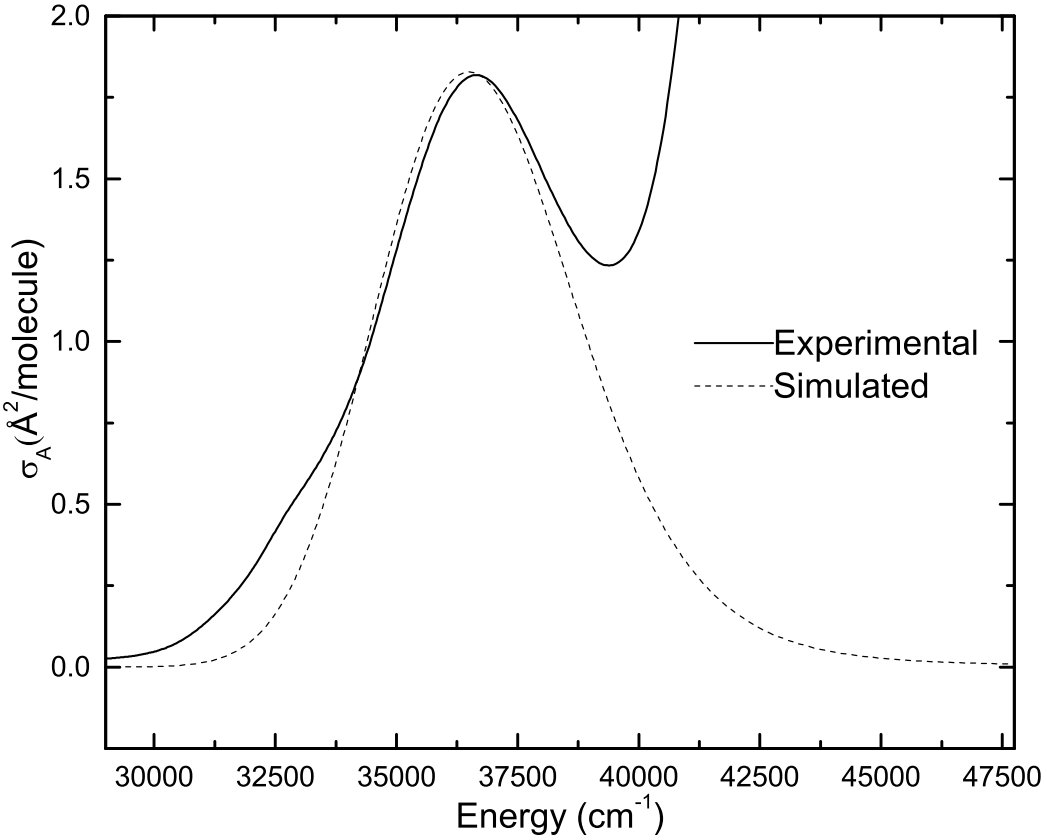

Figure A.9: Experimental (solid line) and simulated (dotted line) absorption spectra of $(dCp)_5$. The simulated absorption spectrum was generated using Equation 3.3 and the parameters in Table A.3. The differences between the experimental and the simulated spectra at higher energies are due to other higher energy transitions which are not modeled in the equation.

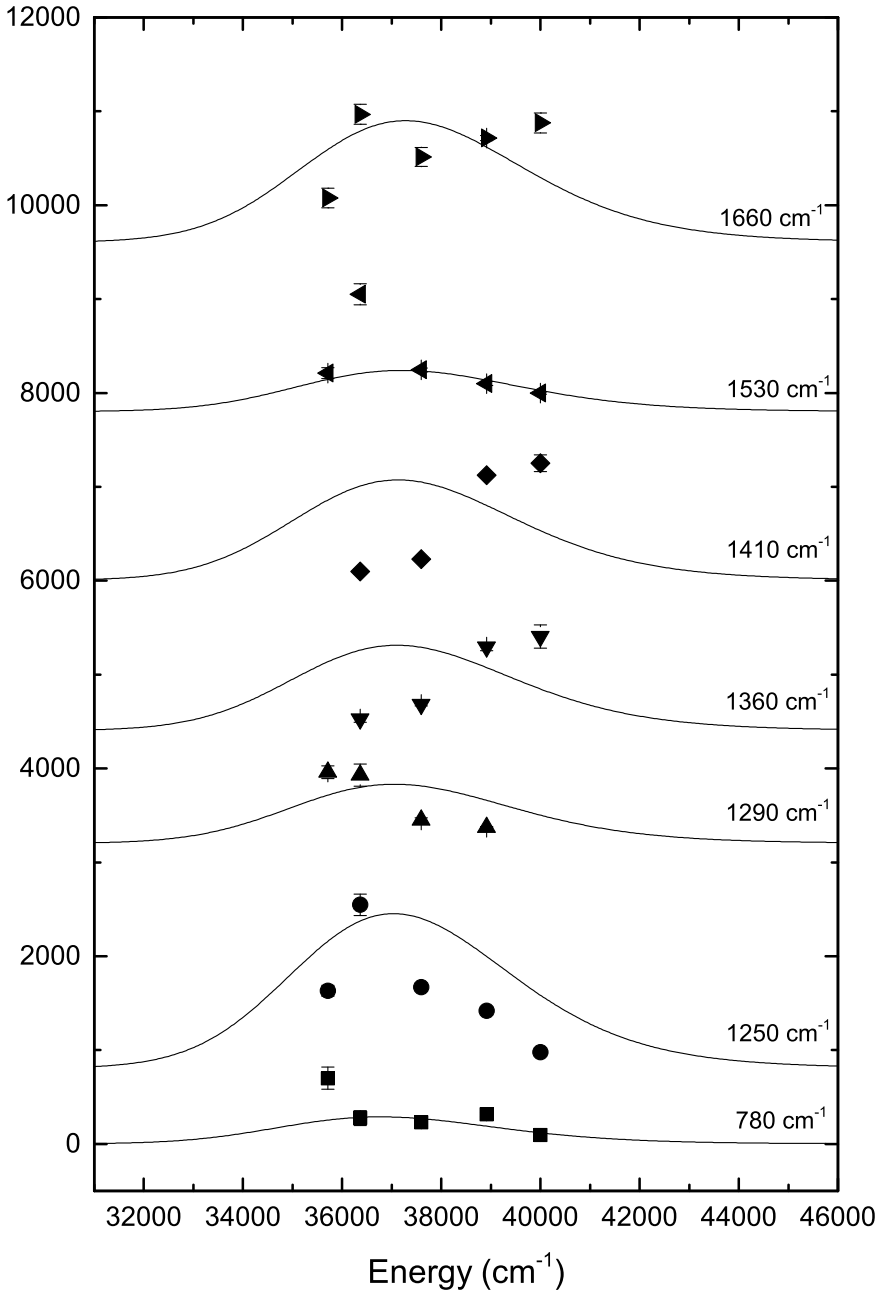

Figure A.10: Experimental (points) and calculated (solid lines) resonance Raman excitation profile for $(dCp)_5$. The excitation profiles were calculated using Equation 3.2 and the parameters in Table A.3.

Table A.3: Harmonic mode parameters for $(dCp)_5$

Mode[a] (cm^{-1})	mode assignment[b]	$\beta/\hbar$ (cm^{-1})
780	def(C2O7) [74], def(C4N8) [8]	296.4
1250	be(N1C6H) [19], n(N1C6) [18]	725
1290	ν(C2N3) [38], ν(C4N8) [13]	451.5
1360	ν(C4N8) [18], be(C5C6H) [17]	544
1410	be(C6N1H1) [30], ν(C6N1) [-19], ν(N3C4) [11]	592.2
1530	ν(C4N8) [17], ν(N3C4) [14]	382.5
1660	ν(C2O7) [76]	664

[a]Frequencies listed here are experimental frequencies. [b]Abbreviations: ν - stretching, def - deformation, γ - out-of-plane bending and be -in-plane bending. The slopes of the excited-state potential energy surface at the Franck-Condon geometry ($\beta/\hbar$) in cm^{-1} were obtained by fitting the experimental cross-sections and absorption spectrum with the following parameters in Equation 3.2 and 3.3: temperature, T = 298 K, zero-zero energy, E_0 = 34400 cm^{-1}, Gaussian homogeneous linewidth, Γ_G = 2100 cm^{-1}, inhomogeneous linewidth, θ = 1200 cm^{-1}, transition length, M = 1.66 Å, and Brownian oscillator line shape, $\kappa = \Lambda/D = 0.1$.

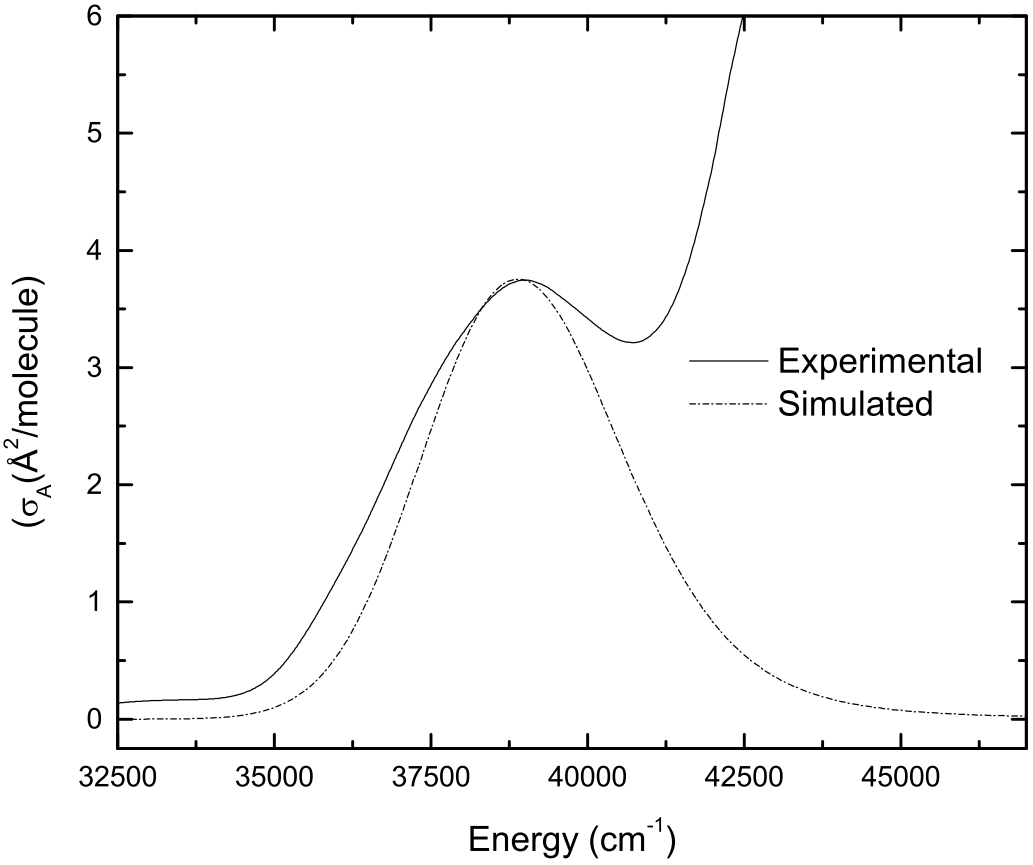

Figure A.11: Experimental (solid line) and simulated (dotted line) absorption spectra of $(dAp)_5$. The simulated absorption spectrum was generated using Equation 3.3 and the parameters from Table A.4. The differences between experimental and simulated spectra at higher energies are due to other higher energy transitions which are not modeled in the equation.

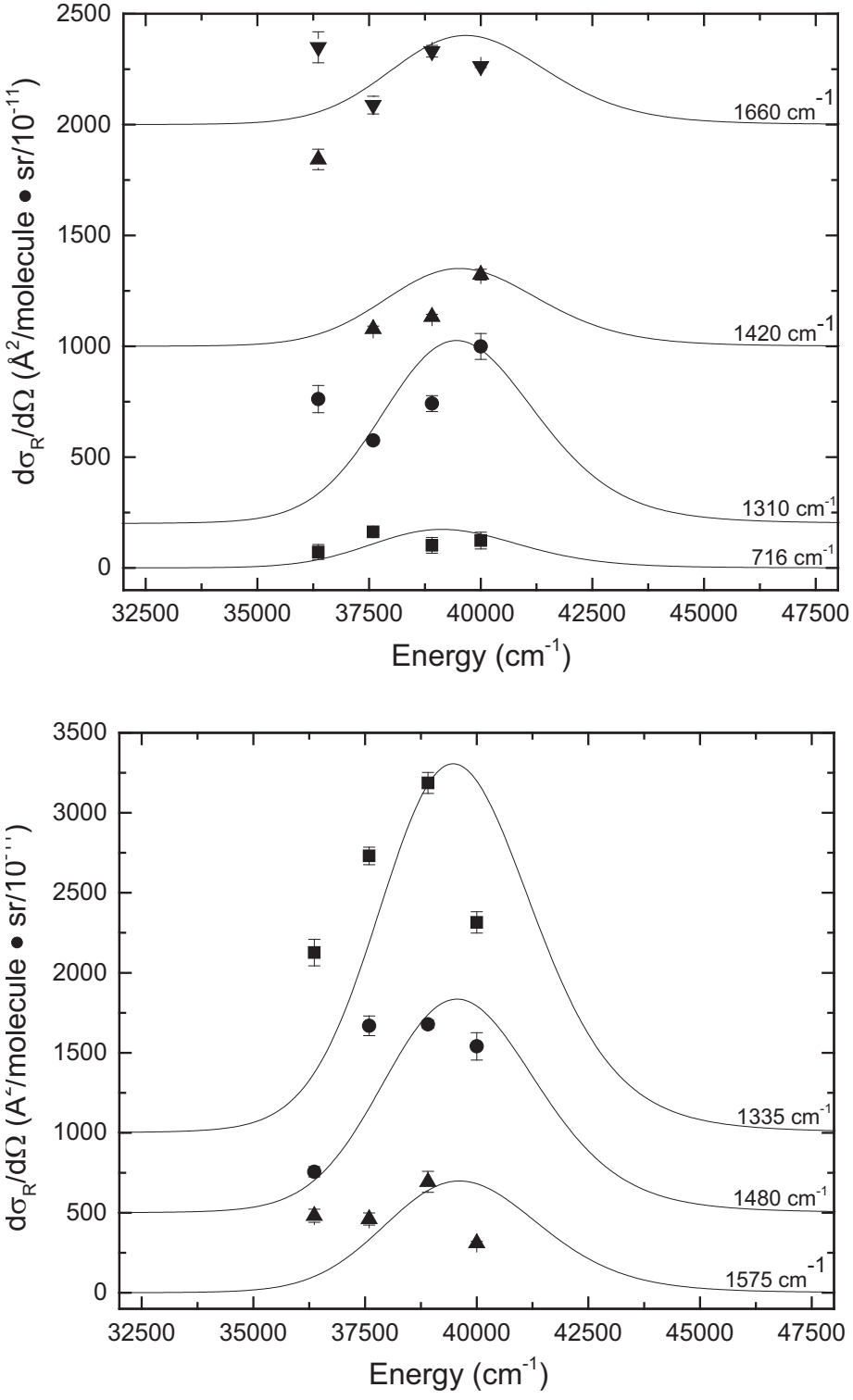

Figure A.12: Experimental (points) and calculated (solid lines) resonance Raman excitation profile for $(dAp)_5$. The excitation profiles were calculated using Equation 3.2 and the parameters in Table A.4.

Table A.4: Harmonic mode parameters for $(dAp)_5$

Mode[a] (cm^{-1})	mode assignment[b]	β/ħ (cm^{-1})
726	be(N7C8N9) [19], ν(N9C'1) [-14], be(C5N7C8) [12], be(C4N9C8) [11]	79.86
1310	ν(N9C8) [30], ν(N3C2) [14], be(C8H) [14]	183.4
1335	ν(N7C5) [-39], ν(C8N7)[12]	307.05
1410	ν(C4N9) [44], be(C8H)[-15]	119.85
1480	be(C2H) [-29], ν(N9C8) [-19], be(C8H)[15]	236.8
1575	ν(C4C5) [48], ν(C4N3) [-31]	173.25
1660	be(NH_2)[73], ν(C5C6) [15], ν(C6N10) [14]	132.8

[a]Frequencies listed here are experimental frequencies. [b]Abbreviations: ν - stretching, def deformation, γ - out-of-plane bending and be - in-plane bending. The slopes of the excited-state potential energy surface at the Franck-Condon geometry (β/ħ) in cm^{-1} were obtained by fitting the experimental cross-sections and absorption spectrum with the following parameters in Equation 3.2 and 3.3 :temperature, T = 298 K, zero-zero energy, E_0 = 34200 cm^{-1}, Gaussian homogeneous linewidth, Γ_G = 3300 cm^{-1}, inhomogeneous linewidth, θ = 50 cm^{-1}, transition length, M = 2.35 Å, and Brownian oscillator line shape, $\kappa = \Lambda/D = 0.1$.

Appendix B

Kinetics and Correlation Plots for miRNA Damage

All the kinetics plots and the correlation plots for all the experiments discussed in Chapter 4 is presented here.

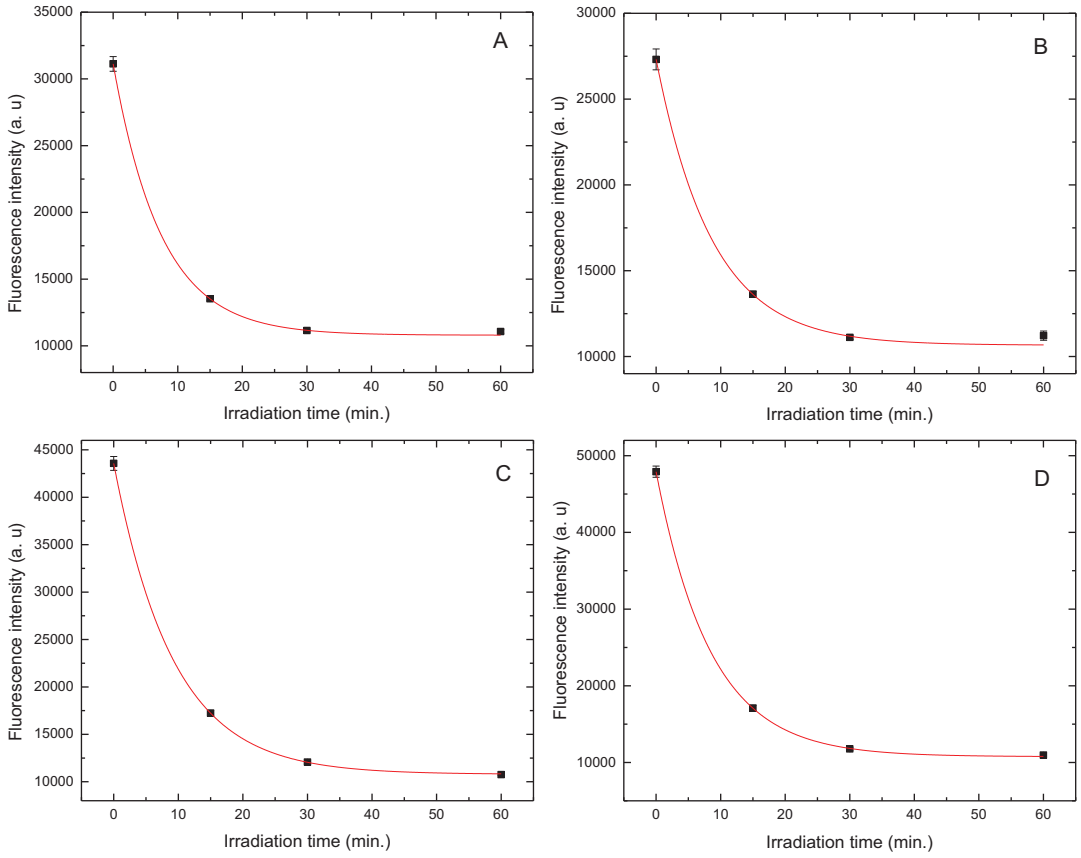

Figure B.1: Probe fluorescence intensity at 530 nm as a function of UV irradiation time for miRNAs *hsa-miR-100* (A and B) and *hsa miR-129b-2* (C and D) for experiment 1. 'A' and 'B', and 'C' and 'D' represent replicates. Experimental details of experiment 1 is described in the text.

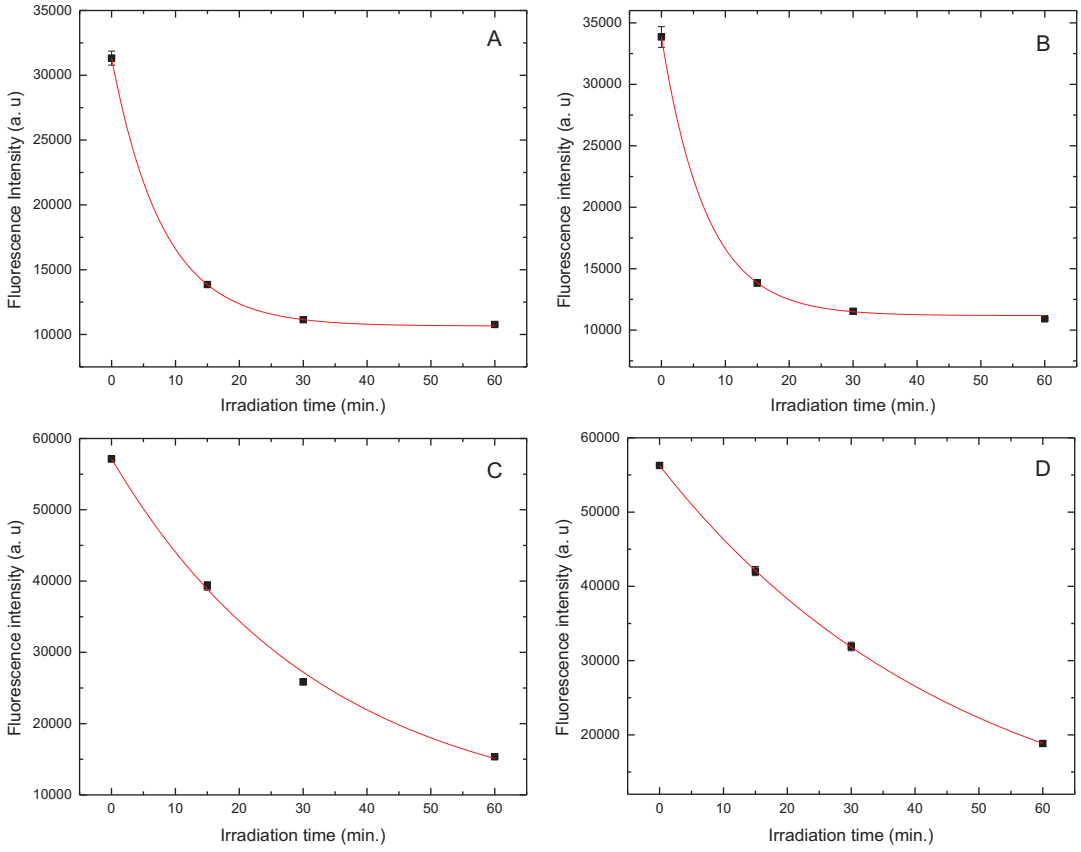

Figure B.2: Probe fluorescence intensity at 530 nm as a function of UV irradiation time for miRNAs *hsa-miR-21* (A and B) and *hsa miR-155* (C and D) for experiment 1. 'A' and 'B', and 'C' and 'D' represent replicates. Experimental details of experiment 1 is described in the text.

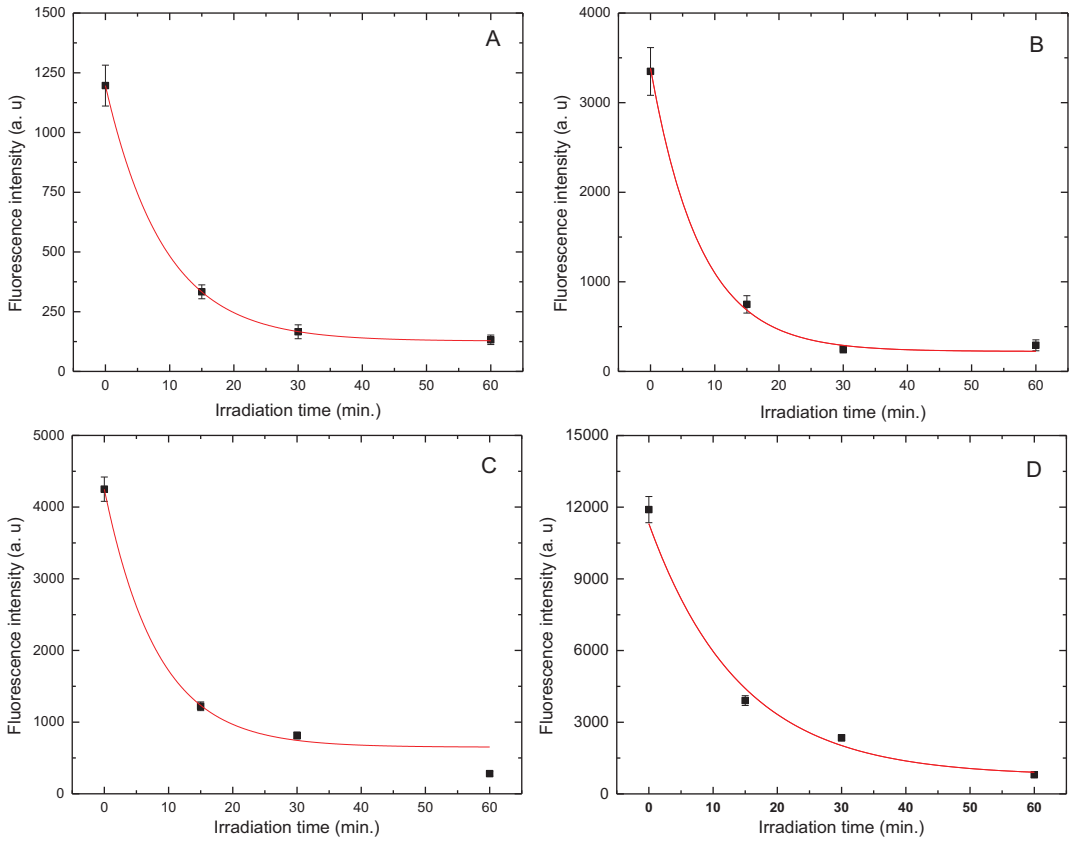

Figure B.3: Probe fluorescence intensity at 530 nm as a function of UV irradiation time for miRNAs *hsa-miR-181-b* (A and B) and *hsa miR-100* (C and D) for experiment 2. 'A' and 'B', and 'C' and 'D' represent replicates. Experimental details of experiment 2 is described in the text.

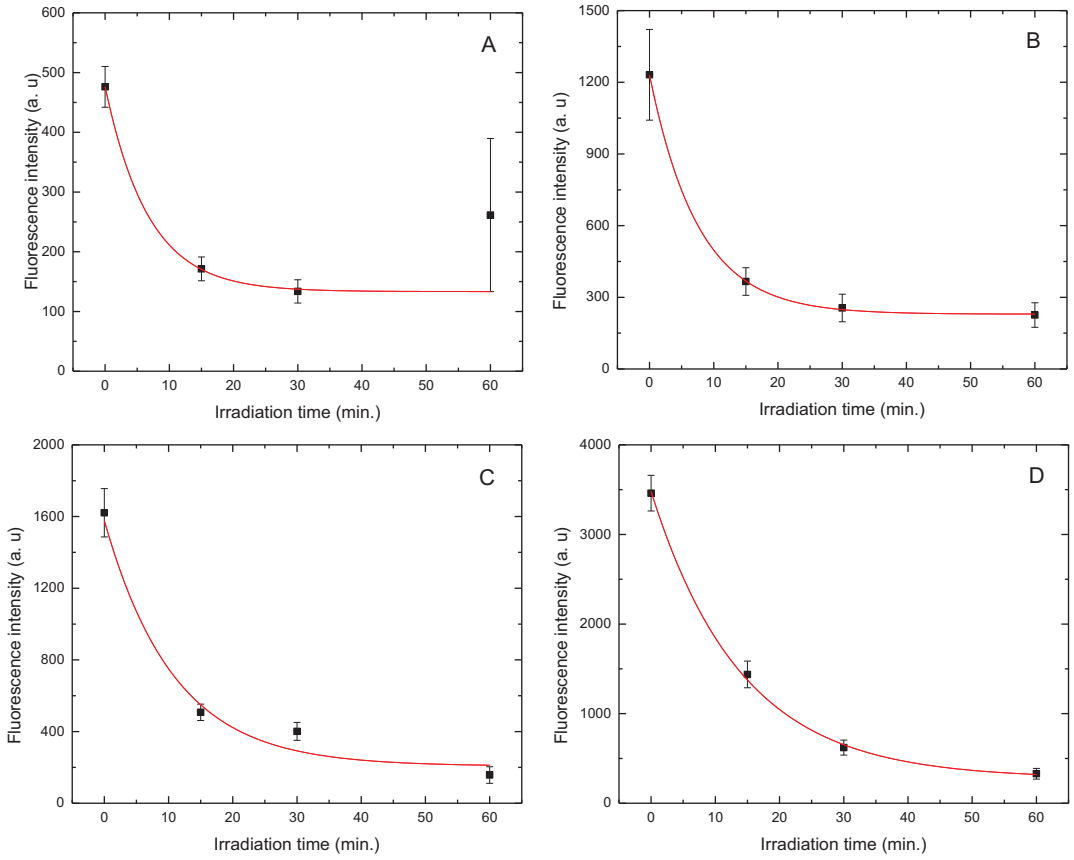

Figure B.4: Probe fluorescence intensity at 530 nm as a function of UV irradiation time for miRNAs *hsa-miR-29-b* (A and B) and *hsa miR-21* (C and D) for experiment 2. 'A' and 'B', and 'C' and 'D' represent replicates. Experimental details of experiment 2 is described in the text.

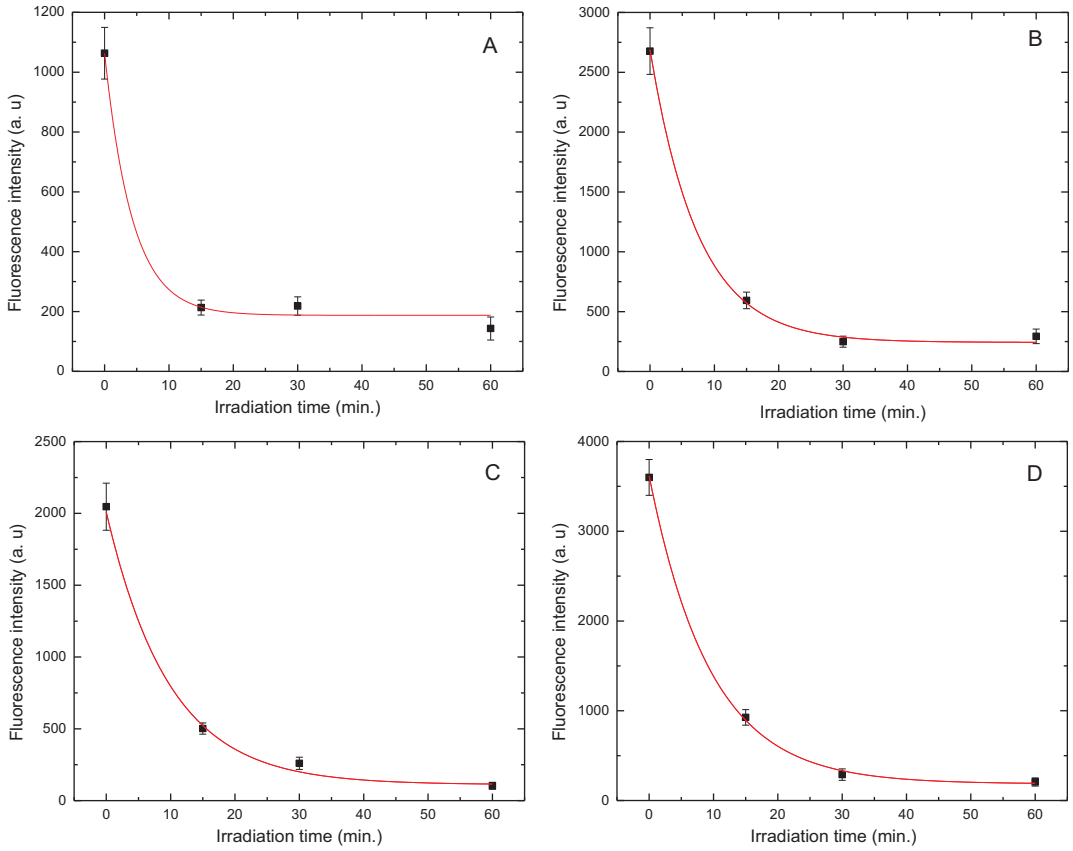

Figure B.5: Probe fluorescence intensity at 530 nm as a function of UV irradiation time for miRNAs *hsa-let-7f-1* (A and B) and *hsa-let-7a-2* (C and D) for experiment 2. 'A' and 'B', and 'C' and 'D' represent replicates. Experimental details of experiment 2 is described in the text.

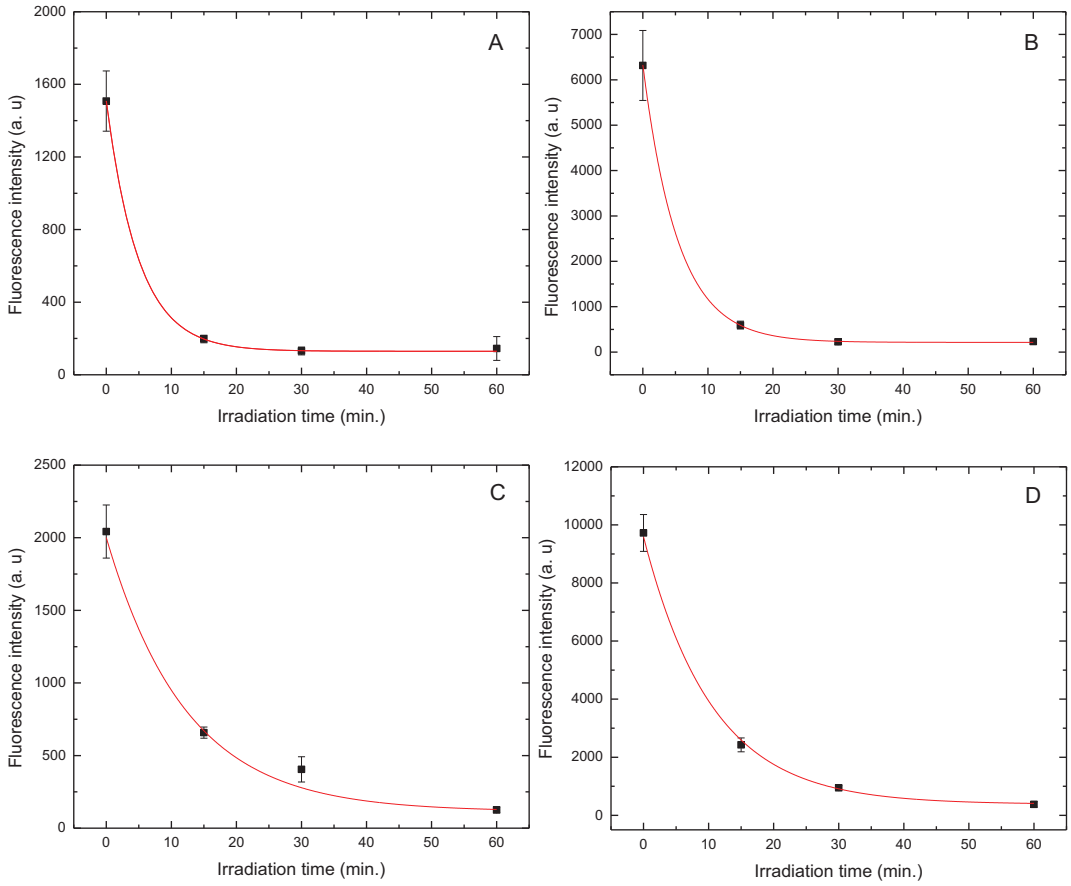

Figure B.6: Probe fluorescence intensity at 530 nm as a function of UV irradiation time for miRNAs *hsa-let-7g* (A and B) and *hsa-miR-155* (C and D) for experiment 2. 'A' and 'B', and 'C' and 'D' represent replicates. Experimental details of experiment 2 is described in the text.

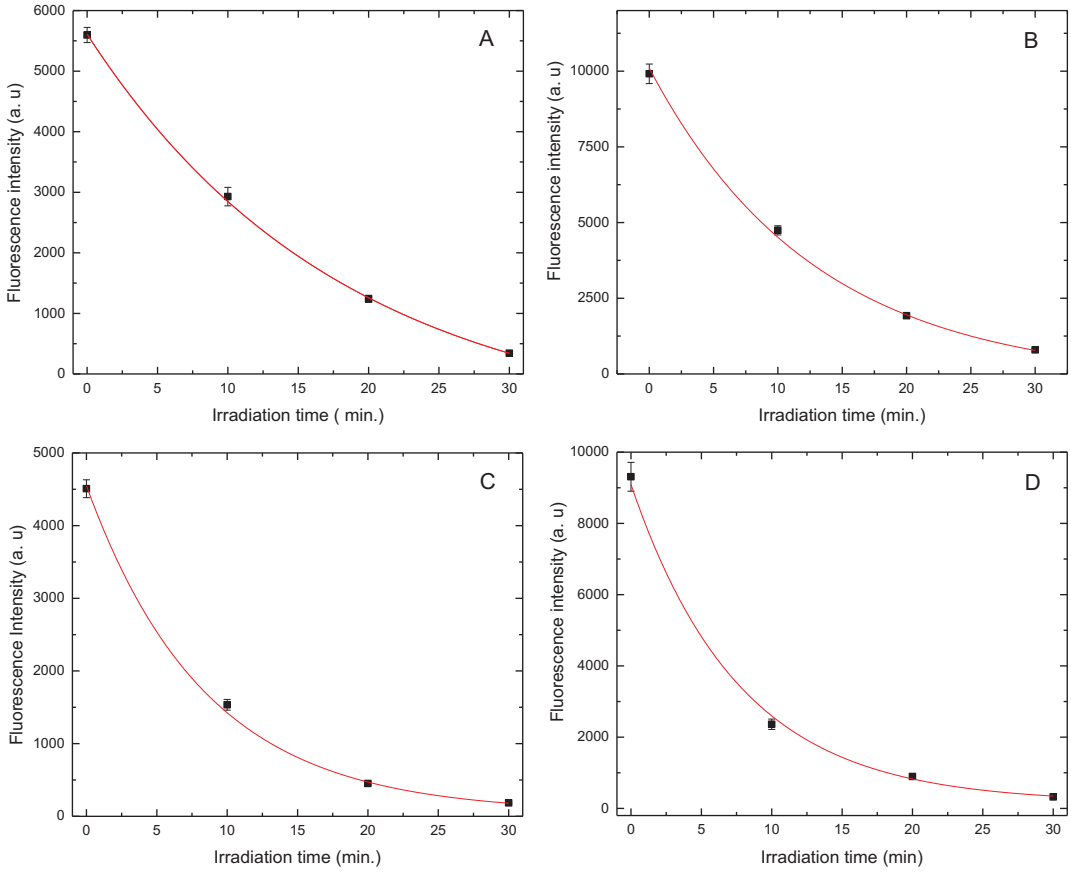

Figure B.7: Probe fluorescence intensity at 685 nm as a function of UV irradiation time for miRNAs *hsa-miR29-b* (A and B), *hsa-miR-21* (C and D) for experiment 3. 'A' and 'B', and 'C' and 'D' represent replicates. Experimental details of experiment 3 is described in the text.

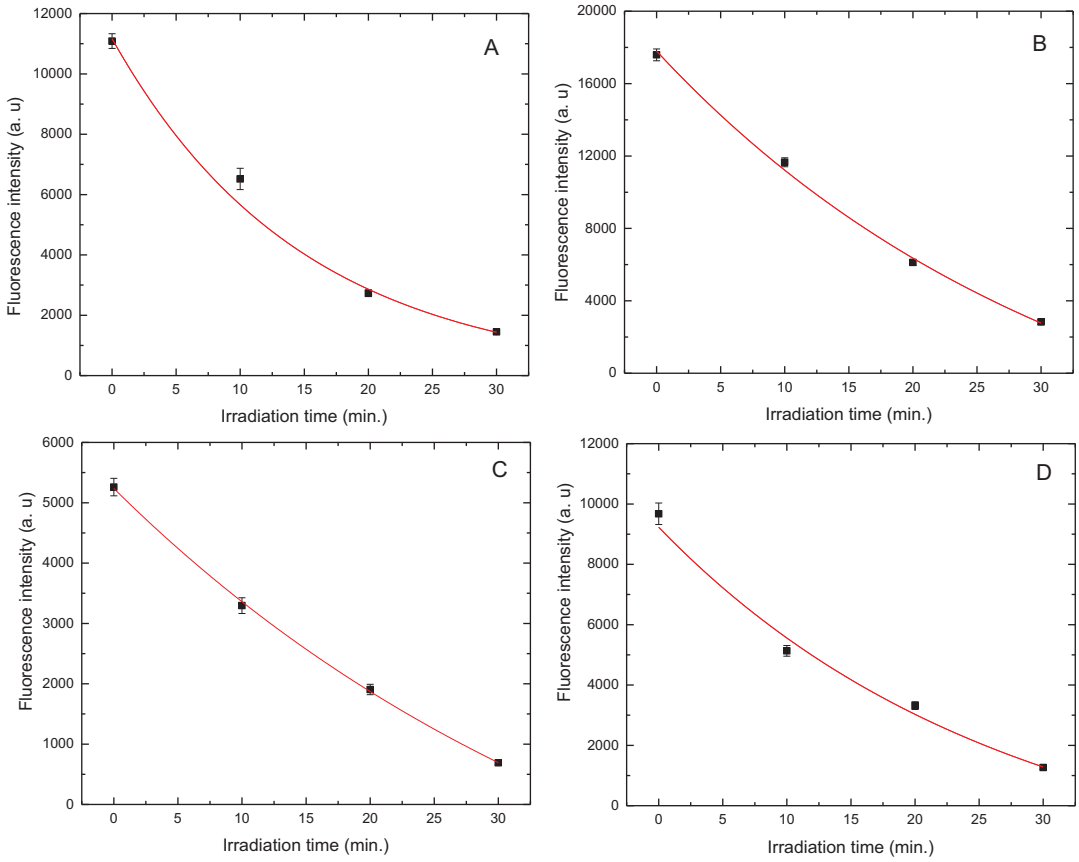

Figure B.8: Probe fluorescence intensity at 685 nm as a function of UV irradiation time for miRNAs *hsa-miR-125b-1*(A and B) and *hsa-miR-155*(C and D) for experiment 3. 'A' and 'B', and 'C' and 'D' represent replicates. Experimental details of experiment 3 is described in the text.

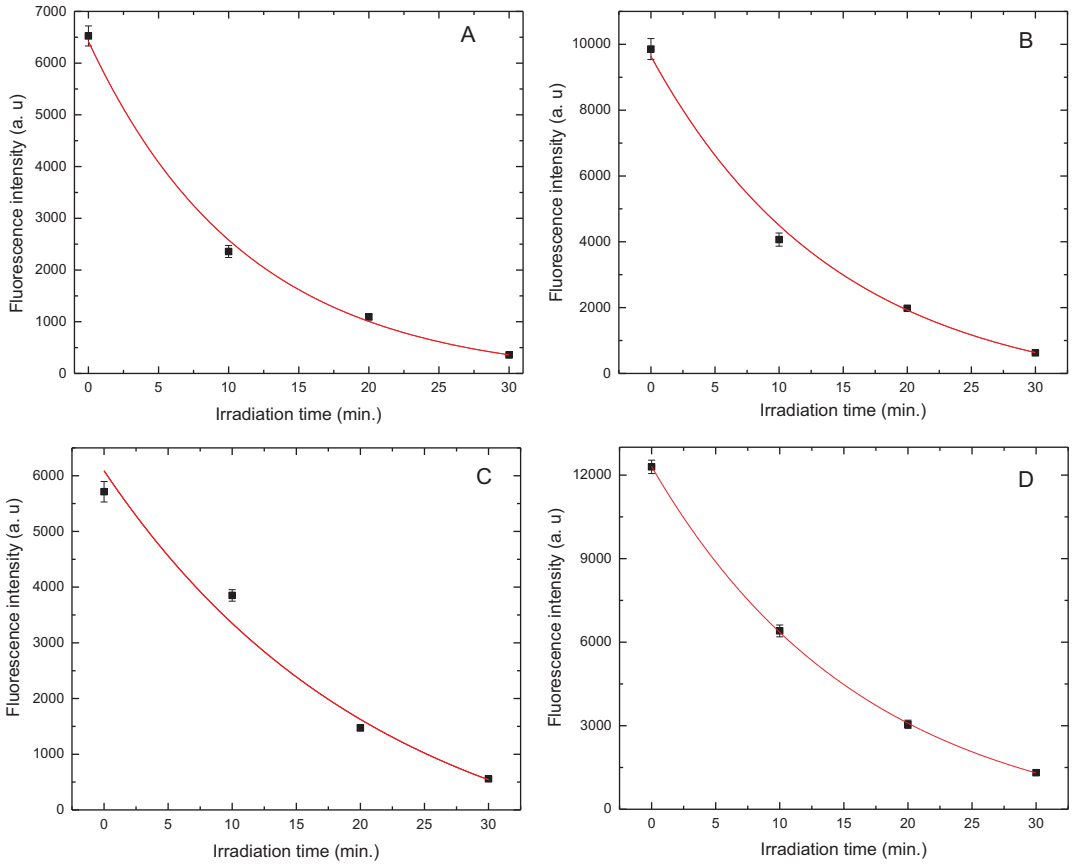

Figure B.9: Probe fluorescence intensity at 685 nm as a function of UV irradiation time for miRNAs *hsa-miR-145*(A and B) and *hsa-miR-10b*(C and D) for experiment 3). 'A' and 'B', and 'C' and 'D' represent replicates. Experimental details of experiment 3 is described in the text.

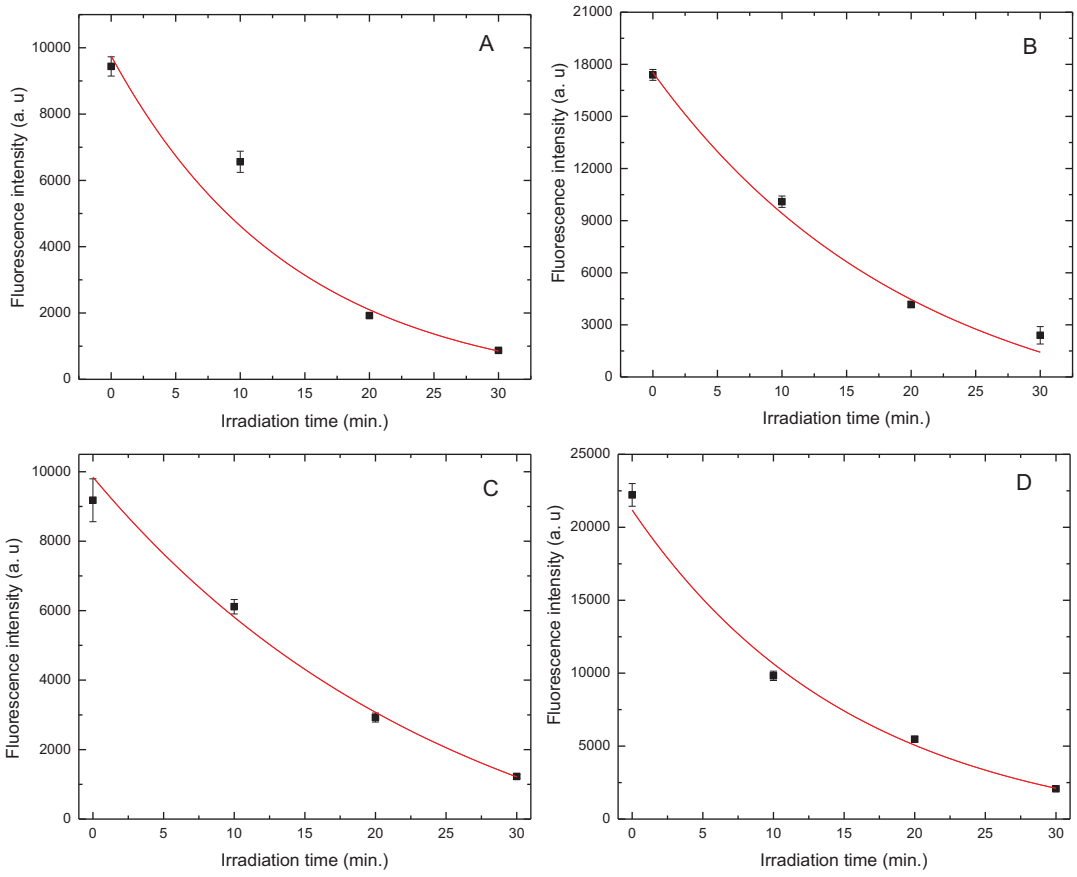

Figure B.10: Probe fluorescence intensity at 685 nm as a function of UV irradiation time for miRNAs *hsa-hsa-miR-17*(A and B) and *hsa-miR-27b*(C and D) for experiment 3. 'A' and 'B', and 'C' and 'D' represent replicates. Experimental details of experiment 3 is described in the text.

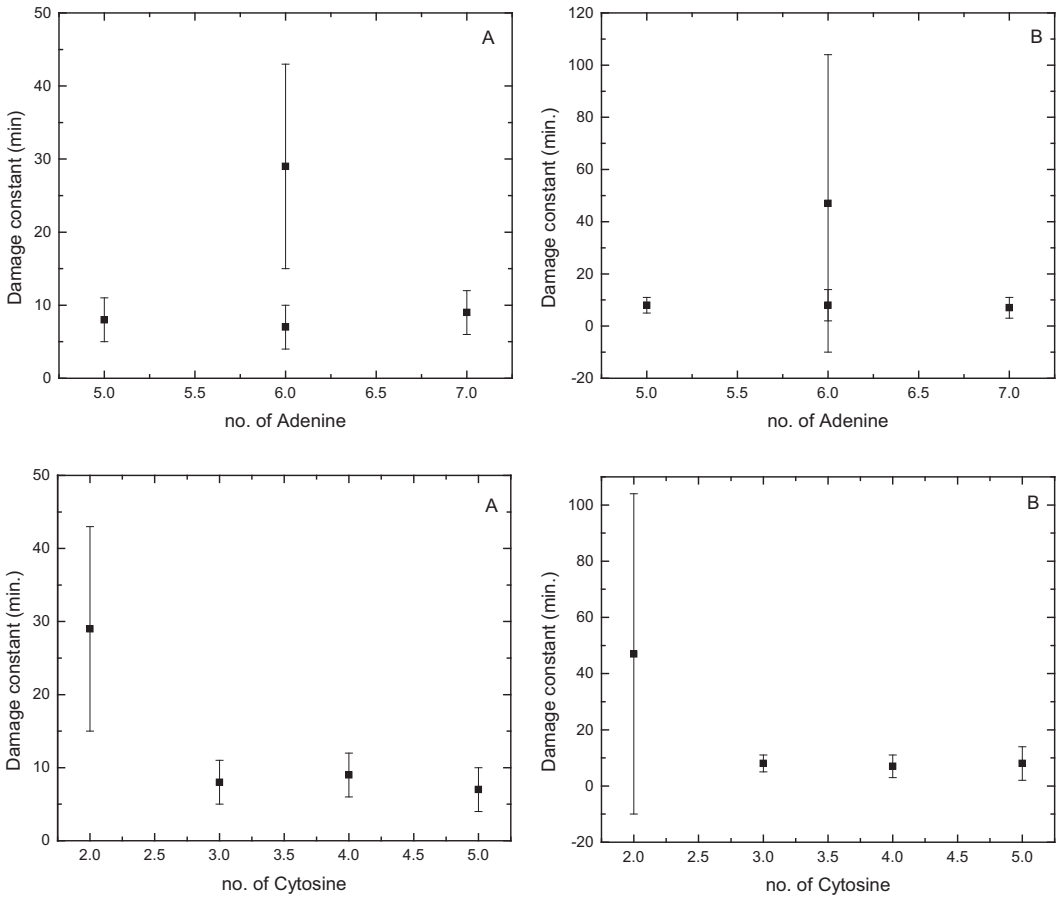

Figure B.11: Damage kinetics as function of number of adenine and cytosine for experiment 1. 'A' and 'B' represents kinetics of replicates.

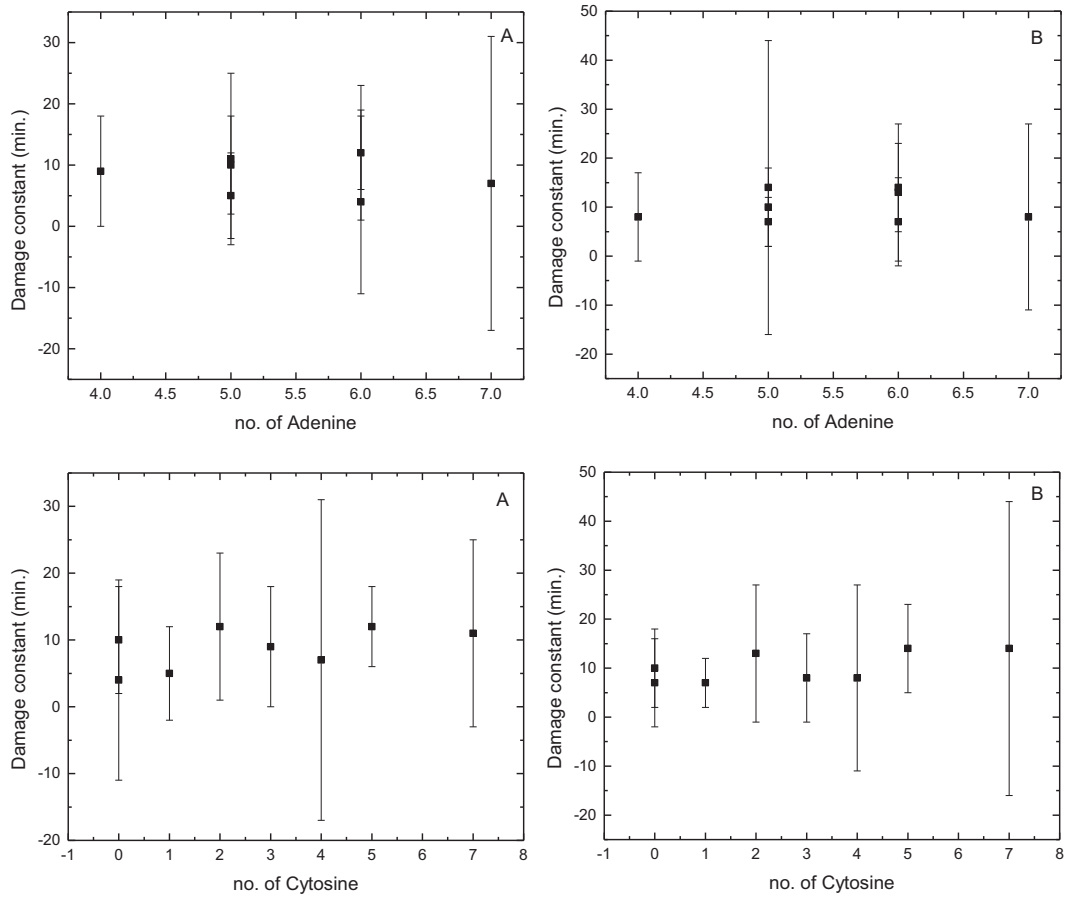

Figure B.12: Damage kinetics as function of number of adenine and cytosine for experiment 2. 'A' and 'B' represents kinetics of replicates.

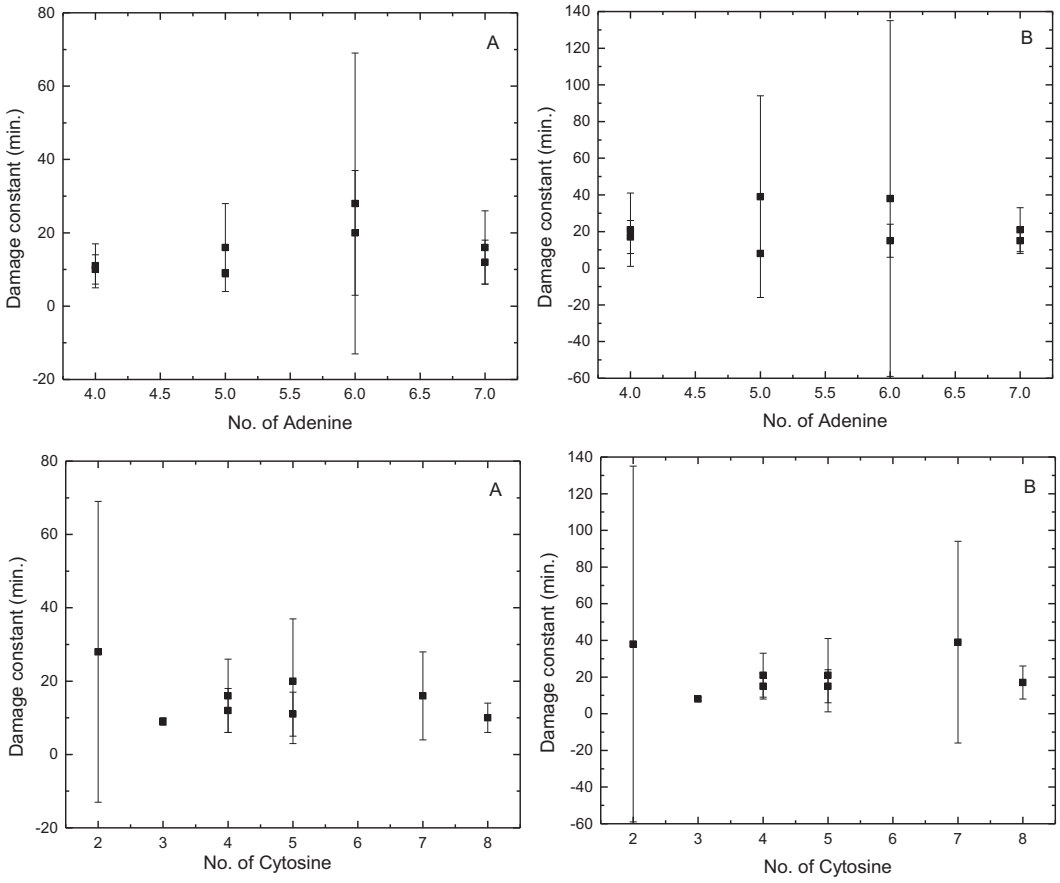

Figure B.13: Damage kinetics as function of number of adenine and cytosine for experiment 3. 'A' and 'B' represents kinetics of replicates.

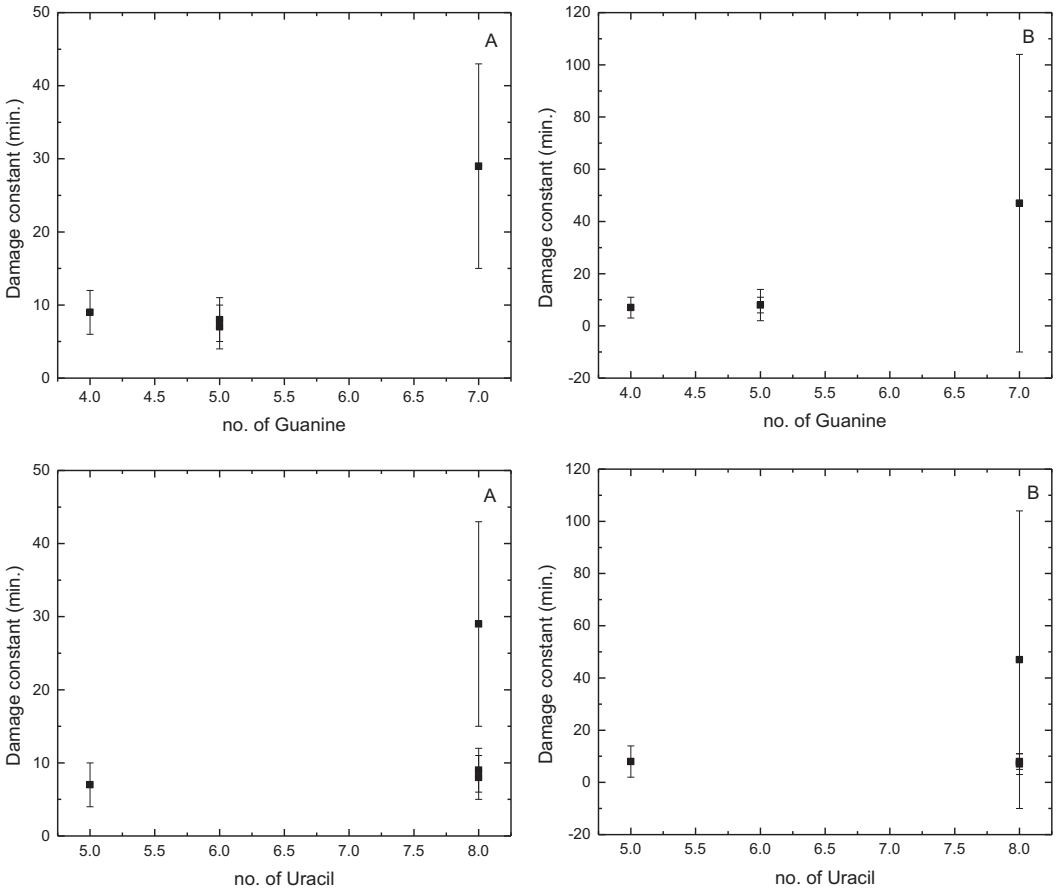

Figure B.14: Damage kinetics as function of number of guanine and uracil for experiment 1. 'A' and 'B' represents kinetics of replicates.

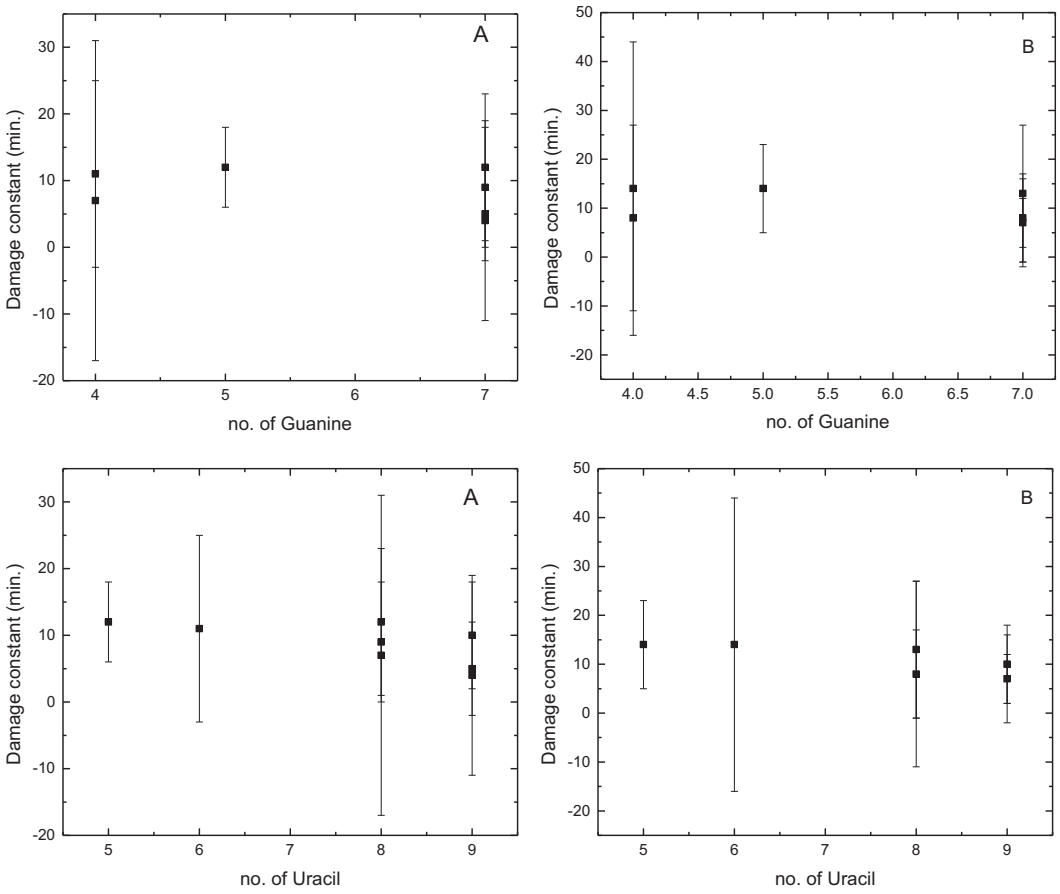

Figure B.15: Damage kinetics as function of number of guanine and uracil for experiment 2. 'A' and 'B' represents kinetics of replicates.

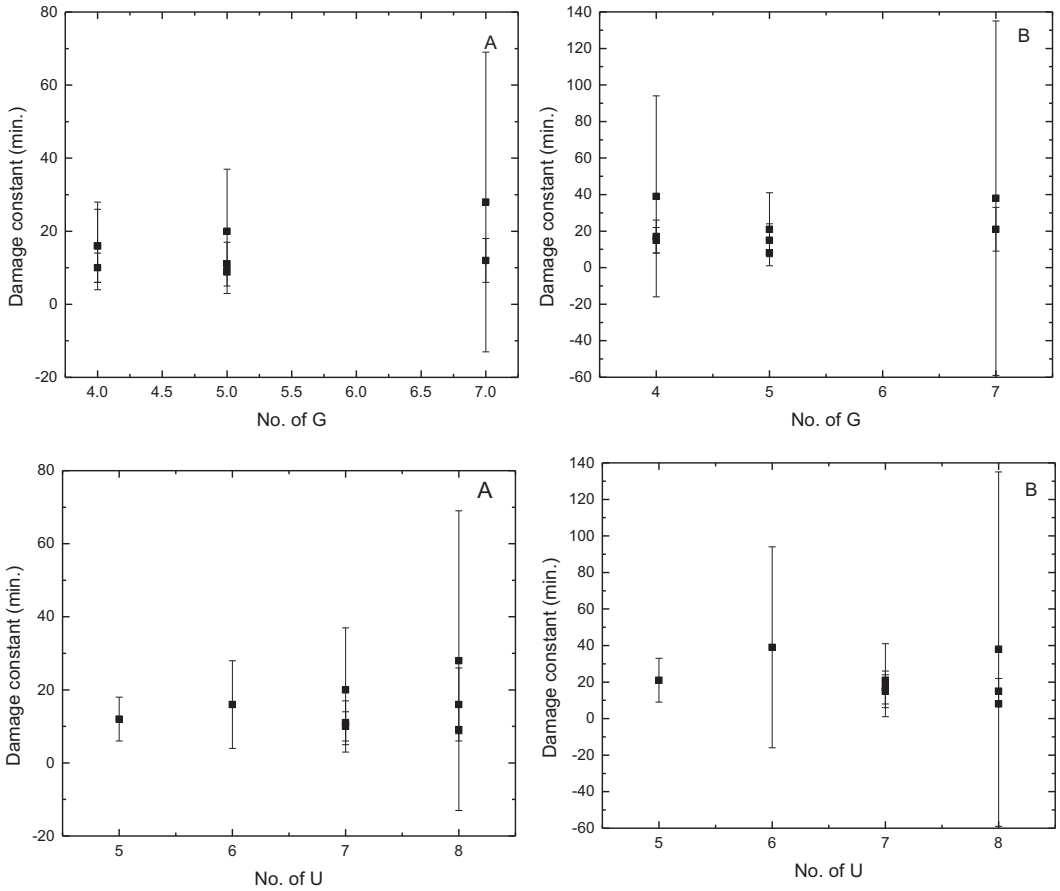

Figure B.16: Damage kinetics as function of number of guanine and uracil for experiment 3. 'A' and 'B' represents kinetics of replicates.

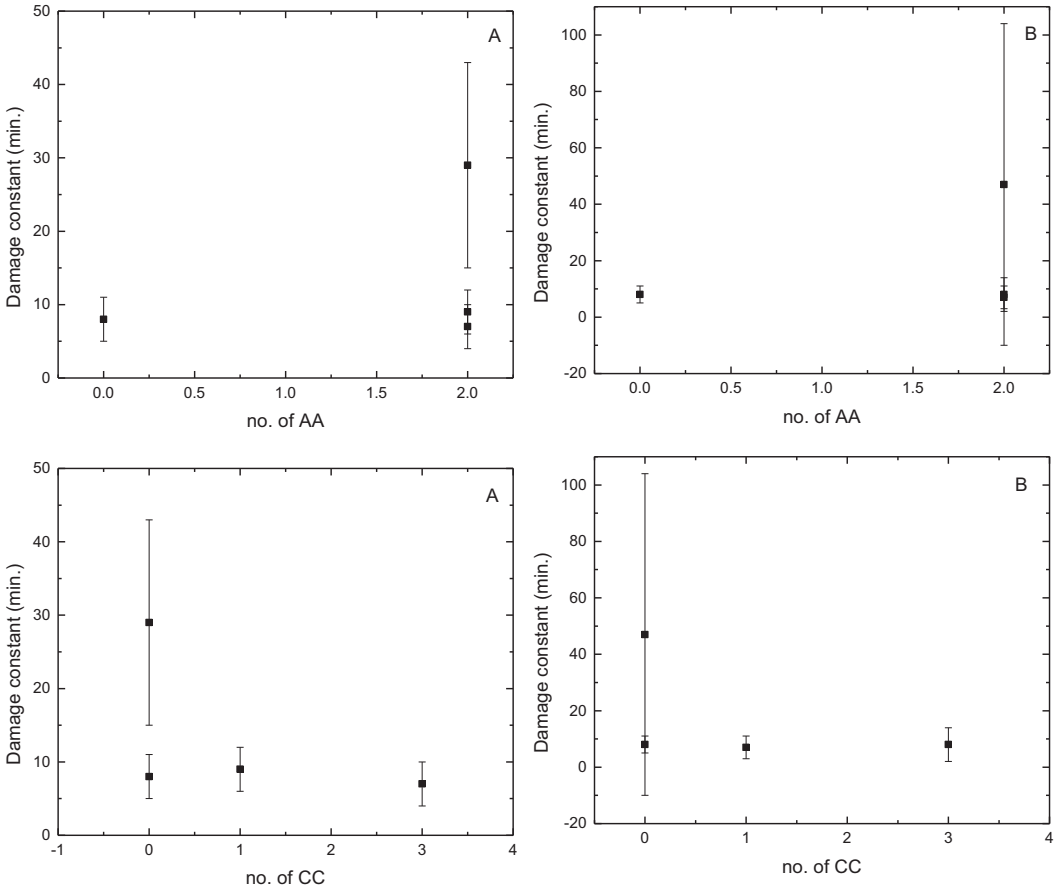

Figure B.17: Damage kinetics as function of number of adenine and cytosine doublets for experiment 1. 'A' and 'B' represents kinetics of replicates.

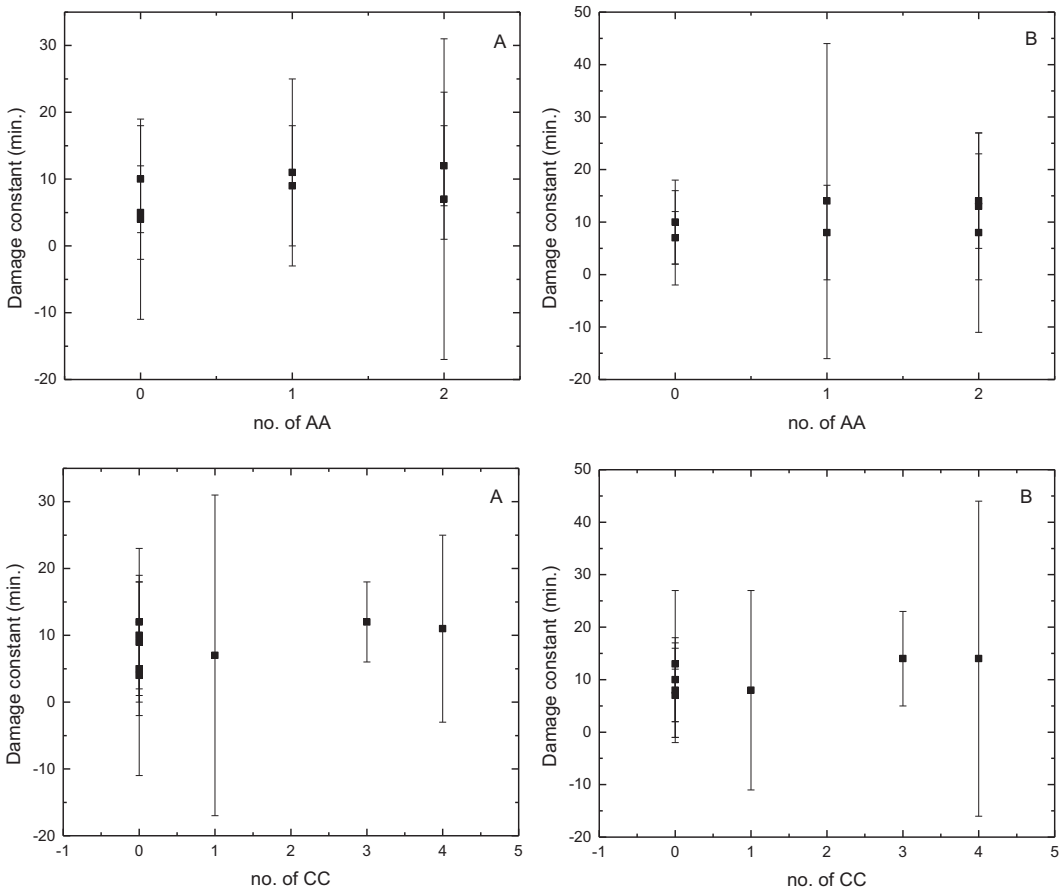

Figure B.18: Damage kinetics as function of number of adenine and cytosine doublets for experiment 2. 'A' and 'B' represents kinetics of replicates.

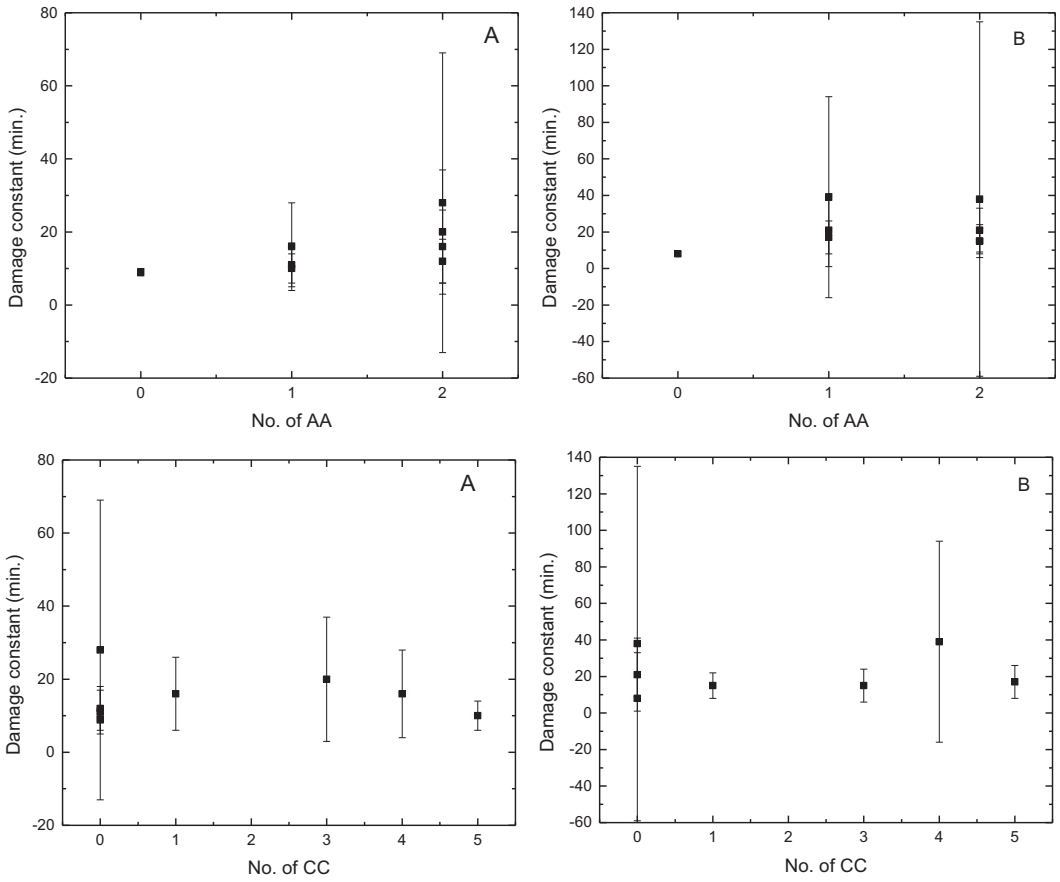

Figure B.19: Damage kinetics as function of number of adenine and cytosine doublets for experiment 3. 'A' and 'B' represents kinetics of replicates.

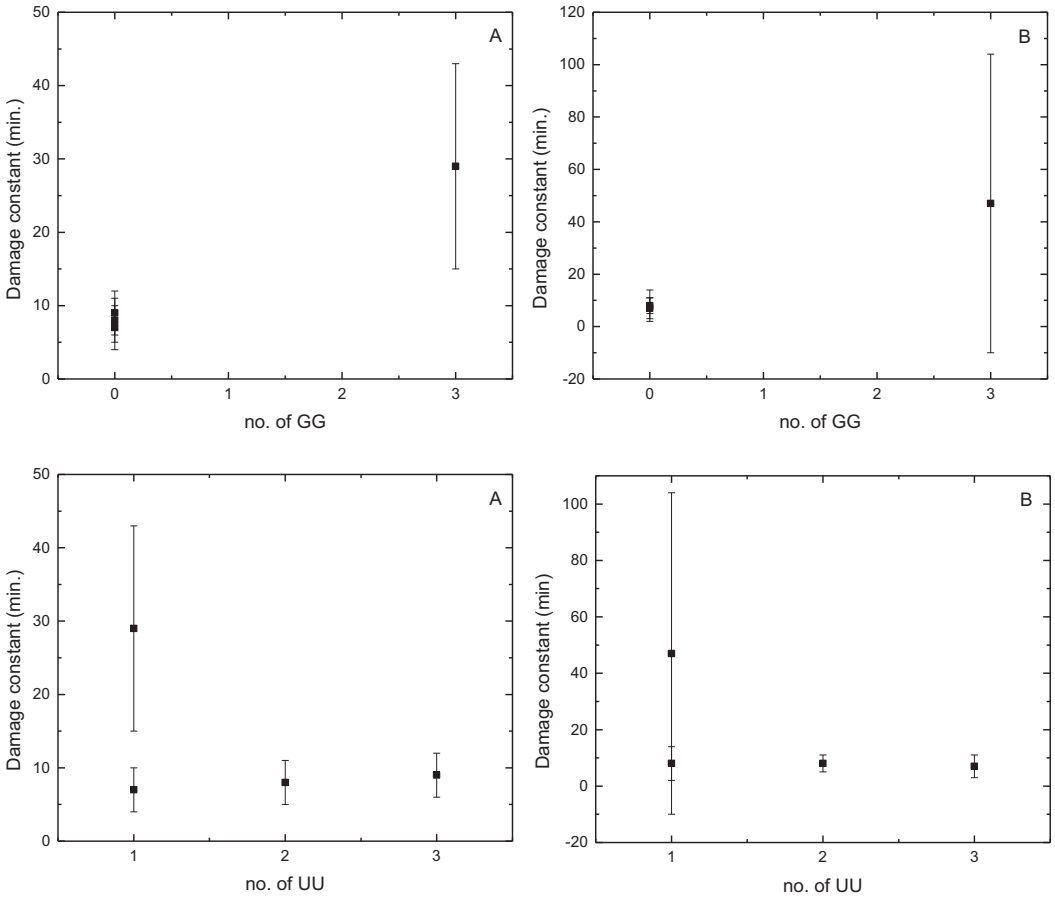

Figure B.20: Damage kinetics as function of number of guanine and uracil doublets for experiment 1. 'A' and 'B' represents kinetics of replicates.

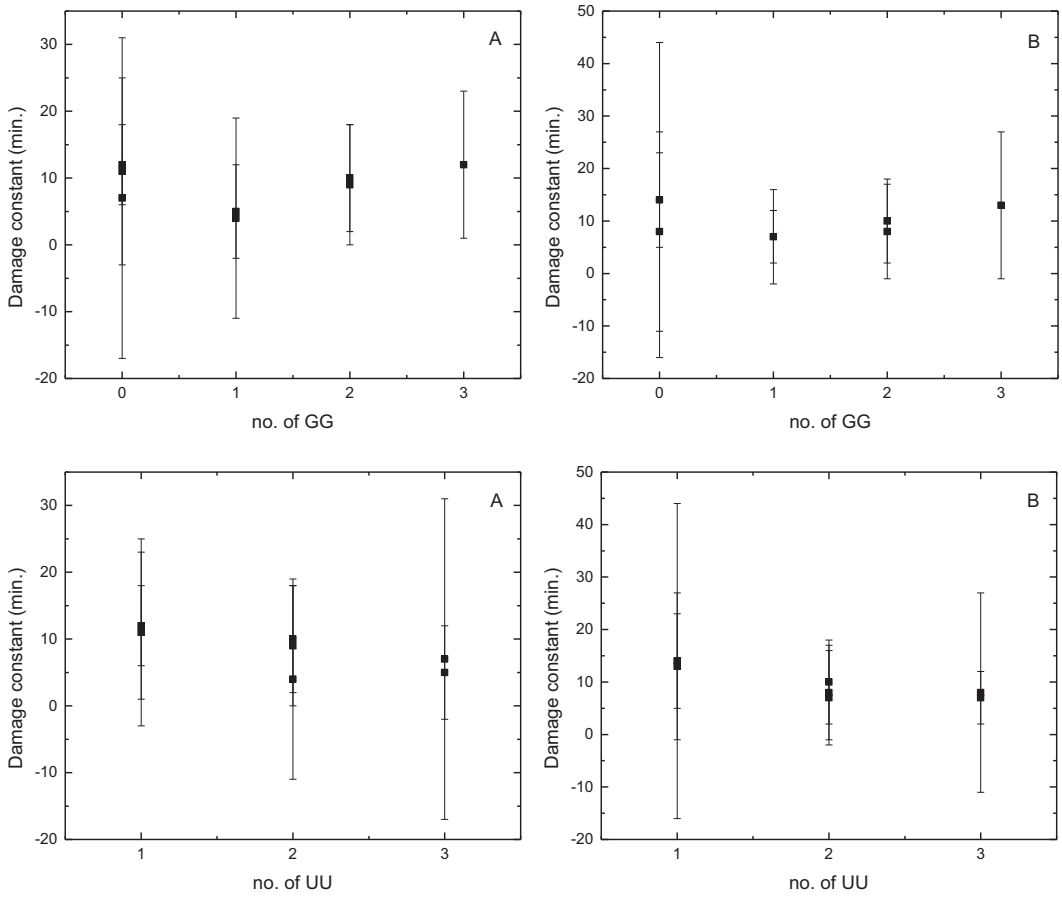

Figure B.21: Damage kinetics as function of number of guanine and uracil doublets for experiment 2. 'A' and 'B' represents kinetics of replicates.

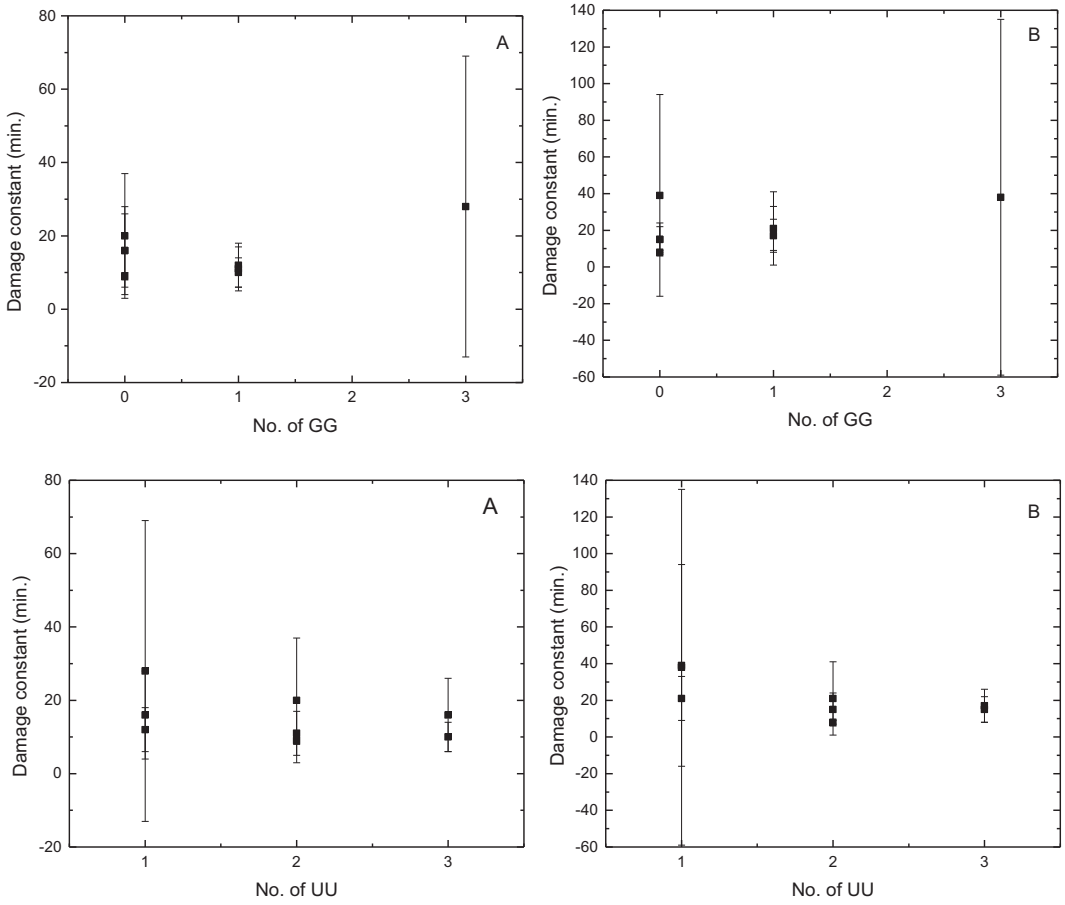

Figure B.22: Damage kinetics as function of number of guanine and uracil doublets for experiment 3. 'A' and 'B' represents kinetics of replicates.

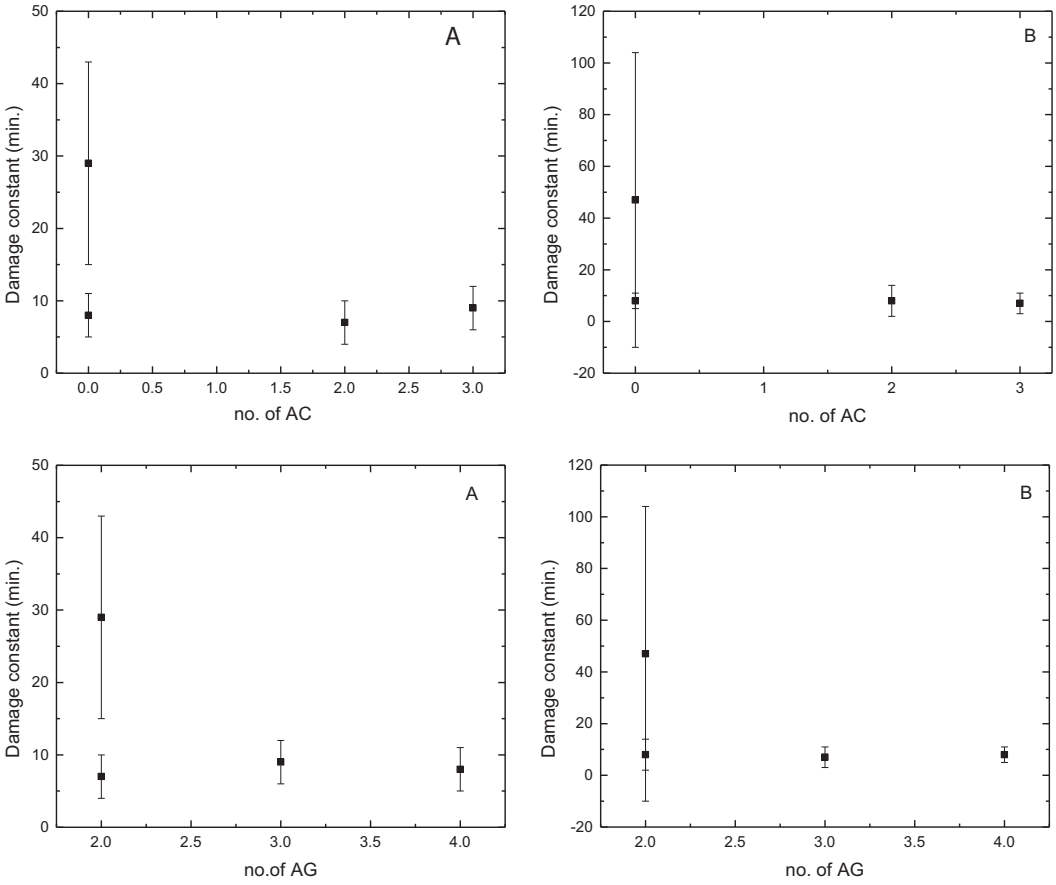

Figure B.23: Damage kinetics as function of number of ACs and AGs for experiment 1. 'A' and 'B' represents kinetics of replicates.

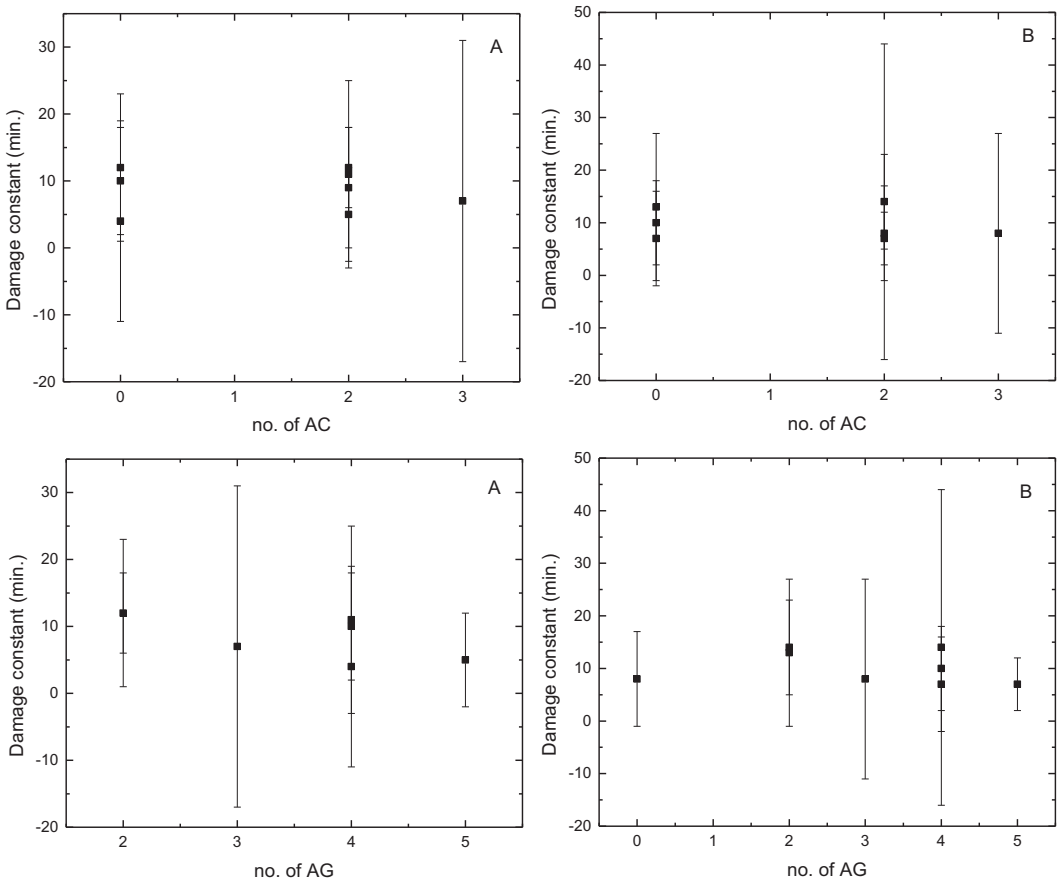

Figure B.24: Damage kinetics as function of number of ACs and AGs for experiment 2. 'A' and 'B' represents kinetics of replicates.

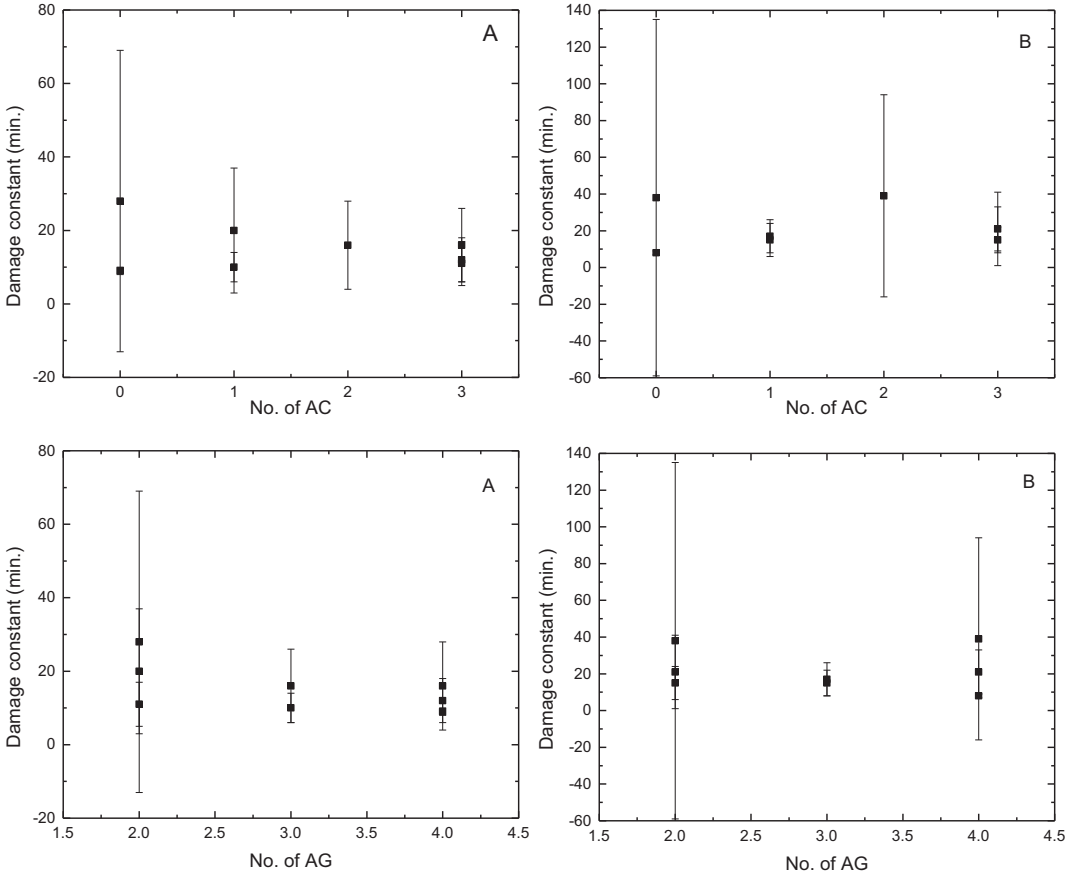

Figure B.25: Damage kinetics as function of number of ACs and AGs for experiment 3. 'A' and 'B' represents kinetics of replicates.

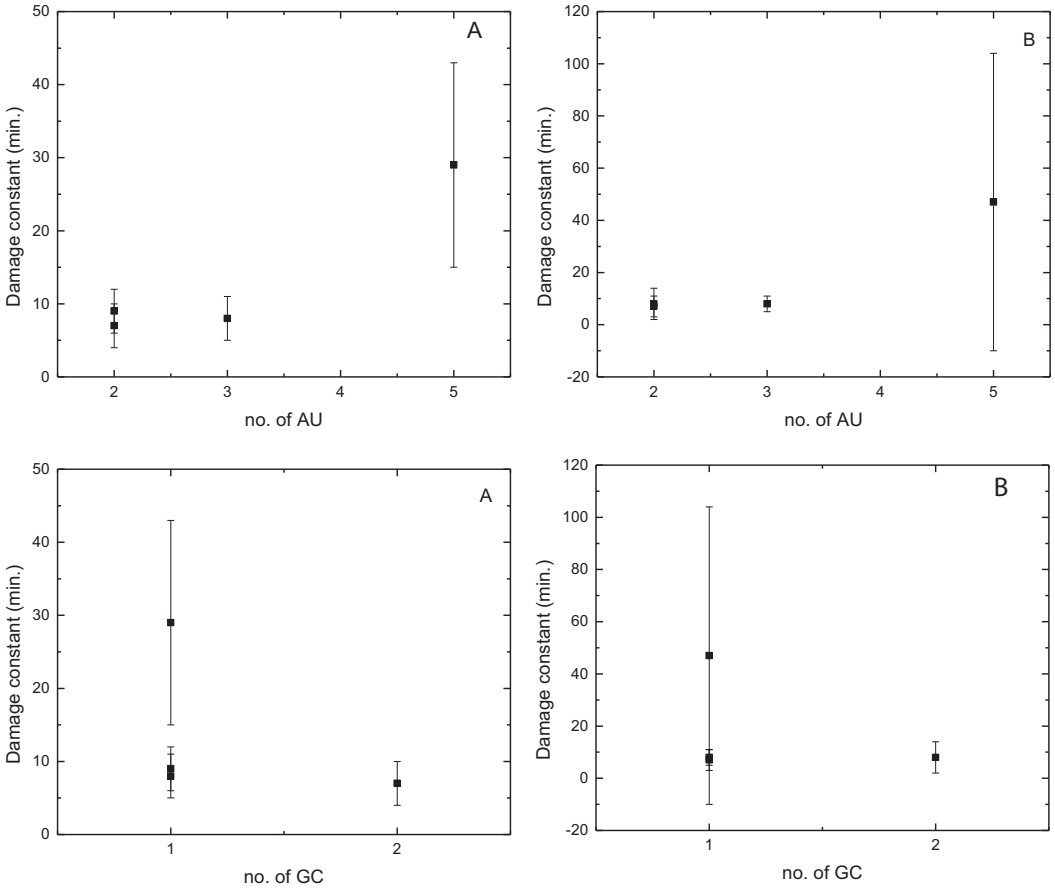

Figure B.26: Damage kinetics as function of number of AUs and GCs for experiment 1. 'A' and 'B' represents kinetics of replicates.

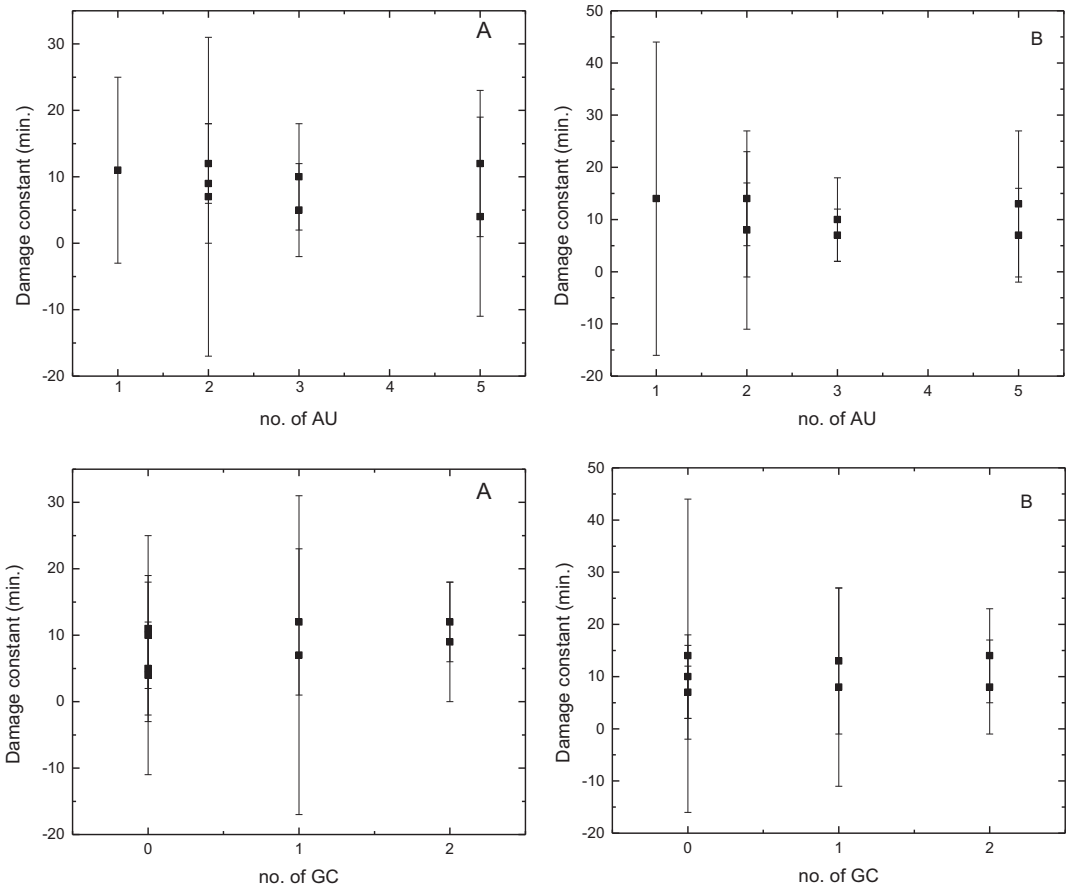

Figure B.27: Damage kinetics as function of number of AUs and GCs for experiment 2. 'A' and 'B' represents kinetics of replicates.

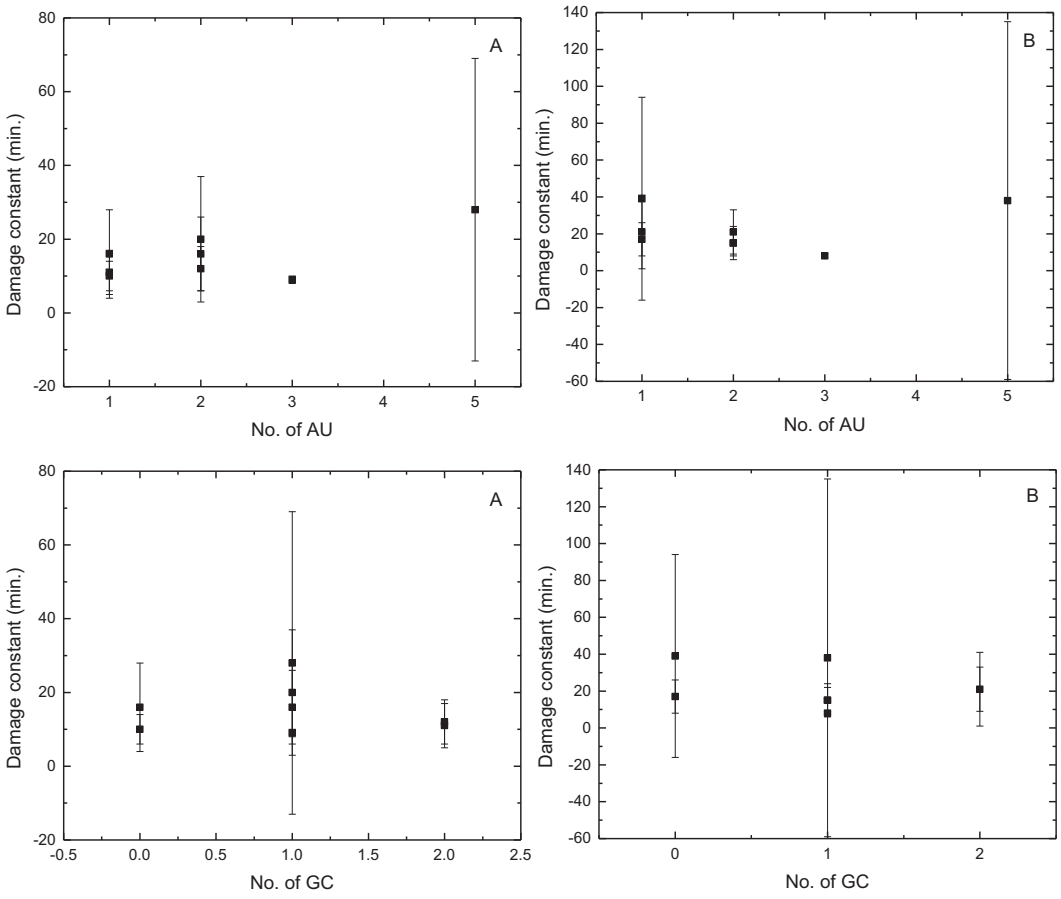

Figure B.28: Damage kinetics as function of number of AUs and GCs for experiment 3. 'A' and 'B' represents kinetics of replicates.

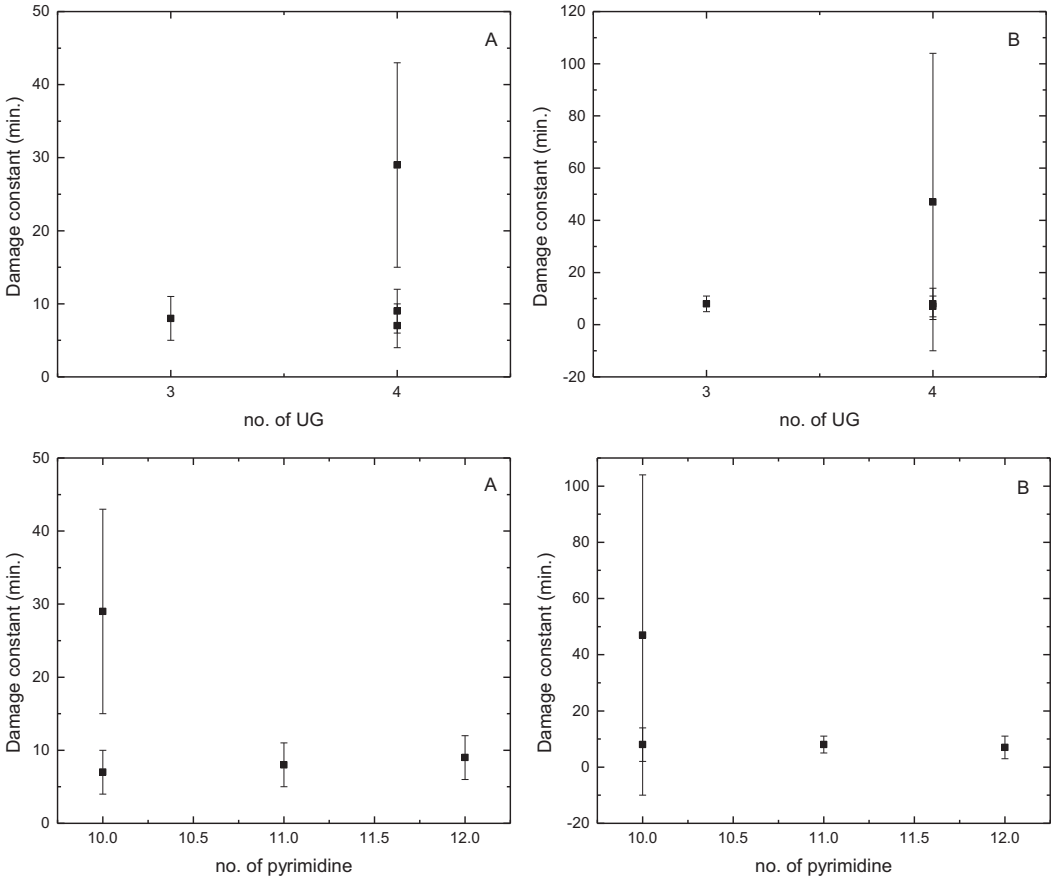

Figure B.29: Damage kinetics as function of number of UGs and pyrimidines for experiment 1. 'A' and 'B' represents kinetics of replicates.

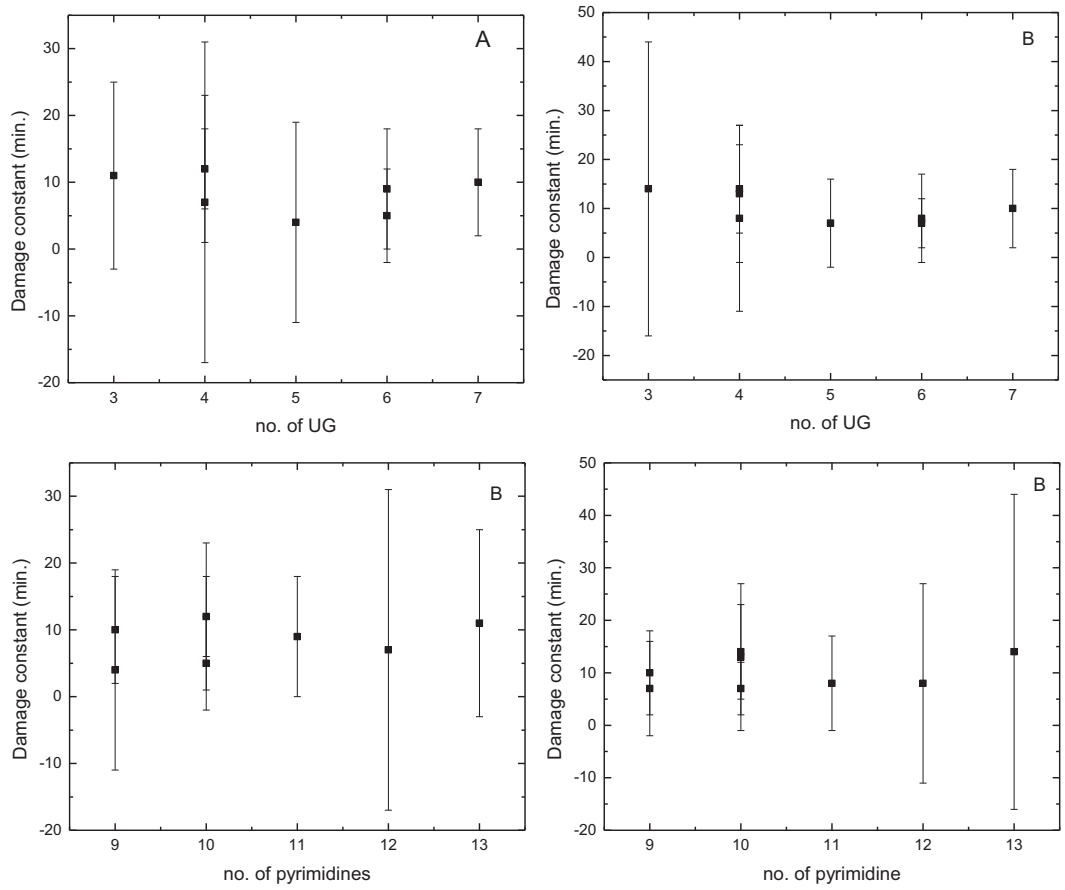

Figure B.30: Damage kinetics as function of number of UGs and pyrimidines for experiment 2. 'A' and 'B' represents kinetics of replicates.

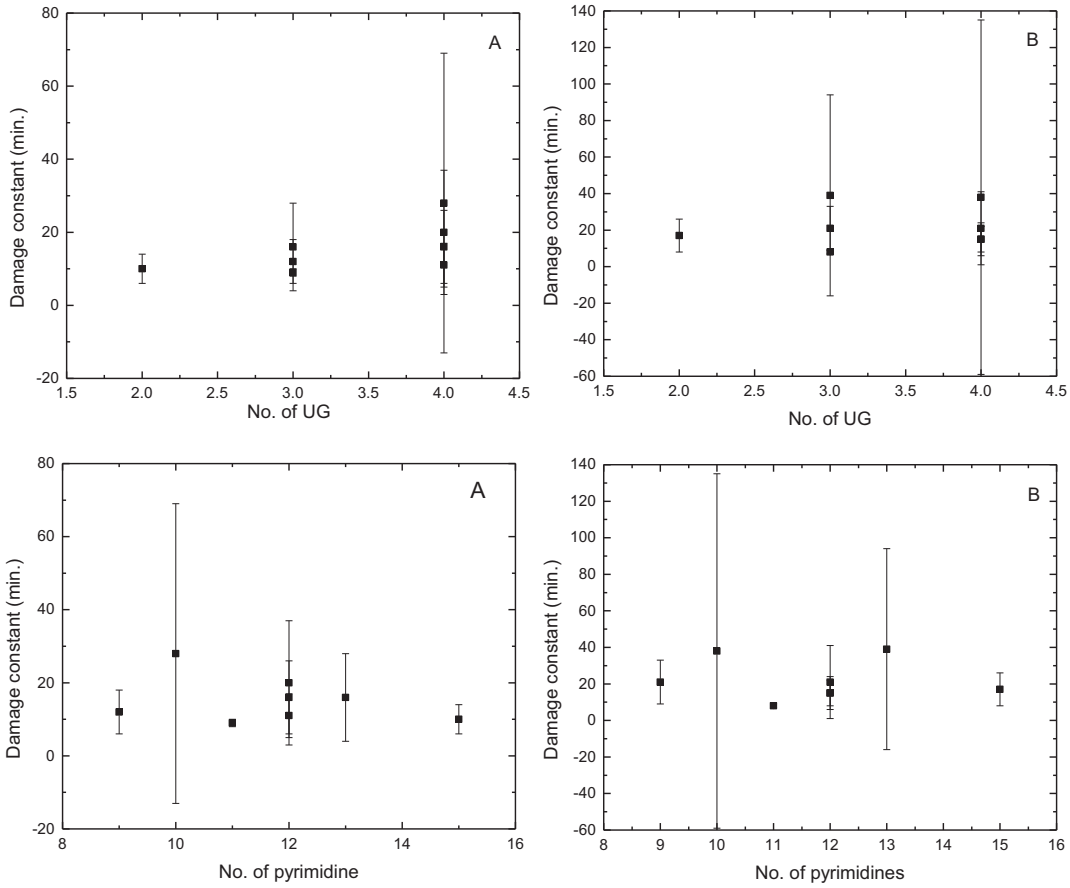

Figure B.31: Damage kinetics as function of number of UGs and pyrimidines for experiment 3. 'A' and 'B' represents kinetics of replicates.

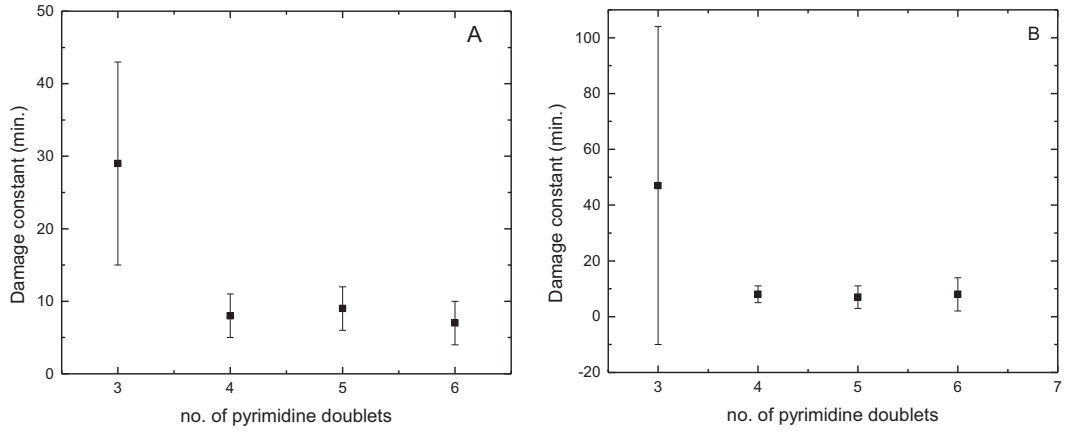

Figure B.32: Damage kinetics as function of number of pyrimidine doublets for experiment 1. 'A' and 'B' represents kinetics of replicates.

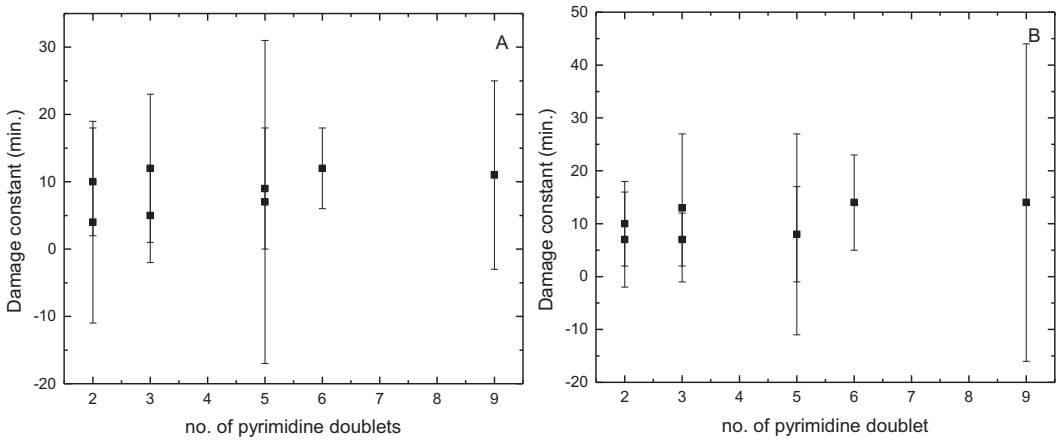

Figure B.33: Damage kinetics as function of number of pyrimidine doublets for experiment 2. 'A' and 'B' represents kinetics of replicates.

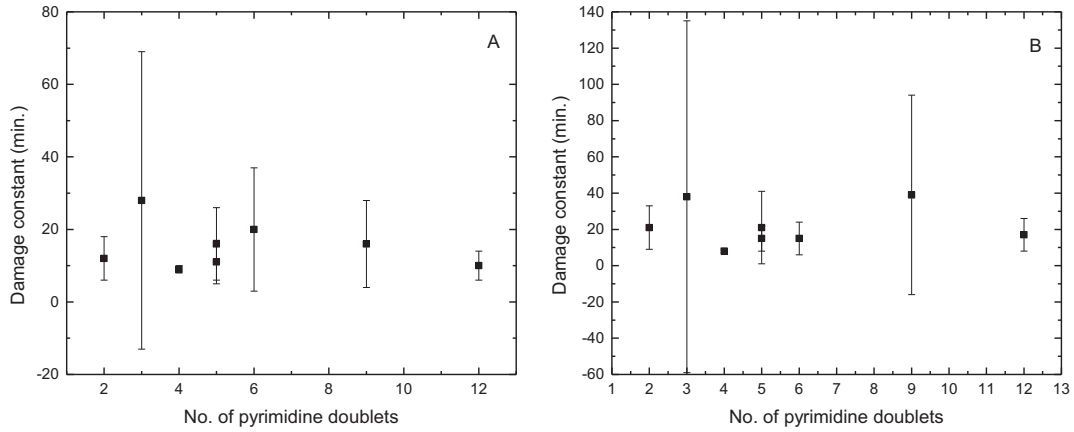

Figure B.34: Damage kinetics as function of number of pyrimidine doublets for experiment 3. 'A' and 'B' represents kinetics of replicates.